POSTER 2026

PROCEEDINGS OF THE INTERNATIONAL STUDENT SCIENTIFIC CONFERENCE POSTER – 30/2026

CTU CZECH TECHNICAL UNIVERSITY IN PRAGUE
FACULTY OF ELECTRICAL ENGINEERING CTU IN PRAGUE
ROHDE&SCHWARZ Make ideas real
IPCEI Microelectronics and Communication Technologies

ISBN 978-80-01-07549-4
Proceedings of the International Student Scientific Conference Poster – 30/2026
Published by the Czech Technical University in Prague in 2026
Faculty of Electrical Engineering
First electronic edition
Number of pages: 189

PROCEEDINGS OF THE INTERNATIONAL STUDENT SCIENTIFIC CONFERENCE POSTER – 30/2026

The objective of the international scientific student conference POSTER 2026 is to provide an international forum for presentation of undergraduate and postgraduate student research work in fields related to electrical engineering.

All contributions were presented as posters in seven parallel sections at the Faculty of Electrical Engineering, Czech Technical University in Prague on May 14, 2026.

The international student conference POSTER 2026, organized by the Faculty of Electrical Engineering, Czech Technical University in Prague, started as an internal meeting of doctoral students in 1995. In 1997, the first International Student Conference POSTER was held. On May 14, 2026 we organized the Conference for the 30th time. As in previous years the conference was held in cooperation with the Faculty of Biomedical Engineering and Faculty of Information Technology.

One of the main goals of the POSTER conference is to promote discussions and interactions among postgraduate and undergraduate students from various countries, universities and fields of study related to electrical engineering. Another important goal is to support independent creative work of students and stimulate practical application of acquired theoretical knowledge since we consider the students' research activity an inevitable part of the whole educational process at all universities.

Students can submit either a two-page abstract or a four-page full paper for publication. They can also opt out of publication of their contributions. A novelty this year was the introduction of a „Work-in-Progress“ category. These contributions are not published.

The program committee of Poster 2026 conference selected a total of 74 papers for presentation at the conference. The contributions are divided into seven sections:

- Biomedical Engineering
- Communications
- Electronics and Instrumentation
- History of Science and Technology
- Informatics and Cybernetics
- Natural Sciences
- Power Engineering

A total of 39 contributions come from Czech Technical University in Prague, 2 from other Czech universities and 33 contributions are from abroad. Criteria of acceptance were based on the originality of scientific contribution and good English. Each paper was reviewed by at least two members of the respective section of the Technical Programme Committee.

We would like to thank all students who produced outstanding research results and contributed to this proceeding.

Last but not least, we would like to express our gratitude to all colleagues from the Office for Science, Research and International Relations and from the Computing and Information Centre who helped us a lot in preparation of the proceedings and organization of the conference.

Prague May 4, 2026

Libor Husník
on behalf of the Organizing Committee of POSTER 2026

LIST OF PAPERS

Paper ID	Title of the paper	First Author	Other Authors (if any)	Publication
BI01	Influence of light on the brain	Theodore Křenek		Full Paper (4 pages)
BI05	Growth-Driven Redesign of a 3D-Printed Pediatric Orthoprosthesis Based on Clinical Gait Observation	Lilli Anders		Full Paper (4 pages)
BI08	EMD methods for suppressing muscle artifacts	Lenka Jungmannová		Full Paper (4 pages)
BI10	Endovascular Laser Ablation: Influence of Wavelength and Fiber Geometry	Michal Zelený		Full Paper (4 pages)
BI11	Adaptive Self-tightening Donning Mechanism for Exoskeletons	Raphael Hoffmann	Lara Schweitzer	Full Paper (4 pages)
BI13	Active Upper Limb Exoskeleton for Arm Rehabilitation	Forouzan Salehi Fergeni	Mohamed Aziz Touahria, Marc Buehlmann	Full Paper (4 pages)
BI15	Discovering wave equations for nonlinear sound beams from data	Tereza Filipská		Full Paper (4 pages)
BI16	Model Predictive Control in the Critically Ill Rat	Lorenz Michael		Full Paper (4 pages)
BI17	In-Depth Phenotyping of White Matter Hyperintensities	Matteo Agresti		Extended Abstract - work in progress (2 pages)
BI19	EEG Artifact Classification using Machine Learning and Neural Networks on Clinically Collected Data	Franka Nordmann		Full Paper (4 pages)
C01	Silicon Nitride Photonic Splitters for Power Management in Short-Wave-Infrared Region	Viktória Pikulíková	Adam Petrovic	Full Paper (4 pages)
C03	A Proposal for a Communication Protocol for Distributed Measurement Systems with High Jitter	František Rusnák		Full Paper (4 pages)
C04	Towards Multi-Snapshot FDR-Controlled Localization for Emergency Response Radar	Christoph Loeser		Full Paper (4 pages)
EI01	Analytical eigenfrequencies approximation of perforated square plates	Aneta Furmanová		Full Paper (4 pages)
EI02	Distributed Wireless Structural Health Monitoring System for Aircraft Structures	Šimon Pecháček		Full Paper (4 pages)
EI03	Automated gm/ID Based Design of Analog Circuits using Genetic Algorithms	Matej Foukal		Full Paper (4 pages)
EI05	Device Simulation of a Fully Interdigitated Bidirectional Phase Control Thyristor	Vojtěch Brandštýl		Extended Abstract (2 pages)
EI07	Gallium oxide photonic devices for on-chip applications	Marek Zdurienčík		Extended Abstract (2 pages)
EI08	Polymer Waveguides with a Circular Core Shape Fabricated by the Microdosing Method	Lukas Veigl		Full Paper (4 pages)

Paper ID	Title of the paper	First Author	Other Authors (if any)	Publication
EI11	Testing a New Generation of Hardpix2 Devices Using the Timepix2 Detector at the CERN PS Beam	Ondrej Pavlas		Extended Abstract (2 pages)
EI12	Transport characterization of exfoliated layered tellurides as a platform for spin-orbit heterostructures	Lukáš Poklop		Extended Abstract - work in progress (2 pages)
HST02	Coal Mining Technologies and the Transformation of the Industrial Landscape: The Ostrava-Karviná Region from the Late 19th Century to Contemporary Conversion	Klára Ciesarová		Full Paper (4 pages)
HST03	Hydroelectric Beginnings on the Vltava: Engineering, Municipal Enterprise, and the Making of the Štvanice Power Plant (1880-1914)	Elisa Angeles		Full Paper (4 pages)
HST04	From Workers' Colonies to Post-war Housing Estates: Spatial and Social Transformations of Industrial Housing in Western Bohemia (from the end of the 19th century to the end of the 1960s)	Tomas Jurica		Full Paper (4 pages)
HST05	Professor Antonín Svoboda's visit to Prague in January 1975: historical context, course and interpretation of archival sources	Jaroslav Kalvoda		Full Paper (4 pages)
HST06	Emanuel Šlechta: Professor, Innovator, and Entrepreneur in the Interwar Period	Jiří Sedlacek		Full Paper (4 pages)
HST07	The Food Processor in Czechoslovakia (1930-1960): A Technological Object Between Planned Economy and Rationalization of Domestic Work	Martin Dominik Hrtus		Full Paper (4 pages)
HST08	Visual Sources for Business History and the History of Technology. Production, Quality Control, Logistic and Technology Transfer in the Case of Colombian Steam Locomotives Purchased from Skoda (1927-1932)	Jorge Alonso Rodriguez Ortiz		Full Paper (4 pages)
HST09	The Representation of the Earth on the Astronomical Clocks	David Knespl		Full Paper (4 pages)
HST10	Celdit between Autarky and Energy Security: The Electrochemical Cellulose Industry in Times of War II	Jacopo Basseta		Full Paper (4 pages)
HST11	The Role of Licensed AVRM Aircraft Clock Production in the Development of Industrial Wristwatch Manufacturing in Czechoslovakia in the 1950s	David Hamr		Full Paper (4 pages)
HST12	Building the Tunisian Educational System after Independence (1956-1965): the 1958 Reform and the Role of Mahmoud Messadi	Amani Mansouri		
HST13	The Walter Company	Daniel Kyselka		Full Paper
IC01	Towards Reliable Programmer Attribution in Educational Source Code	Marek Horváth		Extended Abstract (2 pages)
IC02	Statistical Evaluation of Source Code Metrics for Programming Style Identification	Matěj Džamba	Marek Horváth	Extended Abstract - work in progress (2 pages)

Paper ID	Title of the paper	First Author	Other Authors (if any)	Publication
IC03	Deep Learning Methods for Source Code Author Identification	Serhii Yemets	Marek Horváth	Extended Abstract - work in progress (2 pages)
IC04	Gamified Cybersecurity Training Environments for Phishing Awareness and Secure Digital Practices	Lenka Bubenkova		Extended Abstract (2 pages)
IC05	Estimation of slip and slide effects in urban rail vehicles	Jiří Nábělek		Extended Abstract (2 pages)
IC08	Multi-Objective Model Selection Pipeline for Network Flow Classification	Jan Svoboda		Extended Abstract (2 pages)
IC10	From Logic to Programming: A Computational Perspective on Transparent Intensional Logic	Samuel Novotný		Extended Abstract (2 pages)
NS01	Controlled Phase Transitions of a Water Droplets Observed using Advanced Environmental Scanning Electron Microscopy (A-ESEM)	Vojtěch Hlavička		Extended Abstract (2 pages)
NS03	Toward an Automated System for Indifactor Alignment using UNET Segmentation	Oliver Klimt		Extended Abstract - work in progress (2 pages)
NS04	Fusion Proton Spectrometry in Z-pinch Plasma	Marketa Vlckova		Full Paper (4 pages)
NS08	Fusion Proton Source Characterization in Z-pinch Discharges	Veronika Matějková		Full Paper (4 pages)
NS09	PsyTools: An Open-Source Python Toolbox for Standardized Psychoacoustic Analysis	Eugen-Maximilian Stangl	Julia Donnerer	Extended Abstract (2 pages)
PE01	LTO Battery Storage Revival: BMS Design Correction and Long-term Validation of 0 V Discharge Resilience	Hanna Hoch		Full Paper (4 pages)
PE05	Deciphering Relaxation Time Distributions in Prussian Blue-based Sodium-Ion Batteries	Roman Morozov	Tom Poehlmann	Full Paper (4 pages)
PE07	Evaluation of Heat Transfer and Mechanical Trade-offs in SLA-Printed Boron Nitride (BN) Composites	Adriana Nováková	Ondřej Pražák, Jaroslav Pazourek	Full Paper (4 pages)

Influence of light on the brain

Theodore KŘENEK[1]

[1]Dept. of Biomedical Technology, Czech Technical University, nám. Sítná 3105, 272 01 Kladno, Czech Republic

krenethe@cvut.cz

Abstract.

The human circadian rhythm is regulated by the suprachiasmatic nuclei of the hypothalamus, which are particularly sensitive to the blue component of light. Modern lifestyles expose individuals to artificial light at night, potentially contributing to sleep deprivation. This study investigated whether short-term exposure to intense bright light increases vigilance in partially sleep-deprived individuals and whether it potentially compensates for sleep-related reductions in alertness. EEG was recorded in a control group and a partially sleep-deprived group. After preprocessing, spectral analysis was performed to estimate power in the alpha (8–13 Hz) and beta (13–30 Hz) frequency bands associated with vigilance. Light exposure increased alpha and beta power in both groups. However, between-group differences in power changes were not statistically significant. These findings suggest that bright light exposure enhances electrophysiological markers of alertness irrespective of prior sleep duration.

Keywords

EEG, intense light exposure, partial sleep deprivation, cognitive performance, FieldTrip.

1. Introduction

Vigilance is necessary for humans to adequately react to external stimuli. With vigilance lower than necessary, it would not be possible in the long-term for people to effectively interact with the external environment. Unfortunately, the right amount should not be taken for granted since it is influenced by a variety of outer and inner factors. Not only do metabolic processes have an influence, but also the amount of physical activity. For instance, a healthy lifestyle, including psychological well-being, a balanced diet, a regular daily routine, and exercising, has a positive effect.

Unfortunately, it is impossible in today's society to always eliminate all the negative factors, since they include unhealthy life habits, taking certain medication or sleep deprivation. In fact, sleep deprivation, whether partial or complete, represents a frequent problem not only in adolescents, but also in adults.

Sleep deprivation is nowadays a widespread phenomenon. Not only are students sacrificing sleeping time to study or party, but also some professions face a considerable risk of insufficient sleep. According to a survey by The Medical Defense Union [1], up to 90 % of doctors surveyed said that due to the nature of their profession, they do not get enough sleep, and 35 % of doctors surveyed said that lack of sleep has greatly affected their ability to care for patients.

However, sleep deprivation affects a wider range of professions. In addition to doctors, it also affects firefighters, approximately 60 % according to [2], and other healthcare professionals according to [3]. The risk of reduced sleep duration affects virtually all shift workers, from public transport operators and managers to catering staff.

This paper aims to analyse the impact of bright light exposure on the human brain, more specifically, whether or how this exposure changed the level of vigilance reduced by partial sleep deprivation. With further research, the bright light exposure could become a supporting treatment to individuals with sleep-affecting disorders.

2. Methods

This study consisted of several main steps: acquisition of the EEG dataset, preprocessing the data, spectral analysis, and finally, statistical evaluation to determine the significance of changes. For calculations, Matlab 2024b was used in combination with the open-source Fieldtrip toolbox [4] designed for EEG analysis in Matlab.

2.1. Dataset

The dataset was obtained from researchers at the National Institute of Mental Health, and the study protocol was approved by the local Ethics Committee. A total of 47 participants (29 women and 18 men) were included in the study, with a mean age of 16.89 ± 1.85 years. Participants were assigned to one of two groups: a control group (n = 25), whose members slept for eight hours, and a partially sleep-deprived (SD) group (n = 22), whose members slept for four to five

hours. Participants with a history of neurological, psychiatric, or sleep disorders were excluded from the study. Additional exclusion criteria included the use of medications affecting sleep or vigilance, daily caffeine consumption exceeding 300 mg, and a history of substance abuse.

2.2. Protocol of measurement

EEG recordings were obtained in two experimental sessions. The first session was conducted immediately after awakening in a controlled sleep laboratory environment in the morning. The second session took place immediately following a 10-minute exposure to bright light in a dedicated light pavilion. During each session, EEG activity was recorded using a 22-channel montage based on the international 10–20 electrode placement system. Signals were sampled at 1 kHz and recorded with an average reference. Bright light exposure was provided by a high-intensity LED light source (172,500 lm) with a balanced full-spectrum emission profile comparable to natural daylight (patent US 2021/0164624 A1).

2.3. Preprocessing

EEG signals are inherently contaminated by a variety of artifacts originating from both biological and technical sources. Biological artifacts commonly observed in EEG include ocular movements and blinks, cardiac activity, and muscle activity. Eye movements and blinks predominantly affect low-frequency components (< 8 Hz), whereas cardiac and muscle activity can introduce high-frequency noise (> 30 Hz). Spectral analysis focused on the alpha (8–13 Hz) and beta (13–30 Hz) frequency bands. As the first step, the data were downsampled to 250 Hz. Subsequently, the data were filtered by using a band-pass FIR filter between 8 and 30 Hz using a Hamming window to minimize phase distortion and ensure precise temporal alignment. Movement-related artifacts were minimized during data acquisition by continuous monitoring of participants, who were instructed to remain still throughout the recordings. [4]

Residual muscle activity and saccadic/microsaccadic eye movements were not removed, as doing so would have required exclusion of substantial time periods from the analysis, potentially biasing spectral estimates. Their influence on the alpha and beta bands is minimal and unlikely to confound the results.

2.4. Spectral analysis

Spectral analysis was performed to quantify the distribution of power across frequency bands relevant to vigilance. Epoching was not applied, as each recording was treated as a single continuous trial to preserve frequency resolution. For each participant, the preprocessed EEG signals were subjected to a multitaper Fourier transform (MTM-FFT) using the FieldTrip toolbox [5]. The multitaper approach improves the signal-to-noise ratio by applying multiple orthogonal tapers, reducing variance in power spectral estimates. This method is particularly suitable for single-trial EEG data, where conventional averaging across trials is not possible. Hanning tapers were applied to further minimize spectral leakage.

Power spectral density (PSD) was calculated for each channel and session, with particular focus on the alpha (8–13 Hz) and beta (13–30 Hz) bands. Both absolute and relative power values were extracted. Absolute power represents the raw energy within a frequency band, while relative power reflects the proportion of total spectral power contained in that band. The choice to analyze these specific bands is supported by their established association with vigilance and cognitive performance in the literature [6, 7, 8].

2.5. Statistics

All statistical analyses were conducted using non-parametric permutation tests with 1,000 randomizations, which are robust to violations of normality and homogeneity of variance [9, 10]. Within-group comparisons of absolute alpha and beta power before and after light exposure were assessed using paired permutation tests. Between-group comparisons of the change in power were assessed using unpaired permutation tests.

For all analyses, a significance threshold of $p < 0.05$ was applied. Bonferroni correction was employed to control for multiple comparisons across electrodes, preserving sensitivity to spatially extended effects.

In addition to permutation-based hypothesis testing, effect sizes were quantified using Cohen's d. For within-group comparisons, Cohen's d was calculated as the mean difference between pre- and post-exposure measurements divided by the standard deviation of the differences. For between-group comparisons, Cohen's d was computed using pooled standard deviations of change scores.

Comparison of changes within groups

To compare the absolute power spectrum values, the following hypotheses were chosen:

- H_0: Within individual groups, there is no difference in power in selected frequency spectra before and after exposure to light.

- H_A: Within individual groups, there is a difference in power in selected frequency spectra before and after light exposure.

Comparison of differences between individual groups

To compare the absolute power spectrum, were formulated:

- H_0: There is no difference in power between the individual groups in the selected frequency spectra.
- H_A: There is a difference in power between the individual groups in the selected frequency spectra.

3. Results

Permutation testing of EEG band power showed a slight increase in the control group in both the alpha and beta frequency bands when comparing measurements obtained before and after light exposure. The associated t-statistics were positive in both bands. In the alpha band, statistically significant effects were observed over frontal electrodes (Cohen's $d \approx 0.3$), whereas in the beta frequency band significant effects were detected over both frontal and temporal electrodes (Cohen's $d \approx 0.35$, small-to-moderate effect), as shown in Fig. 1.

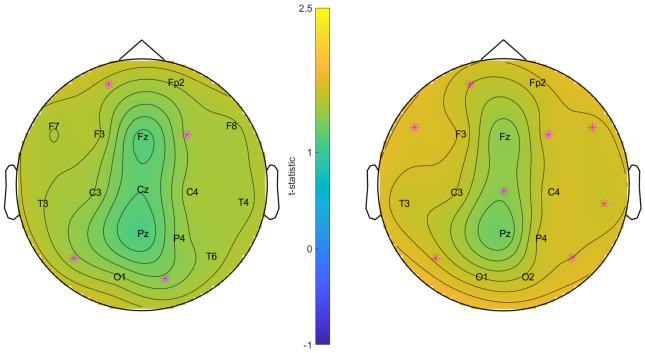

Figure 1. Within control group t-statistics; left: alpha, right: beta.

In the partially sleep-deprived group, permutation testing revealed a statistically significant increase across nearly all electrodes. The only exception was the central electrodes in the alpha band, where a decrease in band power was observed after light exposure. The comparison of pre- and post-exposure measurements is illustrated by the topographic maps in 2. In the alpha band, the frontal cortex and temporal lobes showed a moderate effect with Cohen's $d \approx 0.4$, whereas the effect was comparatively lower in the other parts of the brain. In the beta band, the effect was moderate, approximately 0.5, in the entire brain except for electrodes placed on the midline.

For the between-group analysis, the resulting t-statistics were negative, and no electrodes reached statistical significance after correction. Consequently, no significant differences between the groups were detected (see figure 3).

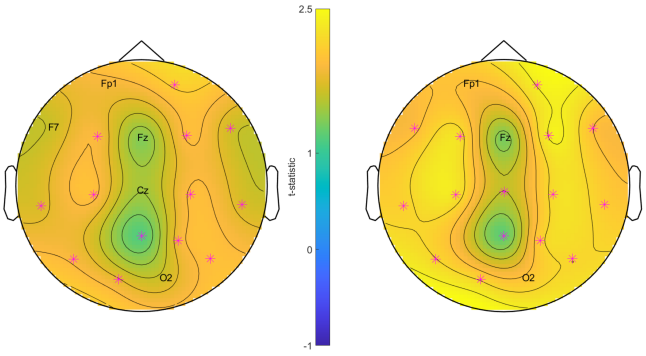

Figure 2. Within SD group t-statistics; left: alpha, right: beta.

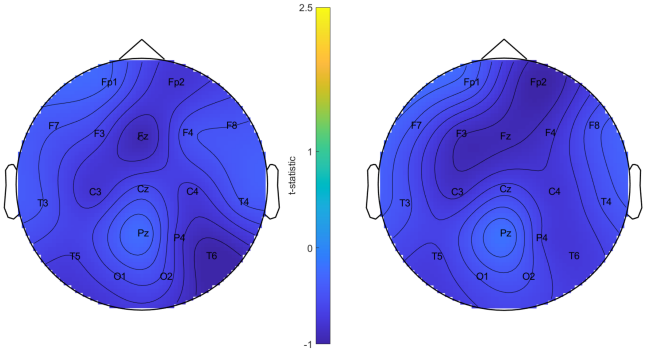

Figure 3. Between group t-statistics; left: alpha, right: beta.

4. Discussion

This study evaluated the EEG power spectrum in terms of absolute band power values, which are commonly used in the literature and are less affected by the loss of overall signal variability.

The control group showed a slight increase in alpha and beta band power after light exposure. Alpha and beta bands are frequently discussed in relation to vigilance and cognitive processing, although their functional interpretation depends on cortical location and task context [6, 8], suggesting a modest enhancement of alertness in this group. In the partially sleep-deprived group, the increase in alpha and beta band power was statistically significant, indicating a stronger effect of light exposure on alertness in sleep-deprived individuals. Although within-group effects appeared numerically larger in the sleep-deprived group, the between-group comparison did not reach statistical significance. Therefore, the data do not support a differential compensatory effect of light exposure in partially sleep-deprived individuals.

Bright light exposure produced small-to-moderate increases in alpha and beta power in both groups. Effect sizes were consistently larger in the sleep-deprived group; however, between-group differences did not reach statistical significance. This suggests that, although both groups exhibited increased alpha and beta activity after light exposure, the magnitude of these changes did not differ significantly be-

	Cohens d					
	SD group		control group		between groups	
electrode	alpha	beta	alpha	beta	alpha	beta
Fp1	0.40	0.42	0.33	0.34	-0.11	-0.12
Fp2	0.45	0.51	0.32	0.35	-0.24	-0.31
F3	0.40	0.48	0.32	0.36	-0.19	-0.27
F4	0.41	0.51	0.31	0.35	-0.16	-0.25
C3	0.42	0.49	0.30	0.34	-0.24	-0.25
C4	0.42	0.47	0.31	0.35	-0.23	-0.24
P3	0.43	0.51	-0.07	-0.12	-0.40	-0.40
P4	0.39	0.45	0.29	0.35	-0.23	-0.20
O1	0.38	0.46	0.31	0.34	-0.18	-0.16
O2	0.36	0.43	0.29	0.35	-0.19	-0.16
F7	0.35	0.41	0.32	0.37	-0.14	-0.14
F8	0.35	0.42	0.32	0.35	-0.14	-0.15
T3	0.37	0.45	0.32	0.35	-0.14	-0.15
T4	0.36	0.45	0.31	0.35	-0.14	-0.16
T5	0.40	0.47	0.31	0.35	-0.22	-0.21
T6	0.42	0.47	0.31	0.36	-0.32	-0.23
Fz	0.29	0.28	0.25	0.29	-0.29	-0.28
Cz	0.31	0.34	0.26	0.29	-0.17	-0.18
Pz	0.25	0.26	0.24	0.27	-0.07	-0.06
AFz	0.33	0.36	0.27	0.34	-0.17	-0.15

Table 1. Effect sizes

tween the control and partially sleep-deprived groups. These results are therefore more consistent with a general alerting effect of light rather than a specific compensatory mechanism.

An increase in beta activity, a potential alerting effect, and an emotional regulatory effect of light exposure were also reported by Kopřivová et al. [11] in the same adolescent sample. While the present study employed a sensor-level spectral analysis across all electrodes, Kopřivová et al. performed a source-level analysis, identifying neural sources of activity in the right insula and fronto-parietal regions. Despite these methodological differences, both approaches showed consistent electrophysiological findings.

Increased power in both beta and alpha bands across most brain regions under bright light was also reported by Luo et al. [12]. Although their study was conducted on healthy adult, not adolescent, individuals and the duration of light stimulation was considerably longer (5 hours vs. 10 minutes), their findings are consistent with those of of the present study.

The study has several limitations. First, the standard 10–20 EEG electrode system lacks sufficient spatial resolution to evaluate increases in power in individual cortical regions. High-density EEG would provide more precise source localization. Since the aim of this study was not to perform exact source analysis, the standard 10–20 system was sufficient for band power estimation at the sensor level. Second, the relatively small sample size may have limited the statistical power of between-group comparisons. Therefore, it is possible that a differential compensatory effect of light exposure exists but could not be detected with the present sample size. Future studies with a larger number of participants would help clarify whether bright light exposure has a specific compensatory effect in sleep-deprived individuals. Third, since this study focused on adolescents, results may not generalize to adult populations or younger children. Last, this study did not include any behavioural or cognitive performance measures, relying solely on EEG.

Understanding the electrophysiological responses to light exposure could have broad practical relevance — from medical workers and shift workers needing to rapidly restore cognitive function, to healthy individuals seeking cognitive enhancement, and those with sleep-related disorders. More broadly, bright light exposure represents a non-invasive and widely accessible intervention that may benefit alertness across a wide range of populations.

5. Conclusion

Short-term bright light exposure increased alpha and beta band power in both rested and partially sleep-deprived adolescents. However, no differential compensatory effect was observed. Bright light may enhance electrophysiological markers associated with alertness, but further research is required to determine its behavioral relevance.

References

1. UNION, The Medical Defence. Doctors More Sleep Deprived Now than after the Pandemic [online]. [N.d.] [visited on 2025-05-24]. Available from: https://www.themdu.com/press-centre/press-releases/doctors-more-sleep-deprived-now-than-after-pandemic.
2. LOCIHOVÁ, Hana; KUPČÍKOVÁ BŘEGOVÁ, Bohdana; ZITTOVÁ, Renata; HRUŠKOVÁ, Jana; BAHULOVÁ, Monika. Sleep Quality of Paramedics in the Czech Republic. *Kontakt* [online]. 2024, pp. 153–159 [visited on 2025-05-24]. ISSN 12124117, ISSN 18047122. Available from DOI: 10.32725/kont.2024.019.
3. KUJAWSKI, Sławomir; SŁOMKO, Joanna; TAFIL-KLAWE, Małgorzata; ZAWADKA-KUNIKOWSKA, Monika; SZRAJDA, Justyna; NEWTON, Julia L.; ZALEWSKI, Paweł; KLAWE, Jacek J. The Impact of Total Sleep Deprivation upon Cognitive Functioning in Firefighters. *Neuropsychiatric Disease and Treatment*. 2018, vol. 14, pp. 1171–1181. ISSN 1176-6328. Available from DOI: 10.2147/NDT.S156501.
4. OOSTENVELD, Robert; FRIES, Pascal; MARIS, Eric; SCHOFFELEN, Jan-Mathijs. FieldTrip: Open

Source Software for Advanced Analysis of MEG, EEG, and Invasive Electrophysiological Data. *Computational Intelligence and Neuroscience* [online]. 2011, vol. 2011, pp. 1–9 [visited on 2025-05-13]. ISSN 1687-5265, ISSN 1687-5273. Available from DOI: 10.1155/2011/156869.

5. MITRA, P.P.; PESARAN, B. Analysis of Dynamic Brain Imaging Data. *Biophysical Journal* [online]. 1999, vol. 76, no. 2, pp. 691–708 [visited on 2026-02-07]. ISSN 00063495. Available from DOI: 10.1016/S0006-3495(99)77236-X.
6. FERREIRA, Camila; DESLANDES, Andréa; MORAES, Helena; CAGY, Maurício; POMPEU, Fernando; BASILE, Luis Fernando; PIEDADE, Roberto; RIBEIRO, Pedro. Electroencephalographic Changes after One Nigth of Sleep Deprivation. *Arquivos de Neuro-Psiquiatria* [online]. 2006, vol. 64, pp. 388–393 [visited on 2025-03-28]. ISSN 0004-282X. Available from DOI: 10.1590/S0004-282X2006000300007.
7. HANZAL, Simon; LEARMONTH, Gemma; THUT, Gregor; HARVEY, Monika. *EEG Markers of Vigilance, Task-Induced Fatigue and Motivation during Sustained Attention: Evidence for Decoupled Alpha- and Beta-Signatures* [online]. 2024-10-18. [visited on 2026-02-20]. Available from DOI: 10.1101/2024.10.16.618638.
8. KAMZANOVA, Altyngul T.; KUSTUBAYEVA, Almira M.; MATTHEWS, Gerald. Use of EEG Workload Indices for Diagnostic Monitoring of Vigilance Decrement. *Human Factors: The Journal of the Human Factors and Ergonomics Society* [online]. 2014, vol. 56, no. 6, pp. 1136–1149 [visited on 2025-05-26]. ISSN 0018-7208, ISSN 1547-8181. Available from DOI: 10.1177/0018720814526617.
9. KIM, Tae Kyun. T Test as a Parametric Statistic. *Korean Journal of Anesthesiology* [online]. 2015, vol. 68, no. 6, p. 540 [visited on 2025-12-23]. ISSN 2005-6419, ISSN 2005-7563. Available from DOI: 10.4097/kjae.2015.68.6.540.
10. NICHOLS, Thomas E.; HOLMES, Andrew P. Nonparametric Permutation Tests for Functional Neuroimaging: A Primer with Examples. *Human Brain Mapping*. 2002, vol. 15, no. 1, pp. 1–25. ISSN 1065-9471. Available from DOI: 10.1002/hbm.1058.
11. KOPŘIVOVÁ, Jana; KAŇKOVÁ, Zuzana; VLČEK, Přemysl; PIORECKÝ, Marek; MAIEROVÁ, Lenka; BENDOVÁ, Zdeňka; SKÁLOVÁ, Kateřina; NEKOVÁŘOVÁ, Tereza. Bright Light Exposure Reduces Negative Affect and Modulates EEG Activity in Sleep-Deprived and Well-Rested Adolescents. *Frontiers in Behavioral Neuroscience* [online]. 2025, vol. 19 [visited on 2026-03-09]. ISSN 1662-5153. Available from DOI: 10.3389/fnbeh.2025.1673093.
12. LUO, Xue; RU, Taotao; CHEN, Qingwei; HSIAO, Fan-Chi; HUNG, Ching-Sui; YANG, Chien-Ming; ZHOU, Guofu. Temporal Dynamics of Subjective and Objective Alertness During Exposure to Bright Light in the Afternoon for 5 h. *Frontiers in Physiology* [online]. 2021, vol. 12 [visited on 2026-03-09]. ISSN 1664-042X. Available from DOI: 10.3389/fphys.2021.771605.

Acknowledgements

Research described in this paper was supervised by doc. Ing. Marek Piorecký, Ph.D., FBMI ČVUT in Prague and National Institute of Mental Health. The author would like to express gratitude for his patience, guidance, insightful feedback, and valuable advice during the preparation of this paper.

The author would also like to thank PhDr. Jana Kopřivová, Ph.D., National Institute of Mental Health, for providing an interesting study and the opportunity to work on such a topic.

About Authors...

Theodore KŘENEK was born in Frýdek-Místek and grew up in Turnov. He is currently completing his bachelor's degree in Biomedical Technology at the Faculty of Biomedical Engineering, Czech Technical University in Prague, where he intends to continue with a master's degree program.

Growth-Driven Redesign of a 3D-Printed Pediatric Orthoprosthesis Based on Clinical Gait Observation

Lilli ANDERS[1]

[1]Chair of Medical Information Technology, RWTH Aachen, Pauwelsstraße 20, 52074 Aachen

anders@hia.rwth-aachen.de

Abstract. *Early gait acquisition is a critical milestone in child development but can be significantly delayed in children with congenital lower limb deficiencies such as fibular hemimelia. Assistive devices can support early mobility; however, many pediatric prosthetic solutions are designed for older patients and often fail to address the rapid growth and anatomical variability of toddlers.*

This work presents a case study understanding the functional development of a toddler using a modular 3D-printed orthoprosthesis during early gait development. Clinical observations conducted during regular hospital follow-ups were used to analyze gait progression and identify limitations of both the initial orthoprosthesis and a subsequently used clinical prosthetic device. Based on these findings, design requirements for an adapted orthoprosthesis were obtained.

A redesigned modular orthoprosthesis was developed using additive manufacturing, combining improved load distribution, ventilation and growth-adaptable structural components. The observations provide practical insights for the adaptation of pediatric orthoprosthetic designs to the changing functional requirements that occur during early walking development.

Keywords

Additive Manufacturing, CAD Design, Observational Gait Analysis, Fibular Hemimelia, Pediatric Orthoprosthesis.

1. Introduction

Independent walking typically emerges between 18 and 24 months of age and represents a critical milestone in early childhood development. The acquisition of gait contributes significantly to neuromuscular coordination, balance control and motor learning [1, 2].

For children with congenital lower limb deficiencies, such as fibular hemimelia, this developmental process can be severely impaired, delaying independent mobility and limiting opportunities for physical and social participation in daily life. Fibular hemimelia is the most common congenital longitudinal deficiency affecting the lower limb and is frequently associated with limb length discrepancy, joint instability and structural abnormalities of the knee and foot, which can significantly compromise weight-bearing and gait development [3, 4].

Early orthotic and prosthetic intervention is therefore essential to support functional mobility and promote biomechanical development during early childhood. However, many pediatric assistive devices are derived from systems designed for older children or adults and often fail to address the rapid growth, anatomical variability and biomechanical characteristics of toddlers [5]. These devices can be heavy, rigid and require frequent replacement as the child grows.

Recent advances in additive manufacturing have introduced new opportunities for the design and fabrication of customized orthotic and prosthetic devices. Techniques such as fused deposition modeling enable rapid prototyping, cost-effective production and patient-specific geometries that can be adapted to individual anatomical requirements [6]. These capabilities are particularly beneficial in pediatric rehabilitation, where assistive devices must frequently be adapted as children grow. Building on previous work on a modular 3D-printed orthoprosthesis for toddlers with fibular hemimelia [2], this study evaluates the functional development of a child using the device during early gait development. Clinical observations collected during this period are used to identify design requirements for an adapted orthoprosthesis that responds to the evolving functional needs of the child while maintaining the successful principles of the original design.

2. Early Use of the Orthoprosthesis

2.1. Functional Development During Device Usage

Functional development was monitored through regular clinical follow-ups with physicians and physiotherapists at the hospital. During these assessments, the child's gait development and interaction with the orthoprosthesis were documented through observational evaluation.

The child used the same 3D-printed orthoprosthesis for approximately six months and showed strong acceptance of the device, using it as a natural extension of the limb. During this period, the device supported the early stages of walk-

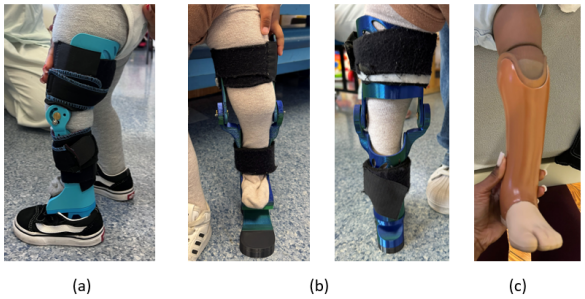

Fig. 1. Comparison of orthoprosthetic devices (timeline). (a) Initial 3D-printed orthoprosthesis used during early gait development. (b) Child seated in the initial orthoprosthesis after outgrowing the device. (c) Clinical prosthetic device provided by the hospital, featuring a wider socket enclosing the lower limb and foot.

ing and the development of balance and knee control. After six months of use, the device fractured due to continuous mechanical loading and the increasing motor activity of the toddler. The modular design of the orthoprosthesis allowed a slightly enlarged version to be reprinted to adapt to the child's growth.

After approximately nine months of use, however, further reprinting and resizing of the device became increasingly difficult (Fig. 1(a)–(b)). The anatomical structure of the child's leg had changed significantly, requiring more substantial geometric and functional adaptations than simple scaling of the existing design could provide.

2.2. Transition to a Clinical Prosthetic Device

To ensure continuous mobility support, the hospital provided a clinical prosthetic device that allowed the child to insert the leg including the foot stamp directly into a prosthetic shell, as shown in Fig. 1(c). The foot orientation differs between the two devices. In the 3D-printed orthoprosthesis, the natural foot was positioned at approximately $35°$ of plantarflexion due to the geometry of the internal foot cavity (Fig. 1(a)). In the clinical prosthetic device, the foot is positioned at approximately $15°$. This adjustment allows the foot to be positioned more vertically within the device and eliminates the need for a separate natural foot cavity and an additional prosthetic foot component. Instead, the prosthetic shell itself provides the structural interface between the limb and the ground, simplifying the device geometry while still maintaining walking support.

2.3. Observational Gait Assessment

A functional gait assessment was performed at the hospital when the child first used the new clinical device. The aim was to evaluate how the child's gait had developed during the nine months of using the 3D-printed orthoprosthesis.

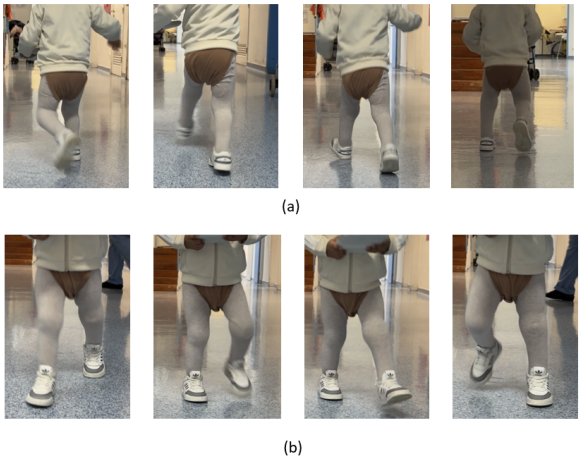

Fig. 2. Observational gait assessment performed at the hospital. (a) Posterior view and (b) frontal view of the child during walking. The image sequence indicates stable gait progression, upright posture, reduced compensatory arm use and controlled knee motion during stance and swing.

The assessment was based on visual observation of gait sequences and focused on clinically relevant criteria including knee control, bilateral limb loading, postural stability, movement symmetry, compensatory strategies and signs of neuromuscular adaptation.

Sequential frames of the gait cycle are shown in Fig. 2(a)–(b). The images indicate that the child is able to initiate gait independently and maintain continuous walking without external support. Upright trunk posture is maintained throughout the walking sequence and excessive body sway appears reduced compared to earlier walking stages. In addition, the arms are no longer prominently used for balance, showing improved postural control and reduced reliance on compensatory upper-body stabilization.

A key aspect of the functional development was the child's knee movement. The orthoprosthesis integrated three predefined knee flexion settings of $45°$, $60°$ and $90°$. The maximum flexion angle could be adjusted through a simple pin mechanism [2]. During the initial walking phase the joint was limited to $45°$ to provide the child with maximum stability. As the child gained confidence and motor control, the pin was repositioned to enable larger flexion angles of $60°$ and later $90°$. The walking sequences show that the child progressed from limited knee control to stable and functional use of the joint. Importantly, these movements occur without additional support at the thigh or knee region, meaning improved activation of the thigh musculature, particularly the quadriceps femoris, which contributes to active stabilization of the knee during walking. Visible weight transfer occurs between both limbs during stepping. The gait pattern appears continuous and relatively symmetric and the child maintains stable forward progression.

Taken together, these observations indicate signs of neuromuscular adaptation during walking. Compared with the earlier walking phase, the child appears to show improved

coordination of the lower limb, reduced compensatory arm use, more controlled knee motion and a gait pattern that more closely resembles typical toddler walking.

3. Design Motivation for the Adapted Orthoprosthesis

Tab. 1. Design requirements for the adapted orthoprosthesis

Clinical Device Limitation	Design Requirement
High device weight	Lightweight additively manufactured structure
Limited ventilation in socket	Open and breathable shell design
Load concentration near knee joint	Distributed load through thigh and calf support
Fixed prosthetic geometry	Modular and scalable components
Limited anatomical adaptability	Patient-specific geometry
Rigid structure	Controlled flexibility supporting natural gait

Although the clinical prosthetic device allows the child to maintain on going mobility, several limitations were identified. Based on these observations, the clinical team requested an adaptation of the previously developed 3D-printed orthoprosthesis.
As previously mentioned, the clinical prosthesis consists of a rigid socket into which the child inserts the leg. The device weighs approximately 500 g and is therefore more than twice as heavy as the initial orthoprosthetic device. In addition, it lacks sufficient ventilation, which may reduce comfort during prolonged use or in warm weather. Further, the limb is primarily suspended inside the prosthetic shell, which results in a concentration of load near the upper contact region close to the knee joint.
Another limitation of the clinical device is the lack of adaptability. The prosthesis is manufactured as a fixed structure and cannot easily be resized or modified as the child grows. Maintaining proper limb length alignment is important to prevent pelvic tilt, making growth adaptation particularly important at this early developmental stage.
The goal of the new design was to retain the functional advantages of the clinical solution while addressing its main limitations to improve comfort for the child. Based on these observations, a set of design requirements for the adapted orthoprosthesis was defined, as summarized in Table 1.

3.1. Design of the Adapted Orthoprosthesis

The adapted device follows a modular three-part design and builds upon the earlier structure, which had already demonstrated successful use. The redesign was guided by the design requirements identified in the previous section.

The back component forms the base of the orthoprosthesis and is connected to the foot platform (Fig. 4(b)). This element can either be printed as a single part together with the platform or printed separately and assembled using screws. The modular structure enables later height adjustments. If the child grows, an additional spacer plate can be inserted between the lower structure and the foot platform without redesigning the entire device.
The front component is connected to the back component via a hinge mechanism located on the right side of the orthoprosthesis (Fig. 4(a-b)). A threaded rod combined with two nuts secures this connection and forms the mechanical joint between both parts. The hinge mechanism allows the orthoprosthesis to open so that the child's leg can be inserted through the lateral opening into the internal leg cavity of the device (Fig. 3(c)). After positioning the leg, the orthoprosthesis is closed and secured using a Velcro-based closure system. The straps are guided around the limb from the posterior side and fastened across the anterior section. This fixation stabilizes the leg within the device and helps distribute the load along the limb rather than concentrating it at the knee joint. Both structural components include ventilation openings. These openings improve air circulation inside the device, reduce heat accumulation during prolonged use and decrease the overall weight of the orthoprosthesis.

In contrast to the earlier orthoprosthesis design, the adapted system no longer includes a secondary prosthetic foot. The natural foot is positioned directly within the device structure, which reduces the overall volume of the orthoprosthesis and improves compatibility with normal clothing and footwear (Fig. 4(a)).
For improved comfort at the knee interface, the design allows the integration of adjustable silicone padding. The amount of silicone material can be adapted according to the child's anatomy to provide a stable and comfortable fit.
The foot platform is printed using thermoplastic polyurethane (TPU). The flexible properties of TPU allow partial energy absorption during ground contact and support smoother rollover during stance, which contributes to a gait pattern closer to natural walking.

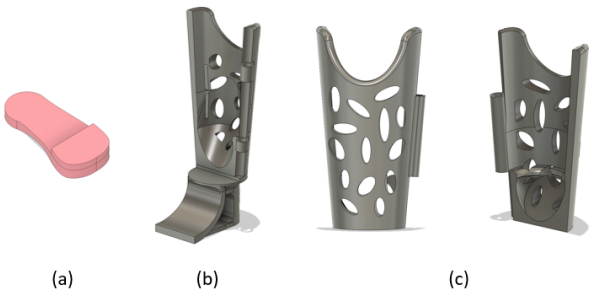

Fig. 3. Modular components of the orthoprosthesis. (a) TPU foot part, (b) back shell including foot platform and anatomical shape of child's leg, (c) front part from both sides, showing anatomical shape.

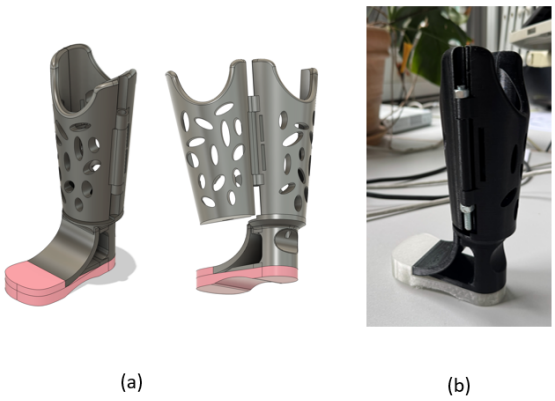

Fig. 4. Adapted 3D-printed orthoprosthesis. (a) CAD Design, (b) 3D-Printed device, ready for testing with the child.

4. Discussion

The observations presented in this study indicate that the initial 3D-printed orthoprosthesis supported the child during early gait development and enabled progressive improvement in knee control and overall gait stability. The device allowed the child to transition from limited knee control to a more stable and coordinated walking pattern, suggesting that such assistive designs can facilitate neuromuscular adaptation during early motor development.

At the same time, the transition to the clinical prosthetic device revealed limitations of conventional pediatric prosthetic solutions. In particular, the increased weight and lack of growth adaptability highlight challenges when applying standard prosthetic designs to very young children.

The redesigned orthoprosthesis presented in this work aims to address these limitations by combining the structural stability of the clinical device with the modularity and customization potential of additive manufacturing. The integrated hinge mechanism allows the device to open for easier fitting and may improve usability in daily use. In contrast to socket-based prostheses, where load is mainly transferred to the proximal knee region, the adapted design aims to distribute forces along the limb through the structural shell and Velcro-based fixation system. Whether the limb can be reliably stabilized within this structure during dynamic walking remains an important aspect for further investigation.

Although the new orthoprosthesis has been successfully manufactured using additive manufacturing, its functional performance must still be evaluated in practice. In particular, usability, comfort, fit and long-term mechanical stability need to be assessed during clinical testing and daily use.

5. Outlook

Future work will focus on evaluating the adapted orthoprosthesis during real-world use. In particular, usability testing with the child will be necessary to assess comfort, stability and the interaction between the limb and the device during walking. In addition, the mechanical properties of the printed components require further investigation, as print parameters such as layer orientation, infill structure, and material selection may significantly influence the durability of the orthoprosthesis under repeated loading conditions.Quantitative gait analysis could complement the qualitative clinical observations presented in this study. Measurements using electromyography (EMG) and force-sensitive resistor (FSR) sensors may provide deeper insights into muscle activation patterns, load distribution and biomechanical performance during walking. Despite these open questions, the promising results obtained with the initial orthoprosthesis indicate that additive manufacturing has strong potential for developing adaptive assistive devices for very young patients with congenital limb deficiencies.

Acknowledgements

The author would like to thank the Chair of Medical Information Technology for providing access to the additive manufacturing facilities used in this work. This project was supported by Instituto Superior Técnico and Fundação para a Ciência e a Tecnologia (FCT) under the supervision of Prof. Hugo Placido Silva and Prof. Cláudia Quaresma. Clinical observations were conducted in collaboration with Hospital Dona Estefânia.

References

[1] ADOLPH, K. E., ROBINSON, S. R. The road to walking: What learning to walk tells us about development. In *Advances in Child Development and Behavior*. Academic Press, 2013, p. 1–40.

[2] ANDERS, L., AGULHEIRO, P., PLÁCIDO DA SILVA, H., QUARESMA, C. Modular lower limb 3D-printed orthoprosthesis for toddlers with fibular hemimelia. *IEEE Access*, 2025, vol. 13, p. 155124–155138.

[3] BIRCH, J. G. Congenital fibular deficiency: A review of thirty years' experience at one institution. *Journal of Bone and Joint Surgery*, 2011.

[4] FULLER, C. B., et al. Lengthening reconstruction surgery for fibular hemimelia. *Strategies in Trauma and Limb Reconstruction*, 2021.

[5] NAVARRO, P. M., COPACI, D., ROJAS, D. B. Design and control of a soft knee exoskeleton for pediatric patients at early stages of the walking learning process. *Bioengineering*, 2024, vol. 11, no. 2, p. 188.

[6] VENNAM, S., et al. 3D-printed personalized assistive devices: A material and design review. *Materials Today Communications*, 2024.

About Authors...

Lilli ANDERS was born in Frankfurt am Main, Germany. She holds a M.Sc. in Biomedical Engineering from Instituto Superior Técnico, Lisbon and has started her PhD at Medit in Aachen. Her research focuses on early neurodegenerative diseases, medical device design, gait analysis and signal processing.

EMD methods for suppressing muscle artifacts

Lenka JUNGMANNOVÁ[1]

[1] Dept. of Biomedical Technology, Czech Technical University, Technická 2, 166 27 Praha, Czech Republic

jungmlen@fbmi.cvut.cz

Abstract.

The methods are based on adaptive signal decomposition into so-called intrinsic mode functions (IMF) without a predefined basis, unlike other methods such as Fourier or wavelet transformation. The aim of this work is to analyze the use of Empirical mode decomposition methods for suppressing muscle artifacts occurring in EEG recordings. In the study, EEMD and my implementation of the MEEMD methods were applied on 16 EEG recordings from an ASSR experiment with chirp simulation. The results showed that muscle artifacts occur primarily in lower IMF components corresponding to high frequencies. After applying both methods, it showed that the change of alpha band has not been statistically confirmed, which may indicate the methods do not damage the useful physiological signal. In the frequency bands 20-40 Hz and 60-80 Hz, the power spectrum has decreased, which is showing the removing artifacts.

Keywords

EEG, Empiracal Mode Decomposition, EEMD, MEEMD, muscle artefacts.

1. Introduction

An electroencephalogram (EEG) is a recording of the electrical activity of the brain using electrodes placed on the surface of the scalp [1]. EEG is divided into several frequency bands that correspond to different brain activities. The delta band ranges from 0.5 to 4 Hz, the theta band from 4 to 8 Hz, the alpha band from 8 to 13 Hz, the beta band from 13 to 30 Hz, and the gamma band from >30 Hz. Individual frequency bands allow us to detect different states, which can then be analyzed [1]. However, some EEG signals are often noisy and contain artifacts, such as muscle or eye movements, which need to be removed before we can analyze the data. Empirical Mode Decomposition (EMD) is often used to decompose this type of signal. [2] Since EEG signals are nonlinear and nonstationary EMD is an ideal tool for their analysis. EMD is based on decomposing the signal into so-called Intrinsic Mode Functions (IMFs), which represent oscillations present in the original signal at different time scales. Unlike classical transformations, such as the Fourier transform, EMD does not use a predefined basis [2]. Based on the above-described properties of EEG and the principles of EMD, this work deals with the practical use of advanced variants of this method, specifically Ensemble Empirical Mode Decomposition (EEMD) and Multivariate Ensemble Empirical Mode Decomposition (MEEMD), in the context of muscle artifact suppression.

2. Methodology

2.1 Data set

The 16 EEG recordings on which I implemented the EEMD and MEEMD methods were EEG recordings where individual patients with drug-resistant depression underwent the ASSR protocol with an hdEEG cap.

The patients were seated in a Faraday cage and kept their eyes open during the experiment. Stimulation was performed using a chirp stimulus, whose frequency spectrum evokes a steady response at a frequency identical to the stimulation frequency, and the frequency of the modulation wave changes during stimulation, causing the subject's neural response to change as well.

In this experiment, a chirp stimulus 1000 ms long was used, with a modulation wave whose frequency decreased over time. Each measurement consisted of 300 chirp stimulations.

2.2 Preprocessing

I preprocessed 16 EEG recordings using the FieldTrip Toolbox [3]. I loaded the raw EEG data as a continuous recording without segmentation into trials. To remove edge artifacts that occur at the beginning and end of the measurement, I trimmed the signal by the first and last 5 seconds of the recording.

For preprocessing, I used a high-pass filter to remove slow drifts. The cutoff frequency was 1 Hz to remove artifacts while preserving information from the upper half of the EEG recording (FIR - Finite Impulse Response with a Hamming window, maximum passband deviation of 0.0022 and a stopband attenuation of -53 dB). Likewise, I used a low-pass filter (same settings as high-pass filter) to eliminate high-frequency noise and aliasing effects. The cutoff frequency was 80 Hz, which still includes gamma activity

but removes high-frequency noise. As another filter, I used a notch filter, which removes network noise at 50 Hz. To minimize edge effects, I used time padding.

Using baseline correction, I remove the DC component of the signal by calculating the average value of the signal in a defined window, which is then subtracted from the entire signal. This entire process ensures that the signal is centered around zero.

2.3 EMD (Empirical Mode Decomposition)

This method works on the basis of the so-called sifting process, which extracts intrinsic mode functions (IMFs) using local extremes in the signal. The IMF component represents oscillations of a certain frequency level and is adaptively derived from the data, so it does not need predefined bases [4].

The algorithm begins by searching for local extremes in the signal *x(t)*, then uses interpolation to create two envelopes from these points (one passing through the maximum and the other through the minimum). From these two envelopes, it creates an average envelope (1), which is then subtracted from the original signal. [4]

$$m(t) = \frac{e_{min}(t) + e_{max}(t)}{2}, \tag{1}$$

where *m(t)* means envelope, $e_{max}(t)$ is maximum envelope, $e_{min}(t)$ is minimum envelope [4].

After deduction (2), the potential IMF *d(t)*. If the resulting function *d(t)* meets the conditions for IMF, it becomes one of the mode functions. These conditions are the extremum condition and the symmetry condition. The extremum condition means that the number of local extrema and the number of intersections with zero must not differ by more than one. The symmetry condition means that the mean value of the upper and lower envelopes must be close to zero at every point. If the conditions are not met, this process is repeated, but with the input signal *d(t)* instead of the original *x(t)*. [4]

$$d(t) = x(t) - m(t), \tag{2}$$

where *d(t)* is potential IMF, *x(t)* is original signal, *m(t)* is mean envelope. [4]

This process, known as sifting, is repeated until the stopping criterion is reached.

$$\sum_t \frac{(d_{k-1}(t) - d_k(t))^2}{(d_{k-1}(t))^2} < \varepsilon \tag{3}$$

There are several different termination criteria, the most commonly used is the standard deviation between two consecutive iterations. This deviation is compared to a threshold value ε, which is usually between 0.2 and 0.3 [2]. If the stopping criterion is met, the resulting function is saved as IMF and the rest of the signal as residuum $r(t)$. [4]

$$r(t) = x(t) - IMF(t), \tag{4}$$

where *r(t)* is residuum, *x(t)* is original signal, *IMF(t)* is IMF function. [4]

As long as the residue is not a monotonic function or contains fewer than two local extrema. We can then reconstruct the original signal by sum all the IMFs and residuum *r(t)*.[4][2]

2.4 EEMD (Ensemble Empirical Mode Decomposition)

EEMD is a single-channel method for decomposing non-stationary and nonlinear signals. The classic EMD method is susceptible to noise, which is why the EEMD method was developed [5]. IMF is created as the average of a set of trials. Each trial consists of a signal and adaptive independent white noise with the same standard deviation. Then, a classical decomposition using EMD is performed. When averaging a set with a sufficient number of trials, any noisy results should cancel each other out, because the adaptive noise in each trial is considered independent. [5]

2.5 MEEMD (Multivariate Ensemble Empirical Mode Decomposition)

This method is based on the principles of EEMD [5], which involves adding white noise, and MEMD (Multivariate EMD [6]), where we connect the signal across all channels. The goal is to preserve the relationships between individual channels while suppressing IMF mixing (mode mixing). The time positions of extremes from all channels are merged into a common set, ensuring that the process runs synchronously across all channels.

2.6 Analysis of results

To compare the methods, I chose to compare the power spectrum in different frequency bands. The alpha band has the most researched frequency response and does not contain muscle artefacts, so the power should not change in order to preserve physiological information. And then I tested it band from 20 to 40 Hz and from 60 to 80 Hz, because muscle artifact has significantly higher power in these bands than gamma EEG activity, I expect a change in these power spectra. I skipped 50 Hz because there was line noise there.

First, I verified normality using the Shapiro-Wilk normality test [7]. Based on the result of this test, I will use either a paired t-test or Wilcoxon's test on each frequency band (8-12 Hz, 20-40 Hz, 60-80 Hz). I always compared the original signal with the reconstructed signal from individual IMFs without IMF1. (represent muscle artifact)

- H_0: There is no statistically significant difference in power spectrum before and after application of the EEMD/MEEMD method.
- H_A: The application of the EEMD/MEEMD method leads to a demonstrable change in

power spectrum, whether an increase or a decrease.

3. Results

3.1 Application of EEMD

I applied the EEMD method in MATLAB to preprocessed EEG data. In the figure we can see decomposed signal into IMFs from first EGG recording of first channel.

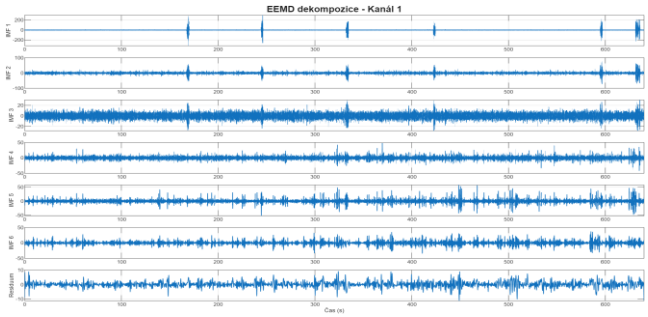

Fig. 2: EEMD decomposition – EEG 1 channel 1

The graph represents the decomposition of the EEG signal, where individual IMF components are sorted according to decreasing oscillation. And during individual IMFs, we can see muscle artifacts that have a significantly greater amplitude than the rest of the signal.

For a better demonstration of muscle artifacts, I zoomed in on the time interval 168-178s.

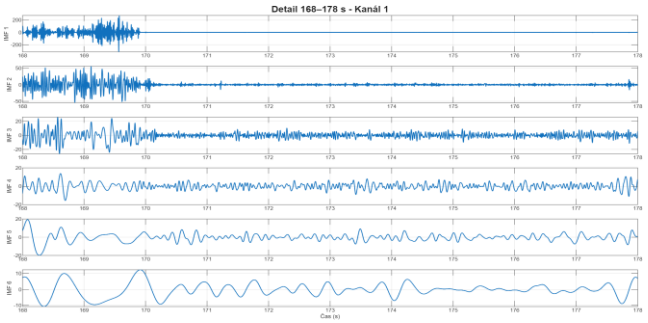

Fig. 3: EEMD detail of time segment (Fig. 1) with muscle artefact

3.2 Application of MEEMD

I also applied the MEEMD method in the same way. In the figure we can see decomposed signal into IMFs from first EGG recording of first channel using MEEMD method.

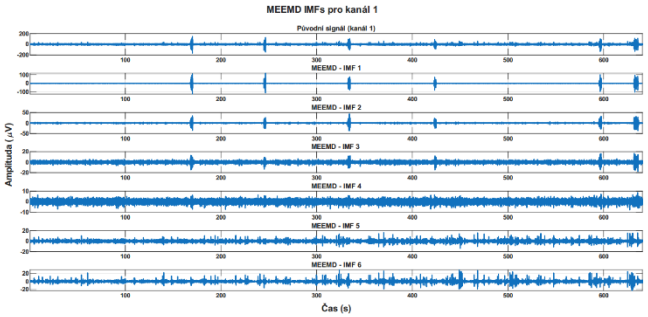

Fig. 1: MEEMD decomposition – EEG 1 channel 1

For a better demonstration of muscle artifacts, I zoomed in on the time interval 168-178s. In the first 5 seconds, we can see a much greater amplitude than in the rest of the signal, which demonstrates muscle artifact.

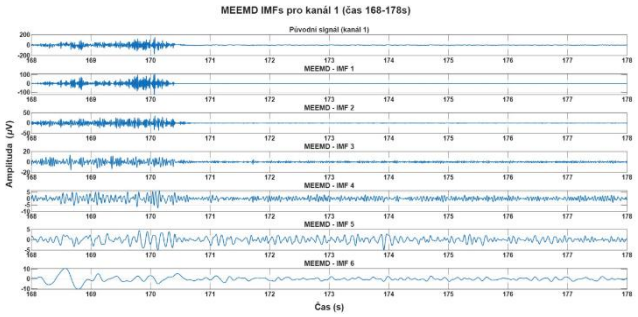

Fig. 4: MEEMD - time segment (Fig. 1) with muscle artefact

3.3 Analysis of results

Based on the Shapiro-Wilk test, we found that none of the data had a normal distribution, so I used the Wilcoxon test for further evaluation. The table shows the mean, median, and SD of power spectrum for each band before applying the method, then after applying EEMD or MEEMD, which are statistically tested towards BEFORE data.

Freq band	Mean	Median	SD	p-value
8-13 Hz - BEFORE	12,4190	10,5120	8,0900	-
8-13 Hz - EEMD	12,1970	10,5320	7,9600	0,6050
8-13 Hz - MEEMD	11,6060	8,2230	8,6110	0,0787
20-40 Hz - BEFORE	15,4860	14,7330	5,1990	-
20-40 Hz - EEMD	13,3670	12,7860	4,1910	0,0004
20-40 Hz - MEEMD	13,3400	12,5350	5,5420	0,0004
60-80 Hz - BEFORE	10,8620	7,7840	8,6310	-
60-80 Hz - EEMD	3,4500	2,7290	1,8460	0,0004
60-80 Hz - MEEMD	4,8170	4,0800	3,3570	0,0004

Tab. 1: *Descriptive statistics of EEG power spectrum*

I always compared the given frequency band (8-12 Hz, 20-40 Hz, 60-80 Hz) before and after using EEMD or MEEMD.

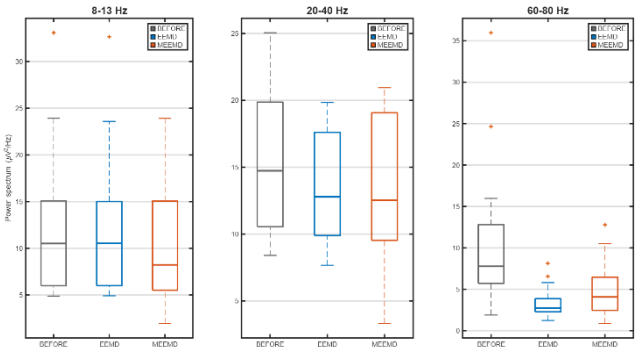

Fig. 5: Distribution of the power spectrum in different bands

4. Discussion and Conclusion

In this study, I first applied the EEMD and MEEMD methods to preprocessed EEG data, which was decomposed into individual IMFs. The EEG power spectrum in terms of absolute band power values in the given frequency spectra was then evaluated.

The EEG signal decomposition was successfully performed. In the individual graphs (Fig. 2, Fig. 1), we can see muscle artifacts that have much higher amplitudes than the rest of the signal, that visually it appears that the muscle artifacts are separable. We can see this in more detail in the following graphs (Fig. 3, Fig. 4).

For statistical analysis I verified the normality of the subsequent data using the Shapiro-Wilk test. I rejected the normality of the data and therefore chose a nonparametric paired test for further analysis.

I compared individual frequency bands, starting with the alpha band, which is the most well-known physiologically and is compared in most literature. The power spectrum in this area should not change significantly after applying the EEMD and MEEMD methods. I tested this statistically, which showed that the power spectrum did not exhibit a statistically significant change (Tab. 1). As for the frequency bands 20-40 Hz and 60-80 Hz, there was a statistically proven change in the power spectrum (Tab. 1). This means that the methods do not damage the EEG signal after IMF1 removal and suppress muscle artifacts.

In box plot (Fig. 5) shows that the distribution of data (median and quartile range) remained virtually unchanged after applying decomposition methods in the alpha band, which visually confirms the assumption that the method does not damage the useful physiological signal. However, according to Fig. 1-4, it appears that a residual artifact remains in the data, which was present in higher IMFs, and that this needs to be addressed in future research.

Acknowledgements

Research described in the paper was supervised by Ing. Jan Štrobl, Ph.D., FBMI CTU in Prague. I would like to thank him for his valuable advice, expert guidance, and patience throughout the entire process and thank National Institute of Mental Health for providing EEG recordings.

References

[1] MERT, Ahmet a AKAN, Aydin. Emotion recognition from EEG signals by using multivariate empirical mode decomposition. Online. *Pattern Analysis and Applications*. 2018, roč. 21, č. 1, s. 81-89. ISSN 1433-7541. Dostupné z: https://doi.org/10.1007/s10044-016-0567-6. [cit. 2025-04-05].

[2] LIANG, Hualou; BRESSLER, Steven L.; DESIMONE, Robert a FRIES, Pascal. Empirical mode decomposition: a method for analyzing neural data. Online. *Neurocomputing*. 2005, roč. 65-66, s. 801-807. ISSN 09252312. Dostupné z: https://doi.org/10.1016/j.neucom.2004.10.077. [cit. 2025-04-05].

[3] OOSTENVELD, Robert; FRIES, Pascal; MARIS, Eric a SCHOFFELEN, Jan-Mathijs. FieldTrip: Open Source Software for Advanced Analysis of MEG, EEG, and Invasive Electrophysiological Data. Online. *Computational Intelligence and Neuroscience*. 2011, roč. 2011. ISSN 1687-5265. Dostupné z: https://doi.org/https://doi.org/10.1155/2011/156869. [cit. 2025-05-26].

[4] RILLING, Gabriel; FLANDRIN, Patrick a GONÇALVÈS, Pablo. On empirical mode decomposition and its algorithms. Online. *IEEE-EURASIP Workshop on Nonlinear Signal and Image Processing NSIP-03*. 2025, roč. 2003, s. 6. Dostupné z: https://doi.org/inria-00570628. [cit. 2025-04-05].

[5] CHEN, Xun; HE, Chen a PENG, Hu. Removal of Muscle Artifacts from Single-Channel EEG Based on Ensemble Empirical Mode Decomposition and Multiset Canonical Correlation Analysis. *Journal of Applied Mathematics*. 2014/01/01, roč. 2014, č. 1, s. 261347. ISSN 1110-757X. Dostupné z: https://doi.org/https://doi.org/10.1155/2014/261347.

[6] MANDIC, Danilo P.; REHMAN, Naveed ur; WU, Zhaohua a HUANG, Norden E. Empirical Mode Decomposition-Based Time-Frequency Analysis of Multivariate Signals: The Power of Adaptive Data Analysis. Online. *IEEE Signal Processing Magazine*. 2013, roč. 30, č. 6, s. 74-86. ISSN 1053-5888. Dostupné z: https://doi.org/10.1109/MSP.2013.2267931. [cit. 2025-04-08].

[7] BENSAÏDA, Ahmed. *Shapiro-Wilk and Shapiro-Francia normality tests*. Online. MathWorks. 2026. Dostupné z: https://www.mathworks.com/matlabcentral/fileexchange/13964-shapiro-wilk-and-shapiro-francia-normality-tests. [cit. 2026-03-09].

[8] THE MATHWORKS, INC. *MATLAB*. Online. MathWorks. 2024. Dostupné z: https://www.mathworks.com/products/matlab.html. [cit. 2025-05-26].

About Authors...

Lenka JUNGMANNOVÁ was born at Prague and grew up at Zvole. She is currently completing her bachelor's degree in Biomedical Technology at the Faculty of Biomedical Engineering, Czech Technical University in Prague.

Endovascular Laser Ablation: Influence of Wavelength and Fiber Geometry

Michal ZELENÝ[1]

[1] Dept. of Physics, Czech Technical University, Technická 2, 166 27 Praha, Czech Republic

zelenm13@fel.cvut.cz

Abstract. *This paper presents a comparative numerical and experimental analysis of Endovenous Laser Ablation at 980 nm, 1470 nm, and 1940 nm using bare and radial fibers. Utilizing a 3D numeric model, we evaluate spatiotemporal heat distribution and the transition from hemoglobin-targeting to water-targeting protocols. Results demonstrate that 1940 nm radiation provides superior thermal confinement within the vein wall, achieving transmural denaturization, while maintaining perivenous temperatures below the safety threshold. Analysis of the emission profiles reveals that while radial fibers enhance circumferential dose uniformity, the choice of wavelength remains the dominant factor in minimizing perivenous thermal load. Experimental validation on bio-mimetic collagen phantoms and ex vivo tissue aligns with the numerical findings, justifying the clinical shift toward high-wavelength, low-power protocols to minimize postoperative morbidity.*

Keywords

Endovenous laser ablation, EVLA, Numerical modeling, Wavelength comparison, Bioheat equation, Laser tissue interaction, Tissue phantoms

1. Introduction

Endovenous Laser Ablation (EVLA) has become the gold standard for treating saphenous vein insufficiency due to its high success rate and minimally invasive nature. The therapeutic success of EVLA relies on selective photothermolysis, where laser energy is absorbed directly by the vein wall from inside, inducing irreversible collagen denaturation and subsequent vessel occlusion.

Historically, EVLA utilized shorter wavelengths in the 1-µm range. Recent clinical trends favor 1470 nm and 1940 nm systems operating at lower power settings. Shorter wavelengths exhibit low absorption in water, leading to deep optical penetration and indirect heating of the vein wall via heat transfer from a carbonized blood coagulum (the "hot-tip" effect). This often results in non-uniform thermal delivery and significant collateral damage to perivenous tissues, manifesting as postoperative pain and ecchymoses. In contrast, modern "water-targeting" wavelengths (1470 nm and 1940 nm) align with the high absorption peaks of water within the hydrated venous matrix. This ensures high optical confinement and direct volumetric heating of the vessel wall.

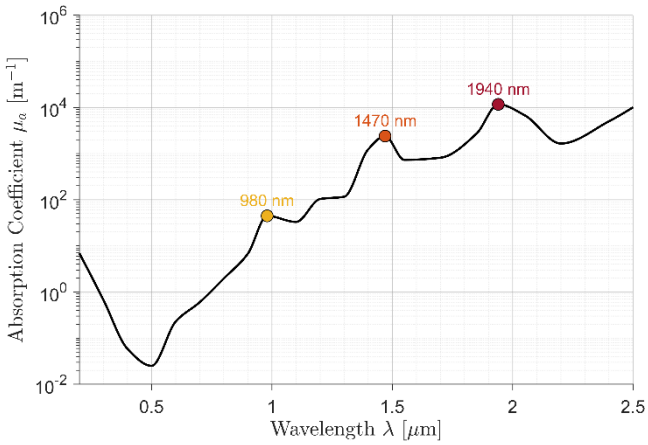

Fig. 1. Absorption spectrum of water [1],[2].

While clinically successful, the optimization of these protocols (specifically wavelength, power, and pullback speed) requires a standardized framework.

This study utilizes a custom-built computer-controlled delivery system and 3D numerical modeling to analyze the spatiotemporal heat distribution, aiming to validate the physical advantages of high-wavelength EVLA in minimizing the perivenous thermal footprint.

2. Materials and methods

2.1 Tissue Phantoms

Three types of phantoms were employed: protein-based phantoms (liquid and solid albumen), ex vivo bovine liver, and a bio-mimetic collagen model.

Solid albumen blocks (30×30×10 mm) were prepared by thermal coagulation at 70 °C and served as initial screening models. Albumen is a suitable surrogate with high water content and a visible denaturation transition. At temperatures exceeding 100 °C, localized carbonization provides a clear visual record of the thermal footprint.

Ex vivo bovine liver samples were utilized to verify coagulation zones (manifesting as tissue whitening) and carbonization thresholds.

For precise cross-sectional analysis, a bio-mimetic collagen model was developed using type I bovine collagen (Devro Ltd.). The gel (3 wt% collagen) was molded into cylindrical samples with a central longitudinal lumen (⌀1.7 mm) to simulate the venous anatomy. To ensure mechanical stability and biological purity, the hydrogels were cross-linked using an electron beam accelerator (Mikrotron MT 25) with a dose of 25 kGy [3].

These phantoms mimic the optical and thermal properties of the venous wall and surrounding hydrated matrix, imitating the clinical EVLA environment.

2.2 Laser Sources and Fiber Optic Delivery

Three diode laser systems (Gigaa Medical) were employed to evaluate the wavelength-dependent thermal effects, specifically the 980 nm (Firelas Cure), 1470 nm (VELAS™), and 1940 nm (VELASII-10H) models.

Laser energy was delivered via 600 µm core diameter silica fibers in two distinct configurations: a standard bare fiber providing forward-firing emission, and a radial fiber (Gigaa-Saturn Side Fiber) providing circumferential emission, hypothesized to ensure a more uniform thermal dose to the vein wall.

To ensure a precisely defined Linear Endovenous Energy Density (LEED), a custom CNC-based linear drive was developed. The positioning system utilizes a T8x2 lead screw (300 mm travel) driven by a TB6600 stepper motor driver and an Arduino Nano microcontroller. To achieve high timing precision, motor pulses are managed via hardware timer interrupts with a resolution of 100 µs.

The entire assembly, featuring a mechanical clamp to secure the optical fiber to the lead screw carriage, achieves a linear resolution of 0.01 mm per step and a controllable speed range of 0.5–12.3 mm/s.

2.3 Thermal Imaging

Surface temperature distribution during the pull-back sequence was recorded using a calibrated FLIR E6 infrared camera (accuracy ±2 °C). Experimental data acquired via thermal imaging served as the primary benchmark for the validation of the numerical model.

2.4 Numerical Modelling

A 3D time-dependent numerical model was implemented to simulate the spatiotemporal thermal distribution during the EVLA procedure. The computational domain represents a collapsed, elliptical vein geometry surrounded by a hydrated tissue matrix. To replicate the clinical pull-back sequence, an internal heat source representing the optical fiber was dynamically translated along the longitudinal axis (z-axis). Specific thermal and optical properties were assigned to the respective computational layers to account for the heterogeneous nature of the vein-tissue interface [4].

The spatial distribution of optical power was calculated using the Diffusion Approximation, accounting for the wavelength-dependent absorption (μ_a) and reduced scattering coefficients (μ_s') coefficients of the venous wall (see Tab. 1). Two distinct emission profiles were evaluated: a forward-firing Bare fiber and a circumferential Radial fiber. The resulting localized fluence rate determines the volumetric heat generation term, Q_{abs}.

The subsequent heat propagation was governed by conduction. The fundamental governing equation for the thermal process is the Pennes Bioheat Equation:

$$\rho c_p \frac{\partial T}{\partial t} = \nabla \cdot (k \nabla T) + Q_{\text{abs}} \tag{1}$$

where T is the local tissue temperature [°C], ρ is the tissue density [kg/m³], c_p is the specific heat capacity [J/(kg·K)], and k is the thermal conductivity [W/(m·K)]. The optical parameters used for the vein wall are summarized in Tab. 1.

λ [nm]	μ_a [cm^{-1}]	μ_s' [cm^{-1}]
980	0.7	37
1470	23	25
1940	115	14

Tab. 1. Absorption coefficients (μ_a) and reduced scattering coefficients (μ_s') for the venous wall [4].

The model was discretized using a structured mesh with a spatial resolution of dx = 0.125 mm and solved iteratively with a fixed time step of dt = 9 ms. Simulations were performed according to used clinical protocols for each wavelength, as summarized in the Linear Endovenous Energy Density (LEED) settings:

- 1940 nm (8 W, 65 J/cm)
- 1470 nm (10 W, 100 J/cm)
- 980 nm (15 W, 150 J/cm)

To facilitate the analysis of these complex 4D datasets, a custom EVLA Interactive Analyzer was developed in MATLAB (see Fig. 2), enabling real-time visualization of thermal gradients and damage integrals.

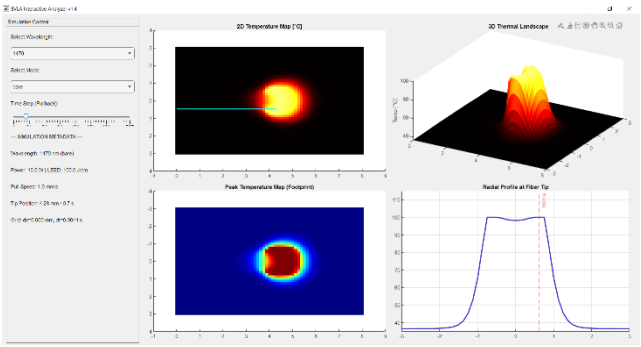

Fig. 2. Interface of the developed EVLA Interactive Analyzer tool, showing real-time thermal gradients.

To quantify the cumulative thermal impact on the venous wall and surrounding structures, the Linear Dose (LD60) was calculated. This parameter represents the time-integral of the temperature excursion above the physiological safety threshold of 60 °C, defined as:

$$LD_{60} = \int_t \max(0, T(t) - 60)\ \mathrm{d}t \quad [°\mathrm{C} \cdot \mathrm{s}] \qquad (2)$$

where $T(t)$ is the instantaneous local temperature. The LD_{60} metric provides a more robust assessment of potential tissue damage than peak temperature alone, as it accounts for the duration of thermal exposure, which is critical for predicting irreversible collagen denaturation and perivenous safety.

3. Results

Numerical simulations reveal that while all wavelengths achieve the target temperature for transmural denaturization (~98 °C at the intima), their perivenous footprints differ significantly.

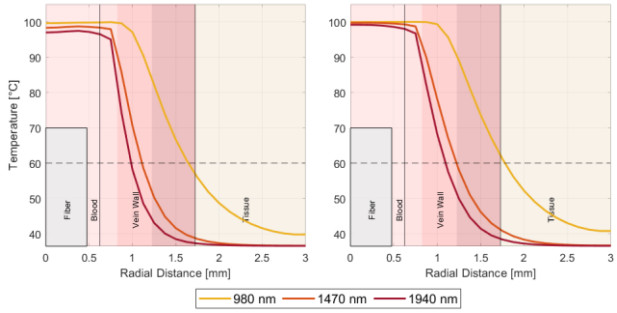

Fig. 3. Radial temperature profiles at the fiber tip for bare (left) and radial (right) fiber configurations. Profiles compare 980 nm (150 J/cm), 1470 nm (100 J/cm), and 1940 nm (65 J/cm) protocols.

While all configurations reach the phase-transition limit (100 °C) at the intima, the 1940 nm wavelength exhibits superior heat confinement. The shaded anatomical regions highlight that for 1940 nm, temperatures in the perivenous tissue remain below the safety threshold (60 °C), whereas 980 nm radiation causes significant overheating in the adventitia and beyond.

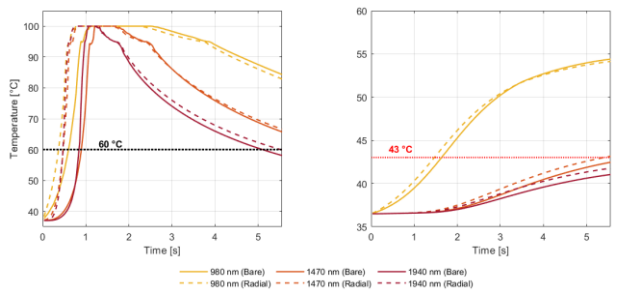

Fig. 4. Temperature evolution at the vein intima (left) and in the perivenous tissue at a 0.5 mm safety margin (right).

For 1470 nm and 1940 nm, the 43 °C threshold is not exceeded in either fiber configuration.

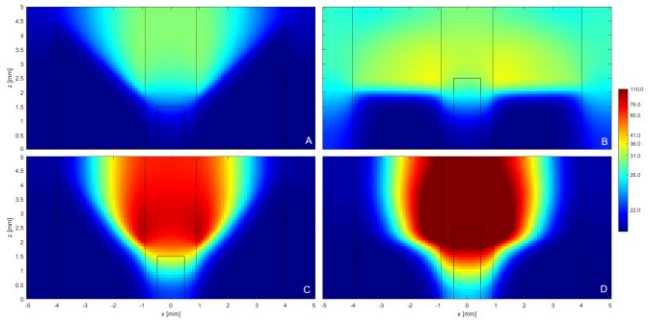

Fig. 5. Comparative modelling of thermal distribution for LEED 80 J/cm in collagen hydrogel. (A) 980 nm Bare, (B) 980 nm Radial, (C) 1470 nm Bare, (D) 1470 nm Radial.

As illustrated in Fig. 5, the 980 nm configurations (at 150 J/cm) exhibit a broad thermal wake, extending deep into the surrounding tissue. In contrast, 1470 nm radiation (even at a lower LEED of 100 J/cm) produces the steepest thermal gradient, effectively confining the heat within the first 0.5 mm of the vessel wall.

	LD_{60} [°C·s] (T_{max} [°C])		
Configuration	**Tunica intima**	**Tunica media**	**Tissue**
980 nm Bare	**190.2 (100.0)**	**170.4 (100.0)**	**108.8 (89.1)**
1470 nm Bare	**111.6 (100.0)**	**65.4 (87.8)**	**0.4 (60.5)**
1940 nm Bare	**72.8 (100.0)**	**29.4 (78.7)**	**0.0 (54.6)**
980 nm Radial	**196.4 (100.0)**	**175.3 (100.0)**	**109.2 (88.3)**
1470 nm Radial	**131.0 (100.0)**	**81.6 (89.9)**	**3.9 (62.5)**
1940 nm Radial	**93.8 (100.0)**	**44.4 (82.1)**	**0.0 (57.2)**

Tab. 2. Calculated thermal load (LD_{60}) and maximum temperatures (T_{max}) for specific anatomical layers. Radial fiber configurations show enhanced energy delivery to the intima compared to bare fibers, especially at 1940 nm.

Data from the thermal load analysis indicate that the Radial fiber geometry provides a more uniform circumferential dose compared to the Bare fiber, which tends to create localized "hot spots" at the tip.

These theoretical findings are further supported by infrared thermography. The IR observations confirm that 1470 nm energy penetrates closer to the phantom surface compared to the highly confined 1940 nm profile, which remains localized even when the source is positioned only 1 mm below the surface.

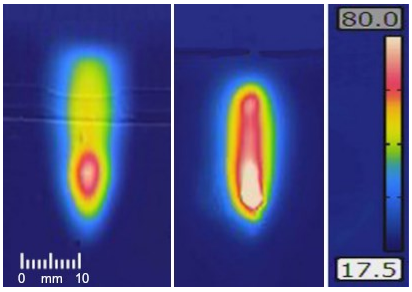

Fig. 6. Comparison of 1940 (left) and 1470 nm (right) thermal footprints via IR imaging. The fiber was positioned 1 mm below the surface.

Experimental results on ex vivo bovine liver further support these findings. The 1940 nm wavelength leads to a more localized and extreme temperature increase, resulting in absorption within a significantly thinner tissue layer. As shown in Fig. 7, 1470 nm radiation produces a wider coagulation zone (whitening), while 1940 nm exhibits intense, localized carbonization within a much narrower region.

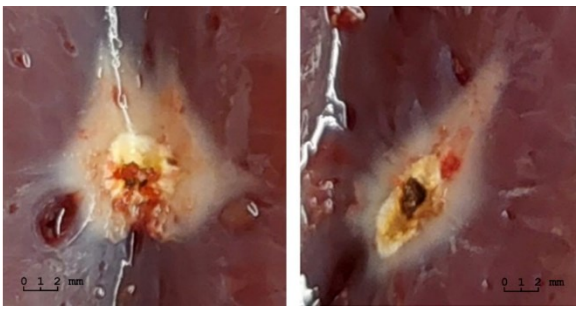

Fig. 7. Ex-vivo bovine liver comparison. The 1470 nm (left) and 1940 nm (right).

A consistent trend was observed in the solid albumen phantoms (Fig. 8). The 1940 nm wavelength produced a more concentrated area of carbonization, emphasizing its high absorption efficiency in the hydrated matrix.

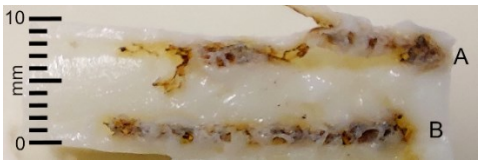

Fig. 8. Coagulated albumen phantoms, LEED = 80 J/cm (8 W, 1 mm/s) for 1470 nm (A) and 1940 nm (B).

These experimental observations verify the "water-targeting" mechanism, which emphasizes high absorption efficiency. These findings directly correlate with clinical practice; high-wavelength protocols achieve a 98% success rate, with only 4.4% of patients requiring follow-up visits due to postoperative pain [5], highlighting the clinical benefit of minimized thermal overflow.

4. Discussion

The 1940 nm wavelength exhibits the steepest thermal gradient, confirming superior heat confinement to the vein wall. This localization is a direct consequence of the water absorption peak, which reduces the effective optical penetration depth.

Interestingly, the impact of fiber geometry (Radial vs. Bare) is wavelength dependent. While the Radial fiber significantly improves dose uniformity for the 980 nm wavelength, its relative advantage diminishes for the 1470 nm and 1940 nm systems. This suggests that at high water-absorption peaks, the optical properties of the tissue itself become the dominant factor in energy localization, potentially simplifying fiber requirements for modern EVLA protocols.

A known limitation of this numerical model is the use of the Diffusion Approximation. This method is inherently less accurate in the immediate vicinity of the fiber tip (the "near-field"), where ballistic photons dominate and the assumption of isotropic scattering is not yet valid. However, for evaluating the global thermal footprint and perivenous load, the model provides robust predictive power. The strong correlation between our bio-mimetic collagen phantoms and the numerical results validates the use of the Pennes equation for clinical protocol optimization.

The development of the EVLA Interactive Analyzer addresses a critical gap in laser surgery education. By visualizing the thermal distribution in real-time, clinicians can better understand why high-wavelength protocols (1940 nm) reduce postoperative ecchymosis despite lower LEED settings. The tool demonstrates that precision, not raw power, is the key to successful ablation.

5. Conclusion

This study provides a comprehensive numerical and experimental validation of the thermal mechanisms governing modern EVLA. The following key conclusions were established:

The 1940 nm wavelength demonstrates the highest optical confinement, concentrating thermal energy within the first 0.5 mm of the venous wall. This ensures effective transmural denaturation while maintaining perivenous temperatures below the nociceptive threshold of 43 °C at the 0.5 mm safety margin. Furthermore, the LD_{60} metric successfully quantifies this safety, showing near-zero cumulative damage for high-wavelength protocols. While Radial fiber configurations provide a more uniform circumferential dose, their relative advantage is ultimately secondary to the selection of the laser wavelength. At 1940 nm, the high absorption coefficient of the venous tissue becomes the primary driver of energy localization.

These findings scientifically justify the transition to low-power, high-wavelength EVLA protocols. The minimized thermal footprint directly correlates with the observed reduction in post-operative pain and ecchymosis, confirming that precision of absorption, rather than raw energy density (LEED), is the critical factor for successful and safe vein occlusion.

The developed EVLA Interactive Analyzer serves as a robust tool for future protocol optimization and clinician education, bridging the gap between theoretical biophysics and surgical practice.

Acknowledgements

Research described in the paper was supervised by doc. Ing. Fabián, PhD., FEE CTU in Prague and supported by the student grant SGS 25/139/OHK4/3T/13.

References

[1] HALE, G. M., QUERRY, M. R. Optical constants of water in the 200-nm to 200-μ m wavelength region. *Applied Optics*, 1973, p. 555-563.

[2] KEDENBURG, S., et al. Linear refractive index and absorption measurements of nonlinear optical liquids in the visible and near-infrared spectral region. *Optical Materials Express*, 2012, p. 1588-1611.

[3] ŠUPOVÁ, M., et al. Preparation and characterization of collagen hydrogels cross-linked by ionizing radiation. *International Journal of Biological Macromolecules*, 2025.

[4] JACQUES, S. L. Optical properties of biological tissues: a review. *Physics in Medicine & Biology*, 2013, Vol. 58, No. 11, R37.

[5] FABIÁN, V., HONĚK, J., HORVÁTH, V., et al. Endovenous laser ablation of saphenous veins - favorable clinical results confirm theoretical advantages of the 1940nm diode laser. *Rozhledy v Chirurgii*, 2022, Vol. 101, No. 8, p. 395-400.

About Author

Michal ZELENÝ was born in Prague. He received his B.Sc. and M.Sc. degrees in Medical Electronics and Bioinformatics (specialization in Medical Technology) from the Faculty of Electrical Engineering, CTU, in 2021 and 2024, respectively. His academic background is reinforced by international academic mobility, having completed three Erasmus+ exchange programs: one at the MCI university in Innsbruck, Austria, and two consecutive stays at Politecnico di Torino, Italy. Since 2024, he has been pursuing his Ph.D. at the Department of Physics, FEE CTU. His current research focuses on biomedical optics, specifically numerical modeling, thermodynamics, and experimental evaluation of laser-tissue interactions during endovenous thermal ablation procedures.

Adaptive Self-Tightening Donning Mechanism for Exoskeletons

Raphael Hoffmann[1], Lara Schweitzer[1]

[1]Medical Information Technology, Helmholtz Institute for Biomedical Engineering, RWTH Aachen University, 52074 Aachen, Germany
Dept. of Electrical Engineering, RWTH Aachen University, 52062 Aachen, Germany

hoffmann@hia.rwth-aachen.de, lara.schweitzer@rwth-aachen.de

Abstract. *One major drawback of modern exoskeletons intended for older adults is the donning system. This system normally consists of straps and belts that require a certain level of fine motor control and range of motion. This often poses a major hurdle and makes the independent use of an exoskeleton nearly impossible, as many users cannot don the device by themselves. To address this problem, we present a novel automatic donning and tightening mechanism that enables elderly users to operate an exoskeleton without external assistance. First, the concept of the mechanism is introduced, followed by a mathematical model describing the motion of the soft actuator employed in the system. Finally, the accuracy of the mathematical model is verified through bending experiments, and the overall reliability of the mechanism is demonstrated by testing it on both a mannequin and human subjects.*

Keywords

Exoskeleton, Soft Actuator, Pneumatics, Elderly

1. Motivation

The aging of the population is leading to a steadily increasing proportion of older adults, accompanied by a growing incidence of mobility and movement limitations. As a result, technical assistive systems are becoming indispensable for maintaining quality of life, independence, and social participation in later life. Within this context, exoskeletons represent a key technological approach. However, the skin and skeletal structures of elderly users are markedly more fragile than those of younger individuals, and their haptic perception, motor abilities, and cognitive functions are often diminished. Therefore, exoskeletons intended for older adults must be specifically tailored to these characteristics.

Most commercially available exoskeletons, including *ReWalk*, *HyperShell*, and *Myosuit*, share a fundamental limitation: they depend on manual fastening systems such as straps, buckles, or other closures. For older adults or users with motor deficits, putting on these devices can be cumbersome, time-intensive, or even impossible without help, particularly in a home environment. Consequently, user acceptance hinges on an exoskeleton that can be donned independently, provides high wearing comfort, delivers adequate fixation forces, and can be adapted to diverse body sizes, shapes, and movement patterns. Hence, robust adjustment mechanisms and user-centered interaction procedures are essential. Existing research mostly addresses specialized use cases and concentrates on the hand. For example, Rose and O'Malley's glove employs a central tightening mechanism inspired by ski-boot closures, while Hernández-Barraza et al. use pneumatic chambers to open and close PVC rings that lock the fingers inside a glove [1, 2]. Both approaches still require manual intervention to secure the device.

Against this background, we propose a general, adaptive self-fastening mechanism for exoskeletons. The goal is a fastening solution that automatically locks itself during donning, eliminating the need for manual adjustments. Such a mechanism would enhance independent usability for elderly and physically impaired users and increase the practicality of exoskeletons in everyday applications.

2. Concept

To achieve automatic donning and self-tightening, the proposed mechanism consists of three main parts, as shown in **Fig. 1**. The first component is a soft actuator made of silicone with a Shore hardness of A00 and consisting of multiple air chambers. Beneath the chambers is a grid of PETG, which is molded into the silicone to create a gradient in material stiffness. Owing to this stiffness gradient, the soft actuator bends when pressure is applied. The design of the soft actuator is adopted and adapted from Van Vlerken et al., who developed it for the automatic attachment of a rehabilitation robot to a patient [3]. After the soft actuator has wrapped around the limb, its end latches onto a magnetic coupling from *FIDLOCK*. Once the coupling is engaged, a motor pulls on a strap that connects the opposite side of the magnetic coupling to the main shell, to which

the actuator is also attached. The motor winds the strap until the tension exceeds a predefined threshold, while the force between the strap and the magnetic coupling is measured by an integrated force-sensing resistor (FSR). The electronics are located remotely in a control box that contains a motor-control unit (`L298N` driver chip). This unit drives both the winding motor and the air pump for the soft actuator. An analog-to-digital converter (ADC) module (`ADS1115`) reads the FSR signal, and a pressure sensor (`MPX5700AP`) monitors the actuator's inflation pressure. An `Arduino Nano 3.x` controls the inflation and deflation cycles by actuating a solenoid valve that holds or releases air in the soft actuator. The `Arduino` serves as the central controller for the entire donning process, adapting the actuation based on the sensor feedback.

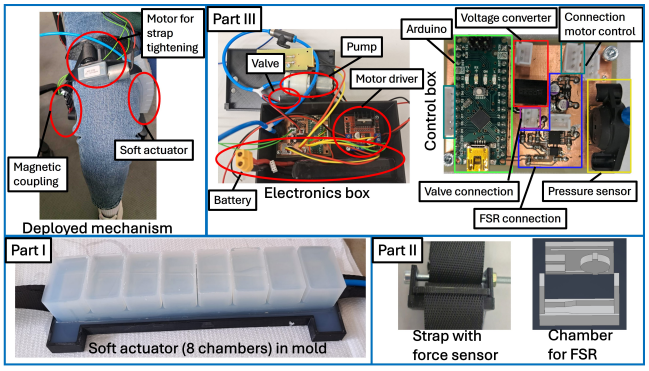

Fig. 1. Self-donning actuator and components

3. Mathematical Model

To predict the motion behavior of the developed soft actuator and to support the design of such actuators, we derive a model for the actuator's bending angle. This angle can then be used to estimate which limb sizes a given soft actuator can wrap around. The following model was originally developed by Alici et al. and is adapted here to describe the behavior of the present soft actuator [4]. It assumes that the design of a pneumatic actuator leads to nonlinear relationships between the input variable (pressure) and the output variable (bending angle).

The material of the soft actuator is an elastomer and follows a nonlinear stress-strain characteristic curve. In addition, geometric nonlinearities occur. The strongest nonlinearities typically occur under compressive stress; however, the model used here primarily considers tensile stress, which can be approximately linear up to about 70% strain. For modeling purposes, the soft actuator in the bent state is considered as a cantilever beam. Assuming constant curvature, the bending angle θ is given by

$$\theta = \frac{L}{r} \tag{1}$$

where L is the total length of the actuator and r is the bending radius.

Using the Euler–Bernoulli beam model, the radius of curvature is calculated as

$$\frac{1}{r} = \frac{M}{EI} \tag{2}$$

where M is the bending moment, E is an effective modulus of elasticity, and I is the second moment of area of the (simplified) cross-section.

Applying a pressure p to the actuator results in a change δL_i of the chamber length L_i due to tensile forces. This force results from the shifted center of pressure e with respect to the neutral axis and from the corresponding total cross-sectional area A_w and inner cross-sectional area A. Considering all model parameters as constant, we can derive the stationary bending angle as a function of pressure:

$$\begin{aligned}\theta(p) = \frac{L}{r} = \frac{M}{EI}\left(L_i + \delta L_i\right) = \frac{pAe}{EI}\left(L_i + \frac{pAL_i}{A_w E}\right) \\ = \underbrace{\frac{L_i A^2 e}{A_w E^2 I}}_{C} p^2 + \underbrace{\frac{L_i A e}{EI}}_{D} p = Cp^2 + Dp.\end{aligned} \tag{3}$$

The second moment of area for the soft actuator is derived by placing the neutral bending axis at the level of the underside of the chambers. This results from the interaction between the inflation of the chamber above and the counter-pressure exerted by the constraining layer. The parameterization of the cross-section for the second moment of area calculation is shown in **Fig. 2**. **Fig. 2(a)** shows a longitudinal section along the actuator centerline with a full chamber, and **Fig. 2(b)** presents the cross-section at a chamber location. White indicates the silicone material, whereas black represents air.

$$I = \frac{l_2(h_2^3 + a^3) - l_1 h_1^3}{3} \tag{4}$$

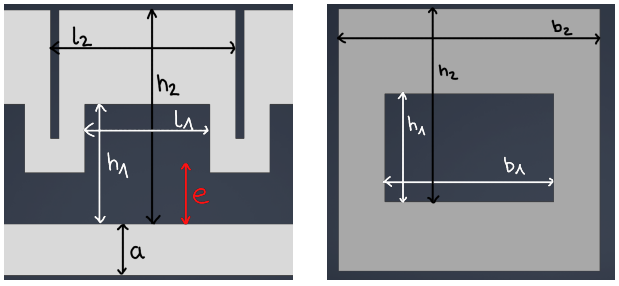

(a) Longitudinal section **(b)** Cross-section at a chamber

Fig. 2. Sectional view of the soft actuator

4. Tests

Two types of tests were carried out to evaluate the donning mechanism. The first was a comparison between the

theoretical mathematical model and the real actuator. The second was a user test, in which the actuator was tested on different people as a proof of principle.

4.1. Mathematical Evaluation

For validation, the bending angle was computed for two versions of the soft actuator using the previously derived model and compared with experimental results.

The experimental setup consists of an aluminum frame and a specially adapted mount for the soft actuator. The soft actuator is securely clamped into this mount using the recesses along its edge, allowing it to hang freely and straight downward. A 4K camera is mounted on the opposite side of the frame, continuously recording the entire bending process (**Fig. 3**). The camera is aligned so that the soft actuator remains fully within the field of view throughout the entire experiment and the movements can be captured precisely. For improved and reliable tracking of the bending angle, the soft actuator is equipped at several points with *ArUco* markers measuring $20\,\text{mm} \times 20\,\text{mm}$, which are detected by the camera. A Python program detects these markers and determines their position as well as the respective rotation angle.

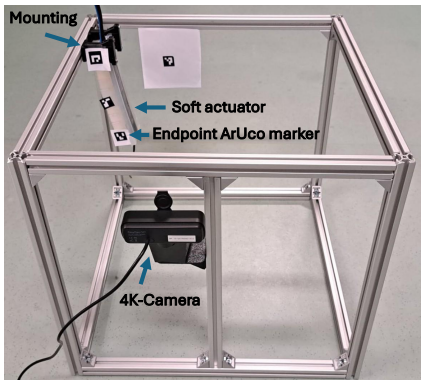

Fig. 3. Measurement setup

The calculation is based on **Eq. 3**. The geometric dimensions were obtained from CAD models or direct measurements of the soft actuators. The area moment of inertia was calculated using **Eq. 4**, and the pressure values were taken from experimental data. The Young's modulus was derived from Larson's data using the heometric Dynamic Analysis curve, in which the silicone is subjected to sinusoidal loading [5]. The lowest value was selected due to the use of very soft silicone (Shore A00). Using these parameters, final bending angles of $201.21°$ (8 chambers) and $266.15°$ (10 chambers) were obtained, compared to measured values of $206°$ and $270°$. The measured angular profile of the soft actuator is shown in **Fig. 4**. The increasing rate of change of angle with respect to pressure is clearly visible, representing the soft actuator curling up.

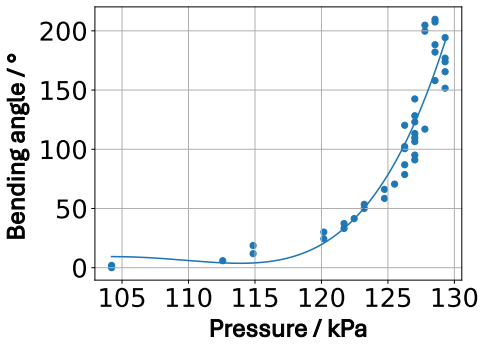

Fig. 4. Measured angular profile for an 8-chamber soft actuator

4.2. User Test

For the user test, the fully assembled donning mechanism, including all sensors and actuators, was evaluated to assess functionality and usability. Initial tests were conducted on a mannequin leg to eliminate injury risk and ensure repeatability, as the leg position and circumference remain constant and are unaffected by muscle activity or clothing.

During testing, the leg was positioned horizontally and the mechanism placed centrally on top. The soft actuator was oriented to one side, while the strap with the magnetic latch hung freely on the opposite side. The mechanism was lightly stabilized to prevent slipping, and the closing process was initiated via a switch. Upon activation, the actuator bent due to pneumatic input until the soft actuator latched onto the magnetic coupling. After a threshold pressure of $115kPA$ was exided and after 2 seconds, the motor wound the strap onto a spindle, increasing the measured force and tightening the closure around the leg until a threshold was reached. Additional tests on three human subjects revealed increased sensitivity to disturbances, primarily due to leg movement and interference from clothing. This required more precise positioning and occasionally multiple attempts to achieve full closure. However, the subsequent tightening and release processes were unaffected, resulting in a secure and stable fit without causing discomfort or pressure points.

As shown in **Fig. 5**, the pressure curve approaches saturation over time. This indicates that the pumped air then mainly bends and inflates the soft actuator, showing that the connection between the soft actuator and the coupling is achieved after around five seconds.

5. Results and Discussion

The comparison between the measured and the calculated final bending angles shows that the model yields reliable results and can be employed to predict other chamber geometries and actuator configurations. In this way, it serves as a useful tool for further optimization of the design. The user test demonstrates that the developed don-

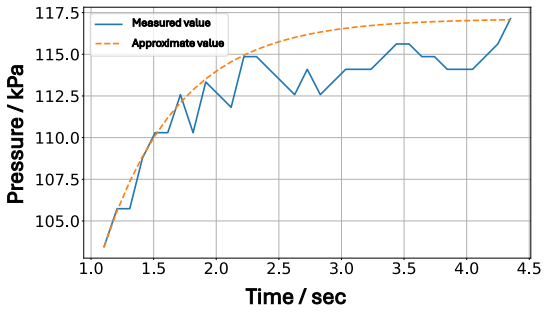

Fig. 5. Pressure trajectory during donning

ning mechanism is fundamentally functional and capable of performing the intended automated closing process. Under controlled laboratory conditions, especially in the mannequin tests, closure was achieved reliably in most cases, confirming that the combination of a soft actuator, a magnetic latch, and a motor-driven tightening mechanism is appropriate for the application. The pressure-versus-time behavior of the actuator was monitored during donning, revealing larger fluctuations than in the static tests. Nevertheless, the actuator inflated reproducibly and produced the required motion. The limited maximum pressure proved sufficient to avoid mechanical interference with the leg, and the bending motion was able to compensate for minor variations in strap length. When the deviations became larger, the magnetic latch could not always lock onto the soft actuator. By contrast, the motor-driven tightening with force feedback behaved consistently, halting automatically at a predefined force and thereby guaranteeing a reproducible clamping force. The total closing time of roughly eleven seconds is short, and the high level of automation provides clear benefits for elderly or motor-impaired users. Tests performed on human legs uncovered additional challenges that arise under realistic conditions. Movement of the leg and the presence of clothing introduced disturbances, increased variability, and occasionally required several attempts before a successful closure could be achieved. These findings highlight the need for further refinement of the positioning strategy and for a latch design that can accommodate larger positioning errors.

6. Conclusion and Outlook

The experimental results confirm that the proposed donning system is capable of donning an exoskeleton automatically, without external help, in a laboratory environment. The silicone soft actuator provides a pressure-controlled bending motion that has prooven effective for this type of application. The accompanying mathematical model offers a useful estimate of the soft actuator motion. Nevertheless, the system is still vulnerable to misplacement and to variations in limb size, which may require several attempts before a secure closure is achieved. Fatigue of the actuator material, especially tearing at the casting interfaces, and the limited clearance required by the magnetic latch represent the most critical weaknesses. Future work should concentrate on strengthening the actuator through refined geometries, alternative elastomers, or improved manufacturing, and on redesigning the latch to tolerate larger gaps. A subsequent phase will involve larger-scale user studies that include long-term wear tests with a diverse cohort of participants to verify durability and usability in everyday settings.

Acknowledgements

The research described in this paper was supervised by Prof. Dr.-Ing. Dr. med. Dr. h.c. Steffen Leonhardt. Additional thanks goes to Dr.-Ing. Marian Walter for advice and support.

The paper was written with the support of *DeepL* and *OpenAI ChatGPT 5.2*, which were used for grammar and spelling correction, text compression, and wording assistance.

References

[1] ROSE, C. G., O'MALLEY, M. K. Hybrid rigid-soft hand exoskeleton to assist functional dexterity. *IEEE Robotics and Automation Letters*, 2019, vol. 4, no. 1, p. 73–80.

[2] HERNÁNDEZ-BARRAZA, L., FRAISZUDDEEN, A., LEE, D., YEOW, C.-H. Development of a novel hybrid securing actuator for a self-securing soft robotic hand exoskeleton. *Frontiers in Robotics and AI*, 2023, vol. 10.

[3] VAN VLERKEN, C., *et al.* Development of an active physical interface for physical human-robot interaction: investigation of soft pneumatic actuator straps for automatic enclosure system. *Actuators*, 2023, vol. 12, no. 6, p. 241.

[4] ALICI, G., CANTY, T., MUTLU, R., HU, W., SENCADAS, V. Modeling and experimental evaluation of bending behavior of soft pneumatic actuators made of discrete actuation chambers. *Soft Robotics*, 2018, vol. 5, no. 1, p. 24–35.

[5] LARSON, K. Can you estimate modulus from durometer hardness for silicones? Yes, but only roughly ... and you must choose your modulus carefully!. 2017.

About Authors...

Raphael HOFFMANN was born in Oberhausen, Germany, in 1998. He received his bachelor in mechanical engineering in 2021 and his master degree in automatic control in 2023 from RWTH Aachen University. He focuses on robotics like exoskeletons and control theory. Since 2024 he is working as a research associate at the Chair of Medical Information Technology at RWTH Aachen University.

Lara SCHWEITZER achieved her bachelor degree in electrical engineering and information technology in March 2026 at RWTH Aachen University. With her bachelor thesis she contributed significantly to this paper.

Active Upper Limb Exoskeleton for Arm Rehabilitation

Forouzan Salehi Fergeni, Mohamed Aziz Touahria , Marc Bühlmann

Medical Information Technology (MedIT), Helmholtz-Institute for Biomedical Engineering, RWTH Aachen University, Pauwelsstr. 20, 52074 Aachen, Germany

salehi@hia.rwth-aachen.de, aziz.touahria@rwth-aachen.de, marc.buehlmann@rwth-aachen.de

Abstract. *Upper-limb motor impairments caused by neurological disorders, stroke, or traumatic injuries have increased considerably in recent years, leading to serious limitations in patients' ability to perform daily activities. Conventional rehabilitation therapies typically require intensive and repetitive training under the supervision of therapists, which can be both time-consuming and costly. Consequently, the development of assistive robotic technologies has gained significant attention in the field of rehabilitation engineering. Among these technologies, upper-limb exoskeletons have emerged as promising solutions to support patients in regaining motor function by providing controlled and repetitive movements during therapy. However, one of the main challenges associated with many existing upper-limb exoskeletons is their high cost, which limits their accessibility for a large number of patients. Therefore, this study proposes the design and implementation of a low-cost upper-limb exoskeleton intended to improve accessibility to rehabilitation technologies for a larger population of patients.*

Keywords

Upper-limb exoskeleton, Motor rehabilitation, Human–robot interaction, Assistive robotics, Low-cost rehabilitation devices.

1. Introduction

Upper-limb motor impairments caused by neurological disorders, stroke, or traumatic injuries represent a significant challenge in modern rehabilitation. Stroke alone remains one of the leading causes of long-term disability worldwide, with more than 101 million people currently living with the consequences of stroke globally [1]. These conditions often result in reduced mobility and a diminished ability to perform daily activities independently. Traditional recovery protocols often place a heavy burden on healthcare systems due to the necessity of continuous therapist supervision and prolonged clinical sessions. While robotic intervention offers a consistent alternative, the prohibitive pricing of current market solutions remains a primary barrier to widespread adoption in home-based settings [2].

Robotic rehabilitation systems have therefore gained increasing attention as tools capable of delivering consistent and repetitive training. Among these technologies, upper-limb exoskeletons are particularly promising because they can assist or guide limb movements while promoting neuroplasticity through repetitive motion training.

Despite their potential, many commercially available rehabilitation exoskeletons remain expensive and complex, limiting their accessibility for a large number of patients. The price of clinical rehabilitation exoskeletons typically ranges from several thousand to tens of thousands of euros, which significantly limits their accessibility in many rehabilitation centers and makes them impractical for home-based rehabilitation. The objective of this work is therefore to design and implement a low-cost active upper-limb exoskeleton capable of assisting forearm motion while maintaining sufficient functionality for rehabilitation exercises (see Fig. 1).

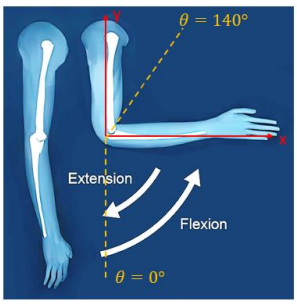

Fig. 1. Range of Motion for Elbow Flexion and Extension [4].

The proposed system integrates sensing, actuation, wireless communication, and control algorithms to support two rehabilitation modes: intent-based force assistance and motion replication from a healthy limb.

2. Materials

The developed exoskeleton system integrates mechanical, electronic, and sensing components designed to facilitate forearm motion around the elbow joint. The

mechanical structure comprises 3D-printed components that provide structural support for the upper arm, elbow joint, and forearm. Actuation is provided by a servo motor mounted at the elbow joint, enabling a single degree-of-freedom motion corresponding to elbow flexion and extension.

The electronic architecture of the system incorporates ESP32 microcontrollers, an MPU6050 inertial measurement unit (IMU), and a load cell force sensor equipped with an HX711 amplifier. The power sub-system consists of a lithium-polymer battery, DC-DC step-down converters, a safety fuse, and control switches. The overall system is organized into two independent modules: a Master unit and a Slave unit. The Master unit, worn on the healthy arm, utilizes the IMU sensor and microcontroller to measure arm orientation and transmit reference motion data via Wi-Fi. The Slave unit is mounted on the affected arm and includes the exoskeleton structure, actuator, force sensor, and control electronics responsible for executing movement commands. This dual-unit architecture enables the exoskeleton to function either as an assistive device responding to user effort or as a rehabilitation tool replicating motion from the healthy limb.

3. Methods

3.1 Hardware Architecture

The mechanical structure of the slave unit used in this work is based on a modified version of the cost-effective upper-limb rehabilitation exoskeleton introduced in [3], which inspired the main concept of the proposed system.

The mechanical components of the exoskeleton were manufactured using a 3D printing process. All structural parts were printed using PETG filament. As a result of the lightweight material and optimized structure, the complete slave unit exoskeleton has a relatively low total mass of 1.09 kg, making it suitable for wearable rehabilitation applications. Fig. 2 illustrates the mechanical design of the exoskeleton. The CAD model of the device, as well as the final assembled prototype, is shown for comparison.

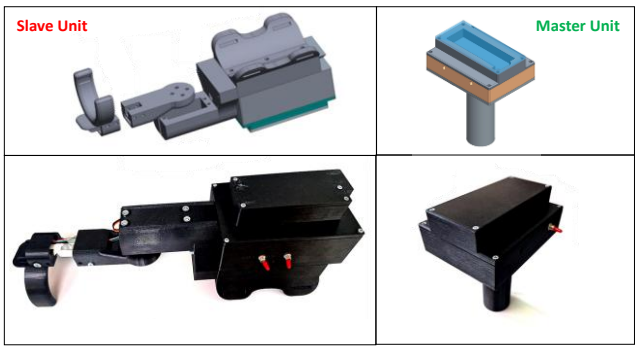

Fig. 2. Mechanical design of the developed exoskeleton.

3.2 System Architecture

The proposed control framework operates through a coordinated dual-node network. The Master module functions as the primary reference generator by digitizing the healthy limb's kinematics, while the Slave module serves as the execution unit, translating received wireless packets into synchronized mechanical torque via its integrated actuation system. The master module generates reference motion data, while the slave module processes sensor inputs and controls the actuator accordingly. Fig. 3 demonstrates the system overview.

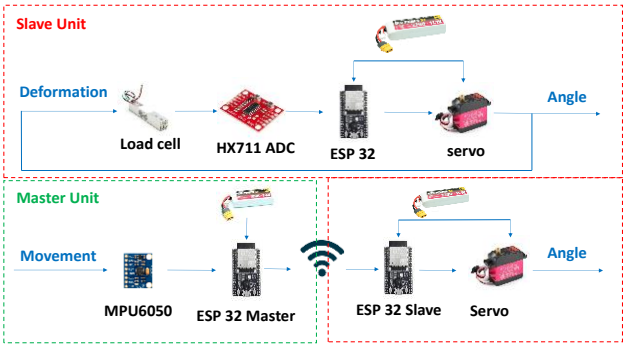

Fig. 3. System overview of the master-slave exoskeleton architecture.

3.3 Force-based assistance mode

In force control mode, the exoskeleton detects the user's movement intention through a load cell mounted on the forearm support. The load cell measures the force applied by the user and converts it into a digital signal using an HX711 amplifier. The measured force signal is filtered to remove noise and small fluctuations using a deadband and low-pass filtering.

A PI control algorithm is used to translate the force measurement into actuator motion. The control objective is to reduce the measured force toward zero. When the user applies force to initiate movement, the controller generates a corresponding actuator motion that assists the intended movement. (See Fig. 4).

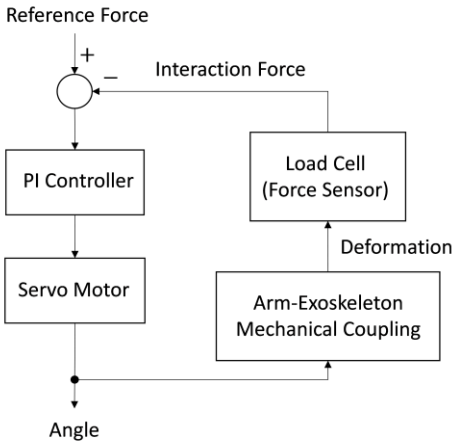

Fig. 4. Control Loop of the Force-based assistance mode.

This strategy enables the exoskeleton to provide assistance only when required, encouraging active participation from the user during rehabilitation.

3.4 Motion replication mode

The second operating mode is designed for rehabilitation exercises based on bilateral training. In the mimic configuration, the motion of the healthy arm is measured using an MPU6050 inertial measurement unit. The sensor provides acceleration and angular velocity measurements, which are fused to estimate the arm's roll angle.

A Kalman filter is implemented to combine accelerometer and gyroscope data. The gyroscope provides smooth short-term angular velocity information, while the accelerometer provides an absolute orientation reference. Sensor fusion reduces measurement noise and limits drift, resulting in a stable estimate of the arm orientation. The estimated angle is mapped to the mechanical range of the actuator and transmitted to the slave unit. The slave controller receives this reference angle and drives the servo motor to reproduce the same movement on the affected arm.

3.5 Wireless Motion Transmission

After estimating the wrist angle, the master ESP32 transmits the reference motion to the slave unit using a TCP communication protocol over Wi-Fi. The transmitted reference angle is mapped to the mechanical limits of the servo actuator:

$$\theta_{servo} = \frac{(\theta - \theta_{min})}{(\theta_{max} - \theta_{min})} \times 120° \quad (1)$$

where θ represents the measured wrist angle, and 120° defines the maximum allowable actuator angle based on the mechanical constraints of the system. This mapping ensures that the human wrist motion is translated into a safe actuator motion range.

3.6 Safety Mechanisms

To ensure safe and reliable human-robot interaction, several safety mechanisms were integrated into the control architecture. These include velocity limiting to avoid sudden actuator motion, servo angle saturation to prevent joint over-extension, and force dead-band filtering to eliminate noise-induced movements. Collectively, these measures ensure stable and predictable operation during various rehabilitation exercises.

4. Results

The developed prototype demonstrates the feasibility of a low-cost exoskeleton system capable of assisting forearm rehabilitation through two primary operational modes. In the mimic mode, the system successfully replicates the motion of a healthy arm onto the affected limb. The experimental validation confirms the efficacy of the stochastic filtering approach. As demonstrated in Figure 5, the raw inertial data were prone to significant jitter; however, the Kalman implementation effectively isolated the true orientation from high-frequency artifacts. This stabilization is vital for preventing erratic motor behavior, thereby ensuring user safety during active mimicry.

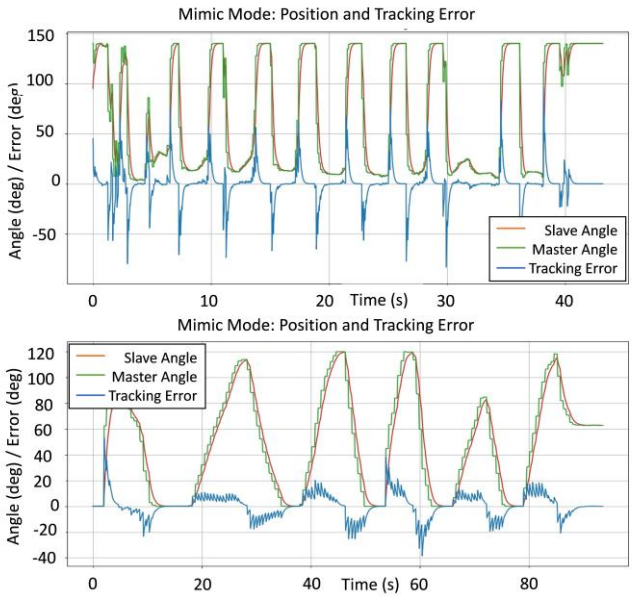

Fig. 5. Angle tracking performance in Mimic Mode. Top: Raw sensor measurements exhibiting high-frequency vibrations; Bottom: Stabilized angle estimation after Kalman filter implementation.

Furthermore, in the force control mode, the exoskeleton responds to user-applied forces detected by the load cell, where a PI controller generates actuator motion proportional to the measured force to facilitate intuitive interaction between the user and the device.

The experimental setup showing the developed exoskeleton worn by a subject during system evaluation is illustrated in Fig. 6.

Fig. 6. Final prototype of the developed upper-limb exoskeleton worn by a user.

The economic feasibility of the developed system is summarized in Tab. 1, which provides a detailed

breakdown of the component costs. When compared to commercially available hand exoskeleton solutions, the total expenditure remains significantly lower, underscoring the cost-effective nature of this design. It should be noted that the costs associated with the 3D-printed mechanical components are estimated, as these parts were fabricated using the internal facilities of the research institute. This approach further highlights the accessibility of the proposed architecture for low-budget rehabilitation and research applications.

Component	Number	Cost per unit (Euro)	Total cost (Euro)
ESP32	2	9.99	19.98
Battery	2	13.60	27.20
Load Cell	1	1.00	1.00
MPU-6050	1	4.33	4.33
Wiring and Connectors	1	1.60	1.60
HX711	1	1.17	1.17
DC/DC DOWN	3	1.30	3.90
Servo Motor	1	26.95	26.95
On/off Switch	3	0.60	1.80
3D Printing Materials	1	~10.00	10.00
Cost for the device	97.93 €		

Tab. 1. Component costs of the developed upper limb exoskeleton.

5. Conclusion

In this study, a functional and budget-friendly upper-limb exoskeleton was successfully prototyped and evaluated. By bridging the gap between high-end clinical robotics and accessible home-rehabilitation tools, this system demonstrates that reliable motion replication and force-assisted interaction can be achieved using an optimized low-cost sensor suite. Two operating modes were implemented: motion replication based on inertial sensing of a healthy limb and intent-based assistance using force control. Experimental evaluation demonstrated that the system can reproduce smooth and responsive movements while maintaining safe interaction with the user.

Future improvements will focus on increasing the number of degrees of freedom of the device in order to better reproduce natural upper-limb movements. Additionally, further work will aim to improve the ergonomic design and enhance the user interface to facilitate patient interaction and usability. These improvements will contribute to making the system more suitable for practical rehabilitation applications and long-term use by patients.

Acknowledgements

This research has been funded by the German Academic Exchange Service (DAAD).

The authors would like to gratefully acknowledge the supervision and support of Prof. Steffen Leonhardt and Dr. Marian Walter from the Chair for Medical Information Technology, Helmholtz Institute for Biomedical Engineering, RWTH Aachen University.

An AI language model developed by OpenAI was used for language editing and text refinement during the preparation of this manuscript.

References

[1] Boardsworth, K., Rashid, U., Olsen, S. et al. *Upper limb robotic rehabilitation following stroke: a systematic review*, 2025, vol. 22, no. 164.

[2] Alkani, R. A., Arjawi, L., Nadim, W. et al. *Telerehabilitation: Optimizing Patient Outcomes and Accessibility in Post-Stroke Recovery*, 2025, vol. 32, no. S7.

[3] Triwiyanto T, Wakidi LF, Pawana IPA. *Exoskeleton for Upper Limb Rehabilitation (EULR) with 3D printing technology based on force sensor*, 2025.

[4] https://chg.osimebcu.co.uk/joints.php

About Authors

Forouzan SALEHI FERGENI received her Bachelor's degree in Electrical Engineering and the M.Sc. degree in Electrical Engineering, majoring in electronic integrated circuits, from Shahid Chamran University, Ahvaz, Iran. She is currently a Ph.D. student at RWTH Aachen University, Aachen, Germany. Her research interests include wearable robotics (exoskeleton), Human-Robot interaction, control systems, and rehabilitation robotics.

Mohamed AZIZ TOUAHRIA received his Bachelor's degree in Electrical Engineering at RWTH Aachen University with a specialization in Communication Engineering. He is currently pursuing a Master's degree in Electrical Engineering at RWTH Aachen University. His research interests include automation and intelligent systems design, with a focus on bridging traditional control engineering and modern AI-based approaches.

Marc BÜHLMANN is an exchange Bachelor's student in Electrical Engineering at RWTH Aachen University with a focus on biomedical engineering. He is the team captain of the AixSense 2026 team for the SensUs student competition and is interested in biomedical technologies and medical devices.

Discovering wave equations for nonlinear sound beams from data

Tereza FILIPSKÁ[1]

[1]Dept. of Physics, Faculty of Electrical Engineering, Czech Technical University, Technická 2, 166 27 Praha, Czech Republic

filipte3@fel.cvut.cz

Abstract.

This study presents a data-driven framework for discovering governing equations of nonlinear sound beams, specifically targeting the Khokhlov-Zabolotskaya-Kuznetsov (KZK) model. By applying a paraxial approximation and transforming full Navier-Stokes numerical data into retarded time, we align wave configurations for efficient sparse identification via a library-based regression algorithm. Using a weak formulation with "bump" test functions, we successfully identified the structural form of the KZK equation. The results show that the nonlinearity coefficient was discovered with a relative error slightly under 1%, demonstrating that this workflow can robustly extract interpretable physical laws from complex, high-fidelity simulations of directional acoustic fields.

Keywords

Equation discovery, weak formulation, KZK equation, nonlinear acoustic, paraxial approximation, retarded time

1. Introduction

Nonlinear acoustic waves manifest in various forms, from resonance phenomena in cavities to free propagation in open space [2, 3]. A critical category consists of devices specifically designed to produce directional sound beams, which serve as a technical workhorse in several high-impact fields. In medical ultrasonography, these models are essential for predicting focal waveforms and shock formation in therapeutic HIFU (High-Intensity Focused Ultrasound), where they help compute heating rates for tissue ablation [5]. Similarly, in lithotripsy, they are used to model high-amplitude pulses for non-invasive kidney stone fragmentation [5]. Furthermore, in underwater acoustics, directional beams underpin the development of parametric arrays, which rely on nonlinear interactions to generate highly directive low-frequency fields [4].

In these applications, three key physical mechanisms - diffraction, thermoviscous absorption, and quadratic nonlinearity - interact at the same asymptotic order [4]. Except for highly simplified cases, these phenomena lack closed-form analytical solutions that quantitatively capture the entire field, necessitating the use of numerical solvers or Physics-Informed Machine Learning.

This study builds on our previous work in data-driven equation discovery, with the primary objective of adapting the methodology specifically for sound beams. To achieve this, we transition from general wave operators to a specialized workflow focusing on the paraxial approximation and retarded time formulation [4]. In the following sections, we demonstrate how this approach allows for the robust identification of the KZK model from full Navier-Stokes numerical simulations, providing a powerful tool for inverse design and optimization of nonlinear acoustic fields.

2. Theory

For sound propagation in two dimensions, the wave equation reads [3]:

$$\frac{\partial^2 p}{\partial x^2} + \frac{\partial^2 p}{\partial y^2} - \frac{1}{c_0^2}\frac{\partial^2 p}{\partial t^2} = 0 \tag{1}$$

where p is the acoustic pressure and let c_0 denote the adiabatic speed of sound. The common way of deriving the equation for beams (the wave equation in paraxial approximation) is to use the Fourier transform and work with a specific limit of the Helmholtz equation. However, this approach is intended for monofrequency waves. In the case of sound beams with variable frequency content, it is more advantageous to make use of the retarded time formulation [4, 2]:

$$p(x, y, t) \;\rightarrow\; q(x, y, \tau), \;\; \tau = t - \frac{y}{c_0} \tag{2}$$

where the definition of the retarded time τ considers propagation of a sound beam along y axis. After substitution and some manipulations, it is possible to arrive at the following:

$$\frac{\partial^2 q}{\partial x^2} + \frac{\partial^2 q}{\partial y^2} - \frac{2}{c_0}\frac{\partial^2 q}{\partial y \partial \tau} = 0\,. \tag{3}$$

The final form of the linear wave equation for beams is obtained by realizing that for waves along y with slowly spatially varying amplitude $|\frac{\partial^2 q}{\partial y^2}| \ll |\frac{2}{c_0}\frac{\partial^2 q}{\partial y \partial \tau}|$ and hence:

$$\frac{2}{c_0}\frac{\partial^2 q}{\partial y \partial \tau} - \frac{\partial^2 q}{\partial x^2} = 0\,. \tag{4}$$

Similarly to our previous article, we will use the linear form of the equation as a starting point for equation discovery – only this time for the case of beams.

To generalize the discovery process, we introduce a set of dimensionless variables:

$$X = \frac{x}{l} \qquad Y = \frac{y}{l} \tag{5}$$

$$P = \frac{q}{\rho_0 c_0^2} \qquad \Theta = \frac{c_0}{l}\tau \tag{6}$$

where l is the characteristic spatial dimension and ρ_0 is the ambient density. By substituting these relations into the previous equation 4, we get the dimensionless form of our target:

$$2\frac{\partial^2 P}{\partial Y \partial \Theta} - \frac{\partial^2 P}{\partial X^2} = f(P) \tag{7}$$

where f is an unknown function of P and its derivatives (not explicitly given above for the sake of simplicity).

3. Data generation

The data used to train and validate the equation-discovery algorithm were generated by numerically solving the full compressible Navier-Stokes equations. Basing the discovery process on these fundamental equations ensures that the underlying physics includes all relevant nonlinear and diffractive effects before any paraxial approximations are introduced [1]. The solution was obtained using the Kurganov-Tadmor central scheme, which is specifically designed for the stable capturing of discontinuities and steep gradients in the pressure profile [6]. The simulation models a 2D nonlinear acoustic beam in the air, driven by a piston source with a Gaussian aperture profile, creating a field in which the beam propagates primarily in one direction (along the y-axis).

A dataset was constructed by simulating ten different scenarios with excitation frequencies varying by $\pm 20\%$. The spatial evolution of the acoustic pressure field P, as shown in Fig. 1, illustrates the transition from a linear source to a nonlinearly distorted beam. For the discovery algorithm, the raw data $P(X, Y, T)$ were transformed into retarded time $\Theta = T - Y$.

This transformation "freezes" the wave profile in the moving frame which is a crucial step for the algorithm to identify the governing operators. As illustrated by comparing Fig. 2 and Fig. 3, the wavefronts that appear tilted in the physical domain (Y, T) due to the propagation velocity, align vertically in the domain (Y, Θ). This alignment is crucial for the algorithm to smooth the data and effectively identify the paraxial operator.

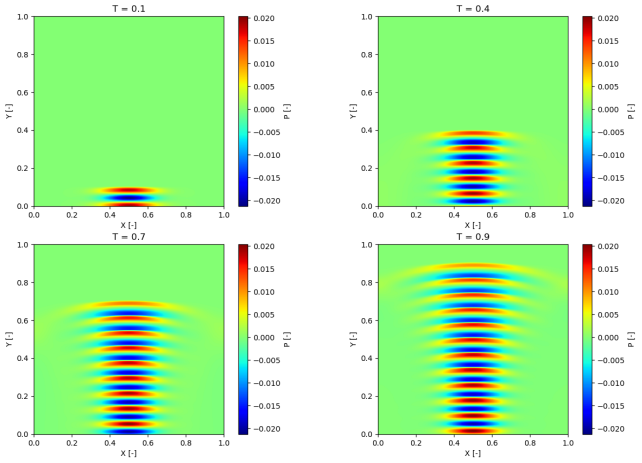

Fig. 1. Evolution of the 2D acoustic pressure field P in dimensionless X, Y coordinates at selected time instants T.

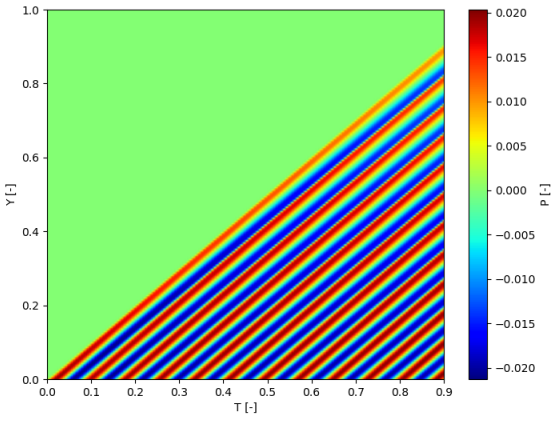

Fig. 2. Space-time plot (Y, T) on the beam axis.

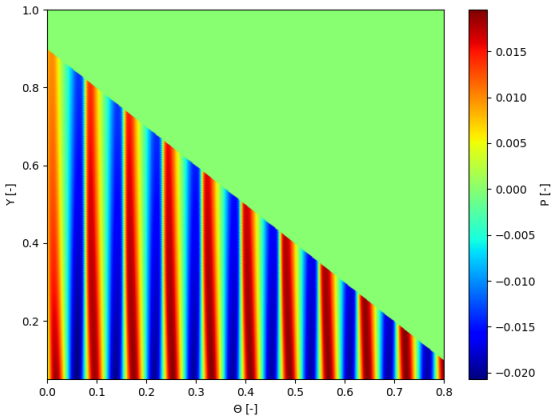

Fig. 3. Transformation to retarded time (Y, Θ).

4. Equation discovery

To identify the unknown function $f(P)$, we employ a supervised library-based regression algorithm. A key feature of our approach is the use of a weak formulation of the governing equations. By integrating with sufficiently smooth "bump" test functions, we effectively transfer the derivatives from the potentially noisy data to the test functions through integration by parts [7, 8].

The physical limits of the simulation constrain data sampling. To ensure the integrity of the weak formulation, each test function is centered at such that its entire support of each the function remains within the computed domain, especially satisfying the condition $\Theta + Y \leq T_{max}$ to prevent the test function from extending beyond the available simulation data. This ensures that the integration by parts remains mathematically valid.

The identification process involves evaluating a predefined library of candidate terms. These terms are processed using L1-regularized least squares (LASSO). An optimal subset of these candidate terms is then identified using the Bayesian Information Criterion (BIC). This methodology ensures effective data smoothing and robust identification of the underlying physical laws even in the presence of nonlinear steepening.

5. Results

On a test set of ten beams, the algorithm successfully identified the structure of the nonlinear term corresponding to the KZK equation:

$$2\frac{\partial^2 P}{\partial Y \partial \Theta} - \frac{\partial^2 P}{\partial X^2} = (1.218 \pm 0.155)\frac{\partial^2 P^2}{\partial \Theta^2};. \qquad (8)$$

The found nonlinearity coefficient exhibits a relative error of approximately 1% compared to the theoretical value for air. The low standard deviation confirms the stability of the identification across different frequencies. The missing damping term corresponds to the weakly nonlinear limit in a gaseous medium, where viscous losses are intractable at the given scale.

6. Conclusions

This study demonstrates a successful data-driven discovery of the nonlinear wave equation for sound beams. The weak formulation proves to be robust against noise and discontinuities, allowing it to be applied to Navier-Stokes data. The algorithm captured the structure of the Khokhlov-Zabolotskaya-Kuznetsov equation, balancing difraction and quadratic nonlinearity. The identified nonlinearity coefficient (1.218) achieved a relative error only slightly under 1% compared to the theoretical values. The results confirm that retarded-time equation discovery is a powerful tool for designing and optimizing high-intensity focused ultrasound (HIFU) fields.

Acknowledgements

Research described in the paper was supervised by RNDr. MgA. Viktor Hruška, Ph.D. (FEE CTU).

This work was supported by the Grant Agency of the Czech Technical University in Prague, grant No. SGS25/136/OHK3/3T/13.

References

[1] FILIPSKÁ, T. *Numerical Modeling of Nonlinear Acoustic Wave Propagation*. Bachelor's Thesis. Prague: CTU in Prague, FEE, 2024. Available from: https://dspace.cvut.cz/handle/10467/115132

[2] HAMILTON, M. F., BLACKSTOCK, D. T. *Nonlinear Acoustics*. Academic Press, 1998.

[3] NAUGOLNYKH, K., OSTROVSKY, L. *Nonlinear Wave Processes in Acoustics*. Cambridge University Press, 1998.

[4] HAMILTON, M. F., MORFEY, C. L. *Model Equations*. In: HAMILTON, M. F., BLACKSTOCK, D. T. (eds.). *Nonlinear Acoustics*. 3rd ed. Cham: Springer Nature, 2024, s. 65–112. Available from: https://doi.org/10.1007/978-3-031-58963-8_3

[5] CANNEY, M. S., KHOKHLOVA, V. A., BESSONOVA, O. V., BAILEY, M. R., CRUM, L. A. *Acoustic characterization of high intensity focused ultrasound fields: A combined measurement and modeling approach*. J. Acoust. Soc. Am., 2008, 124(4), 2406–2420. Available from: https://pmc.ncbi.nlm.nih.gov/articles/PMC2677345/

[6] KURGANOV, A., TADMOR, E. *New High-Resolution Central Schemes for Nonlinear Conservation Laws and Convection-Diffusion Equations*. Journal of Computational Physics, 2000, 160(1), 241–282. Available from: https://doi.org/10.1006/jcph.2000.6459

[7] HRUŠKA, V., FURMANOVÁ, A., FILIPSKÁ, T., VALÁŠEK, J. *Data-driven discovery of weakly nonlinear acoustic wave equations*. J. Sound Vib., 2026, 595, 118745.

[8] STEPHANY, R., EARLS, C. *Weak-PDE-LEARN: A weak form based approach to discovering PDEs from noisy, limited data*. J. Comput. Phys., 2024, 506, 112950.

About Authors...

Tereza FILIPSKÁ is a Master's student at CTU Prague, Czech Republic. Her research interests lie in numerical modeling of nonlinear acoustic propagation and data-driven discovery of wave equations. She received the Dean's Award for her Bachelor's Thesis.

Model Predictive Control in the Critically Ill Rat

Lorenz MICHAEL[1]

[1]Chair of Medical Information Technology (MedIT), RWTH Aachen University, Germany

michael@hia.rwth-aachen.de

Abstract. *Blood glucose regulation in the ICU remains a manual intervention with significant potential for improvement through automation. Testing and validating automated therapy systems in the ICU is difficult due to regulatory hurdles and the risk of harm to vulnerable patients. Animal studies are a crucial step in the development and validation of automated systems for critical care. Models of the glucose-insulin metabolism can aid in the design of controllers, and are useful for investigating physiological assumptions. In this work, a glucodynamic model of a human ICU patient is adapted to represent the glucose-insulin metabolism in a critically ill rat. A model predictive control structure for tight blood glucose control is proposed and compared to manual insulin therapy in in-silico experiments.*

Keywords

Physiological modeling, intensive care, model predictive control, tight blood glucose control, continuous glucose monitoring.

1. Introduction

Patients on the intensive care unit (ICU) often suffer from glycemic variability and acute hyperglycemia, which are both associated with increased mortality and generally worse outcomes [1][2]. ICU-clinicians monitor the blood glucose (BG) level in a patient, and administer insulin based on empirically informed judgement or established protocols. Closed-loop glucose control systems aim at automatically determining the insulin dosage required to achieve and maintain a desired BG level. In-silico simulations provide valuable validation results, but in-vivo experiments remain essential for establishing complex applications such as automated insulin delivery systems in clinical practice. Different glucodynamic rodent models have been proposed to investigate the diabetic glucose-insulin metabolism [3][4]. As a precursor for animal studies in rodents with induced critical illness, this paper adapts an existing mathematical model of the critically ill glucose homeostasis in human to rat physiology. A model predictive control structure is designed, aiming for tight glucose control (TGC) in the presence of measurement noise and pathophysiological homeostasis disturbance.

2. Glucodynamic Modeling

This section will initially present the underlying model for the insulin-glucose metabolism in critically ill patients. Afterwards, physiological differences between humans and rodents are derived from literature and translated to parameter adjustments.

2.1. The Hovorka ICU Model

Several mathematical glucodynamic models have been proposed in the literature, often based on the 'original' minimal model by Bergmann and Cobelli [5]. The model by Hovorka et al., specifically considering critically ill patients, was used for this work [6]. It is a time-variant, nonlinear, physiological model of eighth order. Fig. 1 depicts the model structure.

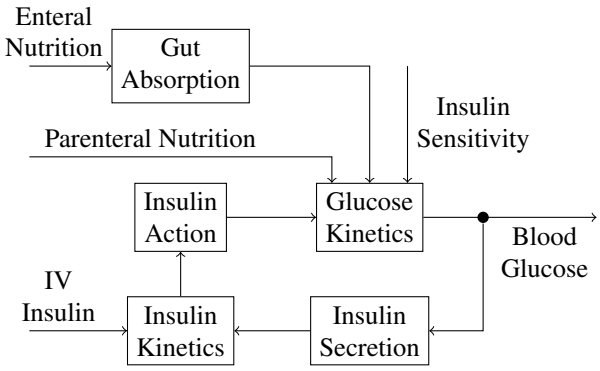

Fig. 1: Structure of the Hovorka ICU model, adapted from [6].

The $Gut\,Absorption$ submodel simulates the digestion of food or other clinical enteral nutrition. Changes in the BG level are derived via a mass balance approach within the $Glucose\,Kinetics$ submodel. It consists of two compartments, one each for accessible (periphal plasma) glucose content and non-accessible (interstitial and intracellular) glucose content. Production and distribution of insulin is repre-

sented by the *Insulin Secretion* submodel. Appearance and disposal of insulin is balanced in the *Insulin Kinetics* submodel. The *Insulin Action* submodel introduces auxiliary states to describe the effect of insulin on i) glucose distribution/transport, ii) glucose disposal, and iii) endogenous glucose production. There are four system inputs. *IV Insulin* describes the current intravenous administration rate of insulin to the patient. *Enteral Nutrition* and *Parenteral Nutrition* depict the current uptake (rate) of glucose, either via the digestive system or directly into the bloodstream. *Insulin Sensitivity* characterizes the effectiveness of insulin on the glucose dynamics. It can change quickly and several-fold in the critically ill, requiring a time-variable consideration in modeling approaches [7]. For the explicit form of the (differential) equations, interested readers are referred to the original publication. Hovorka et al. obtained patient-specific parameter sets by sampling certain parameters from physiologically motivated distributions. Estimation techniques had subsequently been applied to derive the remaining parameters from clinical data.

2.2. Critically Ill Rat Parameter Set

As rodents utilize the same organs for regulating their BG as humans do, the structure of the Hovorka ICU model is used as depicted in Fig. 1. Adaptations to the model parameters are necessary for simulating the rodent metabolism. Due to their smaller size, rodents have a much larger surface-area-to-volume ratio than humans. This results in increased heat loss and a higher metabolic rate, which drives a greater demand for nutrition relative to body weight.

Initially, the body weight parameter was adjusted. It linearly scales certain parameters, for example the distribution volumes of insulin and glucose. Sprague Dawley rats represent a key rat strain for biomedical research. A male adult rat with 500 g of body weight was assumed. Regarding aspect no. 2, rats show an increased insulin response to elevated glucose levels, a faster disappearance rate of insulin and generally increased BG levels [8][9]. To account for the observed differences between rats and humans, the following parameter values were doubled: Non-insulin-dependent glucose flux, fractional transfer rate between the glucose compartments, endogenous glucose production (EGP), insulin sensitivity of the EGP, and insulin sensitivity of glucose distribution/transport. Furthermore, the basal insulin secretion rate and the fractional elimination rate were multiplied with factor 5, and the beta-cell responsiveness was multiplied with factor 10.

Physiological adherence with the rat parameter set was investigated by applying common nutrition- and insulin dosages for rats. A moderate daily nutritional need of 35 grams/kg glucose-equivalents was assumed [10]. In relation to body weight, this is approximately seven times the nutritional need of a human patient on the ICU [11]. Only parenteral nutrition was considered, as animals in critical illness-studies are usually sedated and anesthetized. A small base dosage of 0.1 U/h/kg intravenous insulin was assumed. In relation to body weight, it is significantly higher than in humans. This is in accordance with the afforementioned metabolic differences. Fig. 2 shows the simulated BG level using the critically ill rat parameter set. The insulin dosage is adjusted during the simulation to investigate the dynamic model response.

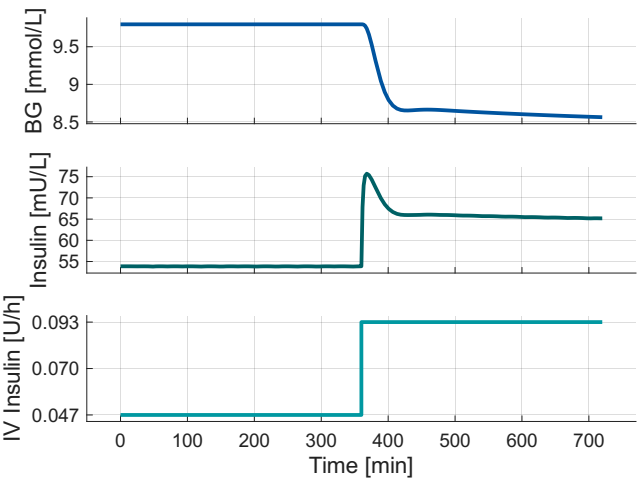

Fig. 2: Simulation results with the critically ill rat parameter set. A new quasi-steady state is established under 1 hour after the increase in insulin dosage. This is physiologically sound, and faster than the simulations in the human patient. With this basic validation in place, a control system was employed to tightly regulate BG in the critically ill rat.

3. Model Predictive Control

Model Predictive Control (MPC) is a control strategy that determines the best control action by using a model of the system to predict its future behavior. At each step, the controller simulates how the system will evolve over a finite time horizon for different possible inputs. Based on these predictions, MPC solves an optimization problem to find the sequence of control inputs that best achieves a specified objective, while adhering to constraints (e.g., input limits or safety bounds). After applying the first control input of this optimal sequence, the process is repeated at the next time step using updated measurements to create a feedback loop. Various MPC approaches for blood glucose control (in the ICU) have been proposed in the literature, yet none for rodents [12][13].

3.1. MPC Design

The optimal input sequence $\boldsymbol{u}^*$ is obtained by solving the optimization problem as shown in Eqs. 1a . . . 1d.

$$\boldsymbol{u}^* = \arg\min_{\boldsymbol{u}} \quad J(\boldsymbol{x}_{pred}, \boldsymbol{u}) \tag{1a}$$

$$\text{subject to} \quad \boldsymbol{x}_{pred} = \boldsymbol{f}(\boldsymbol{x}, \boldsymbol{u}), \tag{1b}$$

$$\boldsymbol{x}_i \in \mathbf{X} \quad \forall i = 1 \dots N, \tag{1c}$$

$$\boldsymbol{u}_i \in \mathbf{U} \quad \forall i = 1 \dots N \tag{1d}$$

The cost functional J assigns a scalar value to each combination of predicted state sequence $\boldsymbol{x}_{pred}$ and input sequence $\boldsymbol{u}$, defining the control objective. Constraint 1b ensures state predictions follow the system model dynamics. $\boldsymbol{f}$ must accurately represent the system, while remaining computationally efficient for repeated evaluations. Constraints 1c and 1d enforce bounds on states and inputs, defining the allowed operation region. The prediction horizon N specifies how many future time steps are considered in the optimization problem.

The following design choices were made to enable TGC: I) A linearization of the Hovorka ICU model around an equilibrium point was used as the internal prediction model. II) The cost functional J attached cost to deviations of predicted BG values to the reference, changes in the input values, and deviations of the nutritional input from the base rate. The BG reference was set at a normogylcemic level of 5.5 mmol/L. Both insulin and nutrition infusions were controlled, with higher cost attached to changing the nutritional dosage. The third component was implemented to maintain proper nutrition, while allowing short-term changes to regulate BG. III) Insulin dosages received an upper bound of 1.5 U/h. Parenteral nutrition could be adjusted within $\pm$ 50 % of the base value.

3.2. Continuous Glucose Monitoring

Clinicians currently obtain BG levels of a patient a few times a day via BGA. Such a low measurement frequency poses the risk of missing extreme values or detecting them too late. Continuous glucose monitoring (CGM) devices generate BG measurements multiple times per hour, and have the potential to greatly improve BG regulation. As a drawback, they require a sophisticated interface to the bloodstream, and add considerable noise and drift. A CGM with a measurement frequency of 1/min, a variance of 0.47 mmol/L, a bias of 0.01 mmol/L, and a measurement delay of 5 minutes was implemented for the simulation. They reflect published data from a non-commercial research device [14].

3.3. Control Architecture

The proposed controller structure for TGC in the critically ill rat is shown below in Fig. 3.

KF describes a linear Kalman filter. As it was integrated into the MPC-algorithm, the block is represented with a dotted border. Pumps are used to deliver insulin and parenteral nutrition to the patient. Dynamics are assumed sufficiently fast, such that controller output and system input are identical

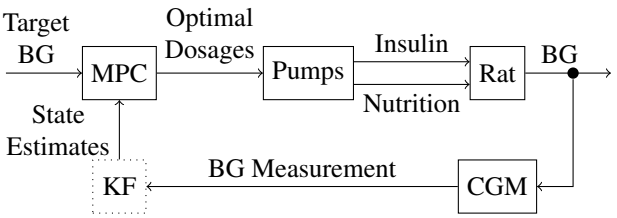

Fig. 3: Control Structure for TGC in the critically ill rat.

4. Results

The control structure was implemented in Matlab Simulink. Sampling time for the MPC was set to 5 minutes, with a prediction horizon of 120 minutes. Recovery from hyperglycemia and regulation to a normoglycemic range were tested with, and without critical homeostasis disturbance. Manual insulin therapy based on the Yale Protocol was used as a reference. Measurements for the manual therapy are assumed ideal (BGA instead of CGM), but are only carried out every 2 hours. The target range has been adjusted to 4.5-6.1 mmol/L. Per-weight insulin dosages were scaled by factor 10 to account for rodent physiology. Evaluation metrics are time-in-target-range (TITR) and mean BG level. Simulation results are shown in Fig. 4.

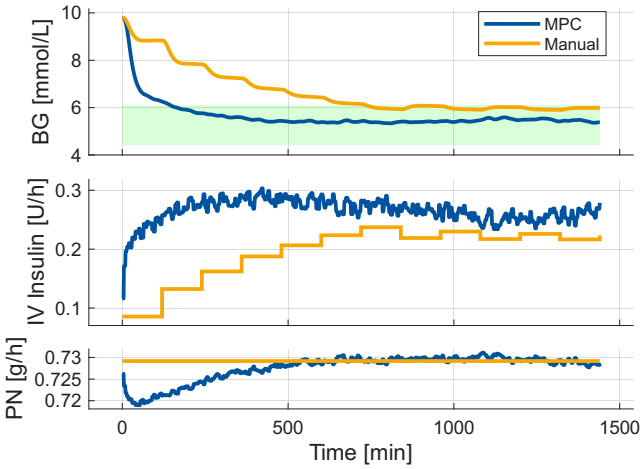

Fig. 4: Simulation results for hypercapnia recovery. The green area illustrates the range for TGC (4.5-6.1 mmol/L). PN: Parenteral nutrition.

Both the MPC and the manual therapy recover normoglycemia. The control range is reached much faster by MPC. Manual therapy shows ripples in the BG level, due to abrupt changes in the insulin infusion. The Yale protocol is designed to minimize hypoglycemic events. This is reflected

in stagnating insulin dosages and no further decrease in BG, once the upper limit of the target range is reached.

Variable insulin sensitivity was simulated in a second experiment. The literature provides insulin sensitivity profiles, resulting from fitting models to clinical data. One specific profile was modeled for the experiment [15]. The simulation results are shown in Fig. 5.

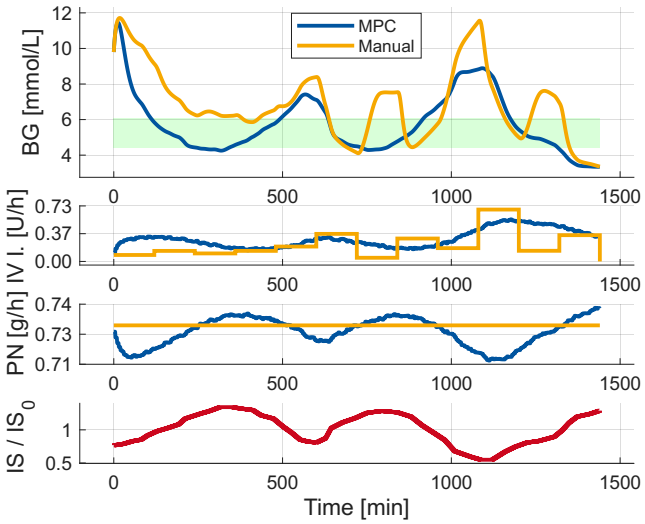

Fig. 5: Simulation results for hypercapnia recovery. The green area illustrates the range for TGC (4.5-6.1 mmol/L). PN: parenteral nutrition, IS: insulin sensitivity.

With variable insulin sensitivity, both conventional and automated insulin therapy cannot regulate the BG inside the tight target range. It is obvious however, that the rat experiences smaller deviations in BG from the reference with the MPC. Evaluation metrics are shown in Table 1

	$\bar{BG}\ [\frac{mmol}{L}]$		$TITR\ [\%]$	
S_I	MPC	Manual	MPC	Manual
Constant	5.67	6.67	89.9	48.9
Variable	5.78	6.87	43.8	23.7

Tab. 1: Comparison metrics for BG regulation via MPC and manual insulin therapy.

5. Discussion

A physiological glucodynamic model could be used to simulate the glucose-insulin dynamics in critically ill rats. Model parameter adjustments do not contradict the literature and established physiological insulin and glucose values with rat-specific input signals. An MPC control structure was deemed well suited to regulate BG in ciritically ill rats. Both, with constant and variable insulin sensitivity, the control structure had lower mean BG, a higher TITR, and has a smoother BG dynamic. Limitations need to be addressed. In reality, model parameters cannot be known a priori and are generally time-variant. For in-vivo implementations, a technique for the generation of an initial parameter set from a few measurements is necessary. Furthermore, online identification methods for the insulin sensitivity have the potential to improve the control performance even further.

Acknowledgements

Research described in the paper was supervised by Prof. Dr.-Ing. Dr. med. Dr. h.c. Steffen Leonhardt.

References

[1] M. FALCIGLIA et al. “Hyperglycemia-related mortality in critically ill patients varies with admission diagnosis”. In: *Critical care medicine* (2009).

[2] J. HERMANIDES et al. “Glucose variability is associated with intensive care unit mortality”. In: *Critical care medicine* (2010).

[3] H. AL ALI et al. “Examining Type 1 Diabetes Mathematical Models Using Experimental Data”. In: *International journal of environmental research and public health* (2022).

[4] JING FAN YANG et al. “Virtual Rodents: Design and Translation of Glucose-Responsive Insulins Aided By Pharmacokinetic Modeling”. In: AIChE, 2019.

[5] R. N. BERGMAN et al. “Quantitative estimation of insulin sensitivity”. In: *The American journal of physiology* (1979).

[6] R. HOVORKA et al. “A simulation model of glucose regulation in the critically ill”. In: *Physiological measurement* (2008).

[7] J. G. CHASE et al. “Tight glycemic control in critical care–the leading role of insulin sensitivity and patient variability: a review and model-based analysis”. In: *Computer Methods and Programs in Biomedicine* (2011).

[8] J. E. BOWE et al. “Metabolic phenotyping guidelines: assessing glucose homeostasis in rodent models”. In: *The Journal of endocrinology* (2014).

[9] G. M. KOWALSKI and C. R. BRUCE. “The regulation of glucose metabolism: implications and considerations for the assessment of glucose homeostasis in rodents”. In: *American journal of physiology. Endocrinology and metabolism* (2014).

[10] K. S. LAAKSONEN et al. “Food and water intake, growth, and adiposity of Sprague-Dawley rats with diet board for 24 months”. In: *Laboratory animals* (2013).

[11] P. SINGER et al. “ESPEN practical and partially revised guideline: Clinical nutrition in the intensive care unit”. In: *Clinical nutrition (Edinburgh, Scotland)* (2023).

[12] L. ORTMANN et al. “Automated Insulin Delivery for Type 1 Diabetes Mellitus Patients using Gaussian Process-based Model Predictive Control”. In: *2019 American Control Conference (ACC)*. IEEE, 7/10/2019 - 7/12/2019.

[13] C.-F. BENNER et al. “Model predictive control of blood glucose in critically ill patients using Gaussian processes”. In: *at - Automatisierungstechnik* (2024).

[14] N. K. SKJAERVOLD et al. “Continuous measurement of blood glucose: validation of a new intravascular sensor”. In: *Anesthesiology* (2011).

[15] CARL-FRIEDRICH BENNER et al. “Parameter identification of a model describing the blood glucose metabolism using clinical data”. In: *Proceedings on Automation in Medical Engineering* (2023).

EEG Artifact Classification using Machine Learning and Deep Learning on Clinically Collected Data

Franka NORDMANN[1]

[1]M.Sc. Biomedical Engineering, Dept. of Electrical Engineering, Technical University of Darmstadt, Karolinenplatz 5, 64289 Darmstadt, Germany

franka.nordmann@stud.tu-darmstadt.de

Abstract. *Electroencephalography (EEG) is highly susceptible to artifacts due to its low amplitudes, making reliable detection essential for clinical and automated analysis. Approaches range from signal-processing to machine learning and deep learning, but limited labeled datasets often require synthetic artifacts. This paper evaluates several machine learning and deep learning models on a clinically realistic dataset containing 27 artifact classes. Although fine-grained classification remains challenging, grouping physiologically similar artifacts improves performance. The implemented multilabel Random Forest achieves a macro F1-score of* 0.627*, while histogram gradient boosting exceeds* 0.82 *for binary detection. These results demonstrate the continued relevance of classical feature-based methods for small EEG datasets.*

Keywords

EEG, Artifact Detection, Machine Learning, Deep Learning, Multilabel Classification

1. Introduction

Electroencephalography (EEG) is widely used in clinical practice for diagnosing and monitoring epilepsy, assessing encephalopathies, and analyzing sleep stages and disorders. Beyond clinical use, EEG supports brain-computer interfaces and cognitive or affective state monitoring [1]. Due to their small amplitudes (20–50 µV) [2], EEG signals are highly susceptible to artifacts. Recognizing and differentiating artifact types is essential to identify technical issues and apply targeted mitigation strategies, and develop robust classifiers [3, 4].

Deep learning approaches currently dominate EEG classification [5]. While often achieving strong performance, they require substantial computational resources, limited interpretability and restricted performance on small labeled datasets, often necessitating semi-synthetic data [5]. As a result, traditional signal-processing, such as wavelet-based methods, and classical feature-based machine learning methods, such as Support Vector Machines (SVM), and Linear Discriminant Analysis, remain widely used, offering competitive performance with greater transparency [6, 7].

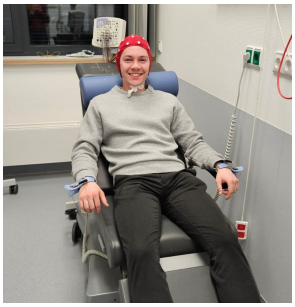

(a) Subject with EEG cap and ECG wrist electrodes

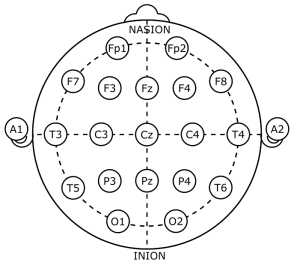

(b) Electrode placement of 10-20 system for EEG [8]

Fig. 1: EEG recording setup and electrode placement

This study evaluates machine learning and deep learning models on a clinically realistic dataset collected with a minimal sensor setup consisting only of EEG and electrocardiogram (ECG). Real induced artifacts, including simultaneous occurrences, were recorded, posing a challenge for reliable classification despite the small dataset size.

2. Materials

The dataset was recorded using a Neurofax (EEG-1200) from Nihon Kohden with an electrode cap. All recordings were made with reference to channel Cz, recording the channels Fp2, Fp1, F4, F3, C4, C3, P4, P3, O2, O1, F8, F7, T4, T3, T6, T5, Fz, Pz, A1 and A2, according to the 10-20 placement (Fig. 1b), resulting in 21 channels plus ECG. EEGs were recorded from 13 different people. A recording setup is illustrated in Fig. 1a.

During recordings, subjects kept their eyes closed and performed 13 instructed movements, associated with ocular activity, muscle activity (face and neck), and respiration. Additionally, electrode artifacts, induced by electrode movements, and spontaneous artifacts were recorded, yielding 27 artifact types in total. As shown in Fig. 2, artifact occurrence differed due to spontaneous repetitions and the exclusion of

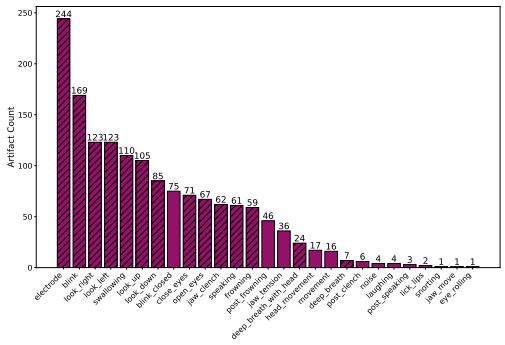

Fig. 2: Artifact counts for both, instructed (hashed) and spontaneous, artifacts.

instructed artifacts not visible in the signal. Artifact duration showed variability both across and within categories, particularly for jaw tension and electrode artifacts.

To prevent data leakage, a group-based 80:20 split was applied, ensuring that all data from each subject were assigned exclusively to either the training or the test set.

3. Methodology

3.1. Preprocessing

EEG data were re-referenced to the average of all channels and filtered with a 50 Hz notch filter to suppress powerline interference.

Recordings were segmented using window lengths of 0.5 s, 1 s, 2 s, and 3 s with 50% overlap. Moreover, event-based segmentation was applied, in which each segment contained a complete artifact setting a maximum segment length of 3 s. Labels were assigned based on a sample threshold, requiring a minimum number of artifact samples for the artifact label to be applied. In addition to binary labeling (artifact vs. no artifact), grouped labeling into six categories (eyes, eyelid, muscle, movement, electrode, extern) was performed. For segments containing multiple artifact types, both singlelabel and multilabel approaches were implemented. Rare artifact types were summarized as "others."

Two types of model input were generated. For a feature-based input, 22 length-independent features per channel were extracted, including statistical, spectral, Hjorth and entropy-based features. This resulted in 22 features $\times$ 22 channels $=$ 484 features in total. Features were standardized to zero mean and unit variance on the training data. For a raw EEG input, window-level within-channel normalization was applied and event-based segments were zero-padded to ensure equal window length.

For grouped classification, minority classes were augmented and the majority class ("no artifact") downsampled to address class imbalance. For raw EEG input, segments were normalized and padded as described above. For feature input, features were computed from augmented segments but excluding spectral centroid and relative ratios.

3.2. Models

Initially, eight different classifiers were trained to distinguish all artifacts and the no artifact class. These models included classical machine learning (ML) models trained on features such as Random Forest, Gradient Boosting, Histogram Gradient Boosting, XGBoost and SVM, and three different kinds of deep learning models, i.e., a one-dimensional (1D) CNN trained on raw EEG and a multilayer perceptron (MLP) trained on features and the raw input, respectively. Multilabel support was implemented for exemplary ML classifiers (Random Forest, SVM and XGBoost) and all deep learning classifiers.

For binary classification these classifiers were adapted to reflect the simplified decision boundary. For the grouped classification task only selected models were used which is explained in Sec. 4. In this scenario, a systematic hyperparameter optimization was conducted using a randomized search approach over 25 iterations.

3.3. Evaluation Criterion

For evaluation of the classifiers primarily the macro F1-score was investigated. By computing F1 scores independently for all classes and taking the unweighted average, all classes are treated equally making it especially useful in imbalanced multiclass and multilabel classifications [9].

4. Results

In the initial fine-grained classification, macro F1-scores range from 0.097 to 0.458, achieved by the single-

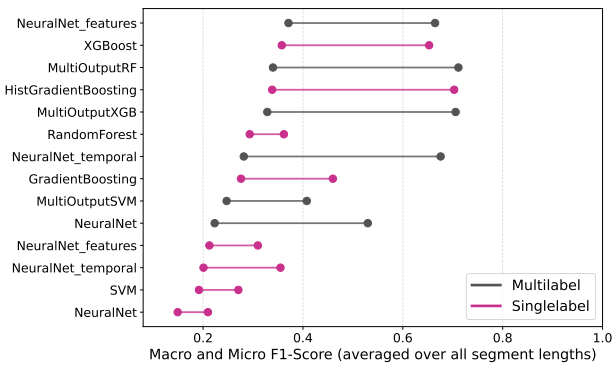

Fig. 3: F1-Scores for the different models averaged over all segment lengths

label XGBoost classifier trained on event-based segments, highlighting the large performance differences across classifiers. Averaging results across all classifiers and segment lengths (Fig. 3) identifies the multilabel feature-based MLP as the overall best performing model, with an averaged macro F1-score of 0.371, closely followed by the single-label XGBoost model. The substantial gap between macro and micro F1-scores in Fig. 3 reflects the dominant influence of the high classification accuracy for the majority class (no_artifact) on the micro F1-score.

Based on these findings, only the best performing models were retained for further analysis including Random Forest and XGBoost (single- and multilabel), HistGradientBoosting, and multilabel feature-based MLP and 1D-CNN.

4.1. Evaluation of Segment Lengths

Comparing the different segment length approaches through averaging F1-scores of the best performing models (see Fig. 4), classification on event-based segments achieves the highest macro F1-score (0.349). This superior performance is consistent with the expectation that analyzing contiguous artifact events allows classifiers to capture the full morphological characteristics and temporal evolution of each artifact. Within fixed segment lengths, 2 s-segments yield the highest macro F1-score (0.352), closely followed by 3 s-segments, indicating that extended temporal context is vital for identifying artifact patterns.

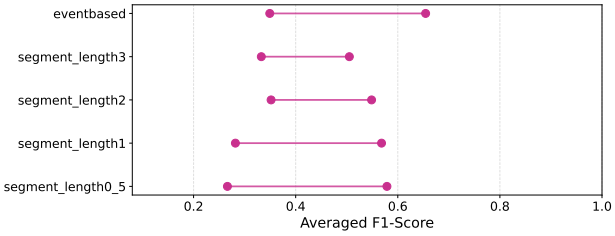

Fig. 4: Averaged micro and macro F1-Scores for the different segment lengths averaged over the best models

4.2. Evaluation of Class-Specific Performance

Evaluating the discriminative power of the XGBoost model for the event-based approach using the normalized confusion matrix in Fig. 5 shows high classification accuracy for artifact-free segments (Recall: 0.853). Specific eye-related artifacts, such as blink and look_right, also achieve high recalls (0.864 and 0.801), indicating that changes in these signals are well captured. Remarkably, jaw_clench artifact reaches perfect recall, reflecting its highly distinctive muscular interference pattern. Some physiologically similar artifacts, such as eye movements, remain difficult to distinguish and rare artifacts, including movements and the aggregated "other" category, are never detected, likely due to

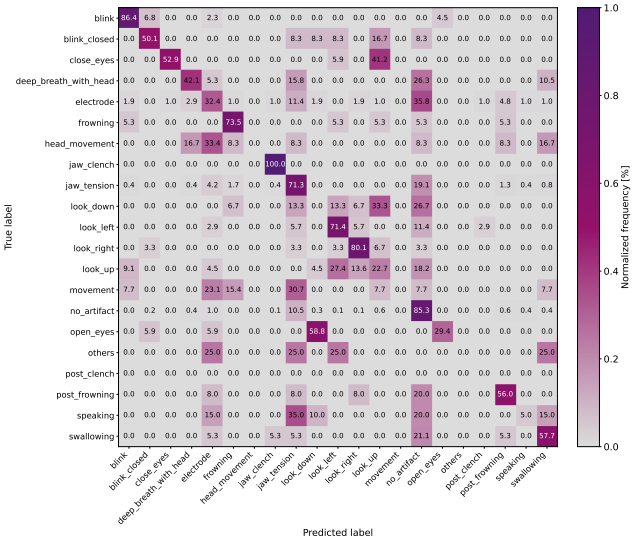

Fig. 5: Confusion Matrix for singlelabel XGBoost-Classifier using event-based segments

limited possibility for the models to learn their characteristics. Lastly, several classes are often misclassified as samples from the majority classes no_artifact, look_up, jaw_tension, or electrode.

Despite the inherent difficulty of the 28-class problem and the extreme class imbalance, the diagonal dominance of the confusion matrix for most artifacts confirms that the XGBoost model has learned decision boundaries.

4.3. Artifact Grouping

When examining the model's performance for binary classification significantly higher macro F1-scores are received. All models trained on features achieve averaged macro F1-scores above 0.80 and clearly outperform the 1D-CNN (0.759) and the MLP trained on raw EEG (0.656). The histogram-based classifier yields the highest averaged macro F1-score of 0.836. This suggests that the handcrafted features are particularly robust for detecting non-physiological signal deviations, offering superior discriminative power compared to automatic feature learning in this context.

Grouping the 27 artifact classes together as described in Sec. 3 also improves performance compared to the fine-grained classification task with averaged macro F1-scores ranging from 0.536 for the histogram based classifier to a maximum of 0.627 for the multilabel Random Forest classifier. However, the normalized confusion matrix in Fig. 6 still reveals confusion clusters between eye and eyelid artifacts, as well as movement and electrode artifacts. This is physiologically plausible, as physical movement is often accompanied by mechanical displacement of the electrodes. The bad classification of movement artifacts might be explained by its rare occurrence in the training dataset.

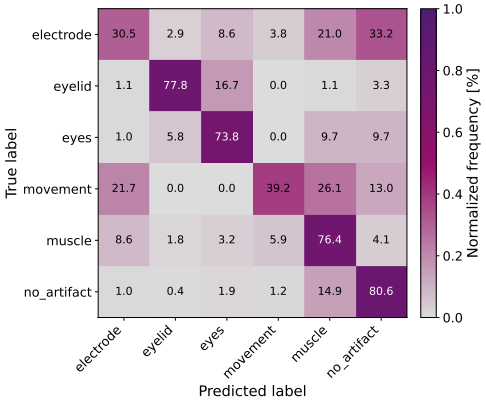

Fig. 6: Confusion Matrix for the XGBoost-Classifier in a grouped classification task

Applying data augmentation and downsampling leads to an overall lower performance compared to grouped classification. Event-based 1D-CNN now achieves the highest macro F1-score (0.497), suggesting that particularly deep learning methods benefit from augmentation. Although, confusion clusters have shifted, they remain, indicating that the selected augmentation methods are not suitable to improve classification.

5. Discussion

The results highlight the complexity of multiclass EEG artifact detection and the effectiveness of ensemble learning with handcrafted features. The progression from a 28-class task to binary classification reveals the impact of task complexity on model reliability. Binary classification significantly increases F1-scores suggesting that the detection of ”contaminated” vs. ”clean” signal is highly robust. The grouped classification task serves as an effective middle ground. This confirms that much of the error in the 28-class task came from ”within-group” confusion which is mitigated when these sub-classes are aggregated.

Limitations of this paper include the dominant no_artifact class and high class imbalance in general, affecting rare-class recall, label noise from non-expert annotation, and the small dataset size limiting deep learning generalization.

6. Conclusion & Outlook

This paper showed that singlelabel XGBoost on event-based segments is the best-performing model for detailed artifact classification (F1 $= 0.458$), while HistGradientBoosting is recommended for fast binary detection (F1 $= 0.836$). Grouped classification mitigated errors from physiologically similar classes, offering a practical compromise for clinical applications.

Future research should focus on improving rare-class detection, e.g., using synthetic artifact generation with Generative Adversarial Networks, hierarchical classification pipelines, where first artifacts are detected in a binary stage and then the type is refined in a grouped stage, and expanding expert-verified datasets to reduce label noise and enable training of more complex deep learning models.

Acknowledgements

Research described in this paper was supervised by Dr.-Ing. Yanhua Zhao and Prof. Dr.-Ing. Christoph Hoog Antink, TU Darmstadt, and Dr. med. Ilia Aroyo, specialist in neurology at Klinikum Darmstadt.

References

[1] SOUFINEYESTANI, M., DOWLING, D., KHAN, A. Electroencephalography (EEG) technology applications and available devices. *Applied Sciences*, 2020, vol. 10, no. 21.

[2] HINRICHS, H. Technik. In: EBNER, A., DEUSCHL, G. (eds.). *EEG*. Stuttgart: Georg Thieme Verlag, 2006, p. 10–17.

[3] ROY, S. Machine learning for removing EEG artifacts: setting the benchmark. arXiv preprint, 2019.

[4] JIANG, X., BIAN, G.-B., TIAN, Z. Removal of artifacts from EEG signals: a review. *Sensors*, 2019, vol. 19, no. 5.

[5] RAJ, V. A., PARUPUDI, T., THALENGALA, A., NAYAK, S. G. A comprehensive review of deep learning models for denoising EEG signals: challenges, advances, and future directions. *Discover Applied Sciences*, 2025, vol. 7, no. 11.

[6] ARPAIA, P., DE LUCA, M., DI MARINO, L., DURAN, D., GARGIULO, L., LANTERI, P., MOCCALDI, N., NALIN, M., PICCIAFUOCO, M., ROBBIO, R., et al. A systematic review of techniques for artifact detection and artifact category identification in electroencephalography from wearable devices. *Sensors*, 2025, vol. 25, no. 18.

[7] BINTE AHMED, S. F., SAKIB, N., ISLAM, M. R., FARUK, T., ISLAM, M. K. Machine learning approaches for motion artifact identification and classification from EEG signal. In *Proceedings of the 7th Asia Conference on Cognitive Engineering and Intelligent Interaction (CEII)*. Los Alamitos (USA), 2024, p. 16–20.

[8] ASANAGI, Electrode locations of International 10–20 system for EEG (electroencephalography) recording. *Wikimedia Commons*, 2010. Available: `https://commons.wikimedia.org/wiki/File:21_electrodes_of_International_10-20_system_for_EEG.svg`

[9] HINOJOSA LEE, M. C., BRAET, J., SPRINGAEL, J. Performance metrics for multilabel emotion classification: comparing micro, macro, and weighted F1-scores. *Applied Sciences*, 2024, vol. 14, no. 21.

About Authors...

Franka Nordmann was born in Recklinghausen, Germany. She received her B.Sc. in Biomedical Engineering in 2023 and is currently pursuing her M.Sc. in Biomedical Engineering at TU Darmstadt. Her academic interests include biomedical signal processing, machine learning, and control systems and robotics for medical devices.

Silicon Nitride Photonic Splitters for Power Management in Short-Wave-Infrared Region

Viktoria Pikulikova, Adam Petrovic

Laboratory of Integrated Photonics and Optical Communications, Faculty of Electrical Engineering and Information Technology, University of Zilina, Univerzitna 8215/1, 010 26 Zilina, Slovak Republic

pikulikova@stud.uniza.sk, petrovic1@feit.uniza.sk

Abstract. *The demand for multi-band photonic integrated circuits (PICs) is driving the development of efficient power splitters beyond the conventional 1550 nm window. In this work, we present compact multimode interference (MMI) splitters on a silicon nitride (Si_3N_4) platform designed for operation at 950 nm and 1310 nm. Numerical optimization using eigenmode expansion (EME) and finite-difference time-domain (FDTD) methods yields ultra-compact footprints of 16.35×4 μm² and 8.94×3.5 μm², respectively. The devices achieve low insertion losses below 0.14 dB and broad bandwidths of 329 nm and 611 nm for respective central wavelengths. These results demonstrate a robust and scalable approach for broadband power distribution, supporting emerging applications in sensing, communications, and quantum photonics.*

Keywords

Integrated photonics, optical power splitter, multimode interference coupler, silicon nitride, strip waveguide.

1. Introduction

Integrated photonics is a cornerstone technology for compact, high-performance optical systems in telecommunications, sensing, and biophotonics [1,2]. A fundamental requirement for PICs is the efficient distribution and routing of light on a chip. In this context, optical power splitters are recognized to be key building blocks, enabling signal broadcasting, parallel processing, and complex feedback loops. Developing reliable, compact splitting structures is therefore critical prerequisite for scaling PICs to complex systems [1-4].

While the 1550 nm band remains dominant for long-haul transmission systems, increasing interest is shifting toward shorter wavelengths. The 1310 nm band supports high-speed, short-reach links in data centers [3,5-8], while the 950 nm region is gaining traction for quantum, LiDAR, and sensing applications. Extending power splitting functions to these bands pave a way for multi-band integrated photonic platforms [9-11]. Among various available splitting approaches, multimode interference (MMI) couplers are excellent choice over directional couplers (DC) or Y-branches. MMIs provide a range of advantages, including improved fabrication tolerance, broad bandwidth, and high uniformity of output signals [1-3,12-14]. These basic characteristics are further amplified by the silicon nitride (Si_3N_4) waveguide platform as it offers ultra-low propagation losses (0.1-0.3 dB/cm), a wide spectral transparency (400-2400 nm), and a low thermo-optic coefficient (2.45×10^{-5} °C^{-1}). Moderate refractive index contrast of 1 and 0.5 for air- and oxide-cladded structures provides an ideal trade-off between device footprint and robust power handling across multiple wavelengths [3,9,15,16].

In this work, we present the design and numerical analysis of high-performance Si_3N_4 power splitters optimized for the fundamental transverse electric (TE) mode. The devices are engineered for efficient power distribution at 950 nm and 1310 nm, supporting next-generation multi-band integrated photonic architectures.

2. Multimode Interference Splitters

The operation of MMI power splitter is based on the self-imaging principle, where an input field is periodically replicated as it propagates along the wide multimode structure. When an optical signal enters the multimode section, it excites a specific set of guided modes. Because these modes travel at different phase velocities, they interfere with each other, creating a predictable pattern of single or multiple replicas of the original field at specific distances along the device [1-3].

The spatial evolution of interference patterns is governed by the beat length of the two lowest-order modes, defined as

$$L_\pi = \frac{\lambda}{2(n_{eff,0}-n_{eff,1})} \quad (1)$$

where λ is the free-space wavelength, n_{eff} is the effective index of the fundamental mode and first higher order mode.

For proposed 1×2 power splitters, we utilize a symmetric interference mechanism. The input waveguide is positioned at the center of the multimode region. In this configuration, only even-order modes are excited. This

significantly shortens the required device length. To achieve a perfectly balanced power distribution at the output, the length of the MMI section is optimized based on the specific condition:

$$L_{MMI}=\frac{3L_{\pi}}{8}. \quad (2)$$

This condition ensures the formation of two symmetric images of the input field, allowing for a compact footprint while maintaining an equal power splitting between the two output ports [1].

3. Simulation results

The proposed power splitters are implemented on a Si_3N_4 platform using a single-etch step fabrication process. The devices are designed for Si_3N_4 core thickness (h_{SiN}) of 400 nm, sitting on top of 4.5 µm thick buried oxide (BOX) layer. The structures are over-cladded by 2 µm thick oxide [9]. Detailed material parameters utilized in the numerical study are summarized in Tab. 1 [17-20].

Material	RI @ 950 nm	RI @ 1310 nm
Core (n_{Si3N4})	2.0159	2.0031
Cladding (n_{SiO2})	1.4511	1.4468
Effective mode index of the input waveguide (n_{eff})	1.6647	1.6317

Tab. 1. Refractive indices (RI) for the core and cladding layers.

The computational analysis was carried out using the Ansys Lumerical suite, employing a dual-method approach. The eigenmode expansion (EME) method was used for initial design and iterative optimization of the MMI geometry, while finite-difference time-domain (FDTD) simulations provided rigorous full-wave validation.

3.1 Optical power splitter for 950 nm

The proposed power splitter employs a multi-section design consisting of single-mode input and output waveguides coupled through a multimode interference (MMI) region, as illustrated in Fig. 1(a-b). Fundamental mode operation is ensured by setting the access waveguide width to $w_g = 0.4$ µm. Efficient coupling into the MMI section is achieved using 25 µm long adiabatic tapers ($w_a = 1.61$ µm, $S = 0.38$ µm), which promote smooth modal transition while minimizing reflection and scattering losses.

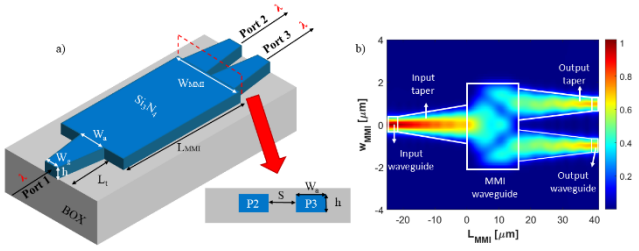

Fig. 1. a) The schematic representation of the 1×2 power splitter, b) propagation of electromagnetic field.

The core of the device is the MMI section with a width of $W_{MMI} = 4$ µm. This dimension was chosen to support a sufficient number of guided modes (at least N+1) required for self-imaging in a 1×N splitter [1]. Based on initial analytical estimates from Eq. (2), the MMI length was further refined through EME-based optimization to $L_{MMI} = 16.35$ µm. This optimized geometry ensures constructive interference at the output plane, enabling balanced power splitting within a compact footprint. Device performance characteristics are shown in Fig. 2. In particular, Figs. 2(a-c) show insertion loss, back-reflections, and power imbalance as a function of the wavelength.

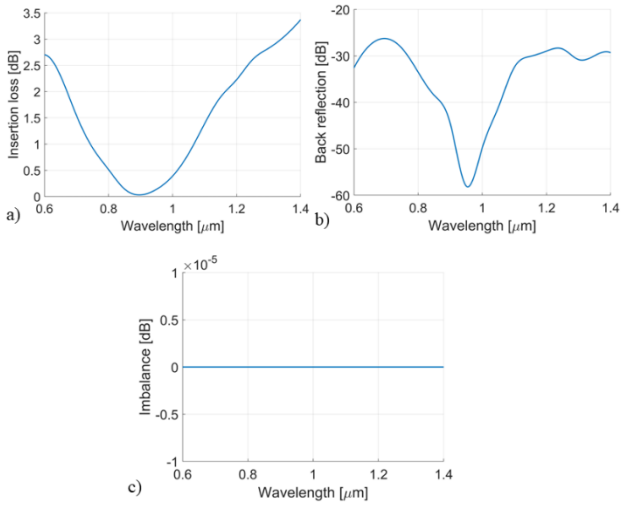

Fig. 2. a) Insertion losses, b) back reflection, and c) power imbalance as a function of wavelength.

The proposed splitter demonstrates high efficiency, with an insertion loss of 0.14 dB at the target wavelength and a minimum value of 0.03 dB at 896 nm. Owing to the high structural symmetry, the power imbalance between the output ports is negligible. Back reflections are strongly suppressed to -58.2 dB, minimizing parasitic feedback. The device maintains high performance over a broad spectral range, with a 1 dB bandwidth of 329 nm (740 nm – 1069 nm). These results confirm that the 16.35 × 4 µm^2 structure combines compactness with robust broadband operation, making it suitable for multi-band integrated photonic applications.

3.2 Optical power splitter for 1310 nm

The 1310 nm power splitter follows the same three-stage architecture, comprising single-mode access waveguides, an adiabatic transition region, and the MMI section. To accommodate the longer wavelength while maintaining single-mode operation, the access waveguide width is increased to $w_g = 0.65$ µm. Efficient coupling into the MMI region is achieved using 25 µm long adiabatic tapers with a width of $w_a = 1.55$ µm and separation $S = 0.32$ µm. These tapers are optimized to ensure the required phase distribution for self-imaging while minimizing scattering losses and back reflections. The MMI section is designed with a width of $W_{MMI} = 3.5$ µm to support the required modal interference. Based on initial analytical modeling and subsequent EME

optimization, the MMI length is reduced to a compact $L_{MMI} = 8.94$ µm. This geometry enables accurate self-imaging, resulting in a balanced 1×2 power split at the output. The corresponding electromagnetic field evolution is shown in Fig. 3(a) and Figs. 3(b-d) show insertion loss, back-reflections, and power imbalance as a function of the wavelength.

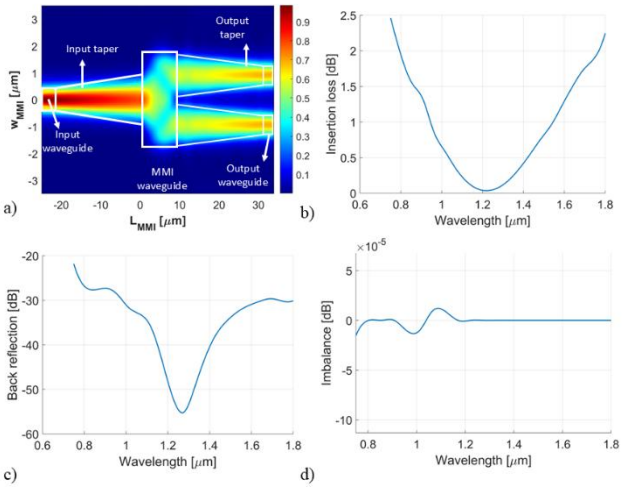

Fig. 3. a) Propagation of electromagnetic field, b) insertion losses, c) back reflection, and d) power imbalance as a function of wavelength.

The proposed 1310 nm splitter demonstrates excellent performance, combining a compact footprint (8.94 × 3.5 µm^2) with low insertion loss (0.14 dB, minimum 0.04 dB at 1219 nm) and near-ideal power balance (~10^{-5} dB). Back reflections are strongly suppressed (-55.25 dB), while a broad 1 dB bandwidth of 611 nm (941–1552 nm) highlights its robustness. These results establish the device as a promising building block for broadband, multi-band integrated photonic systems.

4. Conclusion

This work presents the design and numerical validation of high-performance Si_3N_4 power splitters optimized for operation at 950 nm and 1310 nm. Based on the multimode interference (MMI) principle, the devices achieve a favorable balance between compact footprint and robust optical performance. The splitters exhibit low insertion losses (<0.14 dB) and negligible power imbalance, enabling accurate signal distribution. In addition, they provide broad 1 dB bandwidths of 329 nm and 611 nm, respectively, supporting multi-band operation. These results highlight the potential of Si_3N_4 MMI structures as key building blocks for next-generation integrated photonic systems in communications, sensing, and quantum applications.

Acknowledgements

Research activities presented in the paper are supervised by Assoc. Prof. Daniel Benedikovic, FEIT UNIZA in Zilina. This work is funded by the EU NextGenerationEU through the Recovery and Resilience Plan for Slovakia under the projects No. 09I03-03-V04-00410 and No. 09I05-03-V02-00062.

References

[1] SOLDANO L. B., PENNINGS E. C. M., Optical multi-mode interference devices based on self-imaging: principles and applications, *Journal of Lightwave Technology*, vol. 13, no. 4, pp. 615–627, Apr. 1995, doi: 10.1109/50.372474.

[2] CHUNG L.-W., LEE S.-L., LIN Y.-J., Principles and application of reduced beat length in MMI couplers, *Optics Express*, vol. 14, no. 19, p. 8753, Jan. 2006, doi: 10.1364/oe.14.008753.

[3] FRISHMAN A., MALKA D., An optical 1×4 power splitter based on silicon–nitride MMI using strip waveguide structures, *Nanomaterials*, vol. 13, no. 14, p. 2077, Jul. 2023, doi: 10.3390/nano13142077.

[4] HALIR R. et al., Colorless directional coupler with dispersion engineered sub-wavelength structure, *Optics Express*, vol. 20, no. 12, p. 13470, May 2012, doi: 10.1364/oe.20.013470.

[5] SHI Y., SHAO B., ZHANG Z., ZHOU T., LUO F., XU Y., Ultra-broadband and low-loss silicon-based power splitter based on subwavelength grating-assisted multimode interference structure, *Photonics*, vol. 9, no. 7, p. 435, Jun. 2022, doi: 10.3390/photonics9070435.

[6] AI X., ZHANG Y., HSU W.-L., VEILLEUX S., DAGENAIS M., Broadband 2 × 2 multimode-interference coupler on the silicon-nitride platform, *Optics Express*, vol. 32, no. 6, p. 9405, Feb. 2024, doi: 10.1364/oe.513796.

[7] MALKA D., SINTOV Y., ZALEVSKY Z., Design of a 1 × 4 silicon-alumina wavelength demultiplexer based on multimode interference in slot waveguide structures, *Journal of Optics*, vol. 17, no. 12, p. 125702, Oct. 2015, doi: 10.1088/2040-8978/17/12/125702.

[8] BEHFAR A., GREEN M., MORROW A., STAGARESCU C., Monolithically integrated diplexer chip for PON applications, *OFC/NFOEC Technical Digest. Optical Fiber Communication Conference*, 2005, p. 3 pp. Vol. 2, doi: 10.1109/ofc.2005.192663.

[9] BUZAVEROV K. A. et al., Silicon nitride integrated photonics from visible to mid-infrared spectra, *Laser & Photonics Review*, vol. 18, no. 12, Jul. 2024, doi: 10.1002/lpor.202400508.

[10] JUNG S., KIRCH J., KIM J. H., MAWST L. J., BOTEZ D., BELKIN M. A., Quantum cascade lasers transfer-printed on silicon-on-sapphire, *Applied Physics Letters*, vol. 111, no. 21, Nov. 2017, doi: 10.1063/1.5002157.

[11] LUO W. et al., Recent progress in quantum photonic chips for quantum communication and internet, *Light Sci Appl*, vol. 12, no. 175, 2023, doi: 10.1038/s41377-023-01173-8.

[12] BLASCO-SOLVAS M. et al., Silicon nitride building blocks in the visible range of the spectrum, *Journal of Lightwave Technology*, vol. 42, no. 17, pp. 6019–6027, May 2024, doi: 10.1109/jlt.2024.3404639.

[13] BUCIO T. D., KHOKHAR A. Z., MASHANOVICH G. Z., GARDES F. Y., Athermal silicon nitride angled MMI wavelength division (de)multiplexers for the near-infrared, *Optics Express*, vol. 25, no. 22, p. 27310, Oct. 2017, doi: 10.1364/oe.25.027310.

[14] ZENG G. et al., Temperature-insensitive and fabrication-tolerant coarse wavelength division (de)multiplexing on a silica platform using an angled multimode interferometer, *Optics Express*, vol. 31, no. 13, p. 21161, Jun. 2023, doi: 10.1364/oe.492007.

[15] LI Y. P., HENRY C. H., Silica-based optical integrated circuits, *IEE Proceedings - Optoelectronics*, vol. 143, no. 5, pp. 263–280, Oct. 1996, doi: 10.1049/ip-opt:19960840.

[16] STUTIUS W., STREIFER W., Silicon nitride films on silicon for optical waveguides, *Applied Optics*, vol. 16, no. 12, p. 3218, Dec. 1977, doi: 10.1364/ao.16.003218.

[17] PHILIPP H. R., Optical properties of silicon nitride, *Journal of the Electrochemical Society*, vol. 120, no. 2, p. 295, Jan. 1973, doi: 10.1149/1.2403440.

[18] BÅÅK T., Silicon oxynitride; a material for GRIN optics, *Applied Optics*, vol. 21, no. 6, p. 1069, Mar. 1982, doi: 10.1364/ao.21.001069.

[19] TAN C. Z., Determination of refractive index of silica glass for infrared wavelengths by IR spectroscopy, *Journal of Non-Crystalline Solids*, vol. 223, no. 1–2, pp. 158–163, Jan. 1998, doi: 10.1016/s0022-3093(97)00438-9.

[20] MALITSON I. H., Interspecimen comparison of the refractive index of fused silica, *Journal of the Optical Society of America*, vol. 55, no. 10, p. 1205, Oct. 1965, doi: 10.1364/josa.55.001205.

About Authors...

Viktoria PIKULIKOVA is an Assistant Researcher at the Department of Multimedia and Information-Communication Technologies at the University of Zilina, Zilina, Slovakia. She earned her BSc degree in Communication and Information Technologies in 2024 and is currently pursuing an MSc degree in Telecommunication and Radiocommunication Engineering at the same institution. Her research focuses on the design and analysis of passive photonic integrated devices, with particular emphasis on waveguide couplers and light beam splitters implemented on a silicon nitride platform.

Adam PETROVIC is an Assistant Researcher positioned at the Department of Multimedia and Information-Communication Technology at the University of Zilina, Zilina, Slovakia. He holds a BSc. degree in Communication and Information Technologies. Currently, he is pursuing an MSc. degree in Telecommunications and Radiocommunication Engineering at the home university. His research focuses on the development of low-loss photonic chip interfaces and metaheuristic machine learning optimization techniques.

A Proposal for a Communication Protocol for Distributed Measurement Systems with High Jitter

Ing. František RUSNÁK[1]

[1]Department of control and instrumentation, Brno University of Technology, Technická 12, Brno, Czech Republic

xrusna06@vutbr.cz

Abstract. *This article presents a proposal for an innovative communication protocol for distributed measurement systems with high jitter, which compensates for the negative effects of real-time synchronization. The protocol is based on PTP messaging and combines it with three methods for obtaining timestamps outside the standard communication channel: synchronization using a periodic signal, detection of random non-periodic signals, and acquisition of redundant validation marks. The protocol design meets the requirements for widely available devices used for measurement purposes in galvanically isolated systems.*

Keywords

PTP, Communicating devices, Jitter compensation, embedded, Synchronization protocol, Measurement

1. Introduction

A communication protocol is a set of rules that define the format and method by which data is transmitted between devices. The ISO/OSI reference model used today divides communication into 7 horizontal layers. The abbreviation ISO stands for the standardization organization that issued the standard, i.e., the International Organization for Standardization, and OSI is an acronym for Open Systems Interconnection. The physical layer ensures data transmission at the hardware level using bits. Signals are defined by voltage levels and their duration. The data link layer ensures the grouping of data into frames, which are marked by a header indicating the start of each frame's transmission. This layer identifies the start and end of each frame and also verifies the frame's integrity using a CRC checksum, which is included in every frame. The network layer divides the data into packets, which are addressed using the device's MAC address. The packet header contains both the sender's and recipient's addresses, which aids in its routing. The transport layer ensures that the entire data stream being sent is divided into smaller parts due to the limited size of the packets into which the data is encapsulated. Packets carry information about the addressing of the data they carry. This allows the transport layer to determine the order of received packets and correctly sequence the received data. Unlike the lower layers, the transport layer ensures data reception and proper assembly through acknowledgment. The session layer establishes and terminates communication between two nodes. It may also provide data encryption. The presentation layer ensures the correct interpretation of data. The application layer is the highest layer in the ISO/OSI model and handles communication with the user.

2. Classification of communication into layers according to the ISO/OSI model

The physical layer handles data transmission at the hardware level using bits. Signals are defined by voltage levels and time intervals.

The data link layer groups data into frames, which are identified by a header at the beginning. The layer must detect the start and end of a frame. Frame integrity is verified using a CRC checksum. The network layer divides data into packets that specify the specific MAC address to which the data is sent. The header also contains the sender's MAC address. A packet with this routing information can be routed between several devices forming a simple network.

The transport layer divides the entire stream of data being sent into individual packets, which are transmitted via the lower layers. The transport layer divides the entire stream of data being sent into individual packets, which are transmitted via the lower layers. The transport layer also ensures that all data is sent in the correct order. To enable packets to be sent and reassembled, each packet is marked with a number representing the indexed position of the data in the stream. By querying back using the index, the transport layer verifies whether the packet has arrived. If an error occurs and a packet is lost or must be discarded, the transport layer resends the data and, upon receipt, inserts it into the correct position in the data stream.

The session layer establishes and terminates communication between two nodes. It also handles data encryption if

required by the application. The presentation layer ensures the correct interpretation of data.

The application layer is the topmost layer in the ISO/OSI model. This is the layer through which users communicate.

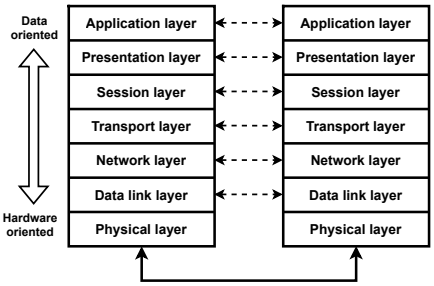

Fig. 1. ISO/OSI model

3. Network topology with measurement nodes

This work focuses primarily on hard-to-access distributed systems that require remote control. One factor that makes it impossible to work in their vicinity is the high voltage, which can reach several or even tens of kilo-volts. The main objective is to prevent direct contact between the system and the rest of the computer equipment. A high-voltage arc could not only destroy the electronics but also pose a safety risk. The primary requirement is therefore to ensure galvanic isolation of the measured system from the rest of the measurement setup.

Distributed measurement systems present a challenge in terms of serviceability. Not only does the application place high demands in terms of galvanic isolation, but it also requires the placement of two or more measurement nodes at distances ranging from a few meters to several tens of meters.

This thesis addresses the challenges of this application by proposing a distributed measurement system designed for hardware devices widely available on the market. The software solution is designed for easy scalability, which will facilitate the implementation of future functionality extensions. The Python programming language was chosen for its user-friendliness. Although Python is an effective tool for testing new projects, it presents a significant disadvantage in terms of command execution latency and time jitter.

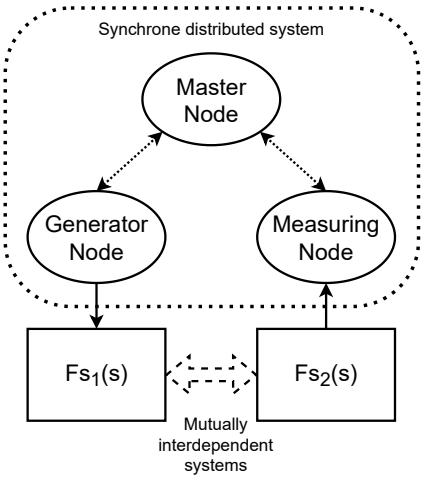

Fig. 2. Proposed topology of measurement nodes

4. A Proposal for Time Synchronization Beyond the Communication Channel

Variable delay times and time asymmetry in communication are the main factors contributing to the inaccuracy of time synchronization between two devices.

4.1. Synchronization Using Common Data Patterns

Variable delay times and time asymmetry in communication are the main factors contributing to inaccuracies in time synchronization between two devices. For applications where time accuracy is not a critical parameter, the proposed synchronization protocol, which operates at the millisecond level, can serve as an effective alternative to implementing the NTP protocol.

The communication channel between two nodes allows clock synchronization only up to a certain accuracy limit, beyond which it is not possible to achieve synchronization using only standard PTP message exchange and filtering algorithms. To increase the accuracy of time synchronization, a method was proposed for obtaining timestamps outside the standard communication network through which devices are synchronized, or at least for providing data to reconstruct the measured data. A prerequisite is a common system that can be measured by the synchronized nodes. This article defines three sources that can be used to obtain a timestamp.

- Synchronization using a periodic signal that propagates throughout the entire measured system. The measured signal is characteristic of the measured system.

- Detection of random, non-periodic anomalies that can be distinguished from the system's typical behavior, and recording of sequences of these anomalies.
- Acquisition of redundant validation markers of measured secondary quantities, which provide supplementary information for the reconstruction of the measured signal over time and coefficients determining the quality of individual measurement samples.

Synchronization using a periodic signal can, for example, utilize the electrical power grid. The measured waveform is an amplitude with a frequency of 50 Hz. Even though the voltage amplitude is heavily contaminated by noise and higher frequencies, mathematical methods can be used to filter out the original amplitude and determine its zero-crossing. The zero-crossing time can be compensated for by a certain offset and used as a timestamp to refine standard synchronization. The work [1] uses a phase-locked loop to detect zero-crossing. The work [2] uses low-pass filters to remove interfering frequencies. Another method involves detecting the zero-crossing using frequency analysis or convolution.

Detecting random, non-periodic features requires a detector capable of identifying expected anomalies in the signal. These anomalies must differ from the signal's normal characteristics. For a power grid, examples include random voltage spikes or specific features in the signal that can be detected using convolutional neural networks. Unlike synchronization using a periodic signal, it is impossible to predict when the next event will occur. The time interval between individual events is not guaranteed. This places higher demands on synchronization negotiation between devices, or necessitates the centralized processing of measured data and the retrospective determination of synchronization events.

The acquisition of redundant validation signals involves measuring a signal whose secondary measured parameters vary over time. It is advisable to select a quantity other than the primary measured quantity as the validation signal, one that provides information for identifying a specific measurement point. The value of the validation measurement should not depend on the characteristics of the measured system. For example, for a second-order system, the frequency of the output sinusoidal signal is easily measurable; its value is equal to the input frequency and does not correlate with the output amplitude. The measurement control loop should ensure measurement validation. For a series of rapidly successive measurements, secondary validation values are assigned to the desired measured values, ensuring their identification for reconstruction. This allows measurements to be taken at intervals shorter than the synchronization time accuracy.

When measuring the transfer function of the dynamic system shown in Figure 2, the desired measured quantity is the output amplitude measured at the system's output as a function of the input amplitude frequency (the ratio of input-to-output amplitudes). The validation parameter is the frequency of the output amplitude, which is easily measurable on a simple sinusoidal signal. The value of the measured output frequency is assigned to the value of the measured output amplitude.

4.2. Definition of Quality Indicators

Quality indicators are used for the retrospective validation of measured samples. Quality indicators relate to a specific sequence of consecutive measured values. The indicators are obtained through a calculation, the result of which is used for the retrospective validation of the measurements. When measuring the system response at a specific frequency, it is desirable to measure the steady-state amplitude value. To do this, it is necessary to perform n measurements, which are represented by the values y_i. The desired value v is the mean value of the measured set and is obtained using the formula 1

$$v = \frac{1}{n}\sum_{i=1}^{n} y_i \tag{1}$$

Determining the slope of the measured signal can be used to determine whether the measurement was taken during a steady-state condition. A straight line described by the formula in 2 is defined.

$$f_L(i) = v + a\left(i - \frac{n-1}{2}\right) \tag{2}$$

Where v is the mean value and the coefficient a determines the slope of the line. Using the least squares method, the minimum area s described by equation 3 is sought between the line 2 and the curve y_i.

$$s = \sum_{i=1}^{n} \left(f_L(i) - y_i\right)^2 \tag{3}$$

The coefficient a is obtained using formula 4.

$$a = \frac{\sum_{i=1}^{n} f(i) y_i}{\sum_{i=1}^{n} f(i) i} \tag{4}$$

Where the function $f(i)$ is expressed as 5.

$$f(i) = i - \frac{n-1}{2} \tag{5}$$

The measurement uncertainty, which reflects not only the slope of the measured waveform but also the noise in the waveform, can also be used as the quality factor u_a 6.

$$u_A = \sqrt{\frac{1}{n\,(n-1)} \sum_{i=1}^{n} (y_i - v)^2} \tag{6}$$

4.3. Communication Protocol Proposal

The following protocol has been designed for the transmission of control commands; it is capable of transmitting three types of messages. The individual types are identified by the header format, which takes the form “DC:” (Direct Control) for basic control commands that are executed as soon as possible after receipt. Messages beginning with “TM:” (Time Message) carry data from the synchronization protocol, which is based on the IEEE 1588 PTP time synchronization standard. Messages with the “TC” (Time Control) header are used to create an event that triggers a given command at a specified time. A local clock synchronized by PTP master messages is used to determine the execution time of a scheduled command.

To maintain the protocol’s readability and usability for the user, the ASCII format was chosen, which is limited to uppercase and lowercase letters, digits, and separators such as colons, periods, and semicolons to separate individual parameters. Encoding numbers in decimal format with a floating decimal point allows for flexibility in transmitting data types. The ASCII format also allows for the transmission of text messages.

To ensure compatibility among different hardware solutions, hardware support is not considered for PTP time synchronization. The lower layers of the ISO/OSI model are kept completely transparent. This work primarily aims to achieve the broadest possible compatibility of the communication protocol with any hardware, even at the cost of reduced time synchronization accuracy. The advantage is the independence of the higher layer from various combinations of hardware resources for data transmission. The role of the physical layer can be fulfilled by Bluetooth, Wi-Fi, or other radio modules that enable the establishment of a transparent connection. The physical transmission device, together with the MCU hardware connection, should provide a transparent channel that behaves like a simple serial line. Once the issues with hardware implementation are resolved, only the transparent channel remains; however, this does not guarantee constant latency or message delivery. The communication protocol is designed to ensure message delivery and their execution in the correct sequence. Each received ”DC” message generates an acknowledgment message upon execution. To maintain message sequence, individual packets are numbered. Only commands that follow an ascending sequence are executed.

The ”DC” confirmation feedback messages are designed to close the feedback loop regarding the actual status of the hardware settings. Thanks to the message structure, it is possible to send a number in a variable format that specifies the value of the hardware setting. However, the hardware is limited by its technical capabilities, and therefore quantization rounding of the requested value is expected. The slave device thus sends a confirmation message containing the actual value that was set within the hardware’s capabilities. This method of acknowledgment was used to achieve broad message compatibility among any hardware that supports these messages but has different hardware capabilities. The master sending the commands therefore always receives a message about the actual hardware configuration that could be achieved under the given circumstances.

5. Data Management Plan

This work is based on hardware that is readily available on the market. The communication protocol design requires only a software implementation to provide support. The software used is available on the public GitHub server in the 97frantarusnak/DiSyNo repository. A proof of concept for communication between devices using DC messages has been conducted. The project is still under development and will be adapted to meet the current needs of future measurements. To verify the functionality of the entire setup, measurements will be performed on a dynamic system. The measurement data will also be published in the repository in CSV format, along with the proposed network topology and the configuration of the measured system.

6. Conclusion

This article describes the design of the key components of a communication protocol intended for communicating devices. The protocol is designed to compensate for high jitter and device delays by pre-scheduling measurement commands and enables the reconstruction of acquired data through the use of additional event indicators and quality-of-service metrics. The protocol aims to limit real-time interactions between multiple devices and presents principles for achieving measurement sampling with a shorter time period than the time accuracy of time synchronization. Three methods for obtaining timestamps outside the standard communication network were described: synchronization using a periodic signal, detection of random non-periodic signals, and acquisition of redundant validation marks. The software and future developments will be published in a public repository.

Acknowledgement

The completion of this paper was made possible by the grant No. FEKT-S-26-8988 - ”Advanced Methods in Cybernetics, Robotics, and Artificial Intelligence” financially

supported by the Internal science fund of Brno University of Technology.

References

[1] L. Stastny, R. Mego, L. Franek, and Z. Bradac, "Zero cross detection using phase locked loop," *IFAC-PapersOnLine*, vol. 49, no. 25, pp. 294–298, 2016. [Online]. Available: https://www.sciencedirect.com/science/article/pii/S2405896316326866

[2] N. M. Rodrigues, F. M. Janeiro, and P. M. Ramos, "Low pass digital filter delay compensation for accurate zero cross detection in power quality," pp. 407–410, 2017. [Online]. Available: https://www.scopus.com/inward/record.uri?eid=2-s2.0-85046481448&partnerID=40&md5=41a87c960bdd0223b327ec36561d3141

About Authors...

Ing. František RUSNÁK was born in 1997. He received the B.S. and M.S. degrees in automation and measurement from Brno University of Technology, Brno, Czech Republic in 2021 and 2023, respectively. He is currently pursuing a Ph.D. degree in cybernetics, control and measurement at the same institution. His research focuses on the analysis and modeling of connectivity and time synchronization in communicating nodes. He is currently involved in a research project dedicated to the development of an measurement system using PTP for synchronization.

Towards Multi-Snapshot FDR-Controlled Localization for Emergency Response Radar

Christoph LÖSER[1,2]

[1]KIS*MED - AI Systems in Medicine, Technical University of Darmstadt, Merckstraße 25, 64283 Darmstadt, Germany
[2]Robust Data Science Group, Technical University of Darmstadt, Merckstraße 25, 64283 Darmstadt, Germany

christoph.loeser@tu-darmstadt.de

Abstract. *False alarms are a critical issue in radar-based person localization for emergency response, where incorrect detections may mislead rescue teams and waste limited operational resources. Recent work has shown that the complex-valued T-Rex selector (CT-Rex) enables false discovery rate (FDR)-controlled localization in the single-snapshot setting. In this work, we propose a multi-snapshot extension of FDR-controlled compressed beamforming based on snapshot-wise CT-Rex selection and temporal support fusion. The CT-Rex selector is applied independently to each snapshot, and the resulting support estimates are aggregated across time via empirical selection frequencies and a persistence threshold. Monte Carlo simulations are conducted to investigate how the fusion threshold and the number of snapshots affect the trade-off between true positive rate and false discovery rate across different signal-to-noise ratio regimes.*

Keywords

false discovery rate control, CT-Rex selector, multi-snapshot localization, support fusion, stability selection, emergency response radar

1. Introduction

Autonomous robotic sensing systems are increasingly developed to support first responders in hazardous environments such as collapsed buildings, fire incidents, or contaminated areas [7]. In such situations, optical sensors including cameras or LiDAR often become unreliable due to smoke, dust, darkness, or severe occlusions [4]. Radar sensing provides a complementary modality that remains operational under these conditions and enables through-obstacle detection and localization [8]. In particular, stepped-frequency continuous-wave (SFCW) radar mounted on semi-autonomous robots has recently been proposed as a promising platform for person localization in emergency response scenarios [5, 8]. In this setting, compressed beamforming and sparse reconstruction have emerged as attractive tools for radar-based localization. In compressed beamforming, the search area is discretized into a spatial grid and localization is cast as the recovery of a sparse coefficient vector whose support corresponds to occupied grid cells [2]. However, classical sparse estimators typically do not provide statistical guarantees on the number of false detections. In safety-critical applications such as emergency response, controlling false alarms is therefore essential. A principled way to address this issue is to control the false discovery rate (FDR) [1]. Recently, the Terminating-Random Experiments (T-Rex) selector has been proposed as an efficient framework for high-dimensional variable selection with finite-sample FDR guarantees [9]. Its complex-valued extension (CT-Rex) enables the application of this framework to array processing and radar localization problems [10]. While first studies focused on the single-snapshot setting, practical SFCW radar systems naturally provide multiple slow-time snapshots. Simple averaging across snapshots implicitly assumes identical sparse supports across time. In realistic rescue scenarios, however, target reflections may fluctuate due to fading, clutter, or motion, which can lead to snapshot-dependent detections.

Motivated by this observation, we propose a multi-snapshot localization framework that applies CT-Rex independently to each snapshot and fuses the resulting support estimates across time. The resulting procedure is closely related to stability selection [3], but exploits naturally occurring radar snapshots instead of artificial resamples. Our contributions are: i) a multi-snapshot extension of FDR-controlled compressed beamforming based on snapshot-wise CT-Rex selection, ii) a temporal support-fusion strategy for identifying persistent target locations, and iii) a simulation study showing how the fusion threshold and the number of snapshots affect the trade-off between detection power and fused FDR.

2. Compressed Beamforming Model

We consider a radar-based localization scenario in which a robotic platform is equipped with a stepped-frequency continuous-wave (SFCW) radar system as in [5, 8] and follow a sparse signal reconstruction approach inspired by the compressed beamforming methodology in [2, 5].

To this end, the environment is discretized into a spatial grid consisting of G grid cells, where each corresponds to a potential target position and is indexed by $g \in \{1, \dots, G\}$. Let $\boldsymbol{g}_g$ denote the spatial coordinates of the g-th grid cell. For each transmit antenna located at position $\boldsymbol{m}_t$ and each receive antenna located at position $\boldsymbol{m}_r$, the round-trip propagation delay associated with a reflection from grid cell $\boldsymbol{g}_g$ is given by

$$\delta_{g,m} = \frac{1}{c_0} \left(\|\boldsymbol{m}_t - \boldsymbol{g}_g\|_2 + \|\boldsymbol{m}_r - \boldsymbol{g}_g\|_2 \right), \tag{1}$$

where c_0 denotes the speed of light. For stepped-frequency radar with frequency steps f_k, $k \in \{1, \dots, K\}$, the corresponding phase shift is

$$e^{-j2\pi f_k \delta_{g,m}}. \tag{2}$$

Stacking the phase shifts across all K frequency steps and M transceiver pairs corresponding to a grid cell yields the steering vector for that grid cell. The steering matrix is then given by

$$\boldsymbol{X} \in \mathbb{C}^{KM \times G}, \tag{3}$$

where the columns comprise the steering vectors, representing the radar responses associated with the individual grid cells.

The radar system collects sequences of measurements, i.e. snapshots, across slow time. We collect these N radar snapshots in the matrix

$$\boldsymbol{Y} = [\boldsymbol{y}_1 \ \dots \ \boldsymbol{y}_N] \in \mathbb{C}^{KM \times N}, \tag{4}$$

where each column $\boldsymbol{y}_n$ represents one radar snapshot. For each snapshot n, the received signal is modeled as

$$\boldsymbol{y}_n = \boldsymbol{X}\boldsymbol{\beta}_n + \boldsymbol{\nu}_n, \tag{5}$$

where $\boldsymbol{\beta}_n \in \mathbb{C}^G$ is a sparse coefficient vector whose nonzero entries correspond to occupied grid cells and $\boldsymbol{\nu}_n \in \mathbb{C}^{KM}$ denotes additive noise. The active set for snapshot n is defined as

$$\mathcal{A}_n = \{g \in \{1, \dots, G\} : (\boldsymbol{\beta}_n)_g \neq 0\}. \tag{6}$$

Collecting the coefficient vectors, the multi-snapshot problem is formulated as

$$\boldsymbol{Y} = \boldsymbol{X}\boldsymbol{B} + \boldsymbol{N}, \tag{7}$$

with $\boldsymbol{B} = [\boldsymbol{\beta}_1 \ \dots \ \boldsymbol{\beta}_N]$, $\boldsymbol{N} = [\boldsymbol{\nu}_1 \ \dots \ \boldsymbol{\nu}_N]$.

3. Proposed Localization Methodology

3.1. Snapshot-wise CT-Rex support estimation

To estimate active grid cells from the multi-snapshot model in (5), we deliberately avoid averaging the measurements across snapshots. Instead, each snapshot $\boldsymbol{y}_n$ is treated as an individual high-dimensional complex-valued regression problem, and the CT-Rex selector is applied independently to each of them [9, 10]. This yields snapshot-wise support estimates

$$\widehat{\mathcal{A}}_n \subseteq \{1, \dots, G\}, \qquad n = 1, \dots, N. \tag{8}$$

CT-Rex augments the design matrix $\boldsymbol{X}$ by random complex-valued dummy variables and performs repeated early-terminated forward-selection experiments to obtain an FDR-controlled active-set estimate [9, 10]. Applied snapshot-wise, this yields one inferential output per snapshot and preserves temporal variability instead of collapsing it through averaging.

3.2. Temporal support fusion

The support sets $\mathcal{A}_n$ may vary across snapshots even for a stationary scene due to fluctuations in reflected amplitudes, clutter, or noise. Nevertheless, targets that remain present in the scene are expected to be associated with grid cells that are selected repeatedly across multiple snapshots. This motivates a *common-support* perspective, in which persistent target locations correspond to indices that appear frequently in the snapshot-wise support estimates.

Following this intuition, the snapshot-wise support estimates $\widehat{\mathcal{A}}_1, \dots, \widehat{\mathcal{A}}_N$ are aggregated across time via their empirical selection frequencies

$$\Phi(g) = \frac{1}{N} \sum_{n=1}^{N} \mathbb{1}\{g \in \widehat{\mathcal{A}}_n\}, \tag{9}$$

where $\mathbb{1}\{\cdot\}$ denotes the indicator function. The fused support estimate is then defined as

$$\widehat{\mathcal{A}}(\tau) = \{g \in \{1, \dots, G\} : \Phi(g) \geq \tau\}, \tag{10}$$

where $\tau \in (0, 1]$ is a fusion threshold. The fusion threshold τ therefore plays the role of a persistence parameter: small values lead to a more inclusive final support and allow detections that occur only occasionally, whereas larger thresholds emphasize grid cells that are consistently selected across snapshots and thus remain stable.

3.3. Relation to stability selection

The proposed fusion strategy is closely related in spirit to stability selection [3]. In stability selection, a variable selection method is repeatedly applied to perturbed or subsampled versions of the data, and variables are retained according to their empirical selection frequency. In our setting, the repeated applications arise naturally from the sequence of radar snapshots rather than from artificial resampling.

This analogy provides a useful interpretation of $\Phi(g)$: grid cells with high empirical selection frequency are considered stable detections across slow time. At the same time,

the present setting differs from classical stability selection in that the repetitions are physically observed radar snapshots and the underlying base selector, CT-Rex, provides FDR control at the snapshot level [9, 10].

4. Simulation Study

In the general formulation above, the snapshot-wise supports are allowed to vary across time. In the first simulation study, however, we consider the simpler setting of fixed target locations across snapshots and investigate how temporal support fusion behaves when only the complex target amplitudes and the noise realizations vary over time.

To assess the performance of the proposed multi-snapshot CT-Rex framework under controlled conditions, we conduct Monte Carlo simulations based on a radar configuration that mirrors the geometry of the real-world emergency response setup in [6]. We synthesize an 8-element virtual linear array from the radar configuration using the transmit antennas indexed by $\mathcal{M}_t = \{1, 17\}$ and the receive antennas indexed by $\mathcal{M}_r = \{2, 6, 10, 14\}$, resulting in $M = |\mathcal{M}_t| \cdot |\mathcal{M}_r| = 8$ virtual transceiver elements. The spatial grid is aligned with a typical room-scale scenario. Specifically, an area of $8.4\ \mathrm{m} \times 4.2\ \mathrm{m}$ is discretized into cells of size $0.3\ \mathrm{m} \times 0.3\ \mathrm{m}$, resulting in 392 grid points and a steering matrix $\boldsymbol{X} \in \mathbb{C}^{137 \cdot 8 \times 392}$.

For each of the $\mathrm{MC} = 100$ Monte Carlo trials, we randomly select $|\mathcal{A}| = 3$ active grid cells to form the underlying target set $\mathcal{A}$ and generate N measurement snapshots according to (5). For each snapshot n, the coefficient vector $\boldsymbol{\beta}_n$ is supported on the same active set $\mathcal{A}$, while the active coefficients are drawn independently as $(\boldsymbol{\beta}_n)_{\mathcal{A}} \sim \mathcal{CN}(\mathbf{0}, \mathbf{I})$. Thus, the target locations remain fixed across snapshots, whereas their complex amplitudes vary. The received signals are corrupted with additive complex Gaussian noise $\boldsymbol{\nu}_n$, where the noise variance is chosen to match the SNR levels $\{-30, -24, -18, -12, -6, 0, 6\}$ dB. For each snapshot, the CT-Rex selector is applied independently at target FDR level $\alpha = 5\%$, yielding support estimates $\widehat{\mathcal{A}}_1, \ldots, \widehat{\mathcal{A}}_N$, and subsequently fused according to (10). Detection performance is quantified in terms of the empirical FDR and the true positive rate (TPR) across the Monte Carlo trials.

We report two groups of results. First, TPR and FDR over SNR are shown for different fusion thresholds τ at fixed N in Figs. 1a and 1b. Second, TPR and FDR over SNR are shown for different numbers of snapshots N at fixed τ in Figs. 2a and 2b.

5. Discussion

The simulation results show that the fusion threshold τ is the key parameter governing the behavior of the fused support estimate. If τ is chosen too small, the fusion step

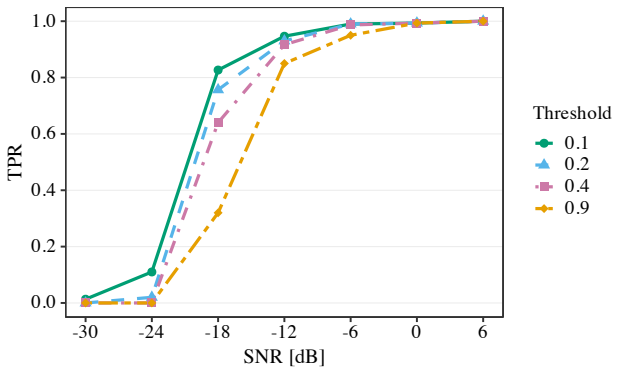

(a) True Positive Rate

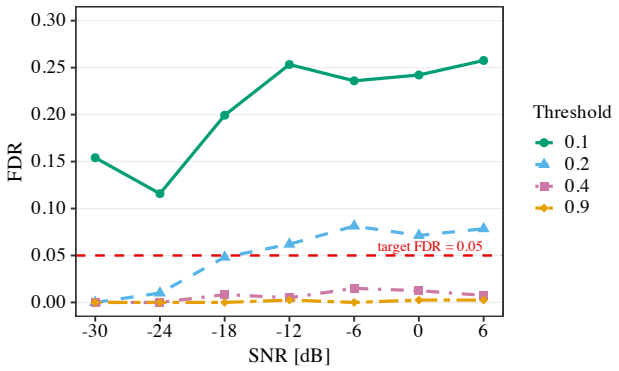

(b) False Discovery Rate

Fig. 1: Influence of the fusion threshold τ on the detection performance for a fixed number of snapshots $N = 10$.

becomes overly inclusive: grid cells that are selected only occasionally are retained in the final support, including spurious detections caused by noise. As a consequence, the FDR of the fused estimate may exceed the target level that is controlled by CT-Rex at the snapshot level. At the same time, small threshold values increase detection power, since weak but repeatedly emerging target locations are less likely to be discarded. In contrast, large threshold values make the fused estimate increasingly conservative. In this regime, only grid cells with very stable selection frequencies are retained. This substantially reduces the fused FDR, often to values clearly below the target level used at the snapshot level, but at the cost of a noticeable loss in power. The results therefore confirm a clear trade-off: small thresholds improve TPR but may violate the desired fused FDR, whereas large thresholds stabilize the fused support but may suppress true target locations.

The simulations further show that the number of snapshots N has a systematic effect on performance. For a fixed threshold τ, increasing N generally improves power, since persistent targets have more opportunities to be selected across repeated CT-Rex runs. In particular, targets with weaker instantaneous amplitudes may only be selected in a subset of snapshots due to noise fluctuations. With more snapshots available, the probability that such targets are se-

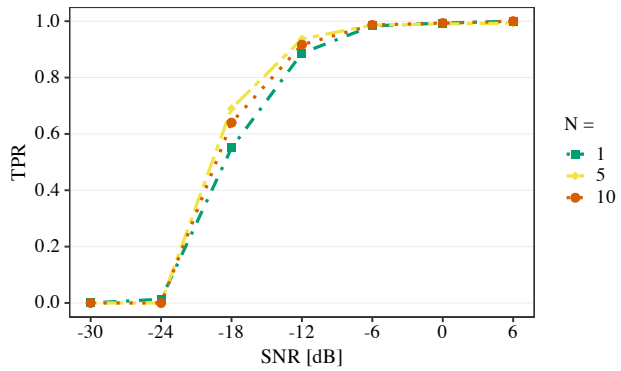

(a) True Positive Rate

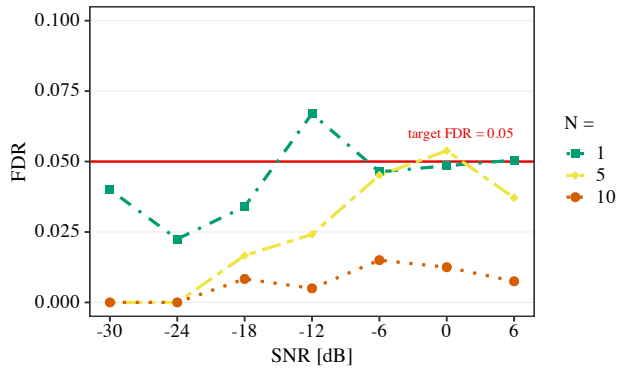

(b) False Discovery Rate

Fig. 2: Influence of the number of snapshots N on detection performance at a fixed fusion threshold $\tau = 0.4$.

lected multiple times increases, which raises their empirical selection frequency $\Phi(g)$ and therefore their chance of passing the fusion threshold. At the same time, the fused FDR decreases with growing N, which supports the interpretation that many false detections are spurious and therefore do not persist across snapshots. In this sense, temporal fusion exploits the instability of false positives and the persistence of true target locations. From this perspective, the empirical selection frequency $\Phi(g)$ can be interpreted as an estimate of the probability that grid cell g is selected by CT-Rex under repeated measurement realizations.

In the present work, the fusion threshold is fixed a priori. The results indicate, however, that an automatic data-driven choice of τ would be highly desirable, ideally such that a target FDR is also respected for the fused support estimate. This is non-trivial, since the appropriate threshold depends not only on the noise regime but also on the number of available snapshots. Developing such an adaptive fusion rule is therefore an important direction for future work.

6. Conclusions

We proposed a multi-snapshot extension of FDR-controlled compressed beamforming for emergency response radar based on snapshot-wise CT-Rex selection and temporal support fusion. The simulations show that the fusion threshold τ governs the trade-off between power and fused FDR, while increasing the number of snapshots improves detection stability and suppresses spurious detections. These findings highlight both the promise of stability-inspired support fusion and the need for adaptive threshold selection in future work.

Acknowledgements

Research described in the paper was supervised by Prof. Dr.-Ing. Christoph Hoog Antink and Prof. Dr.-Ing. Michael Muma, TU Darmstadt in Darmstadt and funded by the LOEWE initiative (Hesse, Germany) within the emergenCITY center [LOEWE/1/12/519/03/05.001(0016)/72].

References

[1] BENJAMINI, Y., HOCHBERG, Y. Controlling the false discovery rate: a practical and powerful approach to multiple testing. *Journal of the Royal Statistical Society: Series B (Statistical Methodology)*, 1995, vol. 57, no. 1, p. 289–300.

[2] MALIOUTOV, D., CETIN, M., WILLSKY, A. S. A sparse signal reconstruction perspective for source localization with sensor arrays. *IEEE Transactions on Signal Processing*, 2005, vol. 53, no. 8, p. 3010–3022.

[3] MEINSHAUSEN, N., BÜHLMANN, P. Stability selection. *Journal of the Royal Statistical Society: Series B (Statistical Methodology)*, 2010, vol. 72, no. 4, p. 417–473.

[4] TORCHALLA, M., SCHNAUBELT, M., DAUN, K., VON STRYK, O. Robust multisensor fusion for reliable mapping and navigation in degraded visual conditions. In *2021 IEEE International Symposium on Safety, Security, and Rescue Robotics (SSRR)*. 2021, p. 110–117.

[5] ECKRICH, C., SCHROTH, C. A., JAMALI, V., ZOUBIR, A. M. Radar based humans localization with compressed sensing and sparse reconstruction. In *2023 24th International Conference on Digital Signal Processing (DSP)*. 2023, p. 1–5.

[6] SCHROTH, C. A., ECKRICH, C., FABIAN, S., VON STRYK, O., ZOUBIR, A. M., MUMA, M. Multi-person localization and vital sign estimation radar dataset. In *IEEE Dataport*, 2023.

[7] SURMANN, H., DAUN, K., SCHNAUBELT, M., VON STRYK, O., PATCHOU, M., BÖCKER, S., WIETFELD, C., QUENZEL, J., SCHLEICH, D., BEHNKE, S., et al. Lessons from robot-assisted disaster response deployments by the German Rescue Robotics Center task force. *Journal of Field Robotics*, 2024, vol. 41, no. 3, p. 782–797.

[8] SCHROTH, C. A., ECKRICH, C., KAKOUCHE, I., FABIAN, S., VON STRYK, O., ZOUBIR, A. M., MUMA, M. Emergency response person localization and vital sign estimation using a semi-autonomous robot mounted SFCW radar. *IEEE Transactions on Biomedical Engineering*, 2024, vol. 71, no. 6, p. 1756–1769.

[9] MACHKOUR, J., MUMA, M., PALOMAR, D. P. The terminating-random experiments selector: fast high-dimensional variable selection with false discovery rate control. *Signal Processing*, 2025, vol. 231, p. 109894.

[10] SCHEIDT, F., MACHKOUR, J., MUMA, M. FDR control for complex-valued data with application in single snapshot multi-source detection and DOA estimation. In *Proceedings of the 50th IEEE International Conference on Acoustics, Speech and Signal Processing (ICASSP)*. 2025, p. 1–5.

About Authors...

Christoph LÖSER was born in Lübeck, Germany, in 1998 and pursued his Bachelor's and Master's degrees in Electrical Engineering and Information Technology at the Technical University of Darmstadt, graduating in 2025. Since March 2025, he has been a PhD student at the KIS*MED - AI Systems in Medicine Group and the Robust Data Science Group in Darmstadt, specializing in data science with a focus on statistically robust methods, high-dimensional data, and biomedical applications. As part of his work, he is involved in the Cyber-Physical Systems program of the LOEWE center, emergenCITY.

Analytical eigenfrequencies approximation of perforated square plates

Aneta FURMANOVÁ[1]

[1]Dept. of Physics, Faculty of Electrical Engineering, Czech Technical University, Technická 2, 166 27 Praha, Czech Republic

furmaane@fel.cvut.cz

Abstract.

Most modern Micro-Electromechanical Systems (MEMS) microphones rely on the electrostatic principle of electroacoustic transduction, typically incorporating moving electrodes paired with perforated backplates in single or double configurations. Building upon previous research regarding the theoretical modeling of acoustic field coupling within these transducers, this work addresses the structural dynamics of the moving electrode. The primary objective is to establish analytical approximations for the eigenfrequencies of square plates clamped at all boundaries, considering both solid and perforated geometries.

For solid geometries, results were obtained using symbolic regression. The eigenfrequency for perforated plates is provided as a discrepancy to the non-perforated case using the normalized eigenfrequency. A quadratic fit based on the perforation ratio proved sufficient. Future work on perforated plates will validate the approximations for plates with other thickness-to-width ratios and for square holes.

Keywords

electroacoustic transducers, perforated plate, data-driven discovery, symbolic regression

1. Introduction

Most modern MEMS microphones utilize electrostatic transduction, featuring moving electrodes and perforated backplates in single or double configurations. Šimonová *et al.* [1] have presented a theoretical model for the coupling between the acoustic field and the vibration of square perforated moving electrodes clamped at all boundaries. Building on this foundation, the present paper focuses on finding an analytical approximation for the eigenfrequencies of the moving electrode structural vibrations.

Analytical formulae for the eigenfrequencies are easily obtainable for membranes and simply supported plates. The eigenfrequency for the (m,n) mode of a rectangular membrane fixed along all edges is

$$f_{mn} = \frac{c}{2}\sqrt{\frac{m^2}{a^2} + \frac{n^2}{b^2}}\,, \tag{1}$$

with a, b being the sides of the membrane and c the wave speed [2]. However, the bending modes of a plate with all clamped edges are a fundamentally different problem than those of a stretched membrane: while the membrane tension T is imposed by external forces and its initial pre-stress, the restoring force in a clamped plate is governed primarily by its flexural rigidity D.

The formula for eigenfrequencies of simply supported plates is obtained as an exact analytical solution of the governing equations:

$$f_{mn} = \frac{\pi}{2}\left(\frac{m^2}{a^2} + \frac{n^2}{b^2}\right)\sqrt{\frac{D}{\rho h}}\,, \tag{2}$$

where $D = Eh^3/12(1-\nu^2)$ is the flexural rigidity, with E being the Young's modulus, ν the Poisson's ratio and h the thickness of the plate.

For plates with all edges clamped, an additional boundary condition (BC) must be satisfied: beyond the zero-displacement requirement (which applies to simply supported edges), the slope of the displacement must be equal to zero as well (see Figure 1). Technically, both the homogeneous Dirichlet and Neumann BC must be satisfied at once. With these constraints, it becomes challenging to find exact analytical solutions that satisfy the governing equation and all the BCs [3].

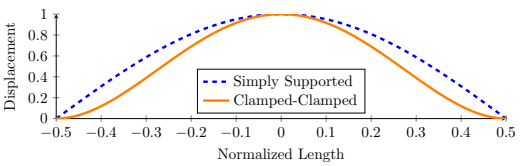

Fig. 1. Displacement in 1D, simply supported vs all clamped edges.

Consequently, obtaining the eigenfrequencies for plates clamped at all boundaries relies on numerical simu-

lations or approximation methods, such as the Rayleigh-Ritz method (see [4]) or numerical solutions of the eigenvalue problem (see, e.g. [5]). Therefore, the aim of this work is to provide an analytical approximation for solid and perforated square plates clamped at all boundaries based on physics-informed machine learning.

2. Non-perforated plates

For finding the eigenfrequency approximation of non-perforated square plates clamped on all sides, symbolic regression with enforced prior knowledge was used. Namely, for the implementation, the open-source library PySR ([6]) was employed.

A single case is defined by Young's modulus E, Poisson's ratio ν, material density ρ, and geometric parameters: the plate's side $2a$ and thickness h. For simplicity, only one material is considered in this paper, silicon.

The dataset was generated using the Solid Mechanics in COMSOL Multiphysics 6.4. The material properties used in COMSOL were Young's modulus $E = 170$ GPa, Poisson's ratio $\nu = 0.28$ and the density of the plate $\rho = 2329\ \mathrm{kg\,m^{-3}}$. A parametric sweep was employed for the geometry parameters in the following ranges: $a \in \{0.3, 0.6, 0.9, 1.2, 1.5\}$ mm, $h \in \{4, 7, 10, 13, 16\}$ μm.

In total 25 combinations of a, h were generated with modes $m, n = 1, 2, 3$, see the modes in Figure 2. Note the symmetries, which are due to the geometric symmetry of the square plate. While the transposed modes (e.g., 21, 31, and 32) are mathematically identical to their counterparts ($m, n = n, m$), numerical simulations in COMSOL yield slightly different eigenfrequencies for these pairs due to finite element discretization, meshing, and numerical precision limits. Therefore, the eigenfrequencies of these symmetric mode pairs are averaged before further processing.

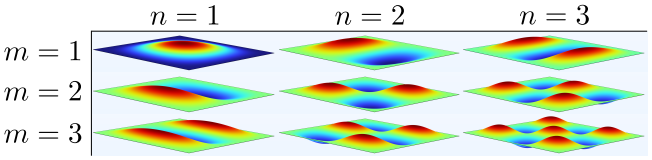

Fig. 2. Eigenmodes of a non-perforated square plate.

Knowledge of the problem can be incorporated into the algorithm's setup. Based on the expressions for eigenfrequency of membranes (Eq. (1)) and simply supported plates (Eq. (2)), the following operators can be expected in the sought expression: `+, −, *, /, ^`. Note that we can theoretically include all possible operators (e.g. trigonometric functions), but by doing so, the search space could grow exponentially. Moreover, the symmetry in m, n is expected due to the square geometry. Therefore, additional penalization for expression not symmetric in m, n was added.

To optimize the regression process, several layers of expert knowledge were incorporated to refine the search space and improve the physical interpretability of the results. Rather than fitting the frequencies directly, the target variable was defined as $(f_{mn} \cdot a)^2$, as this quadratic form is more likely to lead to patterns similar to those found in literature. Furthermore, to ensure physical consistency, both the target and the candidate terms were cast into dimensionless forms.

The target could be non-dimensionalized using the wave speed on the plate as $(f_{mn} \cdot a)^2/c^2$, where $c = \sqrt{Eh^2/(12(1-\nu^2)\rho)}$. However, it is possible that the belief in the term $12(1-\nu^2)$ is too strong of a prior (especially since it is a dimensionless constant). Therefore, it was decided to fit $(f_{mn} \cdot a)^2 \cdot (\rho/E)$ instead, as dimensional analysis provides no other fundamental alternative for scaling the material properties. The objective was set to minimize the L1 distance between the data and the predicted adjusted eigenfrequency. The mode numbers m and n were included as naturally dimensionless variables. Regarding the geometric parameters, the thickness-to-width ratio h/a was utilized as the primary feature, as this ratio is expected to play a role in the plate's vibrational response.

2.1. Results

Symbolic regression provides a Pareto front of candidate results, spanning from parsimonious but less accurate models to highly precise but complex ones that hinder interpretability. Selecting the optimal expression from this front is a trade-off between accuracy and interpretability. Therefore, it was decided to provide two approximations for the eigenfrequencies. The first result resembles the expression for the simply supported plate (Eq. (2)):

$$f_{mn} = 0.228\sqrt{\frac{E}{\rho}}\left(\frac{h}{a}\right)\sqrt{m+n}\sqrt{\frac{m^2}{a^2}+\frac{n^2}{a^2}}\,. \qquad (3)$$

The coefficient 0.228 in Eq. (3) was obtained by the least squares. The relative error boxplots for different modes are shown in Figure 3. For the considered modes altogether, the median of the relative error is 4.69 %, the first quartile is 3.29 %, and the third quartile is 7.52 %, This is unfortunately a higher error than the interval widths provided by Leissa [4] (Tables 4.24–4.27), which are below 3 %.

The other chosen formula

$$f_{mn} = 0.0589\sqrt{\frac{E}{\rho}}\left(\frac{h}{a}\right)\sqrt{\frac{(m+n)^{5.6}}{(mn)^{1.16}a^2}} \qquad (4)$$

reaches better accuracy: for the considered modes altogether, the median of the relative error is 1.71 %, first quartile 1.25 %, and the third quartile 2.17 %.

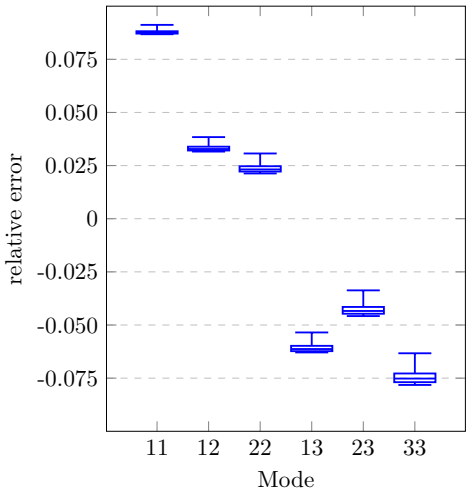

Fig. 3. Results of Eq. (3)

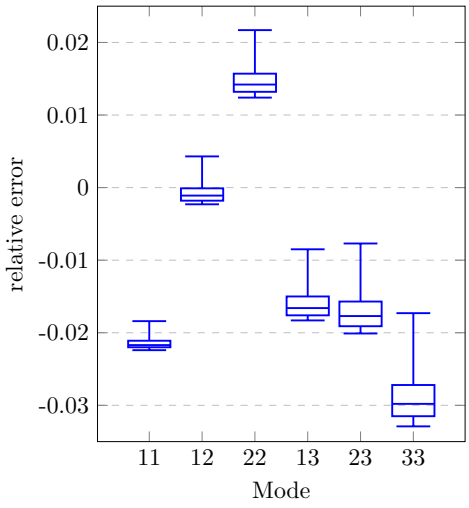

Fig. 4. Results of Eq. (4)

3. Perforated plates

Building upon the non-perforated case, let's now consider the same square geometry with the introduction of a periodic array of perforations. The square perforated plate of side $2a$ has N square holes of side d and pitch p (see Figure 5). The number of holes is equal to $N = 2a/p \times 2a/p$. There are two ways to describe the perforations: either by ligament efficiency $\eta = (p - d)/p$ or by perforation ratio $R = \frac{\pi}{4} d^2/p^2$, which is the ratio of the total area occupied by the holes and the area of the plate.

The eigenfrequency for the perforated plates can be provided as a discrepancy to the non-perforated case. For that, the normalized eigenfrequency was used, defined as the eigenfrequency of the perforated plate divided by the corresponding eigenfrequency of the non-perforated plate.

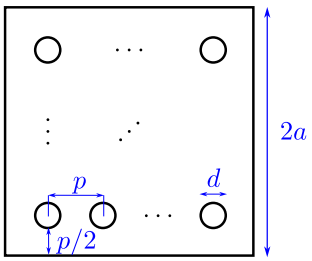

Fig. 5. Schematic drawing of a square perforated plate.

Jhung *et al.* [7] suggest that the normalized eigenfrequency depends only on the ligament efficiency, and not on the mode number. This is demonstrated on a single geometry, a 384 mm x 384 mm aluminium square plate with 3 mm thickness. Within this area, a grid of 24 × 24 holes (N) is arranged with a constant pitch (p) of 16.0 mm. The analysis considers a variable circular hole diameter (d) ranging from 0 to 15.6 mm.

To evaluate the applicability of these findings to perforated plates with MEMS transducers, this paper extends the results of Jhung *et al.* [7] to the micro-scale. While the material is transitioned from aluminium to silicon and the absolute dimensions are reduced, the thickness-to-width ratio of the plate is preserved, so that $2a = 384\ \mu\text{m},\ h = 3\ \mu\text{m}$. The pitch was set as $p = 16\ \mu\text{m}$.

During a preliminary study it turned out a more suitable independent variable for finding the natural frequency fit is the perforation ratio R rather than the ligament efficiency η (R already absorbs some of the nonlinearity so the natural frequency curve is more regression friendly). Therefore, the R was chosen to be regularly spaced as $R \in \{0.1, 0.2, 0.3, 0.4\}$ and the hole diameters were calculated based on R as $d^2 = \frac{\pi}{4} R p^2$.

The use of symbolic regression was unnecessary in this case, since a quadratic fit with a fixed offset to 1 turned out to be sufficient:

$$f_{\text{norm}} = 0.36R^2 - 0.62R + 1\ , \tag{5}$$

with error under 0.3 %. The results data and fit are shown in Figure 6.

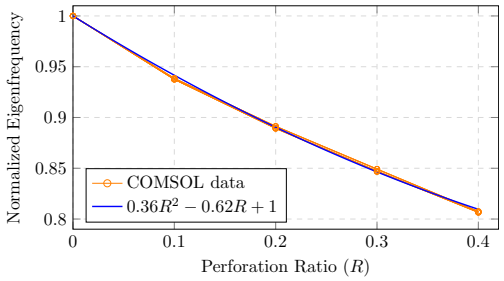

Fig. 6. Normalized eigenfrequency of a perforated square plate, data and polynomial fit from Eq. (5).

4. Conclusion

For plates with all edges clamped, there are no known exact analytical solutions that satisfy the governing equation and boundary conditions. The goal of this work was to provide analytical approximations for the eigenfrequencies of non-perforated and perforated square plates.

Two alternative forms for solid plates were derived using symbolic regression, the better accuracy was achieved by formula not resembling the expression for simply supported plate. Future work on perforated plates is validating the approximations for plates with other thickness-to-width ratios and also for square holes.

Acknowledgements

Research described in the paper was supervised by Dr. Pierrick Lotton (LAUM, France), Ing. Petr Honzík, Ph.D. (FEE CTU) and RNDr. MgA. Viktor Hruška, Ph.D. (FEE CTU).

This work was supported by the Grant Agency of the Czech Technical University in Prague, grant No. SGS25/136/OHK3/3T/13.

References

[1] ŠIMONOVÁ, K.; HONZÍK, P. Modeling of MEMS Transducers with Perforated Moving Electrodes. In *Micromachines*. 2023, 14(5), 921.

[2] GRAFF, Karl F. Wave Motion in Elastic Solids, 1975.

[3] XING, Y.; LI G.; YUAN Y. A review of the analytical solution methods for the eigenvalue problems of rectangular plates. *International Journal of Mechanical Sciences*. 2022, 221, 107171.

[4] LEISSA, A. W. Vibration of Plates, 1969.

[5] ŠIMONOVÁ, K.; HONZÍK, P.; BRUNEAU, M.; GATIGNOL, P. Modelling approach for MEMS transducers with rectangular clamped plate loaded by a thin fluid layer. In *Journal of Sound and Vibration*, 2020, 473, 115246.

[6] CRANMER, M. Interpretable Machine Learning for Science with PySR and SymbolicRegression.jl. In *arXiv*, 2023.

[7] JHUNG, M. J.; JEONG, K. H. Free vibration analysis of perforated plate with square penetration pattern using equivalent material properties. In *Nuclear Engineering and Technology*. 2015, 47(4), 500–511.

About Authors...

Aneta FURMANOVÁ is a PhD student at the Czech Technical University in Prague, Faculty of Electrical Engineering (CTU, FEE). Her research interest lies in data-driven discovery and physics-informed machine learning in acoustics. During her internship at Graz University of Technology, she first focused on implementation of Physics Informed Neural Networks for solving the Helmholtz equation, and later on the faster implementation of the Natural Helmholtz-Hodge Decomposition.

Distributed Wireless Structural Health Monitoring System for Aircraft Structures

Bc. Šimon Pecháček[1]

[1]Dept. of Measurement, Czech Technical University, Technická 2, 166 27 Praha, Czech Republic

pechasim@fel.cvut.cz

Abstract. *This work presents the design and development of a distributed wireless structural health monitoring system intended for aircraft composite structures. The proposed system is based on piezoelectric transducers used for both excitation and sensing of ultrasonic guided waves propagating through the material, with the objective of detecting and localizing structural defects such as cracks or delamination.*

The contribution covers the design of dedicated hardware for driving piezoelectric transducers, enabling both the generation and sensing of ultrasonic waves. It also includes the implementation of embedded firmware on an STM32 microcontroller platform. In addition, the work addresses wireless communication within the sensing network using ultra-wideband technology (UWB), including the design of a custom routing protocol and a synchronization strategy for coordinated operation of distributed nodes. The resulting platform forms a basis for scalable monitoring of complex aircraft structures.

Keywords

Structural health monitoring; aircraft structures; composite materials; ultrasonic guided waves; wireless sensor networks; ultra-wideband communication

1. Introduction

Composite materials are widely used in applications where low weight and high design flexibility are important, such as aircraft structures. Although these materials offer many advantages, they are also vulnerable to certain types of damage. For example, low-velocity impact can cause defects such as delamination or cracks inside the material [1], which are typically more severe than in metals [2].

To detect such defects, non-destructive testing (NDT) methods are used. Among these, ultrasonic NDT is a widely used method in structural health monitoring (SHM) [3], and is also the method used in this work.

Ultrasonic NDT commonly uses a network of piezoelectric transducers that excite and receive ultrasonic waves propagating through the structure. These waves are suitable for defect detection because they are sensitive to common damage types such as delamination and cracks [3].

This work focuses on thin plate-like structures, in which the two most common guided wave types are Lamb waves and shear-horizontal (SH) waves [4]. In the considered application, Lamb waves are the desired wave mode.

The aim of this work is to develop a system capable of generating and measuring Lamb waves while operating wirelessly across multiple nodes and performing time-synchronized measurements. A wireless approach was selected to reduce cabling complexity, system weight, and inter-channel crosstalk. However, this approach also introduces additional challenges, particularly the need for precise time synchronization and operation of battery-powered nodes.

2. Hardware

The hardware is composed of three main functional blocks: a driving circuit, a sensing circuit, and a multiplexer. The design is based on an ultrasonic frequency of 78.3 kHz, which was selected because only the A0 and S0 Lamb-wave modes are excited and is highly sensitive to the defects of interest [5]. Channel routing is performed by high-voltage analog switches (*TMUX7612*), which independently connect selected channels to the transmit and receive signal paths, allowing simultaneous excitation on one channel and measurement on another. The simplified block diagram of the hardware is shown in Figure 1.

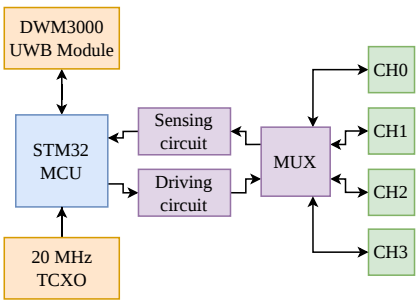

Fig. 1. Simplified SHM system hardware block diagram.

2.1. Driving circuit

The target driving capabilities is a voltage amplitude of $\pm 20\,\mathrm{V}$ for a capacitive load of up to $2.8\,\mathrm{nF}$ at frequencies up to $100\,\mathrm{kHz}$. Since the excitation signal is generated by the STM32 DAC, the output voltage must be amplified to the required amplitude and shifted to zero DC offset.

The required peak current is

$$I_{peak} = \left|\frac{\pm 20}{Z_c}\right| = \left|\frac{\pm 20}{\frac{1}{2\pi f_{max} C}}\right| = 35.19\,\mathrm{mA}. \quad (1)$$

The desired excitation signal is given by Equation (2).

$$V(t) = \frac{1}{2} A \sin\left(2\pi f_{signal} t\right)\left(1 - \cos\left(\frac{2\pi t}{T}\right)\right) \quad (2)$$

Where A is the amplitude of the signal, f_{signal} is its frequency and T is the length of the whole signal. From Equation (2) the maximum needed slew-rate was numerically calculated to be

$$SR = \max\left|\frac{dV(t)}{dt}\right| = 9.84\,\mathrm{V\,\mu s^{-1}}. \quad (3)$$

The selected amplifier was *LTC6090-5*, which meets the voltage, current, and slew-rate requirements.

The driver circuit is depicted in Figure 2.

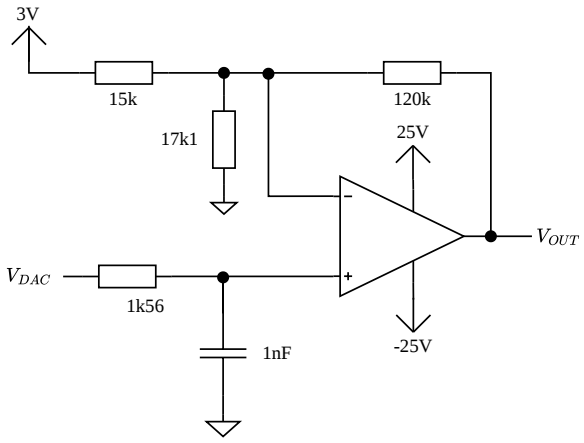

Fig. 2. Driver circuit schematic for amplification of the DAC output signal for Lamb-wave excitation.

A comparison of the generated and desired signals is shown in Figure 3. The signal is generated by the STM32 digital-to-analog converter (DAC) at 1 MSPS, which results in visible steps in the waveform. For this reason, a $100\,\mathrm{kHz}$ RC low-pass filter is used at the DAC output.

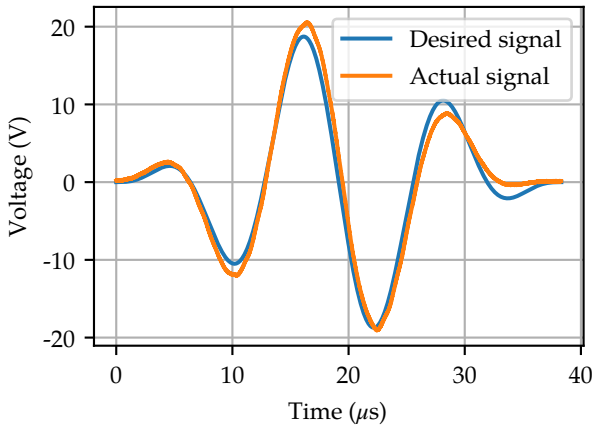

Fig. 3. Comparison of generated and desired excitation signal.

2.2. Sensing circuit

The signals received from the piezoelectric transducers need to be amplified from tens of mV to the full scale ADC voltage range of $0 - 3\,\mathrm{V}$. The signal also contains unwanted frequencies, caused by mechanical movements of the structure and, which must be filtered out to preserve only the driving frequency. The varying signal attenuation between sensors, caused by varying distance between sensors, is compensated by programmable gain amplifier.

The proposed circuit is depicted in Figure 4.

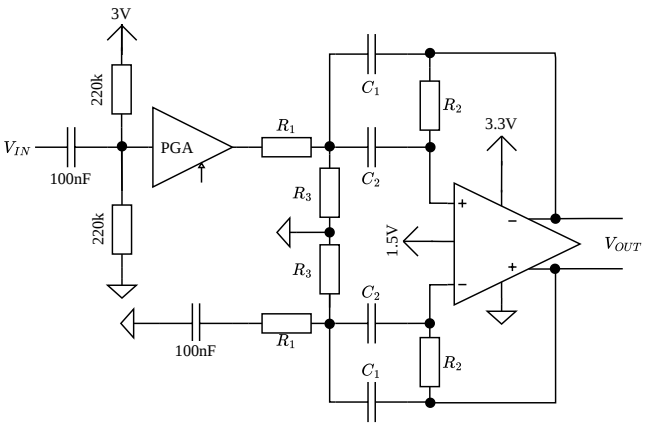

Fig. 4. Amplifier circuit schematic, containing programmable gain amplifier and multi feedback band-pass filter.

The input signal is AC-coupled, biased to $1.5\,\mathrm{V}$, and then amplified by a programmable gain amplifier (PGA). This is followed by a fully differential multiple-feedback band-pass filter with a center frequency of $78.6\,\mathrm{kHz}$, a bandwidth of $39.3\,\mathrm{kHz}$, a quality factor of 2, and a gain of 4. The transfer function of the filter is

$$H(s) = \frac{-\frac{s}{R_1 C_2}}{s^2 + \frac{s(C_1+C_2)}{C_1 C_2 R_2} + \frac{R_1+R_3}{C_1 C_2 R_1 R_2 R_3}}. \quad (4)$$

Where $R_1 = R_3 = 1\,\mathrm{k\Omega}$, $R_2 = 8.2\,\mathrm{k\Omega}$ and $C_1 = C_2 = 1\,\mathrm{nF}$. Comparison between calculated and measured frequency response of the multiple feedback band-pass filter is shown in Figure 5.

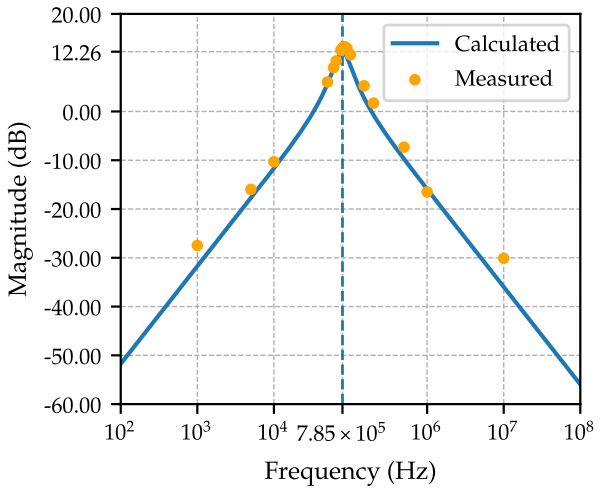

Fig. 5. Comparison of theoretical and actual frequency response of multiple feedback band-pass filter.

The signal is than sampled by 12-bit STM32 Analog-to-Digital converter (ADC) in differential mode. Two internal ADCs are used in interleaved master-slave mode to achieve maximum sampling rate of 7 MSPS.

Parameters of the acquisition chain are summarized in Table 1.

Parameter	Value	Unit
SNR	71.22	dBc
THD	−66.88	dBc
SINAD	65.52	dBc
ENOB	10.50	bits
Offset	1.50	LSB

Tab. 1. Measured dynamic parameters of the acquisition chain.

3. Communication

Ultra-Wide-Band (UWB) communication was selected for this project because it is well suited for wireless personal area networks (WPANs), where high data rates and accurate synchronization are required [6].

The system uses a DWM3000 UWB module operating on channel 5 (6.5 GHz) with a maximum data rate of $6.8\,\mathrm{Mbit\,s^{-1}}$. The module supports frame filtering based on the Personal Area Network (PAN) ID, device addresses, and packet type, as defined in IEEE Std 802.15.4 [7]. It also provides precise timestamping and delayed packet transmission. These features are utilized for three key tasks within the network: message routing, reliable data transmission, and node synchronization.

3.1. Routing

A custom routing protocol is proposed to find a route between any two nodes within the network. The protocol is intended for static networks, where node positions remain unchanged after initialization. Each node stores a routing table containing the cost and next-hop address for all known destinations. The routing table is built in four steps, as shown in Figure 6.

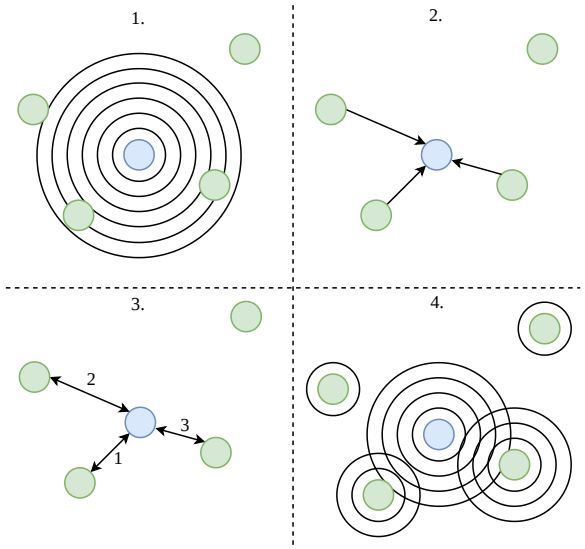

Fig. 6. Steps of building a routing table.

1. When a new node without a routing table wakes up, it waits for a predefined delay based on its address to avoid collisions in the case of a synchronized wake-up. It then broadcasts a neighbor request consisting only of the IEEE 802.15.4 MAC header.

2. Each neighboring node that receives the request waits for a random delay in the range of 0-10 ms before responding. This reduces collisions, since the broadcast acts as a synchronization event. The response again contains only the MAC header.

3. The requesting node waits for 11 ms after the broadcast and stores all responding neighbors in a queue. After the timeout, it requests the routing tables from the queued neighbors and merges them into its own table while keeping the lowest-cost routes. The cost is defined as the number of forwarding hops between two nodes. Other metrics could also be used, such as received signal strength or whether the nodes are in direct line of sight, both of which can be estimated using the DWM3000 module.

4. After constructing its routing table, the node broadcasts a message informing the network that a new node has joined. All nodes forward this message while updating the cost and their routing tables. To avoid unnecessary flooding, a message is forwarded only if it improves the known cost or if it is not already present in cache.

3.2. Reliable transmissions

To achieve reliable high-data-rate communication, the limitations of the DWM3000 module must be taken into account. The module cannot transmit and receive at the same time, and a single transmission can carry at most 112 bytes of payload. Messages therefore have to be split into multiple packets. Each packet contains a cyclic redundancy check (CRC) and must be acknowledged by the receiver.

A Go-Back-N ARQ protocol is used. The sender transmits a new packet every 500 µs without waiting for an acknowledgment. The receiver checks the CRC and stores the received data, but does not acknowledge every packet immediately. Instead, an acknowledgment is sent either after the whole message is received or when the maximum number of unacknowledged packets is reached. If a CRC error occurs, a *not acknowledge* is sent and all out-of-order packets are discarded. The sender then retransmits the data starting from the last acknowledged packet.

With the Go-Back-N protocol, an effective data rate of $1\,\mathrm{Mbit\,s^{-1}}$ was achieved. Message transmission failed in approximately 0.5% of cases, however each failure was reliably detected by both nodes, which allowed the complete message to be retransmitted.

3.3. Synchronization

As the measurements are performed cooperatively by multiple nodes, their operation must be time-synchronized. The sampling rate is 7 MSPS, which corresponds to a sampling period of 142.86 ns. The target maximum clock offset between two nodes is therefore set to half of this value i.e. 70 ns, so that the synchronization error has negligible effect on the measured samples. However, this value corresponds to an ideal case. In practice, the signal changes caused by structural damage are typically larger, and a maximum offset of 1 µs is considered sufficient.

Synchronization between two nodes

To synchronize two nodes between each other an alternative double-sided two-way ranging is used [8]. Two nodes exchange 3 messages, usually named *poll*, *response* and *final*. While the poll and response do not contain any additional data on top of the mac header, the final message contains the timestamp of poll transmit time, response receive time and final transmit time. This exchange is captured in Figure 7.

This approach is great as it corrects for clock drift which is the dominant component of imperfections [8]. From the timestamps a Time-of-Flight (ToF) and clock drift

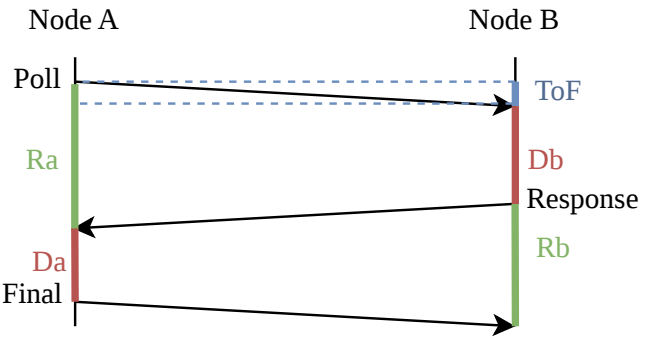

Fig. 7. Two way ranging message exchange.

k_b can be calculated from Equation (5) and Equation (6) respectively.

$$ToF = \frac{(R_a R_b - D_a D_b)}{2\,(R_b + D_b)} \tag{5}$$

$$k_b = \frac{R_b + D_b}{R_a + D_a} \tag{6}$$

From these, the delay D between two clocks can be calculated from Equation (7).

$$D = poll_{tx} - ((poll_{rx} - ToF)\,/k_b) \tag{7}$$

However, a hardware pulse or event is still required to trigger the measurement. For this reason, the following synchronization method is proposed. Both devices use temperature-compensated oscillators with a frequency stability of 0.5 ppm to drive a timer with period T. Each timer resets the time stamping clock of the DWM3000 module every period and one node designated as the master initiates a two-way ranging exchange with the other node. The slave node then estimates its delay from Equation (7) and using a PD controller with $K_p = 1$ and $K_d = 1$ adjusts its timer period T using Equation (8).

$$T(k) = T(k-1) - K_p D(k) - K_d\big(D(k) - D(k-1)\big) \tag{8}$$

The synchronization performance was evaluated over a period of 2 hours with period $T = 1\,\mathrm{s}$, using one master node and two slave nodes. The measured results are presented in Table 2, which summarizes the delay between the master and each slave node.

Parameter	Slave 1	Slave 2
Mean	0.2 ns	0.6 ns
Standard deviation	67.0 ns	61.5 ns
Peak-Peak	496.0 ns	462.0 ns

Tab. 2. Delay between master and slave triggers during synchronization.

The results show that the target clock offset is satisfied in approximately 70 % of cases, as the clock offset distribution is Gaussian. However, due to noise, the instantaneous delay may occasionally exceed the acceptable limit. In such cases, the master node broadcasts an invalidation message, and the affected measurement is repeated at the next trigger event.

4. Results

As a result of this work, 3 measurement devices were manufactured and assembled, pictured in Figure 8.

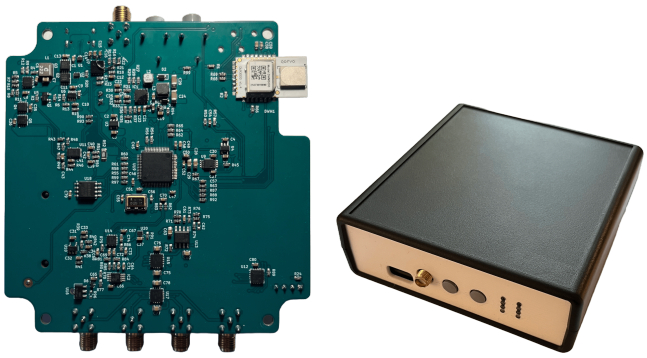

(a) Printed circuit board (b) Device with enclosure

Fig. 8. Photographs of the developed hardware: (a) printed circuit board (PCB) and (b) fully assembled device.

To validate the practical applicability of the developed devices, experiments were performed on a composite plate of dimensions $450\,\mathrm{mm} \times 250\,\mathrm{mm}$ using 12 piezoelectric transducers. An artificial defect was introduced at the VZLU testing facility by a $5\,\mathrm{J}$ impact, resulting in a dent of depth $0.7\,\mathrm{mm}$ and internal delamination. The defect localization results are shown in Figure 9.

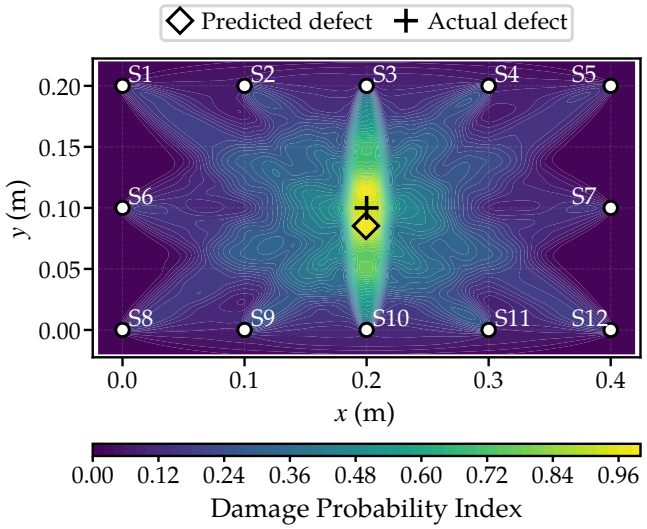

Fig. 9. Localization of a defect caused by 5 J impact.

5. Conclusions

This paper presented the development of a distributed wireless structural health monitoring system intended for composite aircraft structures. The proposed hardware enables excitation of piezoelectric transducers and acquisition of ultrasonic responses using a programmable analog front-end and a 12-bit STM32 ADC with a sampling rate of up to $7\,\mathrm{MSPS}$. In addition, a UWB-based communication layer was implemented using the DWM3000 module, including custom routing, reliable packet transmission, and node synchronization. Experimental results showed that the proposed synchronization method provides sufficient timing accuracy for coordinated measurements across multiple wireless nodes. The developed system was further validated on a composite specimen with an impact-induced defect, where successful defect localization was demonstrated.

Acknowledgements

This work was supervised by Ing. Stanislav Drozd and supported by the Technology Agency of the Czech Republic under Project No. TQ15000233 and by the Grant Agency of the Czech Technical University in Prague under Grant No. SGS25/056/OHK3/1T/13.

References

[1] RICCI, F., MONACO, E., BOFFA, N.D., MAIO, L., MEMMOLO, V., Guided waves for structural health monitoring in composites: A review and implementation strategies, *Progress in Aerospace Sciences*, 2022, vol. 129, p. 100790.

[2] MAIO, L., MONACO, E., RICCI, F., LECCE, L., Simulation of low velocity impact on composite laminates with progressive failure analysis, *Composite Structures*, 2013, vol. 103, pp. 75–85.

[3] TANVEER, M., ELAHI, M.U., JUNG, J., AZAD, M.M., KHALID, S., KIM, H.S., Recent Advancements in Guided Ultrasonic Waves for Structural Health Monitoring of Composite Structures, *Applied Sciences*, 2024, vol. 14, no. 23, p. 11091, publisher: Multidisciplinary Digital Publishing Institute.

[4] PHILIBERT, M., YAO, K., GRESIL, M., SOUTIS, C., Lamb waves-based technologies for structural health monitoring of composite structures for aircraft applications, *European Journal of Materials*, 2022, vol. 2, no. 1, pp. 436–474.

[5] ŠEDEK, J., ŠEDKOVÁ, L., VÍCH, O., Frequency-integral method for impact damage detection in carbon fibre reinforced thermoplastic composites by Lamb waves, *Ultrasonics*, 2025, vol. 154, p. 107697.

[6] RAHAYU, Y., RAHMAN, T.A., NGAH, R., HALL, P., Ultra wideband technology and its applications, *2008 5th IFIP International Conference on Wireless and Optical Communications Networks (WOCN '08)*, 2008 pp. 1–5, iSSN: 2151-7703.

[7] IEEE Standard for Low-Rate Wireless Networks, iSBN: 9781504466899.

[8] NEIRYNCK, D., LUK, E., MCLAUGHLIN, M., An alternative double-sided two-way ranging method, *2016 13th Workshop on Positioning, Navigation and Communications (WPNC)*, 2016 pp. 1–4.

About Authors...

Šimon PECHÁČEK is a master's student at the Czech Technical University in Prague, Faculty of Electrical Engineering, Department of Measurement. His work focuses on embedded electronics, ultrasonic measurement, wireless communication, and printed circuit board (PCB) design.

Automated gm/ID Based Design of Analog Circuits using Genetic Algorithms

Matěj FOUKAL[1]

[1]Dept. Microelectronics, Faculty of Electrical Engineering,
Czech Technical University, Technická 2, 166 27 Praha, Czech Republic

foukamat@fel.cvut.cz

Abstract. *Analog circuit design remains difficult to automate due to strong parameter coupling, non-convex design spaces, and the high computational cost of repeated circuit simulation. This paper presents a framework for automated analog circuit sizing that combines the gm/ID design methodology with genetic-algorithm (GA) optimization.*

The proposed approach operates on pre-characterized transistor lookup tables (LUTs), enabling direct evaluation of candidate solutions without invoking circuit simulation inside the optimization loop. This significantly reduces computational cost while preserving sufficient accuracy.

The framework is technology-agnostic and supports systematic exploration of design trade-offs under user-defined performance targets and constraints.

Keywords

analog circuit optimization, automated sizing, gm/ID methodology, genetic algorithm, design space exploration

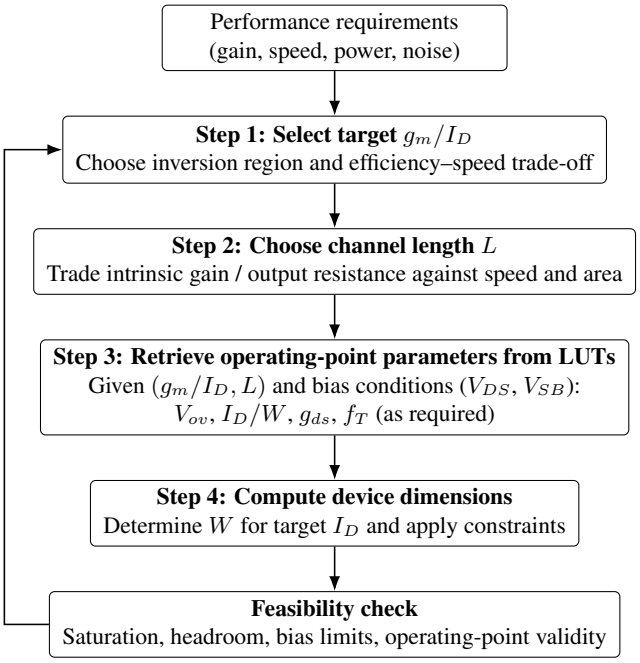

Fig. 1: gm/ID-based transistor sizing flow.

1. gm/ID-Based Device Modeling

The gm/ID method is a systematic design approach that uses transistor figures of merit as the primary tuning knobs of analog circuits that relate directly to the key performance targets.

In this work, transistor behavior is characterized through simulation across a range of channel lengths L, gate-source voltages V_{GS}, drain-source voltages V_{DS}, and source-bulk voltages V_{SB}, following the methodology described by Murmann and Jespers [1]. This process generates lookup tables (LUTs) containing key device parameters such as I_D/W, output conductance g_{DS}, threshold voltage V_T and parasitic capacitances.

In the simplest use case (Fig.1), the method can be applied to determine the sizing of a single transistor. For a given V_{DS} and target drain current I_D, the designer selects a desired g_m/I_D and channel length based on performance trade-offs. Using the LUT data, the corresponding current density I_D/W is obtained, allowing the transistor width W to be computed as

$$W = \frac{I_D}{I_D/W}. \tag{1}$$

The key advantage of this approach is that once the LUTs are generated, transistor behavior can be evaluated without repeated circuit simulation. This enables fast estimation of operating points and performance metrics, making the gm/ID methodology particularly suitable for integration with automated optimization techniques.

However, when additional parameters such as supply voltage V_{DD} and bias current I_D are treated as design variables, the resulting search space becomes high-dimensional and strongly non-convex. Under these conditions, manual tuning becomes inefficient and motivates the use of automated optimization methods.

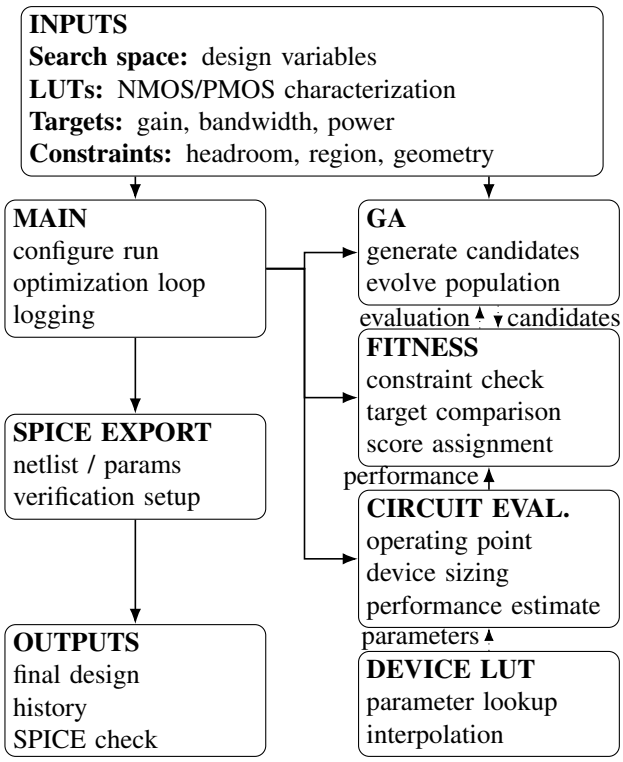

Fig. 2: Automated gm/ID-based sizing workflow.

2. Optimization Method

Analog circuit sizing can be formulated as a constrained optimization problem, where device dimensions and bias conditions must satisfy performance targets such as gain, bandwidth, and power consumption while respecting saturation and headroom constraints.

Performance metrics depend simultaneously on multiple interrelated parameters, limiting the applicability of gradient-based optimization methods [2].

Due to the non-convex nature of the design space, population-based search methods such as genetic algorithms are more suitable than gradient-based approaches. The population-based search enables exploration of multiple regions of the design space simultaneously, reducing sensitivity to local extrema [2].

This combination makes GA particularly suitable for integration with LUT-based device modeling, forming the basis of the automated design framework described in the next section.

3. Automated Design Framework

The automated design framework is illustrated in Fig. 2. It consists of a control layer that orchestrates the optimization process and an evaluation layer that estimates circuit performance using pre-characterized device data.

The workflow begins with the definition of the design problem, including the search space, performance targets, and feasibility constraints. These parameters define the candidate solutions explored during optimization.

Candidate solutions are generated by the GA and iteratively refined with the fitness evaluation block. Each candidate is decoded into circuit parameters and evaluated using LUT-based estimation.

To support this process, each candidate solution is encoded as a vector of design variables

$$\mathbf{x} = [I_D, L_n, L_p, (g_m/I_D)_n, (g_m/I_D)_p, \ldots], \qquad (2)$$

where the exact parameter set depends on the circuit block. For example, the bias block includes the reference voltage V_R, while the differential pair includes tail current I_{tail}.

The device parameters required for circuit evaluation are obtained directly from LUTs, ensuring consistency between optimization variables and physical transistor sizing. Circuit-level metrics are estimated using standard small-signal relations [3], for example

$$A_v \approx g_m \cdot r_o, \qquad \text{GBW} \approx \frac{g_m}{2\pi C_L}, \qquad P \approx V_{DD} \cdot I, \quad (3)$$

where I denotes the relevant block current.

The fitness evaluation enforces feasibility constraints and assigns a scalar score, enabling iterative improvement of candidate solutions. The optimization objective is formulated as a weighted fitness function

$$F(\mathbf{x}) = w_1 \cdot f_P(\mathbf{x}) + w_2 \cdot f_{A_v}(\mathbf{x}) + w_3 \cdot f_{\text{GBW}}(\mathbf{x}), \quad (4)$$

subject to feasibility constraints

$$\mathbf{x} \in \Omega_{\text{valid}}, \qquad (5)$$

where Ω_{valid} enforces operating region, headroom, and geometry constraints.

A typical normalization used in this work is

$$f_P = \frac{P}{P_{\max}}, \quad f_{A_v} = \frac{A_v}{A_{v,\text{target}}}, \quad f_{\text{GBW}} = \frac{\text{GBW}}{\text{GBW}_{\text{target}}}, \qquad (6)$$

allowing direct comparison of competing objectives. A more detailed formulation of the fitness function, chromosome definitions, and constraint handling is provided in [4].

Transistor-level SPICE simulation is used only after optimization for final verification of selected designs. This separation significantly reduces computational cost while preserving accuracy in the final evaluation stage.

4. Case Study: Automated Sizing of Operational Amplifier Building Blocks

To demonstrate the applicability of the proposed framework, the methodology was applied to a two-stage CMOS

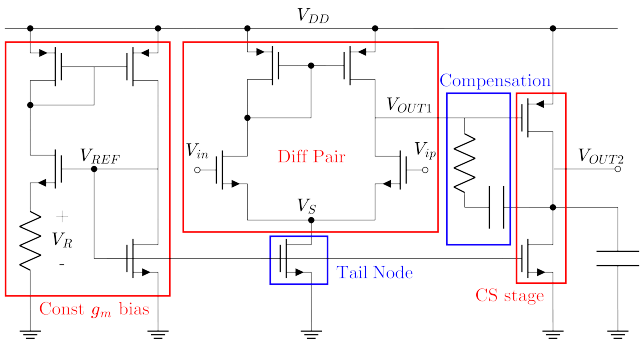

Fig. 3: Op-amp block decomposition with optimized sections highlighted.

operational amplifier decomposed into multiple functional building blocks, as shown in Fig. 3. The optimized blocks include a constant-g_m bias circuit, a MOS differential input pair, and a second-stage common-source amplifier, while auxiliary circuitry is designed conventionally and verified through SPICE.

This modular decomposition reduces the dimensionality of the optimization problem. Each block is optimized independently using the same framework structure, while the chromosome content, feasibility checks, and objective weights are adapted to the specific design task. More detailed block formulations are given in [4].

4.1. Bias Circuit Optimization

For the constant-g_m bias block, the chromosome consists of branch current I_D, channel lengths (L_n, L_p), target $(g_m/I_D)_n$, and reference voltage V_R. The objective is minimum current under valid operating-point constraints.

A representative run used 200 generations with 30 individuals and completed in approximately 10 minutes. The optimized solution operates in weak inversion with

$$I_D \approx 10\ \text{nA}, \quad I_{\text{tot}} \approx 20\ \text{nA}, \quad (g_m/I_D)_n \approx 18.9\ \text{S/A}, \tag{7}$$

demonstrating the ability of the framework to identify ultra-low-power biasing conditions.

4.2. Differential Pair Optimization

For the differential pair, the chromosome is defined as

$$\mathbf{x}_{\text{DP}} = [I_{\text{tail}}, L_n, L_p, (g_m/I_D)_n, (g_m/I_D)_p]. \tag{8}$$

A constrained optimization run (200 generations, 30 individuals, ∼13 minutes) with weights $w_P = 0.7$, $w_{A_v} = 0.2$, and $w_{\text{GBW}} = 0.1$ produced a low-power operating point:

$$I_{\text{tail}} \approx 20\ \text{nA}, \quad A_v \approx 53.9\ \text{dB}, \quad \text{GBW} \approx 30\ \text{kHz}. \tag{9}$$

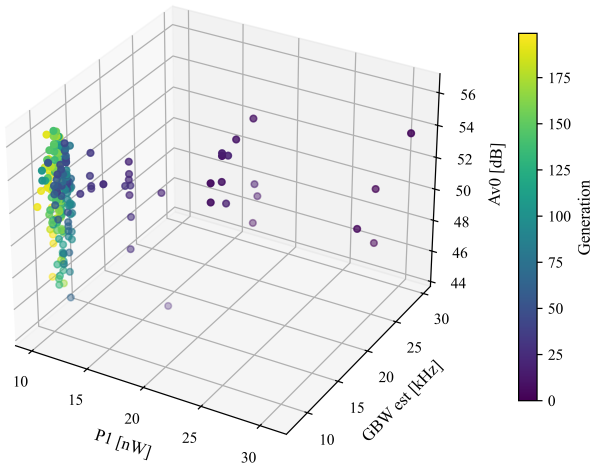

Fig. 4: Evolution of power-oriented GA population in power, GBW, and gain space (color indicates generation).

To explore trade-offs, three optimization modes were evaluated. The evolution of candidate solutions in the power, GBW, and gain space is shown in Fig. 4, illustrating convergence of the genetic algorithm toward a compact region of feasible operating points.

Gain-oriented:

$$A_v = 56.4\ \text{dB}, \quad \text{GBW} = 119\ \text{kHz}, \quad P = 115.6\ \text{nW} \tag{10}$$

with long-channel devices $(L_n = L_p \approx 30\ \mu\text{m})$.

Bandwidth-oriented:

$$A_v = 44.6\ \text{dB}, \quad \text{GBW} = 412.5\ \text{kHz}, \quad P = 399.1\ \text{nW} \tag{11}$$

with shorter devices $(L_n \approx 5.4\ \mu\text{m}, L_p \approx 5.1\ \mu\text{m})$.

Power-oriented:

$$A_v = 46.1\ \text{dB}, \quad \text{GBW} = 10.2\ \text{kHz}, \quad P = 10\ \text{nW} \tag{12}$$

corresponding to ultra-low-current operation.

4.3. Common-Source Stage and Limitations

The common-source stage was optimized under fixed contextual conditions inherited from the surrounding amplifier. In contrast to the previous blocks, this stage exposes a limitation of LUT-based sizing.

While transistor-level parameters can be evaluated locally, the output DC operating point is defined by circuit-level current balance and is not uniquely determined from LUT data alone. As a result, the achieved gain-bandwidth product does not meet the target, despite satisfying bias and gain constraints.

This limitation indicates that purely LUT-based optimization is insufficient for certain circuit topologies and mo-

tivates hybrid approaches combining LUT-based search with targeted SPICE evaluation, as discussed in [4].

The framework explores large discrete design spaces while maintaining practical runtimes, with representative optimization runs converging in approximately 10 to 13 minutes for the considered amplifier blocks.

Overall, the case study demonstrates that the proposed framework enables systematic exploration of design trade-offs across multiple circuit blocks, supports different optimization objectives, and produces physically interpretable solutions within practical runtime.

5. Verification

To validate the accuracy of the proposed framework, representative solutions obtained from the optimization stage were verified using transistor-level SPICE simulations.

Metric	Reference	SPICE	Comparison
Bias Circuit			
I_D	10.0 nA	9.88 nA	1.2%
I_{tot}	20.0 nA	19.6 nA	2.0%
$(g_m/I_D)_n$	18.9 S/A	18.6 S/A	1.6%
g_m	189 nS	184 nS	2.7%
Region	**Subthreshold**	**Subthreshold**	**—**
Differential Pair			
$I_{\mathbf{tail}}$	20.0 nA	19.6 nA	2.0%
g_m	189 nS	181 nS	4.2%
r_o	210 MΩ	190 MΩ	9.5%
A_v	53.9 dB	53.4 dB	0.5 dB
GBW	30 kHz	27 kHz	10.0%
Region	**Subthreshold**	**Subthreshold**	**—**
Common-Source Stage			
I_D	$\leq$ 100 nA	9.15 nA	**within target**
A_v	$\geq$ 50 dB	53.9 dB	**meets target**
GBW	$\geq$ 30 kHz	14.2 kHz	**below target**
Region	**Subthreshold**	**Subthreshold**	**—**

Tab. 1: Verification of LUT-based predictions and GA-optimized designs using SPICE simulation.

For the bias circuit and differential pair, the reference values correspond to LUT-based predictions obtained during the optimization process. The results show strong agreement with SPICE simulation.

While the achieved bias current and DC gain of the common-source stage satisfy the design requirements and the circuit operates in the intended subthreshold region, the gain-bandwidth product does not meet the specified target.

This discrepancy highlights an important limitation of the gm/ID methodology when applied to single-ended gain stages. The gm/ID methodology characterizes device behavior at a given operating point but does not explicitly determine circuit-level DC node voltages. In a common-source stage, the output operating point is defined by current balance, and without explicit output-bias constraints, it cannot be uniquely determined during LUT-based sizing.

As a result, gm/ID-based automation alone is not sufficient to reliably design such stages. For the common-source amplifier, combining the genetic algorithm with transistor-level SPICE evaluation provides more robust operating-point resolution and performance verification, at the cost of increased computational effort.

6. Conclusion

This paper presented a framework for automated analog circuit sizing that combines the gm/ID methodology with genetic-algorithm optimization.

By leveraging pre-characterized device data, the proposed approach enables efficient exploration of large design spaces without repeated circuit simulation inside the optimization loop. The results demonstrate that the method can identify feasible solutions and reveal trade-offs between key performance metrics.

Acknowledgement

This work is based on the author's diploma thesis conducted at National Taiwan University of Science and Technology as part of a double-degree program.

The author would like to thank prof. Po-Ki Chen, prof. Ing. Jiří Jakovenko, Ph.D., and Ing. Dalibor Barri, Ph.D., for their supervision and technical consultations.

References

[1] JESPERS, P. G. A., MURMANN, B. *Systematic Design of Analog CMOS Circuits*. Cambridge: Cambridge University Press, 2017.

[2] HAUPT, R. L., HAUPT, S. E. *Practical Genetic Algorithms*. 2nd ed. Hoboken: Wiley, 2004.

[3] RAZAVI, B. *Design of Analog CMOS Integrated Circuits*. 2nd ed. New York: McGraw-Hill Education, 2017.

[4] FOUKAL, M. *Automated gm/ID-Based Design of Analog Circuits Using Genetic Algorithms*. Master's thesis. Taipei: National Taiwan University of Science and Technology, 2026.

About Authors...

Matej FOUKAL received the M.Sc. degree from National Taiwan University of Science and Technology in January 2026 as part of a double-degree program with the Czech Technical University in Prague, where he is currently pursuing further studies.

Device Simulation of a Fully Interdigitated Bidirectional Phase Control Thyristor

Vojtěch Brandštýl

Dept. of Microelectronics, Czech Technical University, Technická 2, 166 27 Praha, Czech Republic

brandvoj@fel.cvut.cz

Abstract. *This paper presents a 2D TCAD simulation study of an improved, Fully Interdigitated Bidirectional Phase Control Thyristor (BiPCT). In this updated concept, the cathode, anode, and gate regions are interdigitated across the whole active area so both antiparallel thyristors can use the full device surface. The original snowflake-shaped amplifying gate is replaced by hexagonal gate segments, which provide a more uniform layout and support more even triggering. The simulations examine the ON-state behavior, blocking capability, and reverse-recovery process of the device. Both unirradiated and irradiated structures are analyzed to evaluate how irradiation-based lifetime control affects the ON-state performance and the switching-off behavior of the Fully Interdigitated BiPCT.*

Keywords

Thyristor, thyristor circuits, thyristor commutation, TCAD simulation.

1. Introduction

For power converter topologies that use antiparallel-connected Phase Control Thyristors (PCTs), the Bidirectional Phase Control Thyristor (BiPCT) has been introduced as a way to reduce device footprint and improve the performance-to-cost ratio [1]. Recent work has extended this concept to a Fully Interdigitated BiPCT structure, where the cathode, anode, and gate regions are arranged in hexagonal pattern across the entire active area. This layout allows both antiparallel thyristors to use the full device surface through interdigitated anode and cathode, with the anode regions also acting as cathode shorts.

The Fully Interdigitated BiPCT aims to achieve more uniform and faster current spreading and more controlled triggering, which is especially important for high-current operation. In this new concept, the original snowflake-shaped amplifying gate is replaced by distributed amplifying gate realized as hexagonal gate and cathode segments. These segments create a more regular geometry and help support more even turn-on and turn-off thanks to the parallel operation of all segments. The comparison of the two topologies is shown in Fig. 1.

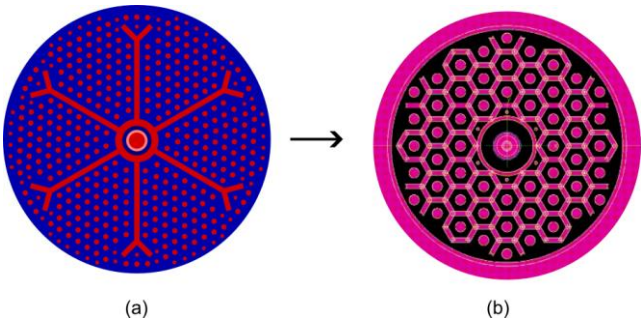

Fig. 1. (a) BiPCT with snowflake topology amplifying gate (b) Fully Interdigitated BiPCT with hexagonal segments.

To better understand the behavior of this improved BiPCT, this work uses 2D TCAD simulations to study its ON-state characteristics, blocking capability, and reverse-recovery process. Both unirradiated and irradiated structures are analyzed.

2. The Device under the Test

The device analyzed in this work is a Fully Interdigitated BiPCT designed for symmetric operation in both current directions. The hexagonal segments contain circular cathode shorts working as anode regions on the opposite surface. The cathode shorts and anode regions are placed in the center of each hexagon. For the purpose of the 2D simulation the hexagonal segment is approximated by a circle segment.

3. Device simulation

For this study, the Fully Interdigitated BiPCT is represented using 2D TCAD simulations. The purpose of the simulation work is to determine suitable dimensions of the anode and cathode regions that enable both turn-on and turn-off operation for unirradiated and irradiated structures, while allowing analysis of ON-state behavior, blocking capability, and the reverse-recovery process. Only one segment of the structure is simulated, using cylindrical

symmetry to reduce computational effort. The simulated structure top view and cross section is depicted in Fig. 2.

Turn-on simulation circuit is depicted in Fig. 3. The ON-state is evaluated by driving the device with a current source I_1 ramped from 0 A to 2000 A. A second current source, I_2, applies a gate current pulse to switch the device ON. For reverse recovery, the current source is replaced by a voltage source set to −200 V. The commutation inductance L_1 defines the rise of current in time *di/dt* during voltage commutation. An RLC snubber is included to limit voltage overshoot during the turn-off process.

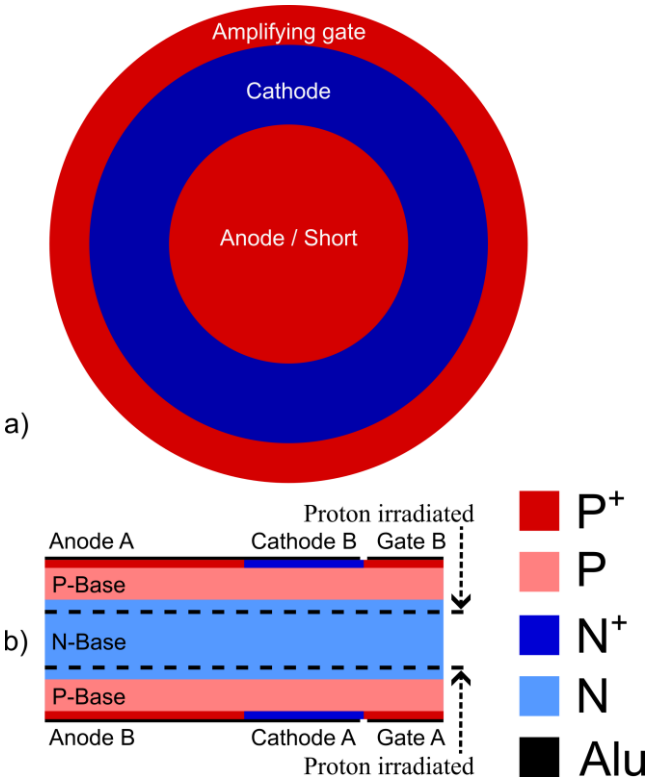

Fig. 2. BiPCT simulated structure. (a) Top view on one circular segment (with the aluminum electrodes hidden). (b) Cross section with doping layers.

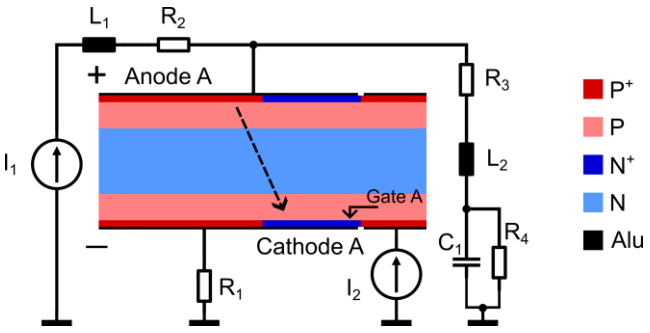

Fig. 3. Turn on simulation circuit.

4. Simulation results

The required forward and reverse blocking capability was evaluated for several BiPCT thicknesses. In all simulated cases, the device achieved a blocking voltage above 4.5 kV, as shown in Fig. 4.

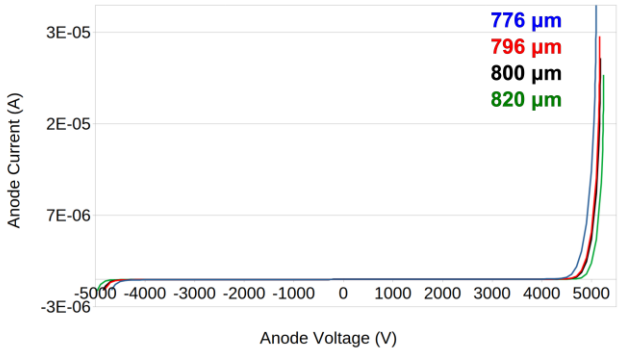

Fig. 4. Voltage blocking characteristics for different thickness.

ON-state performance was analyzed for different cathode-to-anode area ratios. An example of the ON-state plasma distribution is presented in Fig. 5. Tab. 1 summarizes the ON-state voltage and reverse-recovery results. The goal of the simulations is to identify the anode and cathode areas providing lowest ON-state voltage while maintaining reliable turn-off during reverse recovery. The simulations are ongoing, and the final results will be presented in the full paper in greater detail.

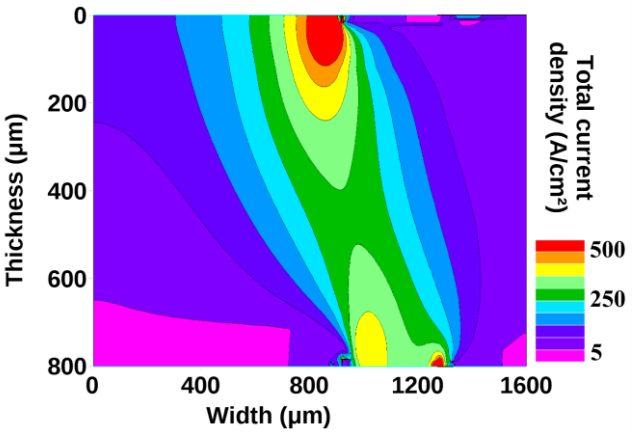

Fig. 5. Total current density of one segment at 2 kA.

Shorted area (%)	Proton Irradiation dose	V_T @ 2 kA (V)	Reverse recovery result
50	UNIRR	3.1	OFF
40	UNIRR	2.6	ON
40	Dose #1	5.7	OFF
35	Dose #1	5.4	OFF
30	Dose #1	5.3	ON
30	2 * Dose #1	13.4	OFF

Tab. 1. ON-state and reverse recovery simulation.

References

[1] J. VOBECKY, The Bidirectional Phase Control Thyristor, *IEEE Trans. on Electron Devices*, vol. 67, no. 7, pp.2844 - 2849, Jul. 2020. doi: 10.1109/TED.2020.29916902.

Gallium oxide photonic devices for on-chip applications

Marek ZDURIENČÍK

Dept. of Physics, University of Žilina, Univerzitna 8215, 01026 Žilina, Slovakia

zduriencik@fyzika.uniza.sk

Abstract. *Gallium oxide has emerged as material from group of ultra-wide bandgap semiconductors with exceptionally large bandgap of 4.8 – 5 eV. Because of the wide bandgap, gallium oxide is transparent in broad range from near-IR to UV spectrum, meaning full transparency in VIS spectrum. Compared to other wide-bandgap material platforms, gallium oxide offers cost effective melt-growth techniques and excellent material stability at high temperatures. From optical perspective, gallium oxide combines low optical absorption with almost lossless nonlinear optical characteristics, making this material attractive for high-power photonics. Motivated by Ga_2O_3 properties and the fact that this field is still relatively young, this work is focused on creating foundation for Ga_2O_3 photonics. Work is focused on design of Ga_2O_3 manufacturing process and development of gallium oxide photonic devices. Presented process was designed to create Ga_2O_3 microstructures with research-grade quality for photonic applications. Prepared structures are the first demonstration of Ga_2O_3 on-chip photonic components. Following characterization will create strong base for Ga_2O_3 as material platform for semiconductor industry.*

Keywords

Gallium oxide, ultra-wide bandgap materials, integrated photonics.

1. Introduction

Gallium oxide is currently widely investigated in electrical engineering for its unique properties. The bandgap of Ga_2O_3 (4.8 eV) [1] is a key parameter for use in power electronics. Despite its poor thermal conductivity and lack of p-doping, Ga_2O_3 has the potential to become a new material platform for electrical engineering. In the field of photonics, Ga_2O_3 has been investigated for its low nonlinearities, birefringence [2], broadband transparency (UV-IR), absorption in the UV region, and refractive index (n~1.95) suitable for integrated photonics [3]. Currently, there is only few studies showing successful preparation of Ga_2O_3 photonic devices. Strip waveguides prepared on Al_2O_3 substrate were investigated for waveguiding purposes and resulting losses reached 3.7 dB/cm. For Ga_2O_3 waveguides prepared on SOI substrate, losses reached 12.7 dB/cm [4]. Ga_2O_3 diffraction gratings showed great performance withstanding high-power laser pulses, suggesting high-power photonic applications [3].

The presented devices were patterned using direct laser writing (DWL) and laser interference lithography (LIL) into photoresist layers. The Ga_2O_3 photonic devices were subsequently fabricated using Ar plasma etching. The resulting photonic devices on the chip were analysed using scanning electron microscopy (SEM), confocal scanning microscopy (CLSM), and atomic force microscopy (AFM).

2. Methodology

In the first step, we simulated the waveguide properties of the structures to confirm their functionality. Simulations of the waveguide structures confirm the good waveguiding performance of the designed Ga_2O_3 elements. The Ga_2O_3 parameters were examined using finite-difference time-domain (FDTD) simulations. Structures with heights ranging from 150 to 200 nm and widths >1 µm were investigated. Air was assumed as the surrounding medium, and the substrate material is Al_2O_3 (n~1.78). The results demonstrate propagation of both fundamental and higher-order modes in the Ga_2O_3 waveguide for wavelengths in the VIS (400 nm and 650 nm) and UV (300 nm) spectra (fig. 1).

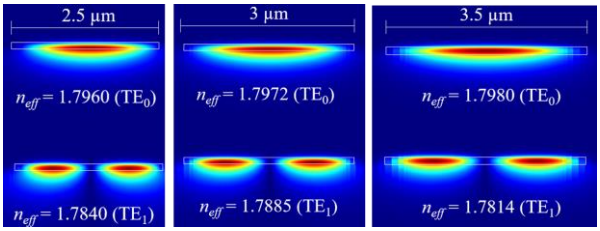

Fig. 1. *The selected optical field simulations: TE_0 and TE_1 modes, propagated through Ga_2O_3 strip waveguides with widths of 2.5 (left), 3 (center), and 3.5 µm (right) and height of 200 nm at an excitation wavelength of 650 nm.*

In the experiments, we used DWL lithography to create strip waveguides as a fundamental element of photonic circuits, which perform the task of signal transmission and connections between parts of the circuit. Subsequently, by modifying the exposed paths, we achieved smooth changes in the direction of the waveguides and thus changes in the direction of radiation propagation. The first Y-branch power splitters were prepared by combining the modified paths. The geometry

of the element was designed so that when the direction of radiation changes, the losses at the bends of the waveguide were as low as possible. Using LIL, Ga_2O_3 diffraction gratings were prepared as a basis to produce coupling elements and gratings on the chip. The same procedure was then applied to already manufactured waveguides to achieve the first ever Ga_2O_3 gratings on the waveguide. Such elements have wide applications in sensors, as spectral filters or as coupling elements. Samples were etched by Ar plasma etching to create physical structure into Ga_2O_3 layers. Following AFM, CLSM, SEM analysis revealed prepared photonic elements.

3. Results

Strip Ga_2O_3 waveguides with height of 180 nm and three different thicknesses (2 µm, 5.5 µm and 7.5 µm) were prepared. Patterning was done by custom-made DLW lithography setup. SEM and CLSM analysis proved functional Ga_2O_3 process (fig. 2). However, high surface roughness was discovered, which can significantly lower the guiding performance of photonic components.

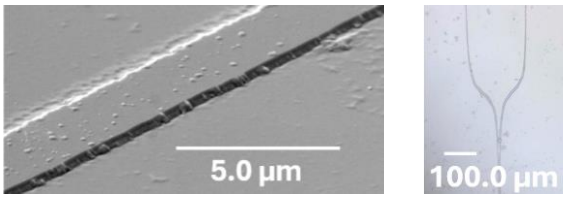

Fig. 2. *SEM image of Ga_2O_3 strip waveguide with width of 7.5 µm and height of 180 nm (left) and CLSM image of Ga_2O_3 power splitter (right).*

Subsequently, LIL was used to pattern Ga_2O_3 diffraction gratings. Adjusted manufacturing process showed increased structures quality. Same process was applied on previously prepared Ga_2O_3 strip waveguides to prepare first Ga_2O_3 gratings on waveguides.

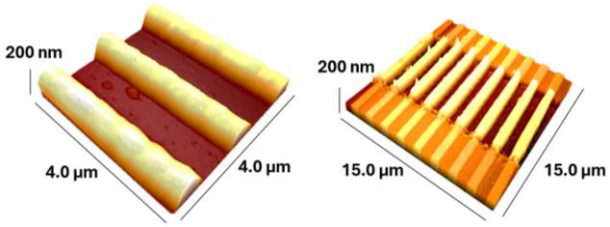

Fig. 3. *AFM image of Ga_2O_3 diffraction grating (left) and grating on waveguide (right) with period of 1.6 µm and height of ≈ 120 nm*

4. Conclusion

Presented work shows the preparation process and the resulting structures of Ga_2O_3 photonic elements. The attached simulations prove the possibility of using Ga_2O_3 for on-chip photonic applications. Analysis of the structures using CLSM, SEM and AFM show the functionality of the manufacturing process, any roughness on the sides of the elements will be removed in the future by an improved process. The prepared elements await detailed optical analysis to determine the loss mechanisms in future on-chip photonic devices. Subsequently, the functional elements will be combined into photonic chips for UV-VIS integrated photonic devices. The presented structures represent a significant advance in the field of Ga_2O_3 photonics and create a strong foundation for a new material platform for electrical and photonic devices.

Acknowledgements

Presented research was supervised by prof. Dušan Pudiš from Department of Physics, University of Žilina. Samples of gallium oxide and etching process was provided by Filip Gucmann, Agata Laurenčíková and Dagmar Gregušová from Institute of Electrical Engineering, Slovak Academy of Sciences. Supporting simulations were performed by Daniel Benedikovič from Department of Multimedia and Information and Communication Technology, University of Žilina.

References

[1] ZHOU, J., CHEN, H., FU, H., FU, K., DENG, X., HUANG, X., YANG, T., MONTES, J., YANG, C., QI, X., ZHANG, B., ZHANG, X., ZHAO, Y. Demonstration of low loss β-Ga2O3 optical waveguides in UV-NIR spectra, *Applied Physics Letter,* vol. 115: 251108, 2019, https://doi.org/10.1063/1.5133845 .

[2] DERESHGI, S. A., LEE, J., CENEDA, D., LARCIPRETE, M. C., CENTINI, M., RAZEGHI, M., AYDIN, K. MOCVD-grown Ga2O3 thin films for polarization-sensitive infrared optics, *APL Mater*, vol. 1, 2024, https://doi.org/10.1063/5.0177705 .

[3] DENG, H., LEEDLE, K. J., MIAO, Y., BLACK, D. S., URBANEK, K. E., McNEUR, J., KOZAK, M., CEBALLOS, A., HOMMERHOLLF, P., SOLGAARD, O., BYER, R. L., HARRIS, J. S. Gallium oxide for high-power optical applications, *Advanced Optical Materials,* vol. 8: 1901522, 2020, https://doi.org/10.1002/adom.201901522 .

[4] HAN, Y., CHEN, W., JIAO, T., YU, H., ZHANG, Z., DONG, X., ZHANG, Y., ZHANG, B. Silicon-based gallium oxide optical waveguide fabricated by MOCVD*, Vacuum,* vol. 238: 114221, 2025, https://doi.org/10.1016/j.vacuum.2025.114221 .

About Author

Marek ZDURIENČÍK was born in Považská Bystrica, Slovakia, in 1999. He completed his secondary education in electrical engineering at the Secondary School of Mechanical Engineering in Považská Bystrica in 2018. He obtained his bachelor's degree in electrical engineering with a specialization in Power Engineering from the University of Žilina in 2022. Subsequently, he pursued a master's degree in electrical engineering with a focus on Photonics, where his research involved grayscale DWL lithography. In 2024, he was awarded his master's degree and began his doctoral studies in Electrical Engineering and Materials at the University of Žilina. His current research is focused on photonics, particularly on the investigation of gallium oxide for photonic applications.

Polymer Waveguides with a Circular Core Shape Fabricated by the Microdosing Method

Lukas VEIGL[1]

[1]Dept. of Microelectronics, Faculty of Electrical Engineering, Czech Technical University in Prague, Technická 2, 166 27 Praha, Czech Republic

veiglluk@fel.cvut.cz

Abstract. *This paper presents the experimental fabrication and characterization of flexible polymer optical channel waveguides, which hold great potential for short-range optical interconnects, sensing, and biomedical applications. The waveguides were fabricated using microdispensing technology (the "Mosquito method") from polydimethylsiloxane (PDMS) elastomers. The LS 6943 polymer was selected as the core material, while Sylgard 184 was used for the optical cladding. The study evaluated the influence of process parameters on the resulting multimode waveguide. Subsequent analysis of optical properties confirmed that the core material consistently exhibits a higher refractive index than the cladding across the monitored spectrum, reliably ensuring the condition of total internal reflection. Furthermore, the selected PDMS elastomers demonstrate high optical transmittance for optical multimode waveguides, fully confirming their suitability for modern optical applications.*

Keywords

Optical waveguide, polydimethylsiloxane, microdispensing method, flexible waveguide.

1. Introduction

Flexible polymer optical waveguides are finding increasingly broader applications in modern sensor and medical fields. The fundamental materials for fabricating polymer waveguides are polydimethylsiloxane (PDMS) elastomers, which offer high elasticity and excellent optical transmittance. The practical potential of biocompatible waveguides has been successfully demonstrated in the treatment of tissue incisions [1].

For the fabrication of channel waveguides, microdispensing technology (often referred to in the literature as the "Mosquito method" [2]) is used, which involves dispensing a liquid core polymer into a liquid cladding polymer. This paper focuses on the experimental fabrication and characterization of optical waveguides using this technology, utilizing the PDMS elastomers LS 6943 and Sylgard 184.

2. Waveguide Fabrication

2.1. Polymer Materials

Two types of PDMS elastomers, namely LS 6943 (NuSil Technology) and Sylgard 184 (Dow Corning), were used to fabricate the optical waveguides. These materials are characterized by excellent flexibility, thermal stability, and high optical transmittance over a broad spectral range [3]. Both polymers are supplied as two-component systems (Part A and Part B) and exhibit similar viscosities, specifically 5400 cP for LS 6943 and 5100 cP for Sylgard 184 [4], [5].

The fundamental prerequisite for the proper functioning of an optical waveguide is to ensure the condition of total internal reflection at the interface, which requires the core material to have a higher refractive index than the cladding material. Based on this condition, the LS 6943 polymer was chosen as the core material, while Sylgard 184 was used for the optical cladding.

2.2. Microdispensing Technology

Microdispensing technology was used to fabricate the channel waveguides. The fabrication principle is schematically illustrated in Fig. 1. Prior to the deposition process, both materials were prepared by mixing components A and B in a specified weight ratio of 10:1. The resulting mixtures were subsequently degassed in a vacuum chamber to eliminate microscopic air bubbles. The process begins with the preparation of a silicone mold placed on a glass substrate, which is filled with a liquid polymer forming the waveguide cladding (in this case, Sylgard 184). Subsequently, the core material (LS 6943) is extruded from a dispensing needle into this liquid cladding under a defined pressure. The precise three-axis movement of the needle is controlled by the stepper motors of the microdispenser [6], while the necessary dispensing pressure is provided by an external dispenser.

The final geometry of the waveguide, particularly its core diameter, depends on the optimization of parameters, primarily the needle scan velocity, the applied dispensing

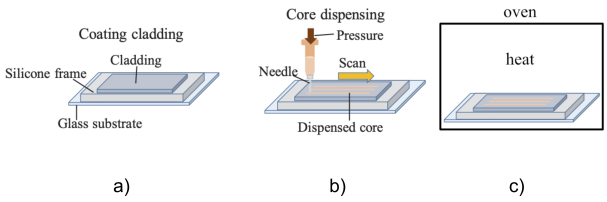

Fig. 1. a) Sylgard 184 mold filled with liquid Sylgard 184, b) writing LS 6943 core layer into liquid Sylgard 184 cladding using microdispenser, c) curing of the LS 6943 channel waveguides and Sylgard 184 cladding layer in the oven.

pressure, and the inner diameter of the used needle [7]. After the core deposition is complete, the entire polymer structure is cured by applying heat in a laboratory oven (in this case, 150 °C for 15 minutes).

3. Results and Discussion

3.1. Fabrication of Optical Channel Waveguides

In the experimental part, optical polymer waveguides were fabricated using microdispensing technology from the aforementioned polymer materials: LS 6943 (core) and Sylgard 184 (cladding). This combination was selected primarily because it satisfies the condition that the refractive index of the core must be greater than that of the cladding, and also because of their similar viscosities. The objective was to optimize the parameters so that the resulting waveguide's core diameter would be approximately 250 µm.

A sample containing five parallel channels was created using the following settings: a channel spacing x = 2 mm, an inner needle diameter D = 0.33 mm, a dispensing pressure p = 1 bar, and a needle scan velocity v = 210 mm/min. Tab. 1 summarizes the diameters d of the individual fabricated channels.

	***d* (µm) for channel no.**				
***v* (mm/min)**	**1**	**2**	**3**	**4**	**5**
210	**363**	**375**	**376**	**378**	**388**

Tab. 1. Diameters of the fabricated optical channels for the combination of LS 6943 (core) and Sylgard 184 (cladding).

The cross-sections of the fabricated waveguide structures were subsequently analyzed using an optical microscope to verify the geometric shape and determine the core diameter (Fig. 2).

The measured values (Tab. 1) indicate that the channel diameters d ranged from 363 µm to 388 µm. The results suggest that to reduce the channel diameter d, future experiments will require either an increase in the needle scan velocity v or a decrease in the applied dispensing pressure p.

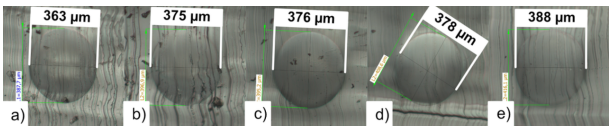

Fig. 2. Microscopic images of the cross-sections of the fabricated waveguide structures: (a) Channel 1, (b) Channel 2, (c) Channel 3, (d) Channel 4, and (e) Channel 5.

3.2. Optical Properties of the Materials Used

To confirm the suitability of the selected elastomers for waveguide applications, their fundamental optical properties, specifically the refractive index n and transmission spectra, were analyzed. For these measurements, bulk samples with size of approximately 15 × 15 mm and between 3 to 4 mm thick were prepared from both polymers. The thickness of the samples was measured using the dial thickness gauge LIMIT12.5/0.001 mm.

The refractive indices RI have been measured using dark-mode spectroscopy with the Metricon 2010/M prism coupler system [8] and the measured refractive index n values for six wavelengths λ (532.0 nm, 654.2 nm, 846.4 nm, 1308.2 nm, 1549.1 nm and 1652.1 nm) are summarized in Tab. 2. These data clearly show that the core material (LS 6943) consistently exhibits a higher refractive index n than the cladding material (Sylgard 184). This ensures that the total internal reflection condition, which is essential for guiding the optical signal, is safely met.

λ (nm)	**$n_{\text{LS 6943}}$ (-)**	**$n_{\text{Sylgard 184}}$ (-)**
532.0	**1.4325**	**1.4154**
654.2	**1.4277**	**1.4107**
846.4	**1.4227**	**1.4064**
1308.2	**1.4183**	**1.4029**
1549.1	**1.4166**	**1.4008**
1652.1	**1.4163**	**1.4006**

Tab. 2. Measured refractive index n values of LS 6943 and Sylgard 184 polymers for selected wavelengths λ.

The continuous dependence of the refractive index n on the wavelength λ (Fig. 3) was subsequently determined by fitting the measured values (from Tab. 2) using the Sellmeier approximation with an infrared correction [9]. This model confirms a stable difference between the refractive indices n of both materials across the entire monitored spectral range.

In addition to the refractive index, the transmittance was also measured on the prepared bulk samples. The measured transmission spectra T of both LS 6943 and Sylgard 184 polymers in the wavelength range from 200 nm to 2200 nm are plotted in Fig. 4. The transmission spectra were measured with a UV-VIS-NIR spectrometer (UV 3600 Shimadzu). The results show that both materials exhibit high optical transmittance across the entire visible and near-infrared spectrum. Both elastomers maintain very good transmittance in the key telecommunication windows around

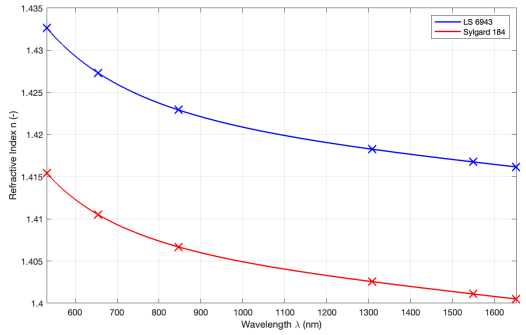

Fig. 3. Refractive index n as a function of wavelength λ for LS 6943 and Sylgard 184.

850 nm and 1300 nm. This fully confirms their suitability for short-range optical interconnects.

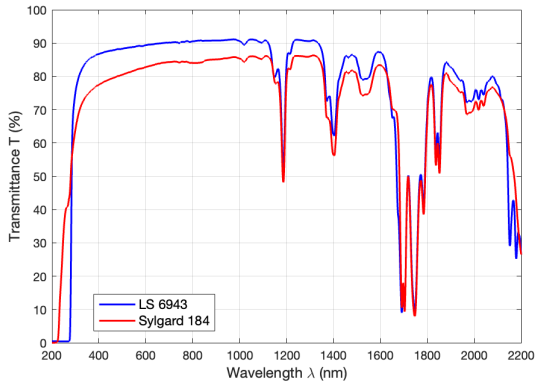

Fig. 4. Transmission spectra measured on bulk samples of LS 6943 (thickness 3.353 mm) and Sylgard 184 (thickness 3.254 mm).

4. Conclusion

In this work, flexible optical channel waveguides were successfully fabricated using microdispensing technology with two PDMS-based elastomers: LS 6943 (core) and Sylgard 184 (cladding). Under the current process parameter settings, core diameters ranging from 363 µm to 388 µm were achieved. To reach the target diameter of 250 µm, further process optimization will be required in the future, specifically by increasing the needle scan velocity or decreasing the dispensing pressure. The optical properties confirmed the suitability of this material combination. The LS 6943 core consistently has a higher refractive index than the cladding, which ensures the condition for total internal reflection. Combined with high transmittance across the entire visible and near-infrared spectrum—particularly in the key telecommunication windows of 850 nm and 1300 nm—these results fully confirm the potential of the fabricated waveguides for the realization of short-range optical interconnects.

References

[1] NIZAMOGLU, S., et al. Bioabsorbable polymer optical waveguides for deep-tissue photomedicine. *Nature Communications*, 2016, vol. 7, p. 10374.

[2] FARUK RASEL, O., ISHIGURE, T. Circular core single-mode 3-dimensional crossover polymer waveguides fabricated with the Mosquito method. *Optics Express*, 2019, vol. 27, no. 22, p. 32465 – 32479.

[3] PRAJZLER, V., CHLUPATY, V., NERUDA, M. Circular large core optical elastomer waveguides fabricated by using direct microdispense fabrication method. *Optik*, 2022, vol. 250, no. 1, p. 168348.

[4] NUSIL TECHNOLOGY. *LS 6943 datasheet*. 2023.

[5] DOW CORNING. *Sylgard 184 datasheet*. 2023.

[6] CHLUPATY, V. *Preparation and measurement of optical polymer waveguides for photonic applications* (in Czech). Master's thesis. Prague: Czech Technical University in Prague, 2021.

[7] SOMA, K., ISHIGURE, T. Fabrication of a graded-index circular-core polymer parallel optical waveguide using a microdispenser for a high-density optical printed circuit board. *IEEE Journal of Selected Topics in Quantum Electronics*, 2013, vol. 19, no. 2, p. 3600310.

[8] PRAJZLER, V., CHLUPATY, V., SARSOUNOVA, Z. The effect of gamma-ray irradiation on bulk optical plastic materials. *Journal of Materials Science: Materials in Electronics*, 2020, vol. 31, no. 24, p. 22599 – 22615.

[9] DE BEUCKELAER, S. *Study of the properties of optical polymer materials and the possibilities of sterilization by gamma radiation* (in Czech). Bachelor's thesis. Prague: Czech Technical University in Prague, 2022.

About Authors...

Lukas VEIGL was born in the Czech Republic in 2001. He is currently a Master's degree student at the Faculty of Electrical Engineering, Czech Technical University in Prague.

Testing a New Generation of Hardpix2 Devices Using the Timepix2 Detector at the CERN PS Beam

Ondrej Pavlas [1,2]

[1]Institute of Experimental and Applied Physics Czech Technical University in Prague, 110 00 Prague, Czech Republic
[2]Faculty of Electrical Engineering, Czech Technical University in Prague, 166 27 Prague, Czech Republic

ondrej.pavlas@cvut.cz

Abstract. *We present the testing of a new-generation device, Hardpix2, developed as an improved successor to the first-generation Hardpix device, which was used in four space missions. The device features a newly designed mainboard based on a Zynq UltraScale+ MPSoC, enabling higher performance, improved data processing capabilities, and more flexible system integration. The system employs a modular architecture in which a hybrid pixel detector is integrated. From an architectural perspective, the system is designed to support detectors from the hybrid pixel detector family, such as Timepix2, Timepix3 and, in the future, Timepix4. The complete setup was tested at the Proton Synchrotron accelerator at CERN. During the testing campaign, the response of the Timepix2 detector to particle interactions was studied.*

Keywords

Electronic Design, Hybrid Pixel Detectors, System-on-Chip (SoC), Particle Tracking

1. Introduction

The development of the next-generation Hardpix2 device is based on the experience gained from the first-generation Hardpix device [1]. The Hardpix2 design concept is based on a modular architecture and the overall structure of the first-generation device. The success of the Hardpix device is demonstrated by its deployment in a total of four devices in space missions (SWIMMR1 and SWIMMR2 (STFC/D-Orbit) and HEKI (two devices)). The primary motivation for the new generation is the increasing demand for on-board data processing and faster readout of measurements from the new generations of hybrid pixel detectors.

2. System Architecture

The modular architecture was preserved from the first generation of the Hardpix device. In the following sections, the internal architecture of the individual system boards will be explained. An overview of the system used for the measurements is shown in Fig. 1.

The Hardpix2 device consists of three printed circuit boards (PCBs). The first board, the communication module, hosts the design and implementation of the interface required for a specific mission application. Examples of such interfaces include 100 Mbit Ethernet, RS-422, CAN (Controller Area Network) bus, and others. Unless otherwise stated, the communication board discussed in this work uses an Ethernet interface. The communication module is connected to the mainboard via a 70-pin board-to-board connector with a height of 3 mm.

The mainboard houses the Zynq Ultrascale+ MPSoC, which controls the operation of the entire device. All required power rails for the MPSoC are implemented on this board. The mainboard also contains 8 Gbit of LPDDR4 memory, 64 MB of flash memory, and two connectors for attaching chipboards. In the current configuration, the chipboard hosts a hybrid Timepix2 detector [2] developed within the CERN Medipix Collaboration. The system is also compatible with a Timepix3 detector variant; however, in the remainder of this text, only the Timepix2 variant is considered. In the current architecture, two chipboards can be used simultaneously.

The chipboard integrates a hybrid pixel detector Timepix2. The detector consists of a 256×256 pixel matrix capable of simultaneously measuring the energy and time of ionizing radiation interactions in the sensor layer. In this work, a Timepix2 chip with a 500 μm silicon sensor was used. The board includes a high-voltage bias supply (0–150 V) for the sensor based on the MAX1932. Current monitoring is implemented using INA138 for the high-voltage section and INA240 for the Timepix2 power supply. A TMP100 temperature sensor and an AD7991 ADC (Analog-to-Digital Converter) are also integrated on the board.

3. Timepix2

Timepix2, developed within the Medipix2 collaboration, is a 256×256 pixel hybrid detector with $55\ \mu\mathrm{m}$ pitch. Each pixel simultaneously measures Time-over-Threshold (ToT) and Time-of-Arrival (ToA). The analog front-end supports adaptive gain and per-pixel threshold adjustment via a 5-bit discriminator and global DACs (Digital-to-Analog Converters). Individual pixels can be masked to reduce power consumption from μA to nA. The digital front-end features 10- and 4-bit counters that support simultaneous or continuous acquisition. Dead time ranges from 6.6 to 18.5 ms at 100 MHz. ToT and ToA clocks are independently configurable, optimizing energy and timing resolution. A Matrix Occupation Monitor prevents overexposure by terminating acquisition when pixel occupancy exceeds a set column threshold.

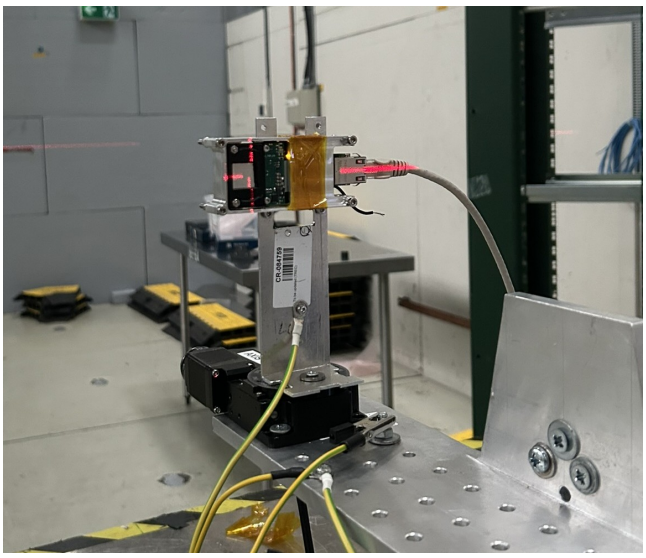

Fig. 1: Measurment setup with Harpidx2 at the CERN Proton Synchrotron beam

4. Functional Testing

4.1. Measurement setup

The detector was tested at the CERN Proton Synchrotron (PS) under realistic hadron beam conditions (15 GeV/c, 90% pions), with 400 ms spills separated by approximately 20 s. It was mounted on a precision rotation stage, adjustable in 1° increments (Fig. 1), enabling systematic measurements at multiple angles to study the angular response of detector.

A Timepix2 detector with a 500 μm silicon sensor was operated at a bias voltage of 110 V in digital ToA18/ToT10 mode with an acquisition time of 5 s. Column Trigger mode with a 200-column threshold prevented frame oversaturation. The detector was oriented at 90° relative to its normal, so particles interacted parallel to the pixel columns, allowing more tracks per frame at larger rotation angles, as shown in Fig. 3.

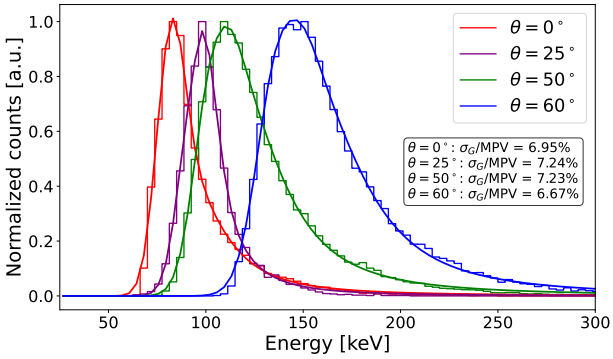

Fig. 2: Comparison of energy deposition spectra measured at different hadron impact angles relative to the sensor normal. The spectra were fitted with a Landau convoluted with a Gaussian function

4.2. Data analysis

The dependence of the deposited energy on the detector's rotation angle was quantitatively evaluated and is presented in Fig. 2. Measurements were in adaptive gain mode of the Timepix2 detector to assess the influence of gain settings on detector performance. Across all tested angles, adaptive gain modes exhibited a consistent relative energy resolution of approximately 8%. For each specific rotation angle θ, only particle tracks whose cluster lengths fell within a selected interval were considered, ensuring that the measured dependence was not affected by secondary particle tracks. An additional condition was that the selected tracks had the same orientation.

5. Result and Future Work

The functionality of the Hardpix2 device was tested in a high-energy physics environment at the CERN Proton Synchrotron (PS). Using a Timepix2 detector, the dependence of the energy deposited in the sensor layer on the detector's rotation angle relative to the incoming particles was measured.

Future work will focus on characterizing the entire system in terms of performance, particularly its capability for on-board data processing. Additionally, emphasis will be placed on integrating the latest hybrid pixel detector developed within the Medipix collaboration, Timepix4.

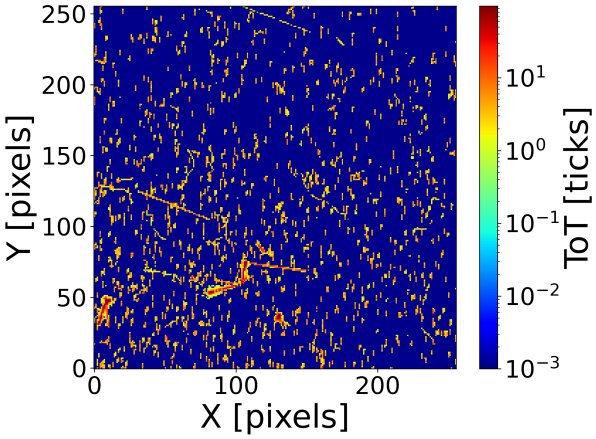

(a) Rotation 25°

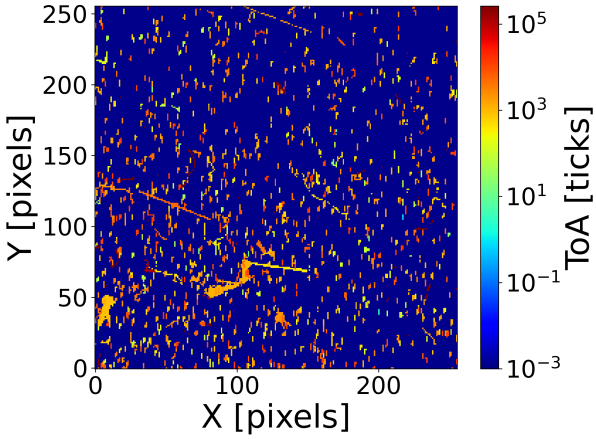

(b) Rotation 25°

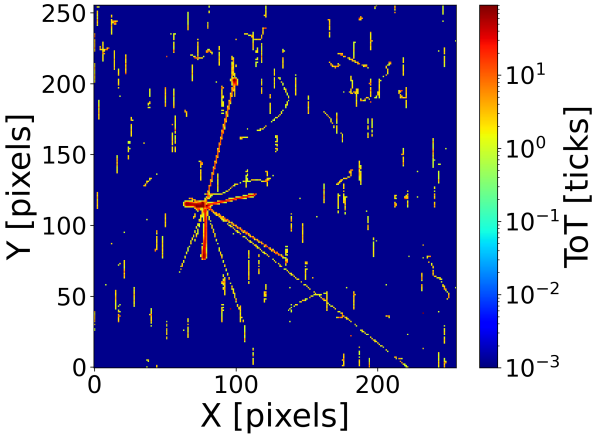

(c) Rotation 60°

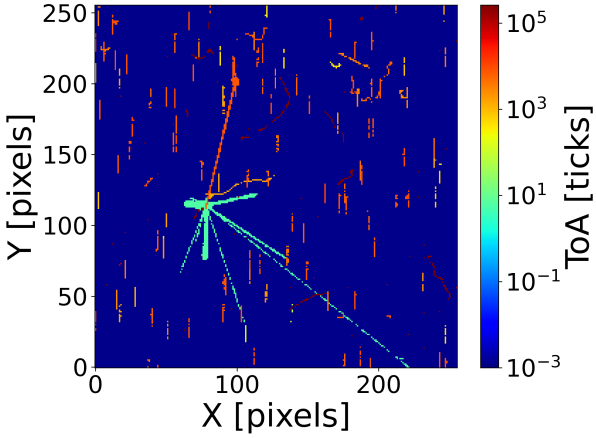

(d) Rotation 60°

Fig. 3: Time-over-Threshold (ToT, left) and Time-of-Arrival (ToA, right) responses of the Timepix2 detector exposed to hadrons at different incidence angles in the CERN Proton Synchrotron beam.

Acknowledgements

We thank the Medipix2 collaboration for developing and providing the Timepix2 ASIC. We are grateful for the support of the PS/SPS coordinators, operators, and technicians

References

[1] R. Filgas, M. Malich, S. Pospíšil, B. Bergmann, T. Slavíček, and A. Calzada-Diaz, "Miniature semiconductor neutron spectrometer hardpix for surface mapping of lunar water," *Acta Astronautica*, vol. 200, pp. 620–625, 2022.

[2] W. Wong, J. Alozy, R. Ballabriga, M. Campbell, I. Kremastiotis, X. Llopart, T. Poikela, V. Sriskaran, L. Tlustos, and D. Turecek, "Introducing timepix2, a frame-based pixel detector readout asic measuring energy deposition and arrival time," *Radiation Measurements*, vol. 131, p. 106230, 2020.

Coal Mining Technologies and the Transformation of the Industrial Landscape: The Ostrava–Karviná Region from the Late 19th Century to Contemporary Conversion

Klára CIESAROVÁ[1]

[1] Dept. of Architecture, Faculty of Civil Engineering, Czech Technical University, Thákurova 7, 166 29, Prague, Czech Republic

klara.ciesarova@fsv.cvut.cz

Abstract *The paper focuses on how coal extraction and processing technologies have long shaped the industrial landscape, its spatial structure, social organization, and environmental burdens. Coal is seen here not just as an energy source or raw material, but as a technological and socio-material system that has fundamentally changed landscapes, cities, and daily life in industrial regions.*

The theoretical framework draws on traditions of historical and cultural geography as well as on the history of technology and material history, which makes it possible to conceptualize the industrial landscape as a technologically shaped space composed of „layered temporal structures" that persist even after the end of mining.

The empirical part is based on the analysis of archival and cartographic sources, urban planning documents, and visual materials, tracing landscape transformations from the 19th century through the period of mining decline. The research is conducted comparatively, placing the Ostrava–Karviná region within a wider European context by comparing it to the Ruhr area.

Keywords

Industrial landscape, coal mining technologies, Ostrava–Karviná mining region, post-mining landscape transformation, Ruhr region.

1. Introduction

An industrial landscape can be understood as a space shaped by culture and technology, where extraction, production, and infrastructure transform territory, labor, and everyday life over time[1].Vidal de la Blache conceptualised such landscapes as milieus in which technical systems and labour co-define ways of life, while railways, roads and factories reorganise movement, settlement and class structures[2]. Drawing on Schlögel, industrial landscapes can be read as spatial archives—palimpsests in which "in space we read time," accumulating layers of power, economy, and daily practice [3] [4]. Within the history of technology and material history, mining history emerged from mining science and focused on mining as an economic sector, later expanding to social history topics such as class, strikes, and state–labour–capital relations. Since the late 20th century, however, it has increasingly integrated material studies, Anthropocene debates, and global history, treating mining as a techno-natural system that shapes and is shaped by landscapes, societies, and climate. The concept of a techno-natural system characterizes mining as a complex of technology and nature, rather than as purely human or purely natural [5]. Building on this techno-natural understanding of technology and material history, Weber criticizes innovation-centric narratives and calls for "following technology through time," beyond first use into repair, reuse, and "after-use" phases in which outdated technologies persist [6],[7]. These extended trajectories generate ruins, scrap, and pollution in landscapes and "ghost towns," giving technologies multilayered temporalities and "afterlives that demand long-term 'aftercare" (remediation, monitoring, heritage management), directly resonating with debates on post-industrial landscapes and coal-region transitions [6].

2. Coal Technologies and the Making of the Ostrava–Karviná Landscape Introduction

An industrial landscape can be understood as a space shaped byThe Ostrava-Karviná Mining District (OKMD) is in the north-east of the Czech Republic (Moravian-Silesian Region), forming the Czech part of the Upper Silesian Coal Basin near the Polish (and relatively close to the Slovak) border. It covers about 320 km of coalfield within a roughly 1 600 km basin protrusion, centred on Ostrava and extending east towards Bohumín,

Orlová, Karviná, Petřvald and Havířov [8] [9]. Black coal was discovered near Ostrava and Karviná in the mid-18th century, but regular mining began in the 1780s and remained small-scale until industrialisation. The key impulses were the Vítkovice ironworks (1828) and the Ostrava–Bohumín railway (1847), which transformed an agricultural region into a major coal-industrial zone. By the early 20th century, the Ostrava-- Karviná district produced most of Czech black coal and underpinned heavy industry in Austria-Hungary and Czechoslovakia. After 1945, it became the socialist "steel heart of the republic" [8]. From the 1990s, deep mining in the Ostrava part declined, and production shifted eastward to a few mines in the Karviná part of OKMD. Coal extraction in the Czech Republic concluded after over 250 years of continuous mining, with the ČSM mine in Karviná closing in early February 2026.

2.1 Mapping Mining Landscapes: Methods and Key Dimensions of Landscape Transformation

In addition to written historical sources, landscape changes can be traceable via historical and aerial maps. These maps enable the mapping of the impacts of mining technologies over time and document the gradual transformation of the territory reconfigured. The following text draws primarily on data generated within the multi-year research project *Black or Green: Industrialisation and Landscape Changes of the Ostrava–Karviná Mining District in the 19th and 20th Century* (GAČR P410/12/0487), funded by the Czech Science Foundation and conducted by P. Popelka, R. Popelková and M. Mulková [8]. It is further complemented by the author's own analysis of archival and cartographic materials, urban planning documents and visual sources, extending the investigation beyond 2009 to capture the most recent phase of post-mining transformation

Coal mining profoundly reshaped the landscape, particularly through geomorphological changes. Its main surface features comprised waste heaps, subsidence depressions, tailings ponds, and mining structures. Later developments included reclaimed sites, dried tailings basins, and landscape modifications due to transport infrastructure. The extent of landscape change primarily depended on extraction volume, mining methods, and coal seam thickness [8], [9]. For the purposes of this text, however, the analysis focuses primarily on three key elements of this transformation: waste heaps, subsidence areas, and the reconfiguration of the urban fabric.

2.2 Evolution of Coal Mining Technologies in in the OKMD (19th–20th Century)

The crucial development in OKMD coal mining technologies was the transition from small, shallow mines to extensive, mechanized deep mining, closely linked to coking and metallurgy. Early extraction relied on shallow pits and primitive shaft/entry workings (30-40 m), limiting both output and spatial impact. In the 1830s and 1840s, the gradual extraction of coal seams above existing haulage and drainage adits and shallow shafts in the Ostrava district led to the establishment of the first deep mines (e. g. Anselm/Eduard Urx, 1835). It essentially combined shaft mining with deep mining, reaching a final depth of approximately 120 metres. Starting in the 1830s, deep mining led to a distinction between the western Ostrava part and the eastern Karviná, where deep mines began operating later, in the 1850s. The primary factor behind this was the establishment of the Vítkovice ironworks in Moravian Ostrava (1828), coinciding with the arrival of the Emperor Ferdinand Northern Railway to Ostrava–Bohumín in 1847. In comparison, the Karviná part only received the Košice–Bohumín line and its sidings in the late 1860s and 1870s. By the 1890s, many mines worked to c. 600 m, using pillar/barrier systems and early longwall with hand filling. From the mid-20th century, electrification and mechanisation enabled longwall mining with controlled caving at depths averaging 930 m by the 2000s. [10] These shifts increased production from thousands of tonnes to over 9.8 Mt by 1913 and more than 20 Mt by 1960, then contracted after 1989 [11].

2.3 Waste Heaps

The most distinctive anthropogenic landforms in the OKMD mining landscape are waste heaps—convex formations created by waste rock from deep coal mining. Their sizes range from small mounds of a few ares to extensive bodies covering over 100 hectares in exceptional cases. With the expansion of deep mining in the late 19th and early 20th centuries, large cone-shaped spoil heaps rose beside shafts and coking plants, becoming powerful symbols of industrial environmental damage. In the 1950s, however, cone heaps were officially banned due to frequent internal fires and significant air pollution. New dumping technologies produced flat, terraced heaps, and policy shifted toward fewer, larger central waste banks in already devastated zones. After 1989, the decline of mining ceased new tipping, and many sites were reclaimed, often through afforestation or adaptive reuse [8], [12].

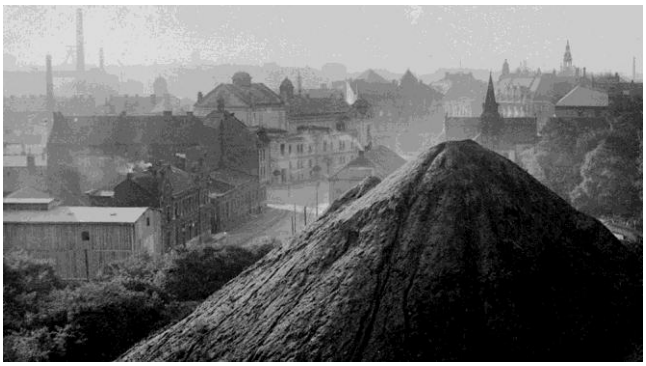

Fig. 1. View of the waste heap at today's Černá louka in the early 20th century (Antonín Dvořák Theatre in the background).

2.4 Submerged Ground Subsidence

Submerged ground subsidence began to appear locally in the late 19th and early 20th centuries, where shallow, poorly back-filled seams caused rapid ground collapse and waterlogging, but they were limited in extent and only sporadically recorded before systematic monitoring started in 1956. It was particularly severe in the Karviná part, where total subsidence locally reached up to 40 m (compared to about 20 m in Ostrava). Iconic examples include the Church of St. Peter of Alcantara (33 m) or the Silesian Ostrava castle (14 m). By 2000, roughly 80 % of the mining area (about 255 km²) had been affected by subsidence. Early, shallow room-and-pillar mining without backfilling led to rapid, severe surface collapse, sometimes within days of extraction. Protective pillars were implemented selectively, primarily beneath central Moravian Ostrava. Elsewhere, limited security measures and intense extraction led to surface destruction, settlement disturbances, and agricultural harm, notably in the Karviná part of OKMD. In the Ostrava part, subsidence was concentrated and addressed earlier in the historic core; following collapses and gas outbursts in the 19th century, a substantial protective pillar was constructed in 1888, later covering 120 hectares, protecting the city center and blocking the mining of 30.3 million tonnes of coal. In contrast, much of Karviná lacked such protection, resulting in significant losses of urban and rural areas to mining activity[8].

Fig. 2. Landscape transformation caused by mining subsidence near the Barbora Mine in Karviná-Doly, showing the loss of urban fabric and the return of agricultural land use (1947–2024).

2.5 Urban Fabric

In the early 19th century, the Ostrava–Karviná basin was mainly agricultural, with over 75% of land used for farming. Deep coal mining altered both regions, but with different results. In Ostrava, mining and the rise of the Vítkovice ironworks caused rapid urban growth. Agricultural land near pits and steelworks was replaced by workers' colonies, factories, and railways; by the 1970s, farmland made up just over 13%. Mining mainly urbanised the countryside: fields turned into streets, industrial sites, and housing, while the historic city center remained largely intact. In contrast, the Karviná region maintained a predominantly agrarian character for a longer period, with over 60% of its land still used for agriculture in the late 1940s. However, intense post-war extraction in deep seams caused widespread subsidence, the creation of tailings ponds, and flooding of depressions, especially in Karviná-Doly and nearby settlements. Fields were destroyed or reclassified, entire neighbourhoods were demolished, and populations were relocated to newly built housing estates. By the turn of the 21st century, former mining cores had become largely de-urbanised, semi-natural post-mining landscapes dominated by forests, scrub and water bodies[8].

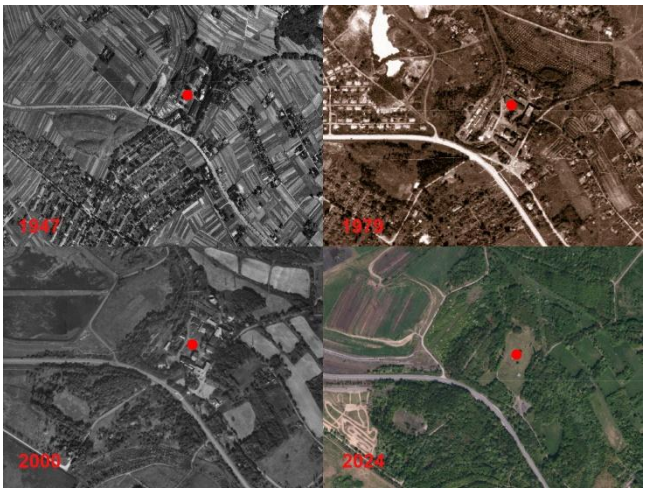

Fig. 3. Urban fabric transformation around the Jindřich Mine in Karviná-Doly (1947–2024).

3. Post-Mining Transformations and Landscape Persistence

After 1989, coal mining in the OKMD declined as the economic and political framework collapsed. The shift from a planned economy led to deregulation, the loss of COMECON markets, and reduced state subsidies, making many deep mines unprofitable amid declining demand from heavy industry. Lower-cost Polish coal increased competition, resulting in the closure of unprofitable mining operations. Additionally, geological exhaustion, rising extraction costs, and stricter environmental regulations accelerated the contraction of the coal sector [5], [8], [12]. In the OKMD, closures began in the older Ostrava pits (late 1960s, decisively 1991–95), after which production shifted east to Karviná. Mining definitely ended in early February 2026 with the closure of the last operating mine, ČSM mine in Karviná, concluding more than two centuries of coal extraction in the region and the Czech Republic.

Although coal extraction gradually ceased at the end of the 20th century, not all physical structures of coal mining technologies have disappeared; instead, they have entered the "after-use and after-care phase" that continues to shape the region's spatial form and identity [6]. For example, a

former waste heap at Doubrava now hosts DinoPark Ostrava, while the still-burning Ema heap has become a protected cultural monument and a popular viewpoint, valued for its distinctive thermophilic vegetation and fauna. Over time, spoil heaps thus transformed from unwanted industrial residues into key morphological, ecological, and cultural elements of the post-mining landscape. Since the mid-20th century, systematic monitoring of submerged ground subsidences has started. Many subsidence basins were filled with water, while some served for slurry or ash disposal. Others were later reclaimed or repurposed for leisure activities, although considerable areas of submerged and often contaminated depressions remained [8]. While mining in Ostrava turned farmland into a dense industrial city, in Karviná it erased agricultural land and historic settlements, leaving a fragmented, partly abandoned post-mining landscape [8]. This condition is particularly evident in Karviná-Doly, an exceptionally compact and spatially well-defined example of a hard-coal mining landscape whose geomorphology has been transformed on a scale of European significance. In this area, pre-industrial, industrial, and post-industrial layers overlap closely, and efforts are ongoing to establish formal heritage protection to recognize their unique cultural significance [13].

3.1 Two Trajectories of Post-Mining Transformation: Culture-Led Regeneration and Persistent Mining Landscapes

Within this broader pattern, two contrasting trajectories of post-mining transformation in the OKDM have crystallised: intensive inner-city regeneration of selected complexes, and the large-scale persistence of mining landscape. In Ostrava, the flagship of the first trajectory is Dolní oblast Vítkovice (DOV), an integrated mine–coke–iron complex that ceased production in 1998. Although demolition was considered, the site was declared a national cultural monument in 2002 and later, through culture-led regeneration, transformed into a multifunctional urban and cultural complex, despite criticism regarding sustainability and land use [12]. European examples include Zeche Zollverein and Landschaftspark Duisburg-Nord in Germany's Ruhr area or coal basin complexes in Belgium.

The second trajectory—the persistence of a post-mining landscape at territorial scale—is most clearly visible in Karviná-Doly. High-resolution analyses reveal preserved traces of the vanished town, its mines (including Gabriela and Barbora) and rail trails embedded in a relief reshaped by undermining. This exceptionally compact and legible ensemble is interpreted as a hard-coal mining landscape of European significance and is increasingly viewed not merely as a brownfield, but as a field laboratory of mining-induced transformation and a candidate for integrated heritage protection [13]. Several European mining regions—such as the Nord-Pas-de-Calais basin, Kopparbergslagen in Sweden and the Erzgebirge/Krušnohoří—have been inscribed by UNESCO as large-scale mining cultural landscapes rather than isolated sites. The Ruhr region has likewise been conceptualised as an integrated industrial landscape, often cited as a reference when arguing that the compact and legible landscape of Karviná-Doly merits similar landscape-based protection [5], [13].

4. Comparative Perspective: Ostrava–Karviná and the Ruhr Area

Both the Ruhr and Ostrava–Karviná are classic hard-coal heartlands where deep-shaft mining, coking and steel production formed tightly integrated coal–coke–steel systems that drove rapid urbanisation. In each case, longwall mining and heavy industry produced comparable anthropogenic landforms – large spoil heaps, extensive subsidence basins (often flooded), and mostly in the Ruhr region over-dimensioned rail and canal corridors – so that mining technology became a geomorphological agent in its own right [6], [8], [14], [15]. Compared with the OKMD, the Ruhr's inner belt functions more as a continuous "industrial city": a broad, polycentric and largely built-up urban strip. By contrast, OKMD remains a patchwork of dense urban nodes, former mining sites, farmland and regenerating areas, particularly east of Ostrava [8], [16]. In the Ruhr, non-urban land is relatively clearly structured into agricultural and forest belts around the metropolitan core. In OKMD, however, open land is more fragmented, mixing remnant farmland with secondary "industrial nature" on waste heaps, subsidence lakes, and abandoned plots within the coalfield itself. While the Ruhr is characterised by continuous chains of dense blocks and industrial quarters, OKMD combines a compact socialist metropolis (Ostrava, Havířov, Karviná) with smaller towns and dispersed miners' colonies embedded in post-mining and rural landscapes [8], [15].

Fig. 4. Regenerated industrial sites: Landschaftspark Duisburg-Nord (left) and Lower Vítkovice, Ostrava (right).

The sharpest divergence between the two regions lies in the political-economic framing of post-mining transformation, which has directly shaped their heritage regimes. In the Ruhr, the coal crisis of the late 1950s initiated a long-term, state-steered restructuring within the framework of Rhenish capitalism. The creation of Ruhrkohle AG (RAG) and successive regional programmes, supported by strong cooperation between firms, unions, and government, cushioned social impacts and created conditions for coordinated regeneration. The IBA Emscher Park (1989–1999) became emblematic of this approach, combining landscape planning, river renaturalisation, and adaptive reuse of major industrial sites, reframing coal infrastructure as a cultural and economic asset [14], [17] [18]. By contrast, OKMD underwent a rapid post-socialist restructuring after 1989. Loss-making mines were quickly

closed, ownership fragmented, and institutional support for regional coordination was comparatively weak. Regeneration in OKMD has generally proceeded through site-specific projects—Dolní Vítkovice (DOV) being the most prominent example—rather than as part of a comprehensive regional strategy. More integrated, landscape-scale approaches are only recently emerging, particularly in post-mining concepts for Karviná. The main challenges of culture-led and „Industriekultur“ regeneration include the potential for touristification and “Disneyfication,” where branding and nostalgia take precedence over issues like labor conflicts, environmental damage and social injustice, weakening critical historical and technological significance of these projects [18]. In Ostrava, however, the later timing of regeneration and the work of heritage professionals—together with lessons drawn from the Ruhr—have helped preserve authenticity to a certain degree. This is particularly evident at the Michal Mine —while at DOV, increasing adaptations raise concerns about a gradual loss of technological flow value, although the emerging industrial museum in the former blast furnaces may help sustain this dimension. Karviná-Doly offers an essential chance to maintain a clearer and more cohesive post-mining landscape, as long as it intentionally incorporates lessons learned from previous regeneration projects.

5. Conclusion

This paper argues that coal mining functions as a techno-natural system, whose extraction, transport, and processing technologies have continually transformed the spatial arrangements, social organization, and environmental impacts of coal-mining regions, with a focus on the Ostrava–Karviná region. These effects often remain layered in time long after production has ceased. Drawing on Weber’s call to “follow technologies through time” and combining this perspective with archival, cartographic, and planning analysis, the study traces how spoil heaps, subsidences, and infrastructures have both transformed over time and endured as material afterlives that continue to organise and structure the post-mining landscape. In comparison with the Ruhr, it shows how shared coal-based socio-technical logics can lead to divergent regimes of remediation and reuse depending on political-economic frameworks. The paper supports the thesis that industrial heritage is not merely a collection of iconic sites, but can also act as a dynamic cultural landscape. Its palimpsest character and techno-environmental legacies call for landscape-scale conservation and more socially grounded, critical models of regeneration that move beyond purely consumptive or spectacle-driven approaches.

Acknowledgements

Research described in the paper was supervised by Assoc. Prof. Lenka Popelová, PhD, FCE CTU in Prague, and by Prof. Marcela Emfertová CSc, FEE CTU in Prague, and supported by the Czech Grant Agency under grant No. 102/01/9999, by the Czech Ministry of Education under grant No. 9999/2024 and by the research program MSM 444222. The research discussed in the paper is also part of the NAKI III project (*Active Conservation of Immovable Industrial Heritage Through New Uses, 2023–2027*) at the Architecture Department, FCE CTU in Prague.

References

[1] PALMER, M., NEAVERSON, P. *Industrial Archaeology - Principles and Practice*, 1. London and New York: Routledge, 1998.

[2] VIDAL DE LA BLACHE, P. *Principles of Human Geography*, 8th edn. London: Constable Publishers London, 1965.

[3] SCHLÖGEL, K. Introduction. In *In Space We Read Time: On the History of Civilization and Geopolitics*. New York: Bard Graduate Center, 2016, pp. 23–30.

[4] SCHLÖGEL, K. Landscapes, Reliefs. In *In Space We Read Time: On the History of Civilization and Geopolitics*. New York: Bard Graduate Center, 2016, pp. 303–312.

[5] BLUMA, L., FARRENKOPF, M., MEYER, T. Introduction: “King Coal” and modern mining history. In *Boom – Crisis – Heritage*, BLUMA, L., FARRENKOPF, M., MEYER, T. (eds.). De Gruyter, 2021, pp. 1–22.

[6] WEBER, H. Beyond Innovation and Use, or Why We Must Follow Technologies through Time. *Histories*, Jan. 2024, vol. 4, no. 1, pp. 51–61.

[7] WEBER, H. Zwischen Persistenz und Verschwinden: Warum Temporalitäten der Technik zum Gegenstand technik- und umwelthistorischer Forschung werden müssen. In *Bergbau und Umwelt in DDR und BRD*, ALBRECHT, H., FARRENKOPF, M., MAIER, H., MEYER, T. (eds.) De Gruyter, 2022, pp. 19–42.

[8] POPELKA, P., POPELKOVÁ, R., MULKOVÁ, M. *Black or green land?: industrialisation and landscape changes of the Ostrava-Karviná mining district in the 19th and 20th century*. Ostrava: Universitas Ostraviensis, 2016.

[9] POPELKOVÁ, R., MULKOVÁ, M. The mining landscape of the Ostrava-Karviná coalfield: Processes of landscape change from the 1830s to the beginning of the 21st century. *Applied Geography*, Jan. 2018, vol. 90, pp. 28–43.

[10] MILOŠ, M., KLÁT, J., KORBELÁŘOVÁ, I. *Cultural Monuments of the Ostrava-Karviná Coalfield*. NPÚ, ÚOP v Ostravě, 2008.

[11] POKLUDOVÁ, A., POPELKA, P. From the “steel heart of Czechoslovakia” to post-industrial space: Boom, crisis and the cultural heritage of the Ostrava-Karviná mining district. In *Boom – Crisis – Heritage*, BLUMA, L., FARRENKOPF, M., MEYER, T. (eds.). De Gruyter, 2021, pp. 161–178.

[12] FRANTÁL, B., PASQUALETTI, M. J., BRISUDOVÁ, L. Challenges, dilemmas and success criteria of recycling coal mining landscapes. *Moravian Geographical Reports*, Dec. 2024, vol. 32, no. 4, pp. 216–232.

[13] ZEZULA, M., KRAVČÍK, R., KRŮL, M., LENART, J., MALINA, O., MARTINEC, P. Brownfield or historic landscape? Digital model of the landscape relief of the vanished Karviná and its interpretation. *Zprávy památkové péče*, 2022, vol. *82*, no. 4., pp. 544-572.

[14] GOCH, S. Betterment without Airs: Social, Cultural, and Political Consequences of Deindustrialization in the Ruhr. *International Review of Social History*, 2002, no. 47, pp. 87–111.

[15] VAISHAR, A. Development of the settlement system in the Ostrava agglomeration and possibilities of its restructuring. *Geografie*, 2002, vol. 107, no. 2, pp. 171–188.

[16] MYGA-PIĄTEK, U., SOBALA, M., ZEMŁA-SIESICKA, A., PUKOWIEC-KURDA, K., NITA, J. Is There Urban Landscape in

Metropolitan Areas? An Unobvious Answer Based on Corine Land Cover Analyses. *Land*, 2021, vol. 51, no. 10, p. 20.

[17] GALGÓCZI, B. The long and winding road from black to green: Decades of structural change in the Ruhr region. *International Journal of Labour Research*, 2014. vol. 6, no. 2, pp. 217–240.

[18] BERGER, S., WICKE, C., GOLOMBEK, J. Burdens of Eternity?: Heritage, Identity, and the "Great Transition" in the Ruhr. *The Public Historian*, 2017, vol. 39, no. 3, pp. 21–43.

About Authors...

Klára CIESAROVÁ is a doctoral student at the Faculty of Civil Engineering of the Czech Technical University in Prague, specializing in industrial architecture research and the transformation of post-mining landscapes as part of the Industrial Heritage program. Her work builds on her master's studies in Monument Preservation and Public Presentation of Industrial Heritage at the University of Ostrava. In her research, she combines approaches from architecture, urban planning, and heritage conservation, with an emphasis on sustainability and the protection of cultural and historical values. She is actively involved in the NAKI III project (*Active Conservation of Immovable Industrial Heritage Through New Uses, 2023–2027*) at the Architecture Department, Faculty of Civil Engineering, Czech Technical University in Prague.

Hydroelectric Beginnings on the Vltava: Engineering, Municipal Enterprise, and the Making of the Štvanice Power Plant (1880–1914)

Elisa Angeles Fernández[1]

[1] Dept. of Electrical Engineering, Historical Laboratory of (Electro) Technology, Czech Technical University, Technická 2, 166 27 Praha, Czech Republic

angeleli@fel.cvut.cz

Abstract. *This paper examines the emergence of hydroelectricity on the Vltava River through the transformation of the Štvanice site between 1880 and 1914. Rather than treating Prague as a peripheral extension of imperial hydraulic modernization, it analyzes how river regulation, municipal territorial strategies, and the expansion of urban electricity supply converged in the creation of the Helmovský–Štvanice hydraulic–electrical complex.*

The construction of the Helmovský weir, the canalization of the Vltava, and the erection of the Štvanice hydroelectric plant are interpreted as interconnected processes shaped by imperial water law, municipal land acquisition, engineering experimentation, and the economic pressures of urban electrification. The study places Štvanice within broader debates on large technical systems, river planning, and the municipalization of utilities. It shows how river engineering, municipal control of land, and the expansion of electrical distribution developed together during Prague's modernization.

Keywords

History of Technology, Industrial heritage, River engineering, Hydropower history, Infrastructure and urbanizations.

1. Introduction

The emergence of hydroelectricity in European cities at the turn of the twentieth century was closely connected to broader transformations in river engineering, urban governance, and electrical infrastructure. Historians of technology have shown that modern energy systems developed through processes of infrastructural integration in which technical devices, institutions, and territorial control evolved together [1,2]. At the same time, environmental historians have emphasized how industrial societies increasingly reconfigured rivers through regulation works that served multiple purposes, including navigation, flood control, and energy production [3,4,5]. Hydroelectric development therefore often emerged within larger hydraulic projects that reshaped both river landscapes and urban infrastructures.

The transformation of the Vltava River in Prague between the late nineteenth century and the First World War illustrates this process. The canalization, the construction of the weirs, and the establishment of the Štvanice hydroelectric plant formed part of a broader reorganization of the river corridor influenced by imperial water legislation, municipal territorial strategies, and growing urban demand for electricity. Examining this case helps to understand how river regulation, municipal infrastructure planning, and early hydroelectric production became interconnected in the modernization of Prague's urban energy system.

1.1 Methodological Approach

This study integrates urban history, history of technology, economic history, and spatial analysis. It draws upon archival documentation from the Národní archiv (Fond Komise pro kanalizování řek Vltavy a Labe, sign. III/1/2-r, kart. 184–186), building documentation from the Archiv stavebního úřadu ÚMČ Prahy 7, and technical plans preserved at the Národní technické muzeum, including František Malý's unpublished manuscript [6]. Published technical literature [7–9], municipal statistical reports [10], and interwar planning analyses [11,12] are used to reconstruct hydraulic design, electrical integration, and institutional coordination.

Together, these sources illuminate the regulatory, technical, architectural, and economic dimensions of Prague's early hydroelectric planning. Conceptually, the analysis engages with large technical systems theory [1], infrastructural integration studies [2,5], and environmental-hydraulic historiography [3,4]

.

2. From Medieval Weirs to Modern River Regulation

Since the Middle Ages, the Prague reach of the Vltava had been structured by wooden "Prague weirs" (staropražské jezy), documented as early as 993 and expanded in the thirteenth and fourteenth centuries [13]. These structures raised water levels for mills and helped stabilize navigation, but they created a fragmented hydraulic landscape. In the nineteenth century these structures had become both an infrastructural obstacle and an energetic opportunity [14]. While the old weirs complicated navigation and limited the hydraulic continuity of the river, they also created controlled drops in water level that could be harnessed for mechanical and later electrical power. As demand for energy grew in expanding cities, these inherited hydraulic infrastructures began to be reconsidered not only as remnants of an earlier milling economy but as potential sites for modern hydroelectric production.

Fig. 1. Water mill on the Čertovka canal (Prague), illustrating the historical use of weirs to power mills. [30].

Industrialization and new metallurgical materials allowed engineers to design the first gated weirs [13], transforming how hydraulic head could be controlled and opening pathways for later hydro-mechanical and hydroelectric uses. This hydraulic history set the background for the city's modernization.

The Austrian Water Law of 1869 declared major rivers public goods and strengthened state control over navigation and hydraulic regulation [15,16]. The Waterway Act of 1901 created the Commission for Channeling the Vltava and Elbe Rivers in Bohemia, institutionalizing systematic canalization [14,17].

Later, the Waterway Act of 1901, created the Commission for Channeling the Vltava and Elbe Rivers in Bohemia (EVW), responsible for planning, standardizing, and contracting hydraulic works. Between 1899 and 1905, the commission supervised a series of regulatory steps downstream of Prague: Klecany, Troja, Libčice, Miřejovice, Vraňany–Hořín; producing technical expertise that would soon be applied to Prague's own canalization [14,18].

3. The Purchase of Štvanice (1898)

The transformation of the Vltava at Štvanice did not begin with turbines or reinforced concrete, but with land.

The decisive precondition for the hydraulic and electrical reconfiguration of this stretch of the river was the municipal acquisition of Štvanice Island in 1898. At the end of the nineteenth century, plans were being developed for a new bridge linking the Northwestern Railway station with Bubny and for the construction of a riverfront road. These proposals exposed a series of conflicts over expropriation costs, ferry rights, and the alignment of future embankments [10]. Private owners had already submitted a river regulation project in 1894 that proposed partial excavation of the island and the elevation of its surface to flood level. Although this plan received administrative approval in 1896, it was never implemented, and negotiations over financial compensation for ferry privileges, riverbank losses, and bridge construction escalated to prohibitive sums [10].

Faced with these demands, the Prague municipal council concluded that outright acquisition was strategically preferable. On 29 April 1898 the city formally purchased Štvanice Island and associated river rights for 880,000 gulden, assuming existing mortgage obligations and committing to staged payments extending to 1906 [10]. The purchase included not only the island's land and buildings but also ferry rights, sand extraction rights, control over riverbanks from Vyšehrad to Holešovice, and bridge toll privileges. Through this transaction, the municipality effectively municipalized a strategic section of the Vltava corridor and removed the legal barriers that had previously constrained large-scale intervention in the river landscape.

The acquisition fundamentally altered the balance of authority over the river. By consolidating ownership, Prague gained the capacity to reshape the island's morphology without prolonged legal disputes. The municipality could excavate, elevate, dredge, or realign riverbanks in accordance with their broader infrastructural plans. In effect, municipal management of urban territory preceded hydraulic modernization. From a perspective, this moment can be understood as an early stage in the creation of the infrastructure needed for later hydraulic and electrical works: before mechanical devices could be installed, the land had to be stabilized alongside with the administrative authority consolidated [1]. Štvanice and its surroundings became infrastructural ground, terrain prepared for elevation against floods, dredging, and structural reinforcement.

Seen in this light, the island was not merely an opportunistic site later adapted for hydropower. Rather, it was deliberately secured as a hydraulic platform within an urban strategy. Prague planners had already envisioned the area as terrain to be stabilized, connected, and integrated into the expanding industrial districts of Karlín and Holešovice. The later construction of the Helmovský weir and the hydroelectric plant at the western tip of the island

must therefore be understood as the culmination of a decade-long process of spatial consolidation. When canalization and construction works began between 1907 and 1913, they could proceed not as piecemeal adaptations but as part of a coordinated reconfiguration of the river corridor. Hydroelectricity, when it arrived, was inserted into a landscape that had already been politically, legally, and spatially prepared for transformation.

4. Canalization, Municipal Investment and Urban Restructuring, (1907–1913)

The canalization of the Vltava between 1907 and 1913 fundamentally reshaped Prague's riverfront. Centered on the construction of the Helmovský weir and a new system of locks around Štvanice Island, the project integrated navigation, hydraulic regulation, flood management, urban redesign, and energy production within a single infrastructural intervention [14]. A public tender launched in 1907 divided the works into seven construction components, ranging from dredging operations to lock-building. The final contracts were awarded to Lanna and Müller & Kapsa, two major Bohemian engineering firms [19]. The works were carried out primarily by the Lanna company, one of the most prominent hydraulic contractors in Bohemia, whose expertise shaped numerous river regulation and navigation projects along the Vltava and Elbe [20].

A central component of the project was the replacement of older river-control structures. Medieval weirs, including the Novomlýnský and the earlier Helmovský structures, were removed and replaced by a new concrete Helmovský weir constructed between 1909 and 1910 [6]. The Novomlýnský weir had been destroyed during a major flood, and its reconstruction formed part of a broader hydraulic reconfiguration of the Prague reach of the river. The new weir raised the controlled water level at Štvanice to about 4 to 4.4 meters, which made it easier to manage navigation and keep water levels stable [6]. Although this increase may seem small, it was really important because it changed the river that used to fluctuate naturally into a controlled one, where the difference in water levels could be measured and therefore and importantly used to power machines.

The canalization works also produced significant spatial restructuring along the river corridor. Several smaller islands in the surrounding area: Primátorský, Korunní, and Jeruzalémský; were partially or completely removed, enlarging the navigable channel and opening new space for new development around Karlín and Holešovice [21,20].

Fig. 2. The Islands on the Vltava River and Karlín by1900 [28].

Fig. 3. The Islands on the Vltava River and *Štvanice according to the design from 1912* [20].

Riverbanks were realigned and stabilized, while dredged material was used to enlarge the western portion of Štvanice Island by approximately 9,000 square meters, giving it its present outline [19]. Navigation canals, separated from the main current by protective walls, enabled vessels to bypass stronger flows, while lock chambers accommodated both cargo and passenger traffic [14].

Even before canalization was completed, proposals to harness the newly regulated flows for hydroelectric generation were already circulating. Two early installations emerged from this context. The now-disappeared Těšnov power plant supplied nearby districts through an underground conduit [9], while the Štvanice hydroelectric plant, constructed between 1908 and 1914, was conceived as a larger and more permanent facility integrated into the new hydraulic infrastructure [20].

Cartographic sources (Figs. 2-3) show the disappearance of small islands, the consolidation of riverbanks, and the clearing of informal workshops and timber yards that had long occupied the floodplain. These changes created new parcels for industrial development and shifted long-established patterns of work, mobility, and land use.

Stable municipal electricity along the river corridor reinforced this transformation, attracting warehouses, metalworking shops, and mechanical trades, and illustrating how hydraulic modernization stimulated local industrial growth [22,18].

Economically and politically, the canalization reflected Prague's broader effort to secure a cheaper and more stable complement to coal-based electricity, reduce dependence on private suppliers, and align with wider Central European trends toward the municipalization of urban utilities [8,11]. Hydroelectric infrastructure therefore functioned both as a technical installation and as a strategic investment by the city. Later planning doctrines would

formalize this idea, arguing that waterpower should be used "up to the economic maximum" within integrated river-basin management [11]. At Štvanice, this integration had already taken place in practice.

These works transformed the Vltava into a coordinated hydraulic system in which the weir, locks, embankments, and power plant operated together. Richard White's description of modern rivers as "organic machines" [3] captures this condition well: the river was not only regulated but also physically reshaped through infrastructure. As Sara Pritchard has shown for the Rhône, twentieth-century river engineering increasingly treated rivers as multi-purpose territorial systems [4]. The canalization works reflect this logic, where navigation, flood control, urban expansion, and energy production were combined within a single transformation of the river corridor.

5. The Štvanice Hydroelectric Plant *(1908–1914)*

The Štvanice hydroelectric plant emerged as a central component of Prague's expanding municipal electrical system. Integrated into the Municipal Electrical Works (MEW), it became the first stable hydroelectric base within the municipal grid. Contemporary records indicate that its original output roughly matched the electricity demand of the city's public lighting, underscoring its strategic role in reducing dependence on coal-based production and private suppliers (LVVC 2023) [20]. Retrospectively, the installation came to be recognized as one of the earliest systematic hydropower projects in the Czech lands. Bartovský later identified it as the only hydroelectric plant built between 1901 and 1918, marking it as a foundational step in the development of modern hydropower in the region (Bartovský 1946, 18) [12]. Hermann's overview of river engineering similarly listed the plant among the early hydroelectric installations associated with navigation works (Hermann 1923) [11].

Fig. 4. Štvanice hydroelectric plant and Helmovský weir. [29].

The conceptual origins of the plant lay in the canalization plans developed during the first decade of the twentieth century. As early as 1905, the EVW Commission had envisioned a hydraulic complex at Štvanice combining lock chambers, a fixed weir, and a power station. Early design work was led by engineer František Sander, whose characteristic maritime aesthetic is visible in the stone platform beneath the plant, shaped like a ship's prow (NA, plans 1909). Sander's drawings were approved and signed by engineer Josef Sixta, the station's chief engineer, while the final architectural articulation of the façades is attributed to architect Alois Dlabač, whose signature appears on later plans. Project documentation was prepared in 1909, definitive plans issued in 1912, and the building formally approved in 1915, with finishing works delayed by the First World War.

The plant itself was constructed between 1913 and 1914 by Müller & Kapsa at the western tip of Štvanice Island, directly adjacent to the Helmovský weir. Designed by Dlabač, the structure was among the earliest reinforced-concrete industrial buildings in Prague (Elektro 2005) [9]. Its architectural composition combined Art Nouveau elements with the monumental expression of early twentieth-century technical architecture. The most distinctive feature was a 22-meter tower crowned with a domed pavilion.

The plant converted the water-level difference created by the Helmovský weir, into electricity (Malý 1968) [6]. It was originally equipped with three vertical Francis turbines manufactured by *Českomoravská-Kolben-Daněk* (Malý 1968; Broncová 2007) [6,21]. Each turbine processed approximately 16 cubic meters of water per second and produced about 474 kW, resulting in an installed capacity of roughly 1.4 MW (Elektro 2005) [9]. Three-phase generators operating at 3,000 volts and 50 Hz produced an annual output of nearly nine million kilowatt-hours (Malý 1968; Bartovský 1946) [6,12]. The turbines were arranged vertically, which shaped the internal layout of the building. Water entered through gated intakes, flowed down through penstocks to the turbines, and was then released back into the river channel. The generator rotor was installed directly above each turbine runner, creating a stacked mechanical system in which the turbine and generator operated on the same vertical axis (Tománek 1928) [8]. This configuration required a tall structure and strongly influenced the building's overall spatial design.

Later reconstruction works revealed important details about the plant's foundations and the challenges of building on a river island. The structure was originally supported by wooden piles driven into the gravel and sand of the riverbed (Elektro 2005) [9]. Because the riverbed soil was unstable, in these later works was reinforced the foundations with injection grouting and micro-piles anchored to bedrock. These interventions illustrate the difficulties engineers faced when trying to establish durable mechanical infrastructure within the shifting terrain of a river environment.

6. Business Networks, Urban Pressures, and the Economics of Early Hydroelectricity

At the turn of the twentieth century, Prague operated a fragmented and increasingly costly electrical landscape. Small municipal stations in Karlín, Smíchov, and Žižkov coexisted with the larger coal-fired Ústřední elektrárna constructed in 1898–1899 (Adressář 1901, 134, 368) [24]. These district systems remained technically disconnected and economically inefficient, while private electrical firms such as *Kolben, Křižík*, and *Siemens & Halske* shaped an uneven but expanding urban electricity market. The result was a patchwork of production and distribution infrastructures that struggled to meet the growing demands of an industrializing city.

Several urban and economic pressures converged to push Prague toward hydroelectric development as part of the canalization of the Vltava. The transition from gas to electric lighting significantly increased municipal expenditures (Erben and Srb 1900, 510–511) [10], while rising coal prices placed additional strain on the city's budget. At the same time, cities across Central Europe increasingly pursued the municipalization of utilities as a strategy to stabilize tariffs, rationalize supply, and reduce dependence on private providers (Millward 2005; Judson 2016) [23,15]. Prague's fragmented district systems were particularly ill-equipped to support the rapid growth of industrial districts such as Karlín and Holešovice, where electricity demand expanded alongside factories, tramway networks, and public lighting.

Even a relatively modest hydroelectric installation could offer significant economic advantages. Public lighting represented one of the most volatile items in the municipal budget, meaning that any reduction in coal consumption or in purchases from private suppliers had an immediate financial impact. Hydroelectricity from Štvanice, though limited in absolute terms, provided a predictable baseline of generation that could offset peak expenditures associated with lighting and electric traction. In this sense, the plant functioned not only as an engineering complement to the canalization works but also as a financial instrument, helping smooth municipal budget fluctuations, reduce exposure to coal price volatility, and support the gradual consolidation of a municipally controlled electrical system.

The 3,000 volts that the plant generated was transmitted into Prague's municipal grid, where transformer stations reduced transmission voltages from 100 kV to 23 kV for urban distribution (Tománek 1928, 51) [8]. Within this emerging high-voltage network, hydropower complemented coal-fired generation in Holešovice, creating a coordinated production system in which different energy sources operated in tandem (Tománek 1928) [8]. The water flow of the Vltava was thus used within a wider urban infrastructure linking river engineering, municipal electricity supply, tramways, and public lighting. Štvanice plant functioned as a nodal element within an expanding metropolitan energy system, illustrating Erik van der Vleuten's argument that infrastructures reshape societies through processes of spatial integration and standardization (van der Vleuten 2004) [2].

Later technical and legislative discourse would formalize the principles already materialized in Prague's system. Hermann argued that thermal power plants should operate as reserve capacity while hydropower be exploited "up to the economic maximum" within coordinated river-basin planning (Hermann 1923, 64) [11]. In such a configuration, steam stations ensured reliability and flexibility, while hydropower provided a stable and economically efficient base load. This complementary relationship between coal-fired and hydroelectric generation was already operational in Prague before its codification in national planning frameworks.

Bartovský (1946, 18) [12] later identified Štvanice as the only hydroelectric plant constructed between 1901 and 1918, highlighting its singular position in the early development of Czech hydropower. After 1919, new legislation formalized principles that had already been materially demonstrated at Štvanice: the integration of navigation and hydropower works, basin-wide coordination of river infrastructure, and the standardization of technical norms across interconnected electrical systems (Hermann 1923; Bartovský 1946) [11,12]. The Štvanice plant responded to rising energy costs, a fragmented electrical system made up of several small, connected power stations, and the growing service demands of a rapidly modernizing city.

7. Conclusions

The development of the Štvanice hydroelectric plant illustrates how hydropower in Prague emerged within a broader transformation of the Vltava River at the turn of the twentieth century. Canalization works, the construction of the Helmovský weir, and the installation of the power station formed part of a coordinated effort to regulate the river, improve navigation, and support the city's expanding demand for electricity.

The weir created a difference in water level that made it possible to generate electricity. This electricity was fed into Prague's municipal grid and used for public lighting, tramways, and nearby industrial districts such as Karlín and Holešovice. River engineering and urban electrification thus became closely connected in the development of Prague's municipal infrastructure.

Institutionally, the project reflected cooperation between state hydraulic authorities and the Municipality of Prague, illustrating an early form of coordination between river regulation and municipal electricity supply that would later be formalized in national legislation.

Acknowledgements

Research described in the paper was supervised by Prof. PhD. Marcela Efmertová, CSc, FEE CTU in Prague. Supported by the research program SGS and Project Barrande.

References

[1] HUGHES, T. P. *Networks of Power: Electrification in Western Society, 1880–1930.* Baltimore: Johns Hopkins University Press, 1983.

[2] VAN DER VLEUTEN, E. Infrastructures and Societal Change: A View from the Large Technical Systems Field. *Technology Analysis & Strategic Management*, 2004, vol. 16, no. 3, p. 395–414.

[3] WHITE, R. *The Organic Machine: The Remaking of the Columbia River.* New York: Hill and Wang, 1995.

[4] PRITCHARD, S. B. *Confluence: The Nature of Technology and the Remaking of the Rhône.* Cambridge, MA: Harvard University Press, 2011.

[5] VAN DER VLEUTEN, E., KAIJSER, A. (eds.). *Networking Europe: Transnational Infrastructures and the Shaping of Europe, 1850–2000.* Sagamore Beach, MA: Science History Publications, 2006.

[6] MALÝ, F. *Vodní dílo na Vltavě v Praze na Štvanici.* Unpublished manuscript. Prague: Národní technické muzeum, 1968.

[7] PAVLOUSEK, V. Zdýmadlo u Štvanice. *Technický obzor*, 1913.

[8] TOMÁNEK, J. *Elektrisace Československa 1918–1928.* Prague: Elektrotechnický svaz Čsl., 1928.

[9] ELEKTRO. Vodní elektrárna na Štvanici. *Elektro*, 2005, vol. 15, no. 3, p. 38.

[10] ERBEN, J., SRB, J. *Administrační zpráva královského hlavního města Prahy za rok 1898.* Prague: Nákladem statistické kommisse, 1900.

[11] HERMANN, G. *Přehled činnosti za prvé pětiletí republiky Československé.* Prague: Ministerstvo veřejných prací, 1923.

[12] BARTOVSKÝ, J. *Vodní cesty a vodohospodářské plánování v Čechách a na Moravě.* Prague: Společnost Dunajsko-oderského průplavu, 1946.

[13] RYŠKOVÁ, M., et al. (eds.). *Methodology for Classification and Evaluation of the Industrial Heritage.* Prague, 2023.

[14] FOŠUMPAUR, P., KAŠPAR, T., ZUKAL, M. Technical Cultural Heritage on the Elbe–Vltava Waterway. *IOP Conference Series: Earth and Environmental Science*, 2019, vol. 290, p. 012152.

[15] JUDSON, P. M. *The Habsburg Empire: A New History.* Cambridge, MA: Harvard University Press, 2016.

[16] GRUFFAT, C. "Beautiful Public Danube." *Austrian History Yearbook*, 2023, vol. 54, p. 41–64.

[17] NEŠVAROVÁ CHVOJKOVÁ, P., et al. Historical Water Structures and Technical Heritage. *IOP Conference Series: Materials Science and Engineering*, 2021, vol. 1203, p. 022014.

[18] FOŠUMPAUR, P., et al. Hydraulic Heritage and Water Management Structures. *IOP Conference Series: Materials Science and Engineering*, 2020, vol. 960, p. 032010.

[19] VÁCLAVOVIC, S. J. Kapitoly z dějin Štvanice V. *Praha7.cz*, 2022.

[20] FAKULTA STAVEBNÍ ČVUT V PRAZE. Technické památky Labsko-vltavské vodní cesty: Vodní dílo Štvanice. Available at: https://www.lvvc.cz/databaze.php (accessed 26 Nov. 2025).

[21] BRONCOVÁ, D. (ed.). *Pražské ostrovy.* Prague, 2007.

[22] KREJČÍ, J., CAJTHAML, J. Historical Vltava River Valley: Transformation of the Prague River Landscape. *ISPRS International Journal of Geo-Information*, 2022, vol. 11, no. 1, p. 35.

[23] MILLWARD, R. Public and Private Ownership of Electricity Supply Systems in Europe. In: BEL, G., FAGEDA, X. (eds.). *Public and Private Ownership in Europe.* London: Routledge, 2005, p. 131–156.

[24] ADRESSÁŘ KRÁLOVSKÉHO HLAVNÍHO MĚSTA PRAHY A SOUSEDNÍCH OBCÍ BUBENČE, HOLEŠOVIC-BUBEN, KARLÍNA, SMÍCHOVA, KRÁL. VINOHRADŮ A ŽIŽKOVA. Prague: Nákladem důchodů obce pražské, 1901.

[25] NÁRODNÍ ARCHIV (NA). Fond: Komise pro kanalizování řek Vltavy a Labe, sign. III/1/2 r, kart. 184–186 (plans from 1909).

[26] STAVEBNÍ ARCHIV ÚMČ PRAHY 7.

[27] MALÝ, F. *Vodní dílo na Vltavě v Praze na Štvanici.* Archival manuscript, Národní technické muzeum, archive no. 1658, Prague, 1968.

[28] CZECH DIGITAL LIBRARY. *The Islands on the Vltava River and Karlín by 1900.* Available at: https://ceskadigitalniknihovna.cz/uuid/uuid:d84b42ec-7864-11ec-875a-fa163e4ea95f (accessed 26 Nov. 2025).

[29] ANGELES FERNÁNDEZ, E. Photograph of the Štvanice hydroelectric plant. Prague, 2025. Personal archive.

[30] ANGELES FERNÁNDEZ, E. Water mill on the Čertovka canal. Prague, 2025. Personal archive.

About Author...

Elisa ANGELES FERNÁNDEZ from Mexico City. She obtained her Bachelor's degree in Landscape Architecture from the National Autonomous University of Mexico (UNAM). Then pursued a Master's degree in the Erasmus Mundus program Techniques, Patrimoine, Territoires de l'Industrie at the University Paris 1 Panthéon-Sorbonne. Currently, a doctoral student at the Faculty of Electrical Engineering CTU in Prague, in the Historical Laboratory of (Electro)Technology(K13116). Her research focuses on the history of industrial heritage, particularly in relation to electrification and hydroelectric infrastructures.

From Workers' Colonies to Post-war Housing Estates:

Spatial and Social Transformations of Industrial Housing in Western Bohemia (from the end of the 19th century to the end of the 1960s)

TOMÁŠ JURICA

Dept. of Architecture, Faculty of Civil Engineering, Czech Technical University, Thákurova 2077/7, 166 27 Praha, Czech Republic

tomas.jurica@fsv.cvut.cz

Abstract.

This paper examines the transformation of industrial housing in the Czech lands from the late nineteenth century to the second half of the twentieth century. The research focuses on the relationship between industrial production and residential urban structures and analyses how this relationship evolved alongside the development of industrial society, changing economic conditions, and different political systems. Industrial housing is interpreted not only as a response to the practical need for accommodation for workers but also as an urban and social phenomenon reflecting broader economic, technological, and ideological processes. The paper therefore explores how different models of industrial housing shaped the spatial organization of settlements and influenced the everyday life of their inhabitants.

The development of industrial settlements in Europe was closely connected with the rapid expansion of industrial production during the nineteenth and twentieth centuries. Growing industrial centres required a stable workforce and therefore also a system of housing capable of accommodating large numbers of workers. In many cases, the construction of residential areas was directly initiated by industrial enterprises seeking to stabilize their labour force and improve productivity. These settlements often developed as workers' colonies or company towns, where the spatial organization of housing, public facilities, and industrial structures reflected the dominant role of the enterprise. In this sense, industrial housing represented an important instrument for organizing labour, structuring everyday life, and shaping the social environment of industrial communities.

The theoretical framework of the research is based on an interdisciplinary perspective combining studies of company towns and industrial archaeology. Research on company towns emphasizes the role of dominant industrial enterprises in shaping residential structures, urban planning, and social relations within industrial settlements. Authors studying company towns highlight the importance of paternalistic industrial policies, in which employers provided housing and basic social infrastructure in order to stabilize and control the workforce. At the same time, industrial archaeology provides a methodological approach for understanding the material and spatial traces of industrial production in the urban landscape, including residential structures associated with industrial activities. These perspectives allow industrial housing to be interpreted as an integral component of a broader industrial landscape rather than as an isolated architectural phenomenon.

The methodological approach of the paper is based on a comparative analysis of three case studies representing different stages in the historical development of industrial housing. The analysis focuses on several key parameters frequently used in the literature on industrial settlements, including spatial organization, the distance between housing and workplaces, building typology, the extent of civic amenities, and the social structure of inhabitants. Particular attention is also given to the institutional and political context in which these settlements were created. The case studies are located in the western region of the Czech Republic and share similar historical and socio-economic conditions connected to industrial development.

The first case study examines the mining colonies in the town of Nýřany near Plzeň, which developed in the second half of the nineteenth century in connection with coal mining in the Nýřany mining district. Their spatial organization represents an early model of industrial housing characterized by a close relationship between residential structures and the industrial workplace. Housing was located within walking distance of the mines and consisted of relatively simple and socially homogeneous units intended mainly for miners and their families. This case illustrates how workers' colonies functioned as spatial tools for organizing industrial labour and stabilizing the workforce in expanding mining regions.

The second case study focuses on the company district of Karlov in Plzeň, built in the early twentieth century for employees of the Škoda Works. This residential complex represents a more advanced form of industrial urbanism, where housing was planned as a larger urban district with developed civic infrastructure. In addition to residential buildings, the district included schools, shops, and community facilities supporting the daily life of the industrial workforce. Despite this more complex structure, the district remained closely connected to the industrial

enterprise, reflecting the paternalistic relationship between employer and workers typical of many company towns.

The third case study analyses the post-war development of the town of Ostrov nad Ohří. After the Second World War, the region experienced significant industrial expansion related to uranium mining in nearby Jáchymov and later to the Škoda Ostrov industrial plant specializing in trolleybus production. Unlike earlier forms of industrial housing, the new urban structure was conceived as an autonomous residential town within the framework of modernist planning and state-directed industrialization.

The final part of the paper compares the three case studies and highlights the transformation of industrial housing models in the Czech context—from workers' colonies closely integrated with production, through company housing districts, to post-war residential towns characterized by greater separation between housing and industry. These changes reflect broader transformations in industrial organization, urban planning, and the political and economic structures shaping industrial regions during modernization.

Criteria	NÝŘANY	PLZEŇ, KARLOV	OSTROV
Period	Late 19th century	Early 20th century	After 1945
Urbanism	Workers' colony	Company town district	Post-war housing estate
Type of planning	Spontaneous	Planned by the company	Centrally planned by the state
Building typology	Small terraced workers' houses (typically 1 storey)	Typical apartment houses in block development (typically 2 storeys)	Complex urban structure (apartment buildings, multifunctional buildings, services)
Civic amenities	Limited	Expanded (school, shops, community hall, Sokol hall)	Comprehensive (schools, House of Culture, shops, services, hospital)
Distance from industry	Very short distance (walking distance – approx. 100–200 m)	Short distance (walking distance – 200–1,000 m)	Longer distance (in the range of several kilometres)
Social structure	Homogeneous	Differentiated	Heterogeneous
Actor of development	Entrepreneur / Company	Industrial enterprise	State

***Table 1** - Comparative Analysis of Industrial Housing Models*

*The results of the comparative analysis are summarized in **Table 1**, which highlights the key differences in urban structure, planning approach, civic amenities, and the spatial relationship between housing and industrial production.*

Keywords

POSTER2026, industrial housing, company towns, industrial archaeology, urbanism, industrial settlements, Czech industrial regions

Acknowledgements

Research described in the abstract was supervised by Prof. PHDR. MARCELA EFMERTOVÁ, CSc., FEE CTU in Prague.

References

[1] BURZOVÁ, Petra; DVOŘÁKOVÁ, Ilona; HEJNAL, Ondřej; RŮŽIČKA, Michal a TOUŠEK, Laco, 2013. *V Plzni na Karlově*. Online. Západočeská univerzita v Plzni. ISBN 978-80-261-0314-1.

[2] CRAWFORD, Margaret, 1999. The "New" Company Town. Online. *Perspecta*. Vol. 30, no. 1, s. 10.

[3] DOLEJSKÝ, Martin, 2026. *Hornické kolonie v Nýřanech u Plzně*. Online. In: Dělnické kolonie.

[4] FRAGNER, Benjamin; VALCHÁŘOVÁ, Vladislava; VORLÍK, Petr; BERAN, Lukáš; et al., 2013. *Charta průmyslového dědictví TICCIH, překlad: Výzkumné centrum průmyslového dědictví FA ČVUT v Praze*. Praha: České vysoké učení technické v Praze. ISBN 978-80-01-05235-8.

[5] GARNER, John S., 1986. He Model Company Town: Urban Design Through Private Enterprise in Nineteenth-Century New England. Online. *Winterthur Portfolio*. Roč. 21, č. 1, s. 4.

[6] HNÍDKOVÁ, Vendula, 2021. Lost in Translation? The Idea of the Garden City and its Migration to the Czech Lands, 1900–1938. Online. *Art East Central*. Roč. 2021, č. I., s. 27.

[7] HRŮZA, Jiří, 2002. *Charty moderního urbanismu*. Praha: Agora. ISBN 8090294545.

[8] HORÁK, MARTIN, 2015. České trolejbusy - historie, současnost, typy, technika, provoz. Praha: GRADA. ISBN 978-80-247-5552-6.

[9] JANUSOVÁ, JANA, 1980. HORNICKÉ KOLONIE V NÝŘANECH U PLZNĚ. Online. *ČESKÝ LID*. Roč. 1980, č. 67, s. 11.

[10] JEMELKA, Martin. Employee Colonies: Nomenclature, Typology and (Dis)continuity. Online. Architektúra a urbanizmus. 2022, roč. 56, č. 3-4, s. 135-147. ISSN 0044-8680.

[11] JEMELKA, Martin, 2025. *Protokolonie*. Online. In: Dělnické kolonie.

[12] JEMELKA, Martin. *Dělnické kolonie*. Online. In: Dělnické kolonie.

[13] KOUTNÝ, Jan, 2004. MODERNÍ URBANISTICKÉ KONCEPCE. Online. *URBANISMUS A ÚZEMNÍ ROZVOJ*. Roč. 7, č. 6, s. 14.

[14] MORAVÁNSZKY, Ákos, 2017. Blow-Up The Powers of Scale. Online. *JOELHO*. No. 8, s. 14. ISSN 1647-9548.

[15] PORTEOUS, J.D., 1970. The Nature of the Company Town. Online. *Transactions of the Institute of British Geographers*. Vol. 1970, no. 51, s. 16.

[16] ŘEPKOVÁ, Hana, 2022. *Regenerace sídlišť v souladu se zájmy památkové péče.* Praha. Národní památkový ústav. ISBN 978-80-7480-178-5.

[17] SAMEC, Tomáš; LEHEČKA, Michal; ORCÍGR, Václav; ŠPAČEK, Ondřej; JANEČKOVÁ, Michaela et al., 2020. *Pražská panelová sídliště jako místa protikladů*. Online. Praha: Sociologický ústav AV ČR. ISBN 978-80-7330-377-8.

[18] TOUŠEK, Ladislav; BURZOVÁ, Petra; RŮŽIČKA, Michal a DVOŘÁKOVÁ, Ilona, 2014. *Karlov mezi industriální a postindustriální společností*. Online. Západočeská univerzita. ISBN 978-80-261-0422-3.

[19] ZEMAN, Lubomír, 2008. *Architektura socialistického realismu v severozápadních Čechách*. Ostrava: NÁRODNÍ PAMÁTKOVÝ ÚSTAV. ISBN 978-80-85034-40-0.

[20] ZEMAN, Lubomír, 1998. *Nový Ostrov: Soubor tradicionalismu 50. let 20. století, Ostrov*. Městský úřad Ostrov. ISBN 80-238-4215-3.

About Author...

Tomáš JURICA was born in Ostrov. He graduated with honours in Architecture and Construction from the CTU in Prague and is currently a PhD student at the Department of Architecture, specializing in Industrial Heritage under the supervision of Prof. Šenberger. His research focuses on the development of residential settlements in relation to industrial production.

Professor Antonín Svoboda's visit to Prague in January 1975: historical context, course and interpretation of archival sources

Ing. Jaroslav KALVODA, MBA [1]

kalvojar@student.cvut.cz

[1] Historical Laboratory of (Electro)Technology, K13116, Faculty of Electrical Engineering, Czech Technical University in Prague, Technická 2, 166 27 Prague, Czech Republic

Abstract

The article focuses on a hitherto little-studied episode in the life of Professor Antonín Svoboda (1907–1980), a prominent Czechoslovak pioneer of computing technology and co-founder of the Research Institute for Mathematical Machines (Czech abbreviation VÚMS). The professor left with his family for a second emigration to the USA in August 1964. In January 1975, he arrived in Prague, essentially incognito, for a visit.

*The study is based on archival materials stored in the Security Services Archive (Czech abbreviation ABS), especially from the volume kept by the State Security (Czech abbreviation StB), as well as from additional judicial and administrative documents, and from the memoirs of professors Antonín Svoboda and Paul Valach (*1958).*

The aim of the paper is ***to reconstruct*** *the course of A. Svoboda's visit to Prague in 1975,* ***to analyze*** *its official and unofficial framework, and* ***to interpret*** *the way in which this event was recorded and evaluated by the state authorities of Czechoslovakia during the so-called "Normalization" period (from 1969 to the late 1980s), a term used to describe the reassertion of political control by regime after the Prague Spring.*

The article places Professor Svoboda's visit in the broader political, institutional and personal context of the 1970s and points out the possibilities ***of using archival sources from security forces*** *in studying the history of technology, especially in the relationship between scientific activity, emigration and state power during the Cold War.*

Keywords

History of technology, history of science, Antonín Svoboda, computing technology, Research Institute for Mathematical Machines (VÚMS), State Security, so-called "Normalization", Cold War, Czechoslovakia, Czechoslovak Socialist Republic (ČSSR), USA

1. Context of the period under review

The period from the 1950s to the 1980s was a period of significant political control and centralization of power and economy in the development of Czechoslovakia. This development followed the events after World War II, and particularly the seizure of power by the Communist Party of Czechoslovakia (Czech abbreviation KSČ) in February 1948. After this political turning point, Czechoslovakia gradually transformed into a socialist state oriented towards the Soviet Union.

Politically, the 1950s were characterized by the consolidation of the power of the Communist Party of Czechoslovakia. The political opposition was liquidated, civil liberties were restricted, and a single-party system was created. The state was governed according to the Soviet model, which emphasized centralized decision-making and strong control of society. A typical feature of this period was also political trials of alleged "enemies of the state." The trials were intended to intimidate society and consolidate the authority of the regime. The security forces, especially the StB, which monitored the political loyalty of the population, played an important role in this. Repressions affected not only political opponents, but also churches, intellectuals (scientists, technicians, etc.) and private entrepreneurs, and significantly influenced Antonín Svoboda and his family. Part of this policy was the effort to ideologically control research, education, culture, and the media.

Economic development was based on the principle of a centrally planned economy (also within the Council for Mutual Economic Assistance) with the determination of the orientation of production, prices and distribution of resources using five-year plans. The development of heavy industry, engineering and arms production became a priority, which corresponded to the strategy of the Soviet bloc. On the contrary, the production of consumer goods and agriculture were often neglected, which led to a shortage of

some goods. The collectivization of agriculture was also an important economic change. Excessive orientation towards heavy industry and insufficient efficiency of the planned economy led to imbalances in the economy. These difficulties culminated, for example, in the currency reform in 1953, which significantly affected the savings of the population and caused public dissatisfaction.

The period under review from the 1950s onwards can be characterized as a stage of strongly centralized political power and radical economic transformation following the model of the USSR. Political repression, collectivization and emphasis on heavy industry fundamentally affected the everyday life of the population and the long-term development of Czechoslovak society and affected the sphere of academic (in research institutions) and technical (in universities and in enterprises) life. This period also laid the foundation for the further development of the socialist (communist) system, which, after the failure of the revival process during The Prague Spring and the consolidation of the regime during the period of so-called “Normalization” (including the non-implementation of the conclusions of the Conference on Security and Cooperation in Europe), persisted until the end of the 1980s.

2. The personality of Prof. Antonín Svoboda

Antonín Svoboda was one of the founding figures of Czechoslovak computing technology and modern cybernetics. [8]

In the autumn of 1936, he was drafted into the Czechoslovak Army and assigned to work on analogue anti-aircraft sights. Before the Nazi occupation of Czechoslovakia, he was sent by the Ministry of Defence to France to use his sight against the Nazis. Before the occupation of France, he had to leave Paris with his wife and newborn twins. The Svoboda family made an adventurous journey via Marseille and Lisbon to the USA, during which one of their sons died.

In the USA, A. Svoboda continued his work on anti-aircraft sights. In 1943, he joined the Radiation Laboratory at the Massachusetts Institute of Technology (MIT), where he participated in the development of the radar-controlled anti-aircraft sight Mark 56. In 1944, he was placed on the Reserved List of Scientific and Technical Personnel in the USA, thus being declared an essential scientist for the war effort. In 1948, he received the Naval Ordnance Development Award from the US government for his contribution. [1]

After World War II, Svoboda was commissioned to write the monograph Computing Mechanisms and Linkages, one of the first books devoted to the design of computing devices, published as part of the Radiation Laboratory Series. He completed the book in Prague in 1946.

After returning to Czechoslovakia**,** he became a key figure in building domestic research in the field of computing technology, was at the birth of the VÚMS and participated in the conception of the first Czechoslovak automatic computers **(**Czech abbreviation SAPO) and vacuum tube computer (Czech abbreviation EPOS).

The pushback from the communist leadership of the VÚMS and the pressure from the StB to establish cooperation can be considered significant factors that contributed to his second emigration in August 1964. His departure represented a significant loss for the Czechoslovak research environment.

After his second emigration, Svoboda worked in the USA as a university teacher and researcher in the field of automatic control and computing technology. He first worked in Phoenix, Arizona, and later lectured at the University of California, Los Angeles (UCLA), where he focused on the issues of analog and hybrid computers, control, and modeling of dynamic systems. He continued to publish professional papers, educate doctoral students, and maintain contacts with the international scientific community. He died in May 1980 in Portland, Oregon. Before that, in January 1975, he came to Prague for a little-known visit.

3. Svoboda's visit in January 1975

Based on the study of volume 581048 "Computer" kept by the StB and stored in the Security Forces Archive, it was possible **to reconstruct, analyze** and **interpret** the historical context and detailed course of Professor Antonín Svoboda's visit to the Czechoslovak Socialist Republic (Czech abbreviation ČSSR) in January 1975.

After the second emigration, Svoboda, his wife Milada, and his son Tomáš were sentenced in April 1965 in the ČSSR for the crime of leaving the republic to unconditional prison sentences of 1.5 years and 1 year, respectively. [2] However, they were not sentenced to forfeiture of property, and thus not to the loss of copyrights to patents. During The Prague Spring, during the rehabilitation trials in May 1968, their sentences were pardoned based on an amnesty by the President of the Republic. [3]

During the period of work before the second emigration for the national enterprise (n.p.) Aritma and VÚMS, Svoboda was the holder of several patents. In August 1974, by decision of the State Notary, 26,237 CZK was deposited in Živnostenská banka (a major Czechoslovak commercial bank) in his favor for the use of his patents for Aritma. In December 1974, the Czechoslovak embassy in Washington, DC sent Svoboda a notification about this. [1]

Svoboda arrived in Czechoslovakia on Wednesday, January 29, 1975, to claim funds deposited in Živnostenská banka. On Thursday, January 30, 1975, at 10:00, he held a meeting at Aritma and subsequently visited the VÚMS at 11:00. [1][4]

As the founder of the VÚMS, Svoboda had significant symbolic capital, which was manifested during his visit in

both a positive response from former colleagues and intense interest from security forces.

3.1 Visit timeline

The records and information contained in volume 581048 "Computer" are not arranged chronologically, and therefore, to meet the objectives of this study, it was useful to reconstruct the timeline of Svoboda's visit to Prague in January 1975.

To better understand the broader context, this timeline is supplemented with important milestones in Svoboda's life, obtained through research in other sources [4] [5] [6] [7] [8], as well as key geopolitical events.

The following timeline in connection with A. Svoboda has not yet been published and thus presents the chronological sequence of the visit to Prague and the milestones of Svoboda's life.

Saturday, March 23, 1957 (8:00 a.m. - 12:15 p.m.)

As a prominent figure in Czechoslovak computer research, Svoboda was monitored by the StB. As part of the so-called recruitment attempt on March 23, 1957, in which the StB tried to recruit Svoboda to cooperate**,** the volume contains his direct statement, in which he unequivocally rejects any form of cooperation with the StB, consisting of monitoring or reporting collaborators. This statement stands in contrast to a later short note by the StB about recruiting him to cooperate, which, however, is not supported in the surviving material by follow-up records of task performance or regular contact. [1]

Period 1957–1964

Svoboda planned the way to emigrate, including the use of balloons or underwater devices. After two attempts through the East Germany and one attempt through Poland, he finally successfully emigrated with his family and the family of his doctoral student (then aspirant) Miroslav Valach (1926–2023) through Yugoslavia. [4]

Sunday, August 16, 1964

Antonín Svoboda (1907–1980), Milada Svobodová (1909–2006), and Tomáš Svoboda (1939–2022) traveled from Prague on a 21-day private trip to Yugoslavia in an IFA passenger car. [1]

The state authorities of ČSSR prevented its citizens from emigrating to the West. Thus, even a trip to the seaside for a summer holiday in the then socialist Yugoslavia was only permitted through socialist Hungary, not through capitalist Austria. Austria was the destination of emigration or a transfer station for emigration to Germany, the USA, Canada, Australia or elsewhere in the West.

Miroslav Valach's son, six-year-old Pavel, broke his leg while the Svoboda and Valach families were in a camp in Yugoslavia. The Valach family, along with Milada Svobodová, who posed as his aunt, obtained permission from the Yugoslav and Austrian border authorities to return to Czechoslovakia via Austria. They did not have to return via the usual route through Hungary, which enabled their subsequent emigration via Austria to Germany. This account is based on oral testimony, primarily from an interview with Antonín Svoboda and corroborated by an interview with Miroslav Valach. [4] [5]

Svoboda and his son Tomáš had permission to travel to Switzerland due to their work on computer development and therefore travelled from Yugoslavia via Italy and Switzerland to Germany, where the two groups met. This reconstruction is likewise based on oral testimony. [4] [5]

Tuesday, September 8, 1964

After the permitted period expired, none of the family returned to Czechoslovakia; a later judgment states that from that date they remained abroad without permission from the Czechoslovak authorities and subsequently traveled to the USA with the intention of settling there permanently. [2]

Autumn 1964

The Svoboda and Valach families were together in Frankfurt in the fall of 1964, waiting for Pavel Valach to recover and be allowed to leave Europe for the USA. [5]

Monday, January 18, 1965

In ČSSR, an inventory of Svoboda's family's property has been carried out. Personal belongings and household furnishings were sold off to various state enterprises (e.g. Klenoty – a state jewelry retailer, Kniha, n.p. – a state book distribution enterprise, Hudební antikvariát – a music antiquarian bookshop, Sběrné suroviny – a state recycling and scrap collection enterprise), and the proceeds were recorded as state income of the Prague 6 District National Committee (Czech abbreviation ONV). [1]

Tuesday, March 2, 1965

The Regional Administration of the Ministry of the Interior (Czech abbreviation MV), (Prague Investigation Department) terminated the criminal prosecution of Svoboda's family with a proposal sent to the Regional Prosecutor's Office. It proposed filing an indictment under Section 109/2 (leaving the Republic), deciding to seize property, and considering the penalty of losing the title of Laureate of the State Prize of the First Degree for Antonín Svoboda. [1]

Monday, March 22, 1965

The District Prosecutor for Prague 6 filed an indictment against Dr. Ing. Antonín Svoboda et al. for the crime of leaving the republic under Section 109/2 of the Criminal Code (Ref.: I Pv 17/64). [1]

Thursday, April 22, 1965

The main trial was held at the District Court for Prague 6 (Ref.: 1 T 59/65) and the verdict was: Antonín Svoboda: unconditional prison sentence of 1.5 years; Milada

Svobodová and Tomáš Svoboda: unconditional prison sentence of 1 year. [2]

The court found that hostile motives against the state were not proven, therefore no forfeiture of property was ordered. [2]

Period 1966–1968

In 1966 Antonín Svoboda joined the University of California, Los Angeles (UCLA), where he was appointed professor in 1968. [6]

Friday, January 5, 1968

The election of Alexander Dubček as First Secretary of the Central Committee of KSČ marked the beginning of the Prague Spring reform process in ČSSR. This period included political liberalization, a relaxation of censorship, and a series of rehabilitations of people convicted in the 1950s. It also involved an attempt at economic reform led by Ota Šik within the socialist system (so-called "Socialism with a Human Face").

Thursday, May 9, 1968

The President of the ČSSR, Antonín Novotný, declared an amnesty (set in the context of the political emancipation of The Prague Spring of 1968), which also applied to the sentences imposed on A. Svoboda and his family.

Thursday, May 16, 1968

The District Court for Prague 6 decided in a closed session that Antonín Svoboda et al. were included in the amnesty of the President of the Republic of May 9, 1968. Their prison sentences were remitted, but without changing the original legal assessment of the act. [3]

Wednesday, August 21, 1968

In the early hours of the morning, troops from five Warsaw Pact states (USSR, Poland, East Germany, Hungary and Bulgaria) entered the territory of ČSSR, forcibly ending the reform phase of The Prague Spring.

Wednesday, August 21–Friday, August 23, 1968

The subsequent military occupation of ČSSR led to the de facto takeover of control over key state institutions, over production in industry, agriculture and the tertiary sector, a fundamental limitation of ongoing political reforms and the gradual onset of a period of so-called normalization.

November 1972–July 1973

In November 1972, a preparatory conference of diplomatic representatives was held in Helsinki, which initiated the process of the Conference on Security and Cooperation in Europe (CSCE).

In July 1973, a conference of foreign ministers was held in Helsinki, which formally launched a multi-stage negotiation process and established its procedural framework for the CSCE. It may be assumed that the ongoing CSCE process and the partial political relaxation associated with it may have contributed to the peaceful course of A. Svoboda's visit to Prague in January 1975.

Thursday, July 4, 1974

The Office for Inventions and Discoveries made an inquiry to the District Court for Prague 6 (OSP6) as to whether Antonín Svoboda had been sentenced to forfeiture of property. The inquiry was apparently related to the resolution of patent claims, and the immediate impetus for this step could not be clearly documented from the available sources. [1]

A similar inquiry to OSP6 regarding the use of Svoboda's patents was made in 1968 by the Aritma company, which thus verified that Svoboda had not been declared to have lost his property in the 1965 court decision.[1]

Wednesday, August 7, 1974

By decision of the State Notary Office of 7 August 1974, 26,237 CZK was deposited in the Živnostenská banka in favor of Antonín Svoboda as a reward for the use of his patents. [1]

Tuesday, August 13, 1974

According to the StB report of August 13, 1974, A. Svoboda obtained passport No. A–1562040 in the USA. [1]

Friday, December 6, 1974

The Embassy of ČSSR in Washington sent Svoboda a letter (Ref.: 31.412/74 – Maj/Pk) to his then-residential address in the USA – Santa Monica, 817 22nd Street. The contents of the letter informed him about the funds deposited in the Živnostenská banka and the need to claim them. A. Svoboda subsequently stated that based on this letter he was allowed to travel to ČSSR. [1]

Wednesday, January 29, 1975

On January 29, 1975, Svoboda arrived in Czechoslovakia. According to documents, the trip was related to the handling of financial matters related to patents. [1]

Thursday, January 30, 1975 (10:00–11:00)

Svoboda was received by Jiří Vodehnal, deputy director for technical development at Aritma Vokovice, presented a copy of the embassy's letter and discussed the payment of the reward for the use of his patent at Aritma. He found out that the payment required opening a foreign account and that the State Bank of Czechoslovakia (Czech abbreviation SBČS) gave permission to pay foreign currency to foreigners. Aritma promised to negotiate with SBČS on the matter and to inform A. Svoboda of the outcome. [1]

Thursday, January 30, 1975
(shortly after 11:00 a.m. – shortly after 12:00 p.m.)

Svoboda visited the VÚMS. After a chance meeting in front of the institute building with staff member Zdeněk Kašpar, news of his presence spread quickly. The director of the VÚMS, Ing. Josef Vraný, verbally permitted Svoboda to enter the institute's premises under certain restrictions (a reserved room, constant escort, prohibition of professional discussions about the institute's tasks).

Antonín Svoboda was then welcomed by the head of Sector 7110 of Basic Systems Research, Assoc. Prof. Jaroslav Vlček; he subsequently met with approximately 30–50 employees. Photo documentation of the meeting was taken, and Svoboda also took his own pictures as he left. He left the premises in a gray-green Renault car with a driver who has not yet been identified. [1] [4]

Thursday, January 30, 1975

Based on the request of Aritma from January 30, 1975, to open a foreign currency account at Živnostenská banka, a total of 57,860 CZK was transferred to A. Svoboda, who lived outside the territory of ČSSR. [1]

Friday, January 31, 1975 (around 10:00)

According to the recording, Svoboda contacted Aritma by phone to learn the outcome of the company's negotiations with the relevant SBČS employee regarding the possibility of paying patent royalties. [1]

Monday, February 3, 1975

The StB report for the Municipal Committee (MěV) of the KSČ states that Svoboda visited Czechoslovakia between January 29 and February 3, 1975. This marks the end of his stay in Prague. [1]

Tuesday, February 4, 1975

The StB report states that the relevant unit learned about Svoboda's visit to the VÚMS only after he left Czechoslovakia, on February 4, 1975. Only then did the agency-operational investigation take place, including securing photographic documentation (2 films, 71 shots). [1] From the available materials, it appears that the visit was not recorded in advance by the StB.

Monday, February 10, 1975

A StB document entitled Proposal to open a file on a person under investigation (PO – prověřovaná osoba) concerning Antonín Svoboda is dated on this day. The document summarizes his arrival on January 29, 1975, his visit to VÚMS on January 30, 1975, and records his address in the USA (Santa Monica, 817 22nd Street) and his employment at the University of California. [1]

Wednesday, February 12, 1975 (10:00–11:45)

Jaroslav Vlček was questioned by the State Security (StB) within the Regional Administration of the National Security Corps (KS SNB). He described Svoboda's arrival at VÚMS, his consultation with Director Vraný, the measures taken (isolation, escort), the atmosphere of the meeting, the photographic documentation, and the circumstances of his departure. [1]

Thursday, February 13, 1975

Dr. Svoboda–emigrant–information about his visit to the Aritma Vokovice and VÚMS is dated. The document systematically recapitulates Svoboda's visit to Aritma and VÚMS and provides information about his passport, address, purpose of stay and the course of the meeting. [1]

Monday, February 17, 1975

The StB report for the Secretary of the Communist Party of Czechoslovakia summarizes Svoboda's visit to Czechoslovakia (January 29 – February 3, 1975), his accommodation at the Hotel Paříž and the purpose of his stay (to settle financial claims at the Živnostenská banka). It also states the intention to take measures to prevent further trips by Antonín Svoboda to Czechoslovakia. [1]

Friday, February 28, 1975

StB operative, Lieutenant Colonel Janák, wrote record No. 9/75, which contains an interview and mediated information from Václav Kovařík, staff member of the VÚMS Hloubětín, about Svoboda's visit, including the reactions of the employees, assumptions about the motives for the reception, and notes on the role of the Communist Party's Plant Committee (Czech abbreviation ZO) and personal ties. [1]

Tuesday, March 11, 1975

The StB report for the 11th administration of the Federal Ministry of the Interior (Czech abbreviation FMV) recapitulates the purpose of Svoboda's trip to Prague, the embassy's letter of December 6, 1974, the patent agenda, the flow of deposited amounts, and the circumstances of the visit to Aritma and VÚMS. It also summarizes the earlier criminal prosecution (1965), the amnesty (1968), property transactions and subsequent measures and findings after the visit. [1]

September 1973–June 1975

Expert negotiations were held in Geneva on the individual baskets of the future CSCE Final Act, covering security, economic and scientific and technological cooperation, and human rights. This parallel process of international de-escalation could have helped to create a broader political framework within which Svoboda's visit to Prague in January 1975 took place successfully.

Friday, August 1, 1975

The Final Act of the CSCE was signed in Helsinki on August 1, 1975, by representatives of 33 European states (including ČSSR), Canada and the USA. The document confirmed the post-war order in Europe and at the same time enshrined commitments in the areas of human rights, cooperation and the free exchange of information. These

commitments were later reflected both in the emergence of initiatives such as Charter 77 and in the gradual expansion of international scientific contacts.

Year 1977

Antonín Svoboda suffered his first heart attack. [6]

Sunday, May 18, 1980

Professor Antonín Svoboda died of another heart attack at his home in Portland, Oregon, USA. [6]

Thursday, November 17, 2022

A. Svoboda's son, musician and professor Tomáš Svoboda, died of a second stroke at his home in Portland, Oregon, USA. [7]

3.2 Photo documentation from the visit

Extensive photo documentation was taken of Svoboda's visit, which is also part of volume 581048 "Computer". The analysis of this photo documentation represents an original research contribution.

According to the archival record, photographic documentation of the visit was carried out on the instruction of Assoc. Prof. Vlček by a VÚMS photographer Hana Mahlerová. The documentation was subsequently handed over to StB and incorporated into the file.

The photo documentation of the visit allows us to reconstruct not only the chronology of A. Svoboda's movements in Prague, but also the social dynamics of the meeting. The images clearly demonstrate the spontaneous and significantly positive response from former colleagues in both Aritma and VÚMS, manifested in physical proximity, gestures of intimacy and mass escorts upon leaving both workplaces. At the same time, the VÚMS management's efforts to keep the visit under a controlled regime (reserved spaces, permanent escort) are evident, which corresponds to the written instructions recorded in the volume. Moreover, the presence of A. Svoboda's own photographic activity indicates his personal motivation to preserve the memory of the meeting. The whole of the photographic documentation thus significantly refines the interpretation of the course of the visit to Prague.

As an illustrative example, at least three photographs can be cited, demonstrating the joyful and friendly atmosphere of the meeting.

Image 1: Photo 1. Svoboda with VÚMS staff during an interview in the office of the Basic Systems Research Sector.
Source: ABS, MT H/MH Fund, Call Number KR–581048 MV, Volume 581048 "Computer", file X60771, page 8/48.

Image 2: Photograph 14. Svoboda is on the phone in the office of the basic systems research sector, Kašpar is holding his arm intimately, who first met Svoboda in front of the institute when he went to the Aritma research center and then announced this at the institute.
Source: ABS, M TH/MH Collection, Call Number KR–581048 MV, Volume 581048 "Computer", file X60771, page 14/48.

Image 3: Photo 48. A group of VÚMS workers who came to see Svoboda off in front of the institute building. In the foreground, Svoboda holding his own camera. The picture shows the ground floor of the VÚMS building and the main entrance.
Source: ABS, MT H/MH Collection, Call Number KR–581048 MV, Volume 581048 "Computer", file X60771, page 31/48.

3.3 Historical visit analysis

Antonín Svoboda's visit to Prague on 29–30 January 1975 is a valuable source for studying the relations between the Czechoslovak scientific community and exiled experts during the period of so-called "Normalization". Archival materials show that the immediate impetus for Svoboda's trip was the claim to patent royalties at the national enterprise Aritma, but its symbolic and professional significance went far beyond the administrative level.

The negotiations at the Aritma company took place in an official and relatively controlled regime, focused on the technical and legal aspects of the payment of patent royalties**.** The institutional response of the company was formally accommodating, but at the same time bound by foreign exchange and administrative restrictions, which were typical for dealing with emigrants. This episode well illustrates the tension between the state's economic interest in exploiting Svoboda's inventions and the political distrust of him as a person.

Svoboda's meeting at the VÚMS had a completely different dynamic. Photo documentation and witness statements alike show an exceptionally warm welcome from former colleagues and students. Repeated physical expressions of closeness (shaking hands, hugging, being escorted to the front of the building) testify to the continuing professional and personal capital of the institute's founder. At the same time, however, the institute's management adopted preventive measures, controlled escort, a reserved space and a ban on professional discussions, which reflect the security framework of the time.

The photographic documentation taken on the instructions of the VÚMS management and subsequently seized by the StB represents a typical example of the secondary use of internal material for operational purposes. The chronological arrangement of the images allows for a detailed reconstruction of the course of the visit and at the same time shows the disproportion between the spontaneous collegial reception and institutional control by the regime.

The meeting thus reveals the duality of Svoboda's position in the mid-1970s: on the one hand, a respected founder of Czechoslovak computing with high symbolic capital, on the other, a politically untrustworthy émigré subject to increased interest and control by security forces. It is this ambivalence that makes Svoboda's visit analytically extremely significant for the study of knowledge transfer, scientific networks, and mechanisms for controlling contacts with foreign countries during the period of so-called "Normalization".

4. Conclusion

The presented study reconstructs, based on the previously systematically unused volume 581048 "Computer", the course and context of A. Svoboda's visit to Prague in January 1975. It shows its significance for understanding the relations between the exiled scientific elite and the institutions of normalizing Czechoslovakia.

The analysis confirms that although Svoboda's journey was officially conducted as a technical-financial agenda linked to patent claims, its impact had a significant professional and symbolic dimension. The interpretation was further refined by comparison with other sources (CBI interviews, private testimonies and university obituaries), which allowed to place the archival records in a broader biographical and institutional context. The study also reconstructs, based on StB archival records, the precise chronology of Antonín Svoboda's visit to Prague in January 1975, thereby providing new insight into the interaction between exiled scientists and the institutions of the Czechoslovak Socialist Republic during the period of so-called "Normalization".

The documents confirm the high heuristic value of archival sources of the security services for research into the history of technology and the biography of A. Svoboda, especially when studying contacts with foreign countries and the mechanisms of their regulation. Despite the fragmentary and purposeful nature of the StB operational records, a convincing reconstruction of the event and its historical significance can be achieved through their critical reading and triangulation with additional sources.

Acknowledgements

Research described in the paper was supervised by prof. Dr. Ing. Martin Pospíšil, Ph.D. (FA CTU in Prague) and prof. PhDr. Marcela Efmertová, CSc. (FEE CTU in Prague) and supported by SGS 2026.

References

[1] SECURITY SERVICES ARCHIVES (ABS), MTH/MH Fund, Call Number KR–581048 MV, Volume 581048 "Computer", files X60762, X60766, X60770, X60771.

[2] ABS, MTH/MH Collection, Call Number KR-581048 MV, Volume 581048 “Computer”, file X60766. DISTRICT COURT FOR PRAGUE 6. Judgment in the case of Dr. Ing. Antonín Svobody and et al., file no. 1 T 59/65, 22. 4. 1965, pp. 97–99.

[3] ABS, MTH/MH Fund, Call Number KR-581048 MV, Volume 581048 "Computer", file X60766. DISTRICT COURT FOR PRAGUE 6. Resolution on participation in the amnesty of the President of the Republic of 9 May 1968 in the case of Antonín Svoboda and co., 16 May 1968, p. 101.

[4] SVOBODA, Antonín. An Interview with Antonín Svoboda. Charles Babbage Institute, University of Minnesota Libraries, 15 Nov. 1979. Available at: https://umedia.lib.umn.edu/item/p16022coll92:0 (accessed 20 Feb. 2026).

[5] VALACH, Pavel. Interview with the author, 9 Dec. 2025 (oral history). Unpublished recording in the author's private archive.

[6] UNIVERSITY OF CALIFORNIA. Antonín Svoboda. In: In Memoriam. Berkeley: University of California, 1981, pp. 255–257. Available at: https://oac.cdlib.org/view?docId=hb0t1nb4k4

[7] PORTLAND STATE UNIVERSITY. Tomas Svoboda (1939–2022). In Memoriam. Portland: PSU, 2022. Available at: https://www.pdx.edu/events/tribute-tomas-svoboda

[8] EFMERTOVÁ, Marcela et al. Czech Footprint in the History of Computing [DVD-ROM]. Prague, Czech Technical University in Prague, 2021, especially pp. 115-135. ISBN 978-80-01-06918-9.

About Author

Jaroslav Kalvoda studied technical cybernetics at the Faculty of Electrical Engineering of the Czech Technical University in Prague (1988), where he defended his diploma thesis Toroidal aviation compass with amorphous ferromagnetic material under the supervision of Assoc. Prof. Ing. Karel Draxler, CSc. He subsequently expanded his education through Continuing Studies in the field of diplomacy at the University of Economics in Prague (2004–2006) and in the field of Business Administration at the University of California, Berkeley (2007–2012) and Stanford University (2007–2020). He subsequently defended his Master of Business Administration (MBA) degree at the Central European Management Institute (2025).

His professional career is at the intersection of technical sciences, management, and the international Czech-American environment, which allows him to combine historical analysis with an understanding of technological development and institutional contexts.

His current research within the Department of History of Science and Technology at the Historical Laboratory of (Electro)Technology, K13116, Faculty of Electrical Engineering of the Czech Technical University in Prague seeks to reconstruct lesser-known episodes of Czechoslovak scientific emigration to the USA and to place technical figures in the broader framework of the Cold War, geopolitics, and knowledge transfer between Europe and the United States, especially during the period of so-called “Normalization”.

Emanuel Šlechta: Professor, Innovator, and Entrepreneur in the Interwar Period

Ing. Jiří Sedláček

Historical Laboratory of (Electro)Technology, Dep.of Economics, Management and Humanities, FEE, CTU in Prague, Technická 2, CZ-166 27 Prague 6

sedlaji6@fel.cvut.cz

Abstract: *This paper focuses on the personalities of the labour organisation movement, including engineer Emanuel Šlechta, who was appointed Secretary of the Czechoslovak Committee for the Scientific Management of Labour upon his return from the USA.*

Keywords

The scientific labour organisation,

1. Introduction

The social anchoring of the personality of Emanuel Šlechta (1895-1960) fully corresponds to the economic and social development of the Czech lands and Czechoslovakia at the turn of the 19th and 20th centuries, between the wars and just after World War II. Šlechta grew up as an only child in a modest family of a chimney sweep in Kutná Hora, where he attended the municipal school and the Higher State Real School, where he graduated with honours in 1914.[1] This entitled him to enter the Czech Technical College in Prague, but he did not complete his higher engineering education until after the establishment of independent Czechoslovakia in 1921 at the Czech Technical University in Prague.[2] His graduation during the first decade of the 20th century was prevented by the First World War and his compulsory involvement in it. After graduating in technology, he began his career as a technical expert, entrepreneur, innovator and university teacher and became a representative of the emancipating Czechoslovakia economically, socially and culturally in the period between the wars. Engineers like him became important figures in the business and technical environment and were at the core of the emerging Czech technical intelligentsia.

It was they who, in the last third of the 19th century, became the key carriers of technical progress in the Czech lands and mediators between the professional and wider public. Through their publications, engineers made a significant contribution to the dissemination of new technical knowledge, both through professional

[1] Archive of the Czech Technical University in Prague, personal fund, Professor Emanuel Šlechta

[2] Ibid.

literature and lectures addressed not only to an educated audience but also to the general public. Šlechta, who had joined this society at the beginning of the 1920s, thus became not only a witness, but above all an active agent of the new era, both positively and negatively, in the general peripeteia that followed.

After the establishment of an independent Czechoslovakia in 1918, the new state inherited favourable economic conditions. From the former Austria-Hungary it took over approximately 70 % of all the industrial production of the monarchy, especially the engineering, armaments, glass, textile and electrical industries. Czechoslovakia thus became one of the most industrialised countries in Europe right from the very beginning of its existence. Another important factor was the high literacy rate of the population and the well-developed technical education, including professional associations, which enabled the training of qualified specialists for the economy.

The economic stabilisation was also supported by the introduction of the Rašín reform in 1919 with the creation of its own currency - the Czechoslovak koruna, and thus a relatively stable financial policy was established. Czechoslovakia had its own tax, banking and customs systems, and soon developed a modern economic infrastructure. In this respect, it was the most economically prepared successor state after the collapse of the multi-ethnic Austro-Hungarian monarchy.

Despite its strong industry, however, Czechoslovakia had to cope with the disintegration of the former monarchy's internal market, which meant the loss of traditional outlets for its products. Foreign trade had to be oriented towards new partners, especially in Western Europe and the Balkans. Moreover, the economic structure of the country was uneven, with the industrialised parts of the country outpacing those with predominantly agricultural production.

Czechoslovakia's international position was strengthened after World War I by the Versailles system, which ensured its existence and recognized its borders. Moreover, the weakening of Austria and Hungary allowed Czechoslovakia to play a regional role. Nevertheless, stronger economic integration in the region was lacking - efforts at economic cooperation under the so-called Little Agreement of 1921 remained limited.

A significant turning point came after 1929 with the arrival of the world economic crisis, which hit Czechoslovakia very hard. Industrial production fell by up to 40%, unemployment reached extreme levels and the crisis hit the border area with Germany hardest, with political consequences. It was only from 1934 onwards that the economy gradually stabilised, mainly thanks to exports and state protectionist measures. Although Czechoslovakia regained its place among the highly industrialised countries of the world in the second half of the 1930s, geopolitical changes in Europe, especially the growing pressure from Nazi Germany, led to a weakening of its international position. The Munich Agreement of 1938 meant not only territorial losses, but also the economic and political weakening of the state.

2. Czechoslovakia – Central European rationalisation

In the inter-war period, Czechoslovakia was essentially a democratic and economically strong, stable state that was able to cope with the initial challenges, but its long-term economic prospects were gradually weakened by external and internal factors. Despite the world crisis, the state maintained a high degree of industrialisation, but the geopolitical situation and the onset of World War II eventually undermined its further independent development.

After the end of World War II in 1945, Czechoslovakia faced the task of rebuilding its destroyed economy, infrastructure and state administration. In May 1945, the Czechoslovak Republic was restored, but with some fundamental changes - the pre-war form of the First Republic was not restored, but a new regime known as the Third Republic (1945-1948) was established. Key political and economic changes took place during this period: nationalisation of large industries, banks and mines took place on the basis of the Benes Decrees, the Communists (KSČ) won the elections in the Czech lands in 1946, while the Democratic Party dominated in Slovakia and the displacement of the German and partly Hungarian population from the borderlands was implemented.

The turning point was February 1948, when the Communists staged a coup d'état and took full control of the state. This was followed by the building of a Soviet-style totalitarian regime which affected all areas of life. There was the liquidation of political opposition, persecution, censorship and the rise of the State Security Service (StB). 1950 brought political trials, repression and arrests of the uncomfortable in the army, the church and among intellectuals.

Stalinization continued under the presidencies of Klement Gottwald (1948-1953), Antonín Zápotocký (1953-1957) and later Antonín Novotný (1957-1968). During the 1950s, ideological control, repression and the cult of personality culminated. After the deaths of Stalin and Gottwald in 1953, there was a slight relaxation, but no real change in the system.

The period 1945-1960 thus represents the transition from democratic renewal to full communist dictatorship. After the hopes of the post-war period came February 1948, which brought the country into an era of communist ideological surveillance of citizens, economic planning and restrictions on civil liberties. It was not until the early 1960s that the first signs of efforts to reform the system began to emerge, but these were not yet politically viable.

It is in this complex context that the mechanical engineer, publicist and originally National Socialist politician Emanuel Šlechta first emerges as an important personality in the 1920s and 1930s. At that time, he established himself as a teacher at the Czech Technical University in Prague and began his entrepreneurial journey of transferring technological innovations, especially from the United States to Czechoslovakia, during his stay there from 1923 to 1926. He thus conveyed to the republic important scientific and technical information (scientific organisation and management of work, rationalisation, linking the technical and cultural social spheres, etc.), which he later applied throughout his subsequent career, and wanted to see directly applied to the Czechoslovak economy and technology. Therefore, he also intensively devoted himself to his own business to gain experience and expert advice and to popularise technical innovations in the trade press.

Tracing Šlechta historically in this context can be done from many angles, but in this paper the authors would like to highlight, within the trajectory followed, the answers to the above questions through three areas that the activities of E. Šlechta, namely his Central European rationalizations in collaboration with Professors František Hasa from Prague and Karel Adamiecki from Poland, the importance of his appearances and support for scientific organization and management of the work, including the interruption of these efforts by his arrest at Buchenwald, and the post-war period that held so much promise for him but ultimately took his life.

3. Professor Emanuel Šlechta

After World War I, in the heat of which he fought on the Russian and Italian fronts as a private soldier and where he was wounded in the arm, which enabled him to leave the war, he received his diploma from the Czech Technical University in Prague in 1921. There, Emanuel Šlechta studied mechanical engineering, pursued higher mathematics, mechanical technology and accounting in industrial plants, and became interested in traveling to further his education.[3]

In 1922, he started working as an engineer in the sugar department of the First Czech-Moravian Machine Factory in Prague, where he participated in the reconstruction of the sugar factory in Ovčary in the Kolín region together with experts from other important companies such as Bráf and Co. and Škoda Plants. Subsequently, with the support of the Masaryk Academy of Labour (abbreviated in Czech as MAP)[4] and its prominent representative Stanislav Špaček (1876-1954)[5], he joined the Mining and Metallurgical Company (Lazarská 7, Prague 2), where he stayed until his arrest by the Gestapo in 1939 and where he began working for the Czechoslovak Committee for the Scientific Organisation of Labour. Labour organisation and management was a modern field that Šlechta had discovered during his stay in the USA and which he transferred to Czechoslovakia. It was primarily the work of the American Frederick Winslow Taylor and the Frenchman Henri Fayol that brought many innovations to industrial practice, especially in administration, management and corporate governance. In Czechoslovakia, these were already promoted and used in practice by the proponents of this scientific theory (Stanislav Špaček, Václav Verunáč) and management practice in large enterprises (Franz Hummelberger - Poldi Kladno, Karel Loevenstein - Škoda Plzeň, Tomáš Bat'a in Zlín).

By that time Šlechta had already completed the aforementioned work experience in the USA, where he worked at The Baldwin Locomotive Works in Philadelphia, was a machine tool designer and headed the department of standardization of locomotive cladding systems at Niles Tool Works in Hamilton, then became assistant chief engineer at The Great Western Sugar Co. in Denver, Colorado, a member of the Society of American Mechanical Engineers (A. S. M. E.) and participated in shop work in the Philadelphia branch of the Society. After returning to Czechoslovakia in 1926, he had excellent knowledge to apply modern scientific organization of work and enough new technical knowledge, which he immediately put to use in his employment at the Škoda Hradec Králové plant.

In December 1927, he became a silent partner in the machine shop of entrepreneur T. Aupek in Kutná Hora.[6] Apparently, he used the funds he earned in America here. It was a machine shop with 15 machines, a foundry and a forge, which employed about 45 people at the time of the boom. He was going to introduce mass production here on the American model and consulted Stanislav Špáček about it.[7] He

[3] Archive of the Czech Technical University in Prague, personal fund, Professor Emanuel Šlechta

[4] Established by Act No. 86/1920 Coll., with the aim of supporting the technical and socio-economic development of the republic through research institutes and expert committees and with the support of President T. G. Masaryk in the amount of 1 million CZK.

[5] Masaryk Institute and Archives of the Academy of Sciences of the Czech Republic, personal collections, NAD 438, Stanislav Špaček, 1896–1951.

[6] A. POSPÍŠIL. Zmizelá Kutná Hora: Stavby první republiky [In Czech; Disappeared Kutná Hora: Buildings of the first republic]. Kutná Hora, 2019 and also Masaryk Institute and Archives of the Academy of Sciences of the Czech Republic, personal collections, NAD 438, Stanislav Špaček, sign. II.b) 1 A, inv. no.: 543, letter from E. Šlechta to S. Špaček from 1. 8. 1929.

[7] Ibid.

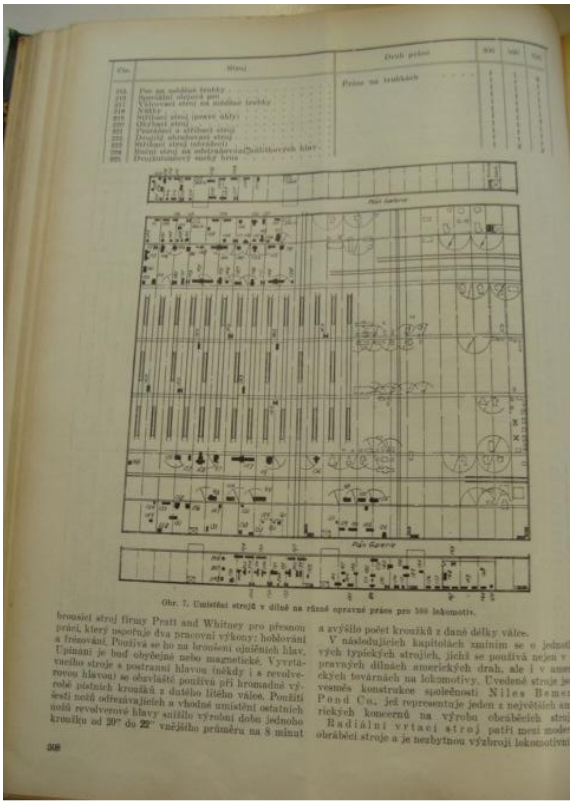

Pict. 1.1 Slechta's article in Strojnický Obzor *(source: Archive of the Czech Technical University in Prague)*

considered what would be the most suitable product (he suggested, for example, American locks with flat keys). He also considered items for modern households, e.g. burners, refrigeration, winterizing machines, etc. He hoped to get a license for production from American companies. His plans were somewhat affected by the coming economic crisis. However, it also brought demand from entrepreneurs to transform their companies to a different kind of production, and so, in addition to his share in Aupek's machine shop, he focused on external consulting for industrial companies. He also had a stake in the ESTA record factory.[8] Together with the banker František Hašek, Mr Šolcký, the director of consumer cooperatives, and Jaroslav Šalda, he significantly influenced the operation of the Melantrich publishing house as a shareholder.

From the plant in Hradec Králové, Šlechta moved in 1927 to Bata's plant in Zlín. He applied his knowledge of the scientific organization of work to the problems in the Bata workshops - he completely rebuilt the machine shops and the forge with hardening shop and designed a different location for the warehouse. He arranged a tool room and made an inventory of all tools and machines, made inquiries about the correct speed of machines, standardized the knives and production procedures used, and focused on the management of mass production where it was not yet working.

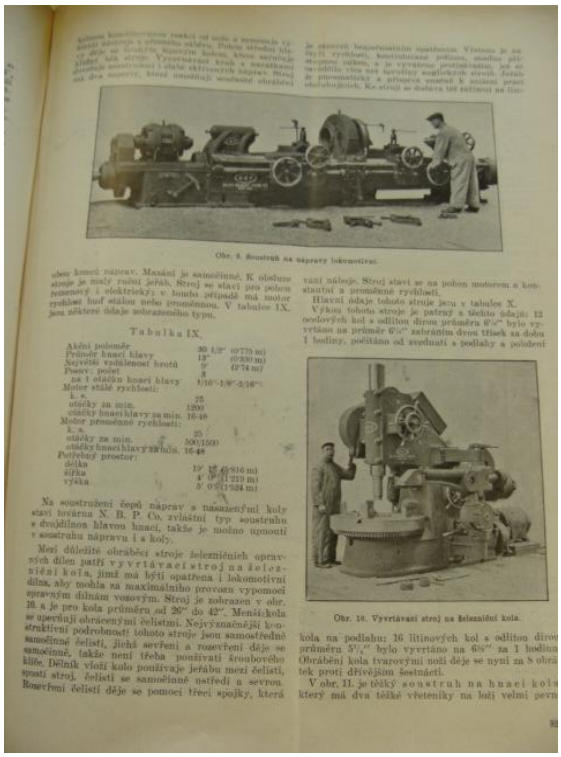

Pict. 1.2 Slechta's article in Strojnický Obzor *(source: Archive of the Czech Technical University in Prague)*

The work carried out here became the basis for his further studies at the Czech Technical University in Prague, where in 1929 he submitted his dissertation The Economic Size of Serial Production. On 28

[8] SZCEPANIK, Petr. Film and the recording industry: the case of Ultraphon. Iluminace 2007, no. 3, p. 102.

November 1928, in connection with his work on the dissertation, he was elected as an expert of the 6th National Economic and Social Department of the Masaryk Academy of Labour. In March 1929, he received the authorization of authorized civil engineer for machine building. This allowed him to conduct design work, sign and verify technical documentation, perform calculations, act as an expert in the field of organisation and management of work and rationalisation in the construction of machinery, and to negotiate on behalf of his clients with the authorities, e.g. when authorising production or construction work. In order to work, he had to be of good civil standing and have a clean criminal record. From 1929 he also held the position of permanent expert witness in the field of general engineering at the Regional Commercial Court in Prague. In 1935 he added to this activity an associate professor's degree in mechanical engineering at the Czech Technical University in Prague. In 1930-1938 he was a permanent adviser on industrial financing to the Anglo-Bank and the Land Bank in Bohemia. These were all important positions which signalled that Šlechta had become a widely addressed and respected expert in the field of engineering, rationalisation and scientific management and organisation of work.

His preparation for a wider embedding of his work in the field of scientific organisation and rationalisation thus led to the opportunity to establish new domestic and international contacts. He sought these mainly from individual national societies, e.g. He also sought out national associations, such as the French Comité National de l'Organisation Française (founded in Paris in 1901) and the Comité International de l'Organisation Scientifique (acronym CIOS), as well as nine other national committees: Belgian (Comité National Belge de l´Organisation Scientifique), Bulgarian (BONOT, Comité National Bulgare de l´Organisation Scientifique), Spanish (Comité National Espagnol de l´Organisation Scientifique), American (Joint Comittee on American Participation in International Management Congress), Dutch (Neederlaandsche Institut voor Efficiency), Italian (Ente Nazionale Italiano per l´Organizzazione Scientifica del Lavoro), Polish (Comité National d´Organisation Scientifique en Pologne), Romanian (Institut Roumain d´Organisation Scientifique) and Czechoslovak (Czechoslovak National Committee for Scientific Organisation, founded 24. 6. 1924 - Czech acronym ČSKO - Comité National tchécoslovaque de l´Organisation Scientifique). In addition, as Secretary of the Czechoslovak Comité, he was in contact with the corresponding corporations in Germany, England, Austria, Estonia, Finland, Greece, Hungary, Japan, Lithuania, Luxembourg, Portugal, Russia, Norway, Switzerland, Turkey, Yugoslavia.[9]

This really assumed that he was able to organize, prepare and implement his work rationally, but also that he was recognized abroad and that he was able to apply his language skills.

The first international congress for the scientific organisation of labour was convened by the Masaryk Academy of Labour in Prague in 1924, where the organising committee was headed by Stanislav Špaček. Other Czech personalities such as František Hasa and Emanuel Šlechta subsequently represented the country on the international expert committees of the various congresses held between 1924 and 1938 (Brussels 1925, Rome 1927, Paris 1929, Amsterdam 1932, London 1935 and Washington 1938). Špáček managed to attract not only representatives of the Taylor Society and the American Engineering Council to the first congress in Prague, but also the leading authorities in the field - Frank Bunker

[9] Zprávy ČSKO, November 1929, volume II, number 9.

(1868-1924) and Lillian Moller (1878-1972) Gilbreth, American pioneers of scientific management and founders of time and motion studies, which became the basis of modern industrial engineering, ergonomics and management. Frank B. Gilberth noticed that some of his workers worked more efficiently than others and recorded and systematically analysed their work movements. From his analysis, he came up with a reduction of these movements and the concept of therblings, which was a characterization of the basic 17 movements that made up any work task.

His wife, Lillian, added psychology to scientific management, promoting the human factor, creativity, and employee well-being. Thus they combined technical efficiency (Frank) with a human approach (Lillian) in the scientific organization of work. Above all, the Gilbreths' approaches were analyzed at congresses by reference to the work they had done in the U.S. Army, in the civil service, and at General Electric. Congresses were also held in various European cities in the 1930s, and the Gilbreths' work influenced the European rationalization movement[10] (under the slogan *Find the least tedious and smartest way to do work comfortably*), including Czechoslovakia, where their findings, Taylor's results of time stages of individual tasks (with a key method based on standardization, division of labor, control, i.e. According to the motto Find the fastest way to make a person work more) and Fayol's theory of leading the company as a whole (according to the motto *Find the best way to organize and lead the whole company*) Psychotechnical Institute.[11] The latter began to test time studies, work norming and ergonomics in public and private enterprises. It had been working since 1921 at the Masaryk Academy of Labour and focused on research on human performance, psychology, physiology and sociology of work - on the scientific approach to work performance. From the beginning, the institute conducted practice-oriented research in real work environments, such as railways, post offices and ministries. Psychotechnical tests have been introduced as a condition for the authorisation of activities, e.g. for tram drivers or train drivers.

Pict. 1.3 Organization of Industrial Plants (1930)
(source: the author's own archive)

Conclusion

Emanuel Šlechta also worked on these activities and found the closest cooperation in the field of rationalisation and scientific management with professors František Hasa (1863-1945) in Prague and

[10] *Applied Motion Study* (1917), *Fatigue Study* (1916), *Management and the Worker* (1924).

[11] The institute was headed by František Šeracký from 1921 to 1936. Just before World War II, the institute was taken over by the Ministry of Education and National Enlightenment. During the war, it functioned as the Institute of Human Labor (Institut für Arbeitswissenschaft) and after 1947, it became the Czechoslovak Institute of Labor and subsequently the Institute of Occupational Safety, and its original purpose essentially disappeared.

Karel Adamiecki (1866-1933) in Poland. Their collaboration was a key moment in

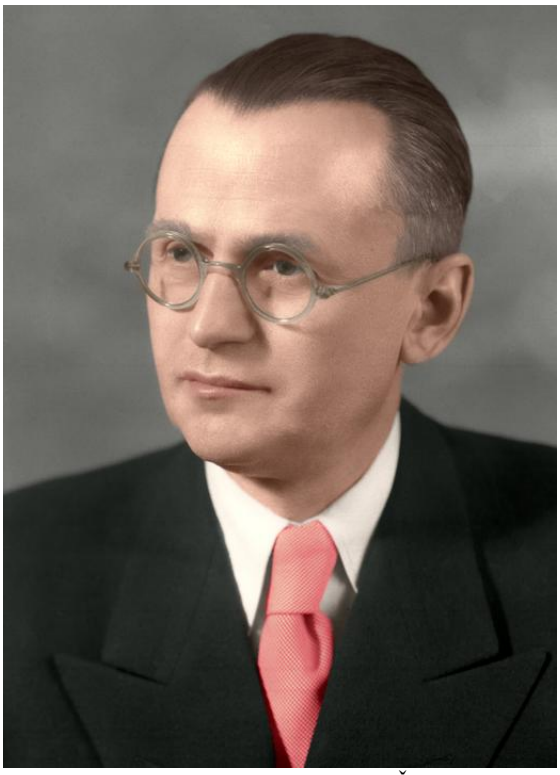

Pict. 1.4 professor Emanuel Šlechta
(source: the author's own archive)

the development of the scientific organisation of work in interwar Central Europe. At that time, Šlechta had already published and had his scientific works positively received by experts and could thus second both personalities. Their activities made a major contribution not only to the professionalisation and rationalisation of industrial processes, but also to the consolidation of an international professional network that linked Czechoslovakia, Poland and other European countries in their efforts to modernise the economy through the principles of scientific management. Their activities brought new methodological tools for the rationalisation of production and public administration, the appropriate selection and assignment of workers in various fields, promoted the internationalisation of professional discourse and helped to create a solid institutional foundation for applied management. Their collaboration was essential for the transition from craft-led production to modern, scientifically organised industry.

Acknowledgements

Research described in the paper was supervised prof. PhDr. Milan Hlavačka, CSc. Supervisor, and prof. PhDr. Marcela Efmertová, CSc. Head of the Historical Laboratory of (Electro)Technology.

References

[1] *Zprávy Československého národního komitétu pro vědeckou organizaci (Zprávy ČSKO):* leden 1929–červen 1929, vydavatel Československý národní komitét pro vědeckou organizaci, Karlovo náměstí 14, Praha 2, nakladatelství „Prometheus“, Praha 8, Na Rokosce.

[2] *Zprávy Československého národního komitétu pro vědeckou organizaci (Zprávy ČSKO):* září 1929–prosinec 1929, vydavatel Československý národní komitét pro vědeckou organizaci, Karlovo náměstí 14, Praha 2, nakladatelství „Prometheus“, Praha 8, Na Rokosce.

[3] Jiří SEDLÁČEK, Marcela EFMERTOVÁ, „Emanuel Šlechta, engineer and entrepreneur in the First Republic of Czechoslovakia“, Praha, Acta polytechnica, speciální číslo Vol. 64 No. 3 (2024): History of Science and Technology.

[4] Jiří SEDLÁČEK, *Emanuel Šlechta: zapomenutý ministr (Emanuel Šlechta: the forgotten minister)*, Hospodářské dějiny-Economic history.

The Food Processor in Czechoslovakia (1930–1960): A Technological Object Between Planned Economy and Rationalization of Domestic Work

Martin Dominik HRTUS[1]

[1] Historical Laboratory of (Electro)Technology, Faculty of Electrical Engineering, Czech Technical University in Prague, Technická 2, CZ-166 27 Prague, Czech Republic

hrtusmar@fel.cvut.cz

Abstract. *The study analyzes the development of food processors (kitchen robots) in Czechoslovakia from interwar expectations to their production in the 1950s. It is based on the observation that the universal kitchen machine was not a natural continuation of interwar technological development, as the range of domestic electrical appliances focused mainly on individual specialized devices. The turning point came after World War II in the context of a nationalized electrical engineering industry and a planned economy. Special attention is paid to the production of the Robot Zbrojovka Brno, its technical design, and the organizational circumstances of its creation. The analysis shows that the design compromises, the production itself, and its subsequent interruption reflected the priorities of a centrally planned economy. The transfer of production to Orlické strojírny and its subsequent stabilization under the ETA brand represented an attempt to integrate a universal machine into a standardized living environment. The kitchen robot is thus interpreted not only as a technical product, but as part of a broader effort to rationalize domestic work in the context of post-war economic policy.*

Keywords

History of science and technology, electrical appliances, food processor, electrification, planned economy, Zbrojovka Brno

1. Introduction

The food processor was one of the most ambitious attempts to mechanize domestic work in Czechoslovakia in the 1940s and 1950s. Unlike individual appliances such as irons or cookers, it was a universal machine designed for multiple tasks in food preparation. However, its development was not a natural outcome of interwar technological progress, but was related to the post-war reorganization of the electrical engineering industry and changes in the economic framework of the state.

Systematic electrification, enshrined in Act No. 438/1919 Coll. [1] and subsequent amendments, created, among other things, the basic infrastructure conditions for the development of domestic electrical appliances. In the interwar period, however, production focused mainly on individual specialized devices, and universal kitchen machines were not among the commonly manufactured products. It was not until after World War II, in an environment of nationalized industry and planned production, that the conditions for their systematic production arose.

This text traces the development of kitchen robots and is based on the thesis that the mechanization of households through their use was the result of a combination of technological possibilities and the economic goals of the state, which linked the rationalization of domestic work to broader social and economic strategies.

2. Interwar prerequisites and the absence of domestic food processors

The development of domestic electrical appliances in interwar Czechoslovakia was directly dependent on the availability of electricity and the production capacity of the domestic electrical engineering industry. However, electricity was initially used primarily for lighting. According to a 1921 statistical survey, 38% of households in Prague had electricity, with only 0.5% using it for purposes other than lighting. [2] This figure suggests that the technological and consumer environment did not yet create the conditions for the wider use of more complex kitchen appliances.

It is worth noting the first mention of the term "robot" [3] in the context of electricity in the article "Everyone Should Have Their Own Electric Robot," [4] published in ZEPOP. [5] In it, the author does not yet refer to universal household appliances, but promotes the wider use of electricity to power machines in craft and factory production, which, among other things, was supposed to lead to less air pollution in Prague. In the same year, a machine that we would today call a food processor was presented to the general public for the first time. [6] This took place at a trade fair organized by the Prague power

plants and featured an American universal machine, KitchenAid. [7] However, this machine does not appear in advertising announcements or professional electrical engineering publications in the following years, so we can assume that it did not reach the market.

In the 1930s, the situation regarding household electrical appliances gradually changed. Electric irons, cookers, and stoves became more common in urban households, and the product range of domestic and foreign companies was relatively wide. In 1937, the Czechoslovak Electrotechnical Union (ESČ) registered 117 models of branded products, including lamps, irons, cookers, stoves, ovens, and vacuum cleaners. [8] However, a universal kitchen machine was not among the registered appliances.

One of the few documented examples of a universally designed device was an imported appliance from the German company Electro-Star. [9]

Fig. 1. Electro-Star universal machine [10]

It was a system based on a vacuum cleaner motor that could be connected to various attachments, such as a meat grinder or a coffee grinder, via a flexible shaft. However, this concept of versatility was probably limited by the practical usability of the individual components. In terms of design, it was more a combination of existing devices than a separately developed food processor.

The absence of domestic production of universal kitchen machines during the interwar period indicates that household mechanization was fragmented. [11] Although electrification was advancing and the electrical engineering industry was capable of producing a wide range of appliances, a universal machine integrating multiple functions was not considered standard household equipment. The food processor did not emerge as a natural continuation of interwar developments, but as a product of specific post-war conditions.

3. Post-war production and Robot Zbrojovka Brno

A breakthrough in the development of kitchen food processors came after World War II. The Porkert company in Skuhrov nad Bělou created the design for a universal kitchen machine (UKS). However, its serial production did not begin until after nationalization under the brand name Orlické strojíren, a national enterprise. [12] The post-war economic environment, characterized by the centralization of production and the transition to a planned economy, created the conditions for a more systematic attempt to manufacture this type of equipment. The creation of this device must be placed in the broader context of post-war efforts to rationalize production (including domestic work) and to acquire new labor. According to the central planners' estimates, between 1951 and 1955, the manufacturing (especially the heavy industry) was going to gain 280,000 employees transferred from agriculture, 50,000 from retirement, and 250,000 women from the household. [13] This massive deployment of women into production was to be made possible, among other things, by the electrification of domestic work. This took place in the context of other measures aimed at reducing the time required for household care. These included, for example, support for collective catering, the production and distribution of semi-finished food products, and the expansion of municipal enterprises focusing on domestic work, such as the Liberated Household / Osvobozená domácnost [14] and the construction of municipal laundries in apartment buildings.

The role of household electrification in this endeavor was expressed by Minister of Industry Bohumil Laušman: "The need to accelerate the program of manufacturing state-of-the-art kitchen appliances so that our housewives can soon enjoy all the benefits of electric kitchens, electric heating, bathrooms, laundry rooms, refrigerators, irons, vacuum cleaners, dishwashers, potato peelers, dough mixers, etc." [15] The need to produce universal kitchen appliances was also reflected in the ESČ's publication of the ČSN ESČ 210–1947 standard for electric kitchen appliances. [18] The chair of the commission that prepared this standard was Blanka Podlešáková, a graduate of the College of Mechanical and Electrical Engineering at the Czech Technical University in Prague. [17]

As part of a two-year economic plan, the production of mechanized kitchen appliances was assigned to Zbrojovka Brno. [18] This step was part of a broader process of converting arms production to civilian manufacturing, which also included, for example, the development of Zetor tractors. The kitchen machine manufactured in Brno, called

Robot, was the first domestic product of its kind to be systematically introduced to the Czechoslovak market.

Fig. 2. Robot from Zbrojovka Brno [19]

The Robot Zbrojovka Brno was characterised by the use of a high-speed commutator motor. Speed control was achieved by switching stages "through zero", i.e. by stopping the first gear and then switching on the second. [20] This was contrary to the wording of the ESČ standard, and the Union had to exempt Zbrojovka. [21] The lubrication method limited the maximum operation of the second speed to approximately five minutes, which constituted a practical limit on its use. The machine weighed approximately 15 kg, which reduced its ease of handling in a domestic kitchen environment. [22]

The machine came with a wide range of accessories. In addition to standard attachments such as a meat grinder, dough mixer, and juicer, it also included less practical accessories, such as a jam mixer, a fork sharpener, and a vacuum pump for canning. The wide range of accessories reflected a desire for versatility but also pointed to a conceptual compromise between technical ambition and users' real needs.

Although the Robot's production was heavily promoted, a significant portion was destined for export. [23] The question of its actual availability on the domestic market, therefore, remains problematic. Examples of the Robot's use appeared not only in film newsreels but also in children's literature, for instance. [24] In Slovakia, the Robot was promoted as an ideal helper for agricultural households, where large quantities of food were expected to be prepared. [25] In the early 1950s, production at Zbrojovka Brno was halted due to the resumption of arms production during the ongoing Korean War. [26] The kitchen robot thus became not only a technological experiment but also an example of a product whose existence depended directly on the priorities of the planned economy.

After production ceased at Zbrojovka Brno, the manufacture of food processors moved back to Orlické Strojírny, which had been part of the Elektro-Praga Hlinsko production and economic unit since 1958; from 1960, the products bore the ETA brand. [27] This organizational shift reflected a broader process of concentrating the production of small household appliances in specialized national enterprises. The new generation of robots differed not only by manufacturer but also in design. The motor and accessories were built into a wooden cabinet, with the top designed to form part of a modular kitchen unit. [28] This solution eliminated some of the problems associated with handling a heavy stand-alone machine, and the robot became an integral part of the kitchen interior. The technical solution thus addressed the limitations of the previous model while also reflecting an effort to integrate the appliance into standardized home furnishings.

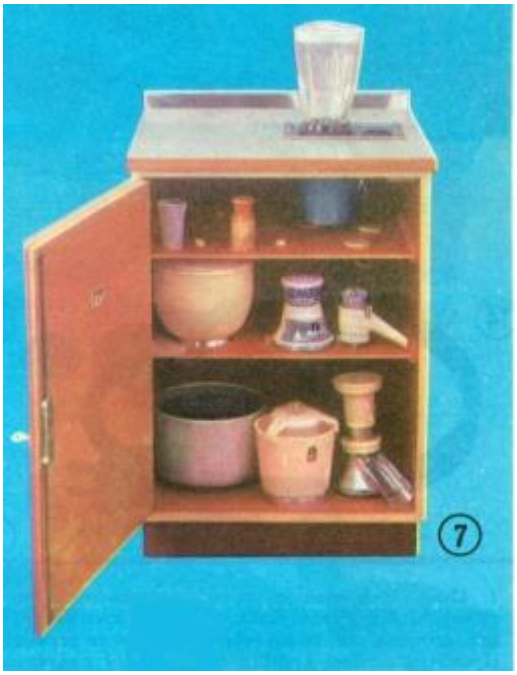

Fig. 3. ETA food processor designed as part of a modular kitchen [29]

4. Conclusion

An analysis of the development of food processors in Czechoslovakia between the 1930s and 1950s shows that their emergence was not a direct consequence of the gradual improvement of domestic electrical appliances in the interwar period. The universal kitchen machine appeared only in a fundamentally changed economic environment, characterized by the nationalization of the electrical engineering industry, the centralization of production, and a focus on the planned fulfillment of production tasks. The mechanization of the household thus became part of a broader economic strategy in which technical solutions were not autonomous but responded to the state's political and organizational priorities.

The Zbrojovka Brno Robot represented an ambitious attempt to create a universal device capable of replacing several separate kitchen tools. Its design, including a high-speed commutator motor, power control system, and extensive accessories, reflected the pursuit of technical versatility but also bore the marks of compromises resulting from production pressures and material limitations. The

export-oriented production and the subsequent cessation of production due to the resumption of arms production also show that consumer goods intended for households were subject to the priorities of a centrally planned economy.

The transfer of production to Orlické strojírny and its stabilization under the ETA brand marked a shift from an experimental model to a more integrated solution that addressed the practical limitations of the previous concept. The incorporation of the drive motor into the cupboard system and its connection to household furnishings reflected the effort to establish the kitchen robot as a stable part of the standardized home interior of the 1950s. Technical development was thus not linear, but shaped by organizational changes and efforts to adapt the product to the real possibilities of the planned economy.

The kitchen robot cannot, therefore, be interpreted solely as a practical kitchen aid. It represented a technological object that emerged at the intersection of electrification, production reorganization, and the state's socio-economic goals. Its existence was linked to the idea of rationalizing domestic work and, indirectly, to efforts to transfer female labor to industry. The tension between the declared universality, technical limitations, and economic priorities reveals that the mechanization of the household was a process conditioned not only by technical possibilities but above all by the political and economic context of the time.

Acknowledgements

This paper was supervised by prof. PhDr. Marcela Efmertová, CSc. of Historical Laboratory of (Electro)Technology, Faculty of Electrical Engineering, Czech Technical University in Prague (FEE CTU in Prague), Technická 2, CZ-166 27 Prague. The author would like to thank her for this supervision.

References

[1] Act on State Support for the Commencement of Systematic Electrification No. 438/1919 Coll. of July 22, 1919. / Zákon o státní podpoře při zahájení soustavné elektrisace č. 438/1919 Sb. z. a n. ze dne 22. července 1919.

[2] *Sčítaní bytů ve větších městech republiky Československé ze dne 15. února 1921*. Prague: Státní úřad statistický 1929, p. 36.

[3] The word robot was introduced in his 1920 play R.U.R. by the playwright Karel Čapek (1890–1938). However, the word was coined by his brother, the painter Josef Čapek (1887–1945), who proposed it as an alternative to the originally intended term "labor."

[4] *ZEPOP*. vol. 2, 1927, no. 2. p. 19.

[5] Administrative and promotional publication issued by the Prague Electric Company.

[6] The name for this appliance varies across languages. Czech and Slovak use the term robot, associated with a specific Czechoslovakian appliance from the second half of the 1940s. English and German have a more universal designation: food processor/Kuchenmaschine. Spanish, French, and Italian again use the term robot (robot de cocina/robot de cuisine/robot da cucina), which is based on the trade name of kitchen appliances manufactured by Robot-Coupe, a company founded in Paris in 1970.

[7] *Zepop*, vol. 2., 1927, no. 3, p. 26.

[8] *Seznam značkovaných výrobků. Stav 1. dubna 1937*. Prague: Elektrotechnický svaz československý, 1937, pp. 7–77.

[9] https://www.starmix.de/en/about/inside-starmix/starmix-history/?srsltid=AfmBOor3EU5TkTtsAdsCCm4y8ljcFFRmRa3thV3vWqnuNfjPSCzRWJPy (cited no-line 28.2.2026).

[10] *ZEPOP*. vol. 4, 1929 no. 4, p. 69

[11] For the concept of a fully electrified interwar household, see, for example, EFMERTOVÁ, M. Elektrifikace a nové prvky v bydlení obyvatelstva Československa mezi dvěma světovými válkami. In HOŘEJŠ, M. (ed.) *Pod značkou „Made in Czechoslovakia“: invence ve službách československého zahraničního obchodu a průmyslové výroby v letech 1918-1992*. Prague: Národní technické museum, 2022. pp. 131–145.

[12] *Historie značky Pokert: 130 let poctivé práce*. https://www.porkert-original.cz/clanek/historie-znacky-porkert-130-let-poctive-prace?srsltid=AfmBOorYSUuIq-VW6sYwARtGCQraSgMUnYyg0DcebKnVHbzwgAS1z9_J (cited on-line 28.2.2026).

[13] KALINOVÁ, L. *Společenské proměny v čase socialistického experimentu: k sociálním dějinám v letech 1945–1969*, Prague: Academia, 2007 p. 52

[14] The original goal of the Osvobozená domácnost cooperative was to take over most of the housework. However, the project was ultimately limited to laundries and dry cleaners. See *Jak fungovala domácnost v socialistickém Československu*. https://www.pametzen.cz/tema-kazdodennost-domacnost (cited online 1.3.2026).

[15] *Elektrotechnický obzor*. vol. 34, 1945, no. 15–16, p. 237.

[16] *Elektrické kuchynské strojky*. Prague: Elektrotechnický svaz československý, 1947.

[17] Archive of CTU in Prague. Collection Vysoká škola strojního a elektrotechnického inženýrství ČVUT 1920–1951 (NAD 2), Catalogues 81–101.

[18] PAULY, J. at al. *Katalog expozice technika v domácnosti*. Prague: Národní technické museum, 2014 p. 63.

[19] https://www.nzm.cz/aktualne-v-muzeu/muzeum-online/sbirkove-predmety/kuchynsky-robot-milacek-zen (cited on-line 1.3.2026).

[20] *Robot Zbrojovky Brno: sen všech hospodyněk*. https://www.ceskatelevize.cz/porady/10116288585-archiv-ct24/222411058210001/cast/886275/ (cited on-line 28.2.2026).

[21] *Zbrojovák*. vol. 4, 1948 no. 11, p. 123.

[22] *Kuchynský robot, miláček žen.* https://www.nzm.cz/aktualne-v-muzeu/muzeum-online/sbirkove-predmety/kuchynsky-robot-milacek-zen (cited on-line 28.2.2026).

[23] See *Robot Zbrojovky Brno: sen všech hospodyněk*. https://www.ceskatelevize.cz/porady/10116288585-archiv-ct24/222411058210001/cast/886275/ (cited on-line 28.2.2026).

[24] *Ohník: časopis pre žiakov 4. a 5. ročníka národných škôl*. vol. 1, 1949, no. 12, p. 6.

[25] *Slovenské pôdohospodárstvo: mesačník pre pôdohospodársku problematiku, pokrok a kultúru : orgán Povereníctva pôdohospodárstva a pozemkovej reformy*. Bratislava: Povereníctvo pôdohospodárstva a pozemkovej reformy. vol. 2, 1947, no. 9. p. 342.

[26] *Fenomén Zbrojovka* https://www.gotobrno.cz/info/fenomen-zbrojovka/ (cited on-line 28.2.2026).

[27] HULÁK, J. *ETA v životě našich domácností*. Prague: Národní technické museum, 2020 p. 75.

[28] SKLENÁŘ, Č. BOHÚŇOVÁ, H. *Vaříme elektricky*, Prague: Vydavatelství vnitřního obchodu, 1959. p. 21.

[29] https://www.retrokatalog.cz/Skrinovy-robot-E-29-d68411019.htm (cited on-line 1.3.2026).

About Author

Mgr. Martin Dominik HRTUS *is a graduate in Economic History at the Institute of Economic and Social History, Faculty of Arts, Charles University in Prague. In 2018, he completed a four-month internship at the Armenian National Museum in Yerevan. He is employed as an assistant at the Historical Laboratory of (Electro) Technology, Faculty of Electrical Engineering, Czech Technical University in Prague, where he also began his doctoral studies in February 2022. The topic of his planned dissertation is the social aspects of electrification in Slovakia.*

Visual Sources for Business History and the History of Technology. Production, Quality Control, Logistic and Technology Transfer in the Case of Colombian Steam Locomotives Purchased from Skoda (1927–1932)

Jorge Alonso RODRIGUEZ ORTIZ[1]

[1]Laboratory of (Electro)Technology, K13116, Faculty of Electrical Engineering, Czech Technical University in Prague, Technická 2, 166 27 Prague, Czech Republic

rodrijor@fel.cvut.cz

Abstract. *This article analyzes Colombia's purchase of steam locomotives from Skoda between 1927 and 1932, focusing on the production processes, quality control, international logistics, and technology transfer associated with this operation. Based on archival documentation and photographic material from the Skoda archive and the General Archive of the Nation of Colombia, the study reconstructs the industrial and commercial dynamics that made this exchange possible. From a perspective that combines the history of technology, business history, and visual history, it argues that the acquisition of locomotives involved the circulation of technical knowledge and transnational networks, although it generated limited technology transfer.*

Keywords

History of Technology, Business History, Visual history, Steam locomotive, Colombia, Czechoslovakia, Skoda, 1927-1932.

1. Introduction

This research is part of the results of a thesis on Colombia's purchase of steam locomotives from Škoda between 1927 and 1932 and is based on documentation from the Regional State Archives of Pilsen in Klášter, Nepomuk, and the General National Archives (AGN). The former is particularly remarkable, as the Škoda archive in Nepomuk has revealed, following research, previously unpublished photographic material and technical information of great documentary value.

In this way, the focus will be on the manufacturing process, quality control, logistics, and technology transfer with the aim of contributing to an understanding of the modernization processes of Latin American countries and railway development linked to international trade circuits, the conditions and challenges imposed by locomotive production and logistics, and international trade rules and regulations.

Based on this framework, the aim is to study and examine the economic, diplomatic, and business circumstances that made the commercial relationship between Colombia and Skoda possible; to reconstruct the processes related to the production and logistics of Colombian locomotives based on archival photographs; and to analyze the scope and limits of the technology transfer associated with the purchase of the locomotives.

The central hypothesis is that the purchase of locomotives from Skoda was not simply a commercial transaction, but rather a process involving the circulation of technical knowledge and the convergence of economic and political interests, in which technology transfer was partially realized.

The case is approached from the perspectives of the history of technology, business history, and visual history. All three converge and allow for the study of the phenomenon, since companies, as producers of technology, play a fundamental role in technology transfer and the circulation of technical knowledge, which must be studied. This transfer is situated in a particular historical context and is influenced by various interests. The contribution of visual history comes from understanding the “image” as a historical document that contains valuable technical information on production processes and logistics.

Within Colombian historiography, approaches to the railway phenomenon have been mainly descriptive, without a systematic analysis of the processes of industrial production, international circulation, commercial negotiation, or local appropriation of technical knowledge. Furthermore, there is a historiographical gap in addressing the role of Latin American countries in the steam locomotive market. Others have addressed the locomotive as a central technological artifact of the modernization process, but have privileged economic, political, and institutional approaches, relegating to the background the analysis of the locomotive as a technological object and a node of knowledge transfer.

In short, it can be said that, based on the wealth of visual material in the Skoda archive, there is a need for research that articulates the technical, production, and commercialization levels, as well as diplomatic relations in international trade, that is, research that examines the locomotive as a sociotechnical object.

2. Steam Locomotive manufacturing and marketing

The manufacture of steam locomotives required skilled labor, large industrial facilities, and an extensive network of suppliers, making international marketing—through tenders, credit, agent networks, and after-sales service—a central element of the business.

Although Great Britain initially dominated the sector, and producers in the United States and Europe later consolidated their positions. The geopolitical reconfiguration following World War I and the need for new markets drove the export expansion of European industry. At the same time, competition from road transport and diesel and electric locomotives began to challenge the future of steam traction. In this context, Czechoslovakian industry, benefiting from a strong metallurgical base, experienced remarkable growth. Companies like Skoda Works adopted an export-oriented strategy, combining production standardization, technical flexibility, and an active commercial policy, further strengthened by the participation of the French group Schneider et Cie.

Latin America became an attractive market for this expansion, particularly in countries like Colombia, where the relative political stability of the early 20th century, along with greater financial resources for infrastructure, favored the importation of railway technology. Relations between Czechoslovakia and Colombia were gradually consolidated with the establishment of consular ties in 1922, diplomatic relations in 1935, and a trade agreement in 1937.

3. The purchase of the steam locomotives

The Colombia-Skoda case highlights the interaction between multiple actors with asymmetrical capabilities. On the supplier's side, the Czechoslovakian firm acted as a European actor with technical, financial, and legal resources, relying on banks, agents, and commercial representatives to ensure contract compliance.

Through Law 61 of 1921, mandatory controls were introduced for government purchases in Colombia. This put the base for more transparent governance. The awarding of orders was to be carried out by the Central Purchasing Board of the Ministry of Public Works (MOP). The oversight of the Comptroller General of the Republic, the Director of the Procurement Department, the Director General of Railways, the Head of the Mechanical Section (Dewhurst), and the Head of the Commercial Section was also taken into consideration. The procedures for legalizing these orders were not only aimed at their authorization by the Central Purchasing Board, but also at their monitoring by the Comptroller's Office. [1] In Colombia, Skoda was initially represented by *Sigllechner & Hugo*, engineers from the former Hugo Stinnes company. On the Colombian side, British engineer *Paul Dewhurst* played a central role as technical mediator with international inspectors and manufacturers, ensuring compliance with specifications, evaluating locomotive performance, and resolving technical disputes. Another key player was the German-Antioquian Bank (BAA).

Although the construction of these steam locomotives was commissioned to various international firms, this article focuses on Skoda's participation in this order for Colombia between 1927 and 1932, an episode barely mentioned in Colombian and Czech historiography.

Overall, Škoda delivered a total of 31 locomotives to Colombia: 17 units for the Pacific Railway, 8 for the Tolima Railway, 2 for the Girardot Railway, 2 for the Nariño Railway, and 2 for the Trunk Railway. From a typological standpoint, these locomotives were organized into three main configurations: 20 units of the 4-8-0 types, intended for both freight and passengers; 7 units of the 2-6-2 types; and 4 units of the 2-4-0 types.

The manufacturing process of the steam locomotive was the result of a complex interplay between technical expertise, industrial organization, and business cooperation networks. Regarding materials and structural design, the main components of the boiler were manufactured from rolled steel, a material that offered high thermal and mechanical resistance, following Dewhurst's specifications. Similarly, the fireboxes were constructed of steel instead of copper, based on criteria of durability and material availability. [2]

The photographs reveal the type of industrial activity in the locomotive factories, which were organized into specialized workshops: a) Steelmaking and rolling mill: steel production; b) Boiler shop: plate bending and riveting of the boiler barrel; c) Frame workshop: chassis manufacturing; d) Machining workshop; e) Assembly workshop: final locomotive assembly; f) Painting and finishing workshop

Fig. 1. Skoda workshops, production of boilers, 1928. [3]

Figure #1 shows a stage in the manufacturing process of locomotive boilers using riveting and machining. The word "Columbia" [Colombia] is visible on the central piece. The worker is using a pneumatic tool or industrial drill, and overhead cranes can be seen on the roofs moving heavy materials. In this phase, after the riveting of the steel plates that make up the boiler body, the holes for the smoke tubes were fitted and machined. This system ensured resistance to high steam pressures.

Figure #2 documents a precision machining stage during the manufacture of a locomotive boiler, specifically the cutting of threads on bolts or screws securing the firebox roof—the area where coal combustion occurs.

Fig. 2. Skoda workshops, Cutting threads for roof screws, 1928. [4]

The operator is on a mobile elevated platform due to the large size of the parts and the need to reach different heights; the machining had to be done with precision.

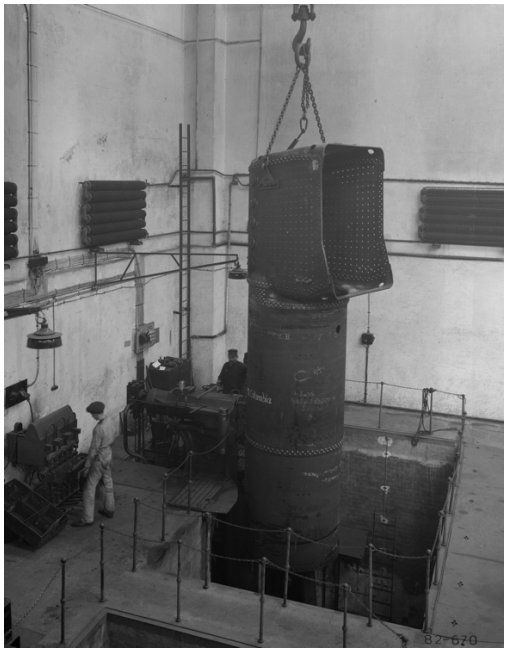

Fig. 3. Skoda workshops, Production of boilers, 1927. [5]

Figure #3 shows a key stage in the manufacturing process of a locomotive boiler, specifically the handling and assembly of the combustion chamber (firebox). The part is handled by an industrial overhead crane with chains to precisely position it during assembly and insert it into the working pit.

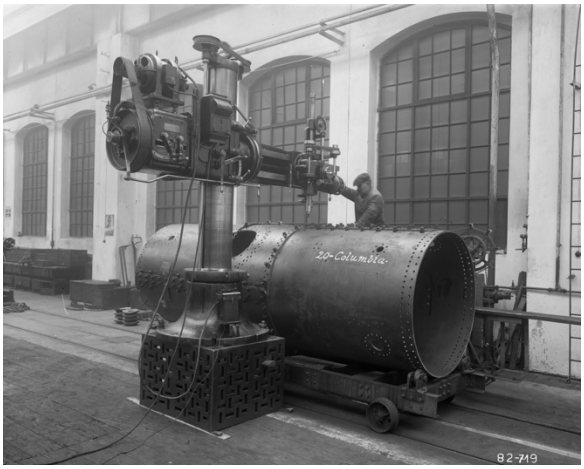

Fig. 4. Skoda workshops, reinforcement of rivet holes, 1928] [6]

Figure #4 shows a workshop for a radial drilling machine, which allowed for drilling large plates, creating holes with great precision, and working with heavy pieces that could not be easily moved. At this time, boilers were not welded but constructed from riveted steel plates.

Fig. 5. Skoda workshops, Overview of the locomotive factory assembly, 1928, [7]

Skoda carried out official testing and quality control. According to the locomotive manufacturing protocol records, each boiler underwent a regularized testing cycle, consisting of a hydraulic test and a steam pressure test. This suggests that the boiler was being prepared for the official pressure test, which involved completely filling the boiler with water, applying pressure using a pump, and checking for leaks or deformations. The hydraulic test was

systematically performed at 240 psi, [8] a pressure used to verify structural integrity without risk of explosion, while the steam test operated at 190 psi, a level corresponding to actual operating conditions.

Fig. 6. Skoda workshops, official acceptance, 1928. [9]

Furthermore, the inspection company Gulick-Henderson Co., Inc. [10] played a significant role in the technical validation of the process (Fig. #6). Its inspection certificates confirmed the manufacturing, materials testing, boilers, and assembly, and ensured the conformity of locomotives and spare parts with the drawings and contractual specifications. Its involvement demonstrates the existence of an internationalized system of technical inspection and certification that accompanied the technology transfer.

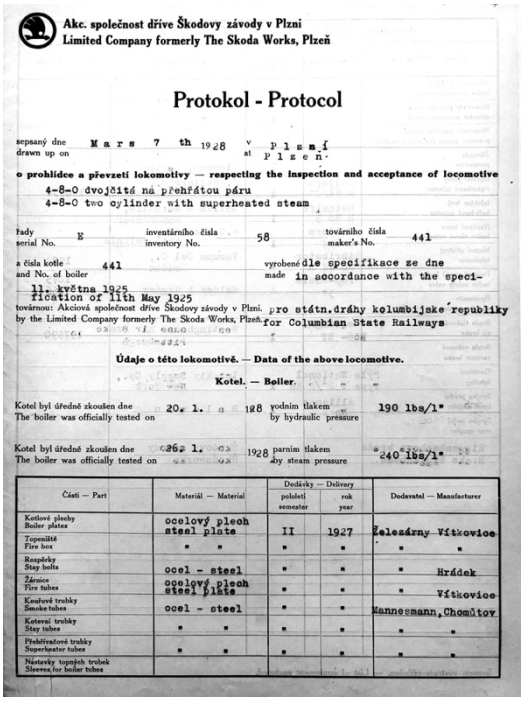

Akc. společnost dříve Škodovy závody v Plzni
Limited Company formerly The Skoda Works, Plzeň

Protokol - Protocol

sepsaný dne drawn up on Mars 7 th 1928 v at Plzni

o prohlídce a převzetí lokomotivy — respecting the inspection and acceptance of locomotive

4-8-0 dvojčitá ná přehřátou páru
4-8-0 two cylinder with superheated steam

řady serial No. E | inventárního čísla inventory No. 58 | továrního čísla maker's No. 441

a čísla kotle and No. of boiler 441 | vyrobené made dle specifikace ze dne in accordance with the specification of 11. května 1925 11th May 1925

továrnou: Akciová společnost dříve Škodovy závody v Plzni. by the Limited Company formerly The Skoda Works, Plzeň. pro státn.dráhy kolumbijské republiky for Columbian State Railways

Údaje o této lokomotivě. — Data of the above locomotive.

Kotel. — Boiler.

Kotel byl úředně zkoušen dne The boiler was officially tested on 20. 1. 128 vodním tlakem by hydraulic pressure 190 lbs/1"

Kotel byl úředně zkoušen dne The boiler was officially tested on 26. 1. 1928 parním tlakem by steam pressure 240 lbs/1"

Části — Part	Materiál — Material	Dodávky — Delivery: pololetí semester	Dodávky — Delivery: rok year	Dodavatel — Manufacturer
Kotlové plechy Boiler plates	ocelový plech steel plate	II	1927	Železárny Vítkovice
Topeniště Fire box	" "	"	"	" "
Kotevky Stay bolts	ocel - steel	"	"	" Hrádek
Žárnice Fire tubes	ocelový plech steel plate	"	"	" Vítkovice
Kouřové trubky Smoke tubes	ocel - steel	"	"	Mannesmann, Chomútov
Kotevní trubky Stay tubes	" "	"	"	" "
Přehřívačové trubky Superheater tubes	" "	"	"	" "
Nástavky topných trubek Sleeves for boiler tubes				

Fig. 7. Protokol, Skoda 441, 1928, Loco. Pacifico 58. [11]

The inspection and acceptance protocol for locomotives manufactured by Škoda Works for Colombia constitutes a key technical and contractual source for understanding the manufacturing, inspection, and delivery process. This type of document had an important contractual function, confirming that the locomotive met the agreed-upon technical specifications, recording the official tests performed, and formally validating the delivery of the machine.

4. Logistics

Addressing the issues surrounding locomotive orders placed by Colombia with Skoda involves analyzing a complex chain of processes that goes beyond the simple purchase of rolling stock. These included defining technical specifications, manufacturing and verifying the locomotives, logistics and transportation procedures, communication among multiple stakeholders—engineers, officials, companies, and sales agents—the exchange of technical and administrative documentation (telegrams, letters, and reports), the receipt and testing of the locomotives, and the subsequent payment processing. This framework reveals the transnational and negotiates nature of the technology transfer.

The purchase, logistics, and payment terms can be determined through the contracts between the parties. The contractors committed to supplying the materials requested by the buyer, although the factory reserved the right to make minor modifications to improve the construction.

Fig. 8. Locomotive for Colombia in a wagon before its shipment, 1928. [12]

In railway supplies, the price of locomotives and other equipment was established on a CIF (Cost, Insurance, and Freight) basis, [13] destined for the ports of Buenaventura or Cartagena. [14] This condition meant that the contractual value included the cost of manufacturing the equipment, its maritime packaging, insurance, and ocean freight to the Colombian port of destination, transferring the responsibility and risk of transatlantic transport to the supplier. However, the contract expressly excluded

expenses incurred after arrival at the port, such as consular fees, tonnage, wharfage, lighthouse fees, manifest fees, and stamp duties, which remained the responsibility of the National Government. This contract was subject in all respects to the laws of the Republic of Colombia and to the jurisdiction of the national courts and would expire in the event of the contractor's breach of any of the conditions and clauses. [15]

Fig. 9. Transport locomotives to Colombia, 1928. [16]

This contractual modality reflects both the standardization of international commercial practices and the state strategy of limiting logistical risks in the importation of heavy railway material.

Regarding documentation such as invoices and packing lists, these had to be translated from Czech to Spanish in quadruplicate and addressed to different railway departments. The packaging and markings had to contain clear specifications to facilitate the identification and handling of the goods, and their unloading had to be marked with the legend in Spanish “Desembarque libre [Free disembarkation]”, [17] administrative measures intended to expedite port reception.

Fig. 10. Transport locomotives to Colombia, 1928. [18]

The locomotives were supposed to be delivered assembled and painted, [19] however, a gap in the sources prevents confirmation of this. It could be assumed that some were delivered assembled and others not, as shown in the photographs (Figs. #9, #10). The logistics of the assembled locomotives likely presented more difficulties, as Colombian ports lacked specialized infrastructure for unloading them, and small boats were required to complete the unloading process. Alternatively, they could be assembled in Colombian railway workshops.

Conclusions

The photographic image contributes significantly to business and technological history by documenting manufacturing and logistical processes characteristic of the European railway industry during the interwar period. Overall, the Skoda locomotive case demonstrates that technology transfer was a negotiated process, involving business, financial, and technical intermediaries, in which international certification and local expertise converged to adapt a global industrial product to the specific conditions of Colombian railways. The purchase of these steam locomotives allowed Colombia to enter the international market and access technology and technical know-how.

Sources reveal how technical knowledge circulated not only through blueprints and machines, but also through inspection reports, the movement of foreign engineers and technicians, and so on. Unfortunately, the case of the Škoda locomotives illustrates a limited form of technology transfer, focused on the supply of equipment, technical assistance, and operational training. There was a positive impact on the efficiency of transporting raw materials destined for the international market, technical training and support were provided, and railway workshops became centers of learning and development. However, no initiative arose to develop a domestic locomotive industry, nor was there political will for a national railway project that would capitalize on this exceptional opportunity. On the other hand, the positive impact on the modernization of the National Railways should be highlighted. Through the experience gained in international trade and negotiation, they restructured their regulatory and legal frameworks and incorporated the transfer of technical knowledge in the areas of business management and accounting.

Although lacking extensive experience in locomotive production, Skoda demonstrated its strengths in both manufacturing and commercial acumen within a competitive international landscape. The relationship between Schneider et Cie and Skoda was also significant; while it represented the involvement of French capital, it nevertheless had a positive impact on expanding trade opportunities in overseas markets.

The Latin American market was undoubtedly important for Skoda, as these young nations required access to goods and technology, and presented an opportunity to access raw materials and generate foreign exchange. Furthermore, the locomotive market opened new commercial horizons, including the arms market, among others.

In short, technology transfer depends on socioeconomic networks, institutional capacities, available technical training, political contexts, transnational economic interests, diplomatic restrictions, internal political controversies, and complex corporate strategies.

Acknowledgements

Research described in the paper was supervised by PhDr. Marcela Efmertová, MSc., FEE CTU in Prague and supported by the EDF history committee in Paris.

References

[1] "Comunicaciones no. 200, no. 266", Colombia, February 14, 1930, AGN, FMOP, SR, Commercial Section, no. 905, pp. 316-325, p. 2.

[2] Arias de Greiff, Jorge, "A Stellar Moment in Mechanical Engineering in Colombia: The Challenges of P.C. Dewhurst Locomotives", in Engineering and Research, no. 18 (1989), p. 55.

[3] Fig. 1. Skoda workshops, production of locomotive boilers for the Pacific Railroad, Bogotá, Colombia [1928]. State Archives of Plzni, photographic documentation.

[4] Fig. 2. Skoda workshops, Cutting threads for roof screws, 1928, Státní oblastní archive v Plzni, fotografická dokumentace.

[5] Fig. 3. Skoda workshops, Production of boilers, 1927, State Archives of Plzni, photographic documentation.

[6] Fig. 4. Skoda workshops, reinforcement of rivet holes, 1928, State Archives of Plzni, photographic documentation.

[7] Fig. 5. Skoda workshops, Overview of the locomotive factory assembly, 1928.

[8] PSI, pounds per square inch: This is a unit of pressure in the imperial system, widely used.

[9] Fig. 6. Skoda workshops, official acceptance, 1928, State Archives of Plzni, photographic documentation.

[10] Gulick-Henderson Co., Inc.: A company founded in New York in 1907, which offered technical engineering services in all major manufacturing centers in the United States, Canada, and Europe.

[11] Fig. 7. Protocol, Skoda 441, 1928, Pacifico 58. State Archives of Plzni.

[12] Fig. 8. Locomotive for Colombia in a wagon before its shipment, 1928, State Archives of Plzni, photographic documentation.

[13] In the contracts, the C.I.F. (Cost, Insurance and Freight) clause established the agreed price: it included the cost of manufacturing, marine insurance, and freight to the port of destination.

[14] "The conditions stipulated in the locomotive contract," Colombia, October 4, 1927, AGN, FMOP, SR, Škoda no. 983, f. 409.

[15] "3 tender locomotives for the FP Škoda," Colombia, September 27, 1927, AGN, FN, AH, no. 554 Box: 38.

[16] Fig. 9. Transport locomotives to Colombia, 1928, State Archives of Plzni, Photographic Documents.

[17] "Order note no. 37", Colombia, July 4, 1929, AGN, SR, FMOP, SC, no. 905, f. 100.

[18] Fig. 10. Transport locomotives to Colombia, 1928, State Archives of Plzni, Photographic Documents.

[19] "Lanchaje por disembarque", Colombia, December 20, 1929, AGN, SR, FMOP, Sub-fund Commercial Orders Pacific Railroads 1920-1930 (SCPFP 1920-1930), no. 985, f. 334.

About Author

Jorge Alonso RODRIGUEZ ORTIZ, was born in Colombia, Santiago de Cali in 1985. Historian from the Universidad del Valle and Master in TPTI Université Paris 1 Panthéon Sorbonne. He is currently pursuing a PhD in History of Science and Technology at the Historical Laboratory of (Electro)Technology at the FEE Czech Technical University of Prague.

The Representation of the Earth on the Astronomical Clocks

David KNESPL[1]

[1]Historical Laboratory of (Electro)Technology, Dep. of Economics, Management and Humanities, Faculty of Electrical Engineering, Czech Technical University in Prague (FEE CTU in Prague), Technická 2, CZ-166 27 Prague 6

knespdav@fel.cvut.cz

Abstract

This study argues that the painted Earth at the centre of the Prague astronomical clock is not a medieval feature of astrolabic dials, but an early modern layer shaped by sixteenth–seventeenth-century cosmographical thought. In astrolabic projection the centre marks the geometric pole rather than the Earth, so the medieval dial did not require a globe. The early modern image is interpreted as an application of Apian's "cosmographic mirror": a superposition of celestial and terrestrial stereographic projections. In this reading the globe, introduced after 1629, served as a simplified world clock relating the Sun's position to meridians and local times.

Keywords

Astronomical clock, stereographic projection, cosmographical mirror, geographical astrolabe, world clock, Peter Apian, Olomouc, Münster, Prague, history of technology.

1. Earth at the Centre

The central issue examined here is whether the Earth motif on astronomical clocks should be understood as a medieval cosmological element or rather as an early modern manifestation of a "World Clock".

In medieval and early modern Europe, two principal types of astronomical clocks emerged: concentric and astrolabic. Each reflects a distinct geometric and cosmological conception. Concentric clocks, especially common in Italy, directly visualize the geocentric cosmos, whereas astrolabic clocks, widespread in Central and Northern Europe, derive from the planispheric astrolabe and represent the visible celestial sphere as perceived by an observer on Earth.

Astrolabic clocks are based on stereographic projection, in which the centre of the dial does not represent the Earth but the geometric pole of projection. In their original medieval conception, the Earth was therefore not depicted as an independent element, unlike concentric clocks, where it naturally occupies the centre of the composition.

On the dial of Prague astronomical clock, the central field was originally empty, as shown by comparable medieval clocks in Bad Doberan and Stralsund. A painted globe is first documented only in 1735 and was probably introduced during the reconstruction after 1629. Later representations of the Earth on the Prague dial correspond neither to its geometric logic nor to its original function.

Fig. 1. Geographic tympanum of Mercator's Florentine astrolabe (Courtesy of Museo Galileo.)

2. Cosmographic Mirror

The conceptual background for the later use of world maps on Renaissance and Baroque astronomical clocks lies in the Cosmographic Mirror (*Speculum cosmographicum*) devised by Peter Apian (1495–1552).

Published in 1524 in *Cosmographicus liber*, the instrument took the form of a paper volvelle: layered rotating chart that transformed the book into an interactive computational device. Its most sophisticated version combined a terrestrial map with a movable celestial layer, both constructed through

stereographic projection. By rotating the upper disc, the user could relate the position of the Sun and stars to specific places on Earth, compare local times, and estimate day length by latitude.

The device expressed the Renaissance idea of correspondence between heaven and Earth, "as above, so below" (quod est superius est sicut quod inferius), uniting cosmography, astronomy, and geography in a single visual model.

Although based instrumentally on geocentric projection, it did not simply represent geocentric cosmology; rather, it reflected the observable relation between celestial motion and terrestrial position as perceived by an observer on Earth, regardless of whether interpreted within a geocentric or heliocentric framework.

Through Gerardus Mercator (1512–1594), this tradition later influenced other astronomical instruments, as the principles of paper volvelle construction were gradually transferred into durable mechanical forms.

3. Geographical Astrolabes

Geographical astrolabes may be understood as luxurious brass realizations of Apian's paper volvelle. They combine the traditional astronomical function of the astrolabe with finely engraved world maps reflecting the most advanced geographical knowledge of their time. By the late sixteenth century, such instruments already included both Americas, new maritime routes around the Cape of Good Hope, the Strait of Magellan, revised concepts of Terra Australis, and the gradual abandonment of the Ptolemaic idea of a continuous southern continent.

A particularly important example is the astrolabe made by Gerardus Mercator, now preserved in Museo Galileo in Florence. Produced around 1570, it contains a double-sided terrestrial plate with polar stereographic projection: one side shows the northern hemisphere down to the Tropic of Capricorn, the other the southern hemisphere. Inserted in place of the usual tympanum, this plate creates a portable image of the world in which terrestrial and celestial spheres are united within a single instrument, closely following the principle of Apian's cosmographic mirror.[1]

Other sixteenth-century astrolabes with geographical plates also survive. Another example in Museo Galileo, dated 1568 and attributed to Egnazio Danti, includes a geographical planisphere alongside standard astronomical plates. Several further examples are preserved in History of Science Museum in Oxford, including instruments by Egidius Coignet and François Morillard, as well as astronomical compendia by Christoph Schissler that incorporate simplified geographical astrolabes.[2]

Taken together, these instruments reflect the growing Renaissance interest in geography stimulated by overseas discoveries and by a new cosmographical understanding of the world.

4. "World Clocks"

The cosmographic mirror, and later the geographical astrolabe, naturally passed from interactive book devices and portable instruments to the dials of monumental astronomical clocks. This development was encouraged not only by their capacity to demonstrate the unity of heaven and Earth and to display contemporary geographical knowledge, but also by one of their practical functions: serving as an early form of world clock, enabling the comparison of time in different parts of the world.

Peter Apian described a simple algorithm: set the outer hour scale, align the pointer with the meridian of the chosen city, and read the local time on the small ring — a procedure that made it possible to compare the times of different places on a single dial.

Fig. 2. Hypothetical reconstruction of the Olomouc astronomical clock (©MgA. Pavel Rozsíval, Vlastivědné muzeum v Olomouci)

5. Olomouc

In its Renaissance form, the astronomical clock of Olomouc probably represented the first documented monumental realization of the cosmographic mirror principle. During the major reconstruction of 1573–1575, carried out by Paulus Fabricius (1519-1589) and the Olomouc clockmaker Hans Pohl (d. 1584), its dial acquired a new interpretative layer that, alongside its astronomical function, visually demonstrated the relationship between solar motion and the Earth's surface. This Renaissance form was later lost through repeated reconstructions, and the present socialist-realist appearance bears no relation to the original.

Fabricius—Viennese mathematician, astronomer, physician to Maximilian II, Holy Roman Emperor, and author of the first map devoted exclusively to Moravia (1569)—be-

longed to the Central European cosmographic tradition shaped by Apian, Frisius, and Mercator. Its influence in Olomouc is further indicated by the later inventory of Hans Pohl's estate, which listed a copy of *Cosmographicus liber*.

The exact form of the astrolabic mater is explicitly defined in the contract concluded between the city of Olomouc and Fabricius on 8 July 1573. It requires a plate on which "the necessary circles, beyond those commonly used, together with a map of the earthly realm as far as the Tropic of Capricorn, are to be engraved in the best possible manner." The plate thus contained not only celestial circles but also a terrestrial map in stereographic projection. Above it moved an openwork celestial rete with solar and lunar indicators, designed by Fabricius to include "the principal and most visible stars of the whole sky," while Hans Pohl provided its mechanical realization. Through the superposition of terrestrial and celestial imagery, the clock became an advanced cosmographic instrument in monumental urban space.

This conception was recalled in 2019–2020 during the exhibition *Olomoucký orloj / 500 let od první písemné zmínky*, organized by Regional Museum in Olomouc (Vlastivědné muzeum v Olomouci), for which a full-scale reconstruction of the dial level was produced. It included a hypothetical plate with the northern hemisphere, designed by analogy with the Mercator astrolabe preserved in Museo Galileo.[3, 4]

6. Münster

The only surviving monumental astronomical clock in which a geographical planisphere beneath the movable astrolabic rete has remained in situ is that of St.-Paulus-Dom astronomical clock in Münster, Germany. The painting was executed in 1662 by the Münster painter Heinrich Schmidts, who used as his model a map by the celebrated cartographer Willem Blaeu (c. 1570–1630), brought to Münster as an honorary gift during the negotiations of the Peace of Westphalia. Cathedral chapter records from 1661–1663 confirm that Schmidts carried out the "illumination" of the clock over a two-year period, including the painting of the geographical planisphere on the mater and the Baroque oak rete partially covering the map.

The geometric basis of the painting is a polar stereographic projection of the Earth centred on the North Pole and extending as far as the Tropic of Capricorn. Its most remarkable and visually striking feature is that the terrestrial projection is mirror-reversed. It was conceived as a visual view "through" the Earth toward the sky. This cartographic procedure follows the logic of astronomical observation: whereas ordinary maps assume a viewpoint from above the Earth's surface, observation of the heavens proceeds from below upward. The Münster dial therefore simulates the perspective of a hypothetical observer near the South Pole looking toward the celestial vault above Münster through an imagined transparent Earth, producing an exact but mirror-inverted image of the continents.

The geographical planisphere thus formed an integral part of the public reading of "World Clock" and demonstrates that the superposition of heaven and Earth in clockmaking practice could be conceived as a visual passage through the Earth toward the celestial sphere.[5]

Fig. 3. Münster clock: geographic planisphere beneath the astrolabic rete, exposed during restoration after removal of the rete (©Stephan Kube, Greven)

7. Prague

The astrolabic dial of Prague astronomical clock most probably originally had an empty central field through which the horizon circle passed uninterrupted. This arrangement corresponds to the fundamental logic of astrolabic clocks, in which the centre does not represent the Earth as a cosmological object but rather the geometric pole of the stereographic projection of the celestial sphere. The same principle can be observed on surviving medieval astrolabic clock dials in Stralsund and Bad Doberan. An astrolabic dial is therefore not an image of a cosmological model of the universe, but a projection of the visible celestial sphere onto a plane, intended for the reading of astronomical phenomena. For this reason, the original medieval form of the Prague astronomical clock did not require a painted globe at its centre.

In the second half of the sixteenth century, the clock administrator Jan Táborský z Klokotské Hory (c. 1500–1572) added to the centre of the dial a lunar-phase indicator for tracking the lunar cycle.[6]

A painted globe in the central field is documented only considerably later. In 1735, Jan Teicher described "a globe on which, because of its smallness, nothing can be distinguished when viewed from below," indicating that an image of the Earth was by then present at the centre of the dial, although its cartographic content was unreadable from the observer's

distance; by that time the dial itself was already in poor condition, as the clock had not functioned or been maintained for many years.[7]

By analogy with other astrolabic clocks, this later image of the Earth may be understood not as a cosmological symbol but as a cosmographic mirror, that is, a simplified form of world clock. The fact that the map did not occupy the entire surface of the fixed plate—as in St.-Paulus-Dom astronomical clock or probably also on the Olomouc clock—does not alter the principle of reading, since for the demonstration of world time only the angular relation of the solar pointer to the meridians marked on the map is decisive, not the size of the cartographic field.

The question of when exactly the globe was added to the Prague astronomical clock, and who conceived this innovation, remains open. It is certain that no globe was present in the second half of the sixteenth century and that the earliest report of its existence—already describing it as difficult to read—dates only from 1735. It is also known that in 1629 the clock underwent a major restoration during which both the astrolabic dial and the calendar plate were completely repainted. A possible initiator of the globe motif may have been the land surveyor and cartographer Šimon Podolský z Podolí, a pupil of Matouš Ornys of Lindperk, who is securely documented as clock administrator in 1597 and probably remained active until at least 1613, when the clockmaker Kryštof Švorcpach is recorded in that role. Podolský died in 1617. As a cartographer, he was undoubtedly familiar with early modern cosmography and with the principle of the cosmographic mirror known from the works of Peter Apian. It therefore cannot be excluded that the idea of inserting a world map into the centre of the Prague dial originated within his intellectual circle, while its practical execution may have taken place later.

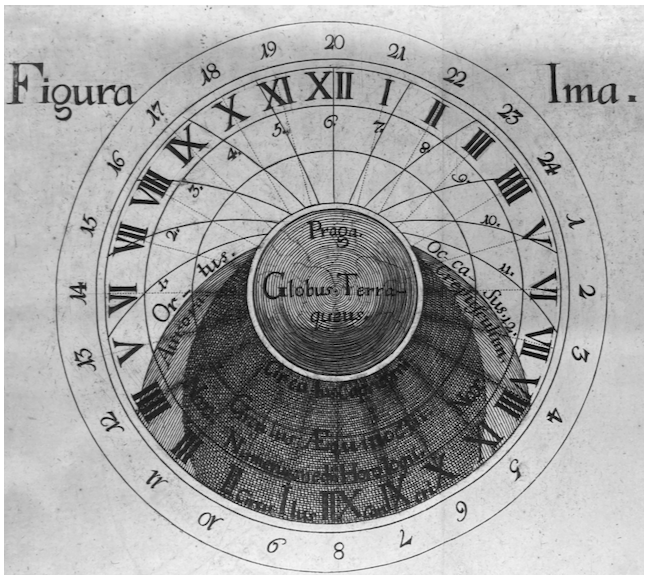

Fig. 4. Prague Astronomical Clock in Teicher's 1735 depiction

8. Conclusion

The dial of an astrolabic astronomical clock is fundamentally a projection of the celestial sphere onto a plane: it represents the visible configuration of celestial phenomena rather than a schematic section through a cosmological model with the Earth at its centre. For this reason, the medieval form of the Prague astronomical clock did not originally require a painted globe in its centre.

The combination of a celestial image with a terrestrial map appears only in the early modern period as a superposition of two independent stereographic projections—celestial and terrestrial. Beyond illustrating the hermetic principle of the unity of macrocosm and microcosm, this arrangement primarily served the practical purpose of relating the position of the Sun or Moon to meridians and local time in different parts of the world. Emerging at a time when heliocentric explanations of the universe were already gradually gaining acceptance, this concept should therefore not be understood as a cosmological model, but rather—like the astrolabic dial itself—as an instrument for converting observed celestial phenomena into temporal and geographical readings. It is probable that the world map introduced on the Prague astronomical clock around 1629, later described by Teicher, fulfilled precisely this function.

References

[1] TURNER, Gerard L'E. The three astrolabes of Gerard Mercator. *Annals of Science*. 1994, vol. 51, no. 4, pp. 329–353.

[2] MUSEUM OF THE HISTORY OF SCIENCE, Oxford. *Astrolabe Catalogue; The Astrolabe, East and West* [online]. Available from: https://www.mhs.ox.ac.uk/astrolabe/

[3] HIMMLER, Radim. *Olomoucký orloj: historie v obrazech a faktech*. 1st ed. Olomouc: Vlastivědné muzeum v Olomouci, 2019.

[4] KNESPL, David; ŠIMEK, Martin. Replika číselníkového patra olomouckého orloje dle zobrazení Josefa Vladislava Fischera z roku 1805. *Zpravodaj Společnosti přátel starožitných hodin*. 2019, no. 34, pp. 20–23.

[5] MOSEL, Bernd. Die Astronomische Uhr im St.-Paulus-Dom in Münster. *Ad Astra*. 2012, no. 28, pp. 32–33, 35–37.

[6] TÁBORSKÝ z Klokotné Hory, Jan. *Zpráva o orloji*. Manuscript, 1570. Archiv hlavního města Prahy, Sbírka úředních knih a rukopisů, sign. 7916 (1587–1642): Zpráva o Staroměstském orloji a další písemnosti spojené s orlojem.

[7] TEICHER, Andrea Gabriel. *Beschreibung des Kunst-reichen Uhr-Wercks Auf dem Rath-Hauss der Königlichen Alt-Stadt Prag*. Osek, 1735.

About Authors...

David KNESPL born in Prague in 1965, graduated from the Faculty of Nuclear Sciences and Physical Engineering at CTU in Prague in 1991. After initial work on computational models in radiobiology, he moved into information technology. His long-standing deep interest in horology led him to doctoral research on the history of the Prague Astronomical Clock.

Celdit between Autarky and Energy Security: The Electrochemical Cellulose Industry in Times of War

Jacopo Bassetta,

[1] Dept. of Electrical Engineering, Historical Laboratory of Electrical Technology, Czech Technical University, Technická 2, 166 27 Praha, Czech Republic; Department of Human, Legal, and Economic Sciences, Leonardo da Vinci University, S. Rocco square 2, 66010 Torrevecchia Teatina (Abruzzo-Italy)

bassejac@cvut.cz

Abstract.

The paper examines Celdit in Chieti as an emblematic case of autarkic industry grounded in the nexus between cellulose, electrochemistry, and energy security. Through the Giordani-Pomilio method and its connection with the Triano hydroelectric power plant, the factory shows how productive continuity depended on the integration of technology, energy, and territorial logistics. The case highlights both the ambitions of Fascist autarky and the structural vulnerabilities of a strategic industrial system in wartime.

Keywords

Celdit; Fascist autarky; cellulose industry; electrochemical production; energy security; hydropower; wartime Italy

1. Introduction

This study was made possible by the continuation of the investigation initiated with the poster presented at the POSTER 2025 competition in Prague, entitled *Energy and War: The Triano Hydroelectric Power Plant as a Strategic Infrastructure in the German Rear Lines in Italy (1939-1944)*. The continuation of that research made it possible to examine more closely the link between the particular configuration of the Triano hydroelectric power plant, located a few kilometers from the historic Celdit plant, and the need to guarantee energy continuity for an electrochemical factory heavily dependent on a constant and stable supply of energy. The reconstruction of the historical framework was also made possible thanks to the documentary recovery work carried out by Marcello Benegiamo, Natalina Quaranta, and Marco Carugno, together with the Ministry of Culture and the State Archive of Chieti, who in 2011 saved the papers and documentation of the Celdit Burgo plant before its definitive material disappearance. All the archival sources used for this study are now preserved at the State Archive of Chieti, in Abruzzo. Today, in fact, the Celdit industrial complex is no longer preserved in its original integrity, having been demolished and erased as an architectural and productive presence within the territory.

2. Autarkic and Electrochemical Industry during the Fascist Years

Between 1925 and 1926, Italy began moving toward a dirigiste economic policy. [1] Although it was not yet an autarkic economic and productive regime, the foundations were laid for a system of exchange controls, protection of certain productive sectors, and direct state intervention. Between 1935 and 1936, historiography identifies the Italian economic turning point as a consequence of the League of Nations sanctions imposed over the Ethiopian conflict, and the regime adopted a rhetorical posture centered on productive self sufficiency and presented autarky as a national necessity. Following the proclamation of the Empire in May 1936, autarky became a structural objective of the Italian economy; however, already in 1933 the body dedicated to industry, the IRI (Institute for Industrial Reconstruction), had been created, and in its wake targeted plans were introduced for chemicals, steel, and domestic fuels with the aim, never fully achieved, of replacing foreign imports. One raw material essential to the regime was cellulose, since Italy depended to a large extent on imported foreign wood pulp. Cellulose soon became a strategic resource. Before and during the Second World War, cellulose represented a strategic resource of fundamental importance, being used mainly in two major industrial sectors, namely paper manufacturing and synthetic textile fibers such as rayon. In the absence of natural wool as a result of the sanctions, synthetic textile fibers were also developed from cellulose. In the mid 1930s there was a sharp rise in domestic demand for cellulose, especially from the paper and textile sectors, but also because of the need for high quality cellulose, obtained

mainly from fibers or wood pulp, for the manufacture of nitrocellulose. It was in this context that CELDIT (Cellulosa d'Italia) emerged, aimed at overcoming the chronic foreign dependence on this raw material. Located at the railway junction near Chieti and linked to the figure of the engineer Umberto Pomilio, author of a patented method based on the production of cellulose derived from straw, CELDIT was able to produce high quality cellulose by using soda and chlorine obtained through the electrolysis of sea salt. This system, patented on an industrial scale in the Italian plant, was characterized by a continuous electrochemical cycle and by high energy requirements. The availability of low cost energy, above all produced locally, would have made the system economically sustainable. The proximity of the Triano hydroelectric power plant would have guaranteed continuity in the energy supply for the strategic production of cellulose.

3. Foundation of Celdit and Cellulose Policies

The foundation of Cellulosa d'Italia represents an emblematic case of resource allocation and economic dirigisme characteristic of the entrepreneurial state in 1930s Italy [2]. The strategic importance of cellulose emerged in the mid 1930s. In June 1935, the National Agency for Cellulose and Paper (ENCC) was established, a corporative body intended to support the publishing sector and coordinate the domestic market. However, it was the autarkic program of the IRI, under the leadership of Vice President Francesco Giordani, later president, that gave major impetus to the cellulose sector. Giordani is in fact widely known, together with U. Pomilio, for the method of extracting cellulose from cereal straw. [3] The emergence of the technological process and of the production site in Chieti, Abruzzo, was shaped by both scientific and personal connections [4]. In fact, during the 1920s F. Giordani had the opportunity to collaborate with Pomilio on the refinement of the electrochemical method for extracting cellulose through the use of soda and chlorine. Pomilio, for his part, was originally from the city of Chieti. The electrification of the Pescara River in the second half of the 1930s, together with the gradual structuring of the industrial system along the watercourse, which envisaged the construction of production plants with attached hydroelectric facilities, made the area of the fourth drop of the Pescara, in the territory of Chieti, a particularly suitable site for the establishment of Celdit. It was precisely here that the cellulose extraction method devised by Umberto Pomilio could be applied, since it required a high availability of energy and an integrated industrial infrastructure. CELDIT was formally established in May 1938. It was created on an equal basis between the IRI and Cartiere Burgo, the largest private company in the paper sector. Burgo imposed on Celdit a ban on producing paper for twenty five years, a sign that the largest Italian paper company sought to protect the market for finished paper products while at the same time restricting Celdit to cellulose production alone. The plant stood on a vast area of about 27 hectares, flanked by a workers' village, and officially entered into operation in July 1940. [5]

4. The Pomilio Patent and the Electrochemical Cellulose Industry

Within the framework of the Italian autarkic economy, this process was considered advantageous for cellulose production for two reasons. The first concerned the civilian conversion of electrochemical plants originally created during the First World War for the production of asphyxiating gases, namely chlorine, a raw material necessary for the extraction process. Secondly, continuous operation was introduced into all chemical processes. Unlike traditional discontinuous methods, or batch processes, which operated in single cycles, continuous operation made it possible to carry out the processes without interruption and without repeating the phases of shutdown, unloading, loading, and restarting of the machinery [6]. The Pomilio method involved three continuous stages: alkaline cooking, which prepared the fibers, chlorination with chlorine produced on site and reacting with lignin, and alkaline washing. Continuous operation was closely linked to the electrochemical nature of the plant. In fact, the Celdit factory did not purchase chemical reagents from outside, since it was able to produce chlorine internally through the electrolysis of sodium chloride solutions, namely sea salt. Electrolysis simultaneously generated soda and chlorine, which were immediately fed into the straw processing cycle. The finished product was an excellent binding material that required one third of the energy needed for wood based cellulose; moreover, plants conceived as closed circuit systems and not dependent on external supplies of soda and chlorine, such as the Celdit plant, required less industrial space than traditional plants. Continuous operation, however, had one major limitation, namely the need to operate at maximum productive capacity in order to reduce fixed costs, and this made Celdit particularly vulnerable during market fluctuations. The plant was regarded as a model of modernity; however, the burden of securing good quality raw material was initially problematic. In 1941, in fact, the combined cost of purchasing and transporting straw, together with processing costs, was almost three times higher than that recorded and tested in Argentina. The fragmentation of landed property and the poor quality of straw fibers from central Italy led to the first mistakes in sourcing straw as a raw material. Military requisitions forced Celdit to purchase straw in the Adriatic coastal area. That area favored the cultivation of shorter stalks and longer ears, and therefore the short fibers were not especially suitable for cellulose extraction. The same did not apply to energy, since Celdit had an adequate energy supply from the Triano hydroelectric power plant, located

about three kilometers away and built with techniques of wartime resilience and concealment.

5. The Triano Hydroelectric Power Plant for the Energy and Productive Resilience of Cellulose

Fig. 1 (Original project of the cellulose production plant (Chieti, Abruzzo), State Archive of Chieti)

Within this framework, the Triano hydroelectric power plant occupies a decisive position in understanding Celdit's productive continuity in wartime. The fourth drop of the Pescara entered into operation in 1941, completing the hydroelectric exploitation of the river precisely at the moment when the wartime economy made the availability of energy from domestic sources increasingly urgent [8]. By 1943, the Pescara had four power plants in operation, all necessary for the productive continuity of the electrochemical industry of central Abruzzo and, in particular, of Celdit in Chieti. The relationship between the new plant and the cellulose factory was not merely one of territorial proximity: a telegram dated 5 August 1939 already attests to the existence of a plant connection between Celdit and the fourth drop of the Pescara, while other documentation shows that SME regarded the fourth power plant as intended to supply the industrial hub of Chieti and the urban area of Pescara. Triano must therefore be read not as a mere background energy infrastructure, but as part of the material apparatus that made possible, at least in principle, the endurance of an autarkic and highly electrochemical production system at the Celdit plant [9]. For this very reason, its entry into operation in the midst of war assumes particular significance: the productive resilience of cellulose depended not only on Celdit's internal organization or on the availability of straw, but also on the stability of the regional energy network and on the protection of the hydroelectric infrastructures from which it drew power.

6. Celdit as a Strategic Industrial System in Wartime

In the context of the Second World War, Celdit progressively assumed the character of an industrial plant of strategic importance, embedded within the productive system that developed in the Pescara Valley between the late 1930s and the wartime period. The production of cellulose from straw, originally conceived as a response to the autarkic needs of the Italian economy, in fact acquired an additional function within the war economy, since it ensured the availability of a raw material essential for the paper industry and for various sectors of chemical production. The Chieti plant was structured as an articulated industrial complex, designed to integrate the different phases of the production process and to manage on an industrial scale the procurement of agricultural raw materials. The presence of railway and infrastructural connections facilitated the transport of straw from the cereal growing areas of central and southern Italy, while the organization of the plant reflected the need to maintain operational continuity in a production cycle heavily dependent on electrochemical processes. Alongside the industrial facilities, a workers' village was built to house part of the labor force employed in the plant. This arrangement shows that Celdit was not merely a productive plant, but an industrial system in which the technological, organizational, and social dimensions were closely interconnected. The Celdit plant began regular operation at the end of July 1940, just one month after Italy's entry into the war. Although production in the first year reached 92,000 quintals of cellulose, output soon underwent drastic declines due to the rationing of electrical energy. In July 1943, the plant was forced to suspend its activities definitively because of the destruction of the Foggia Pescara railway line, which made it impossible to obtain the salt required for electrolysis and the straw coming from the Adriatic area of central Italy. In an attempt to safeguard its corporate structure, the IRI incorporated Celdit into CCS, Cellulosa Cloro Soda. Meanwhile, Fascism collapsed in Italy and Mussolini, once freed, founded the Italian Social Republic. The Allies had landed in Sicily and the Italian campaign began along the German strategic defensive lines established after the Nazi occupation. Celdit, like the Triano hydroelectric power plant, was located near the strongest German defensive line, the Gustav Line.

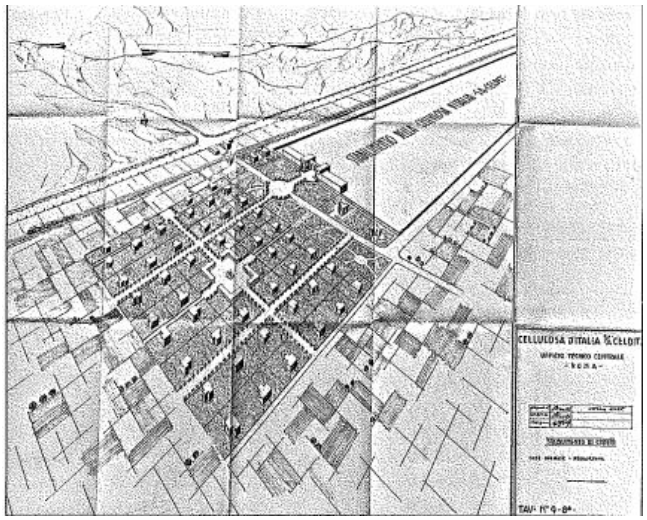

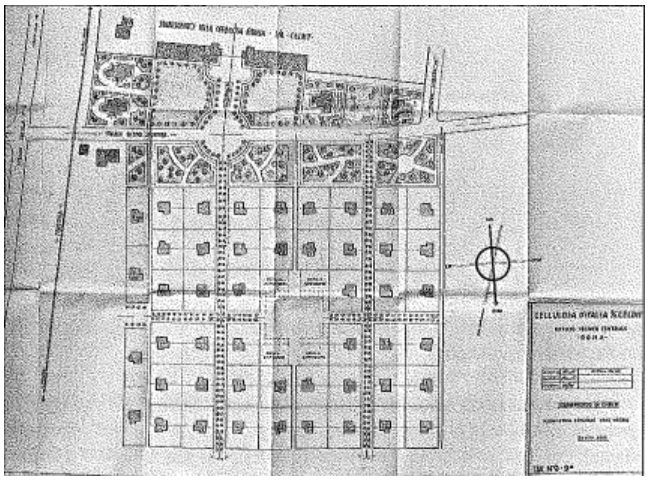

(Fig. 3 e 4. Project of the Celdit industrial village, State Archive of Chieti)

7. Conclusion

Between the beginning of October 1943 and the final phase of the German retreat, Celdit was struck by a process of spoliation and destruction that radically compromised the productive continuity of the plant [10]. With the German military occupation, the systematic plundering of the industrial apparatus began: the machinery was dismantled in preparation for its transfer to the Reich, and a total of 120 wagons of technical material were loaded. Only thanks to a complex delaying strategy and a form of "figurative sabotage" carried out by the leadership of the IRI was it possible to divert 72 wagons to the Cartiere Burgo plants in Treviso, while 48 wagons were actually deported to Germany. The final destruction of the plant, however, did not result from Allied bombing, but rather from the German decision to neutralize directly the productive potential of the site during the retreat: around four hundred mines, strategically placed inside the structure, caused devastating damage, so much so that at the moment of liberation the machinery that remained in Chieti was compromised by 40 percent of its total value. This led to an almost complete reconstruction of the plant, which continued until 1948.

The experience of Celdit therefore shows how the functioning of an industrial system based on electrochemical processes depended not only on the organization of production and the availability of raw materials, but also on the stability of the energy and logistical infrastructures that supported the operation of the entire complex. Within this framework, the opportunity developed over the last year to reconstruct historically the Triano hydroelectric plant has made it possible to advance the research further and to clarify the structural connection between the power plant and Celdit. The investigation has in fact shown that the particular configuration of the power plant, dispersed, disarticulated, and conceived according to criteria of wartime concealment, responded not only to defensive needs, but also to the necessity of guaranteeing energetic continuity to a plant, namely the cellulose plant, that required constant, stable, and abundant energy. Compared with a traditional power plant, such an arrangement therefore increased the wartime resilience of the infrastructure and strengthened the conditions for the productive continuity of the Chieti plant.

Alongside this integration between industrial plant and energy infrastructure, there was also a specific social organization of production. The continuous nature of the electrochemical cycle made the stable presence of workers on site indispensable in order to guarantee immediate availability, shift management, and prompt intervention at every stage of the process. For this reason as well, Celdit must be interpreted not as a simple factory, but as a complex territorial industrial system in which energy, technology, logistics, and workers' settlement were closely interconnected.

The investigation also makes it possible to clarify more fully the historical conditions that made the presence of Celdit in the Pescara Valley possible. The Chieti roots of Umberto Pomilio, the development of the patent with the scientific support of Francesco Giordani, and Giordani's subsequent role at the top of the IRI, first as vice president and then as president, all contributed to creating the technical, political, and institutional conditions for the establishment of Cellulosa d'Italia in Abruzzo. In this way, the historical picture of Celdit's presence in the Pescara Valley is completed, showing how it resulted from the convergence of autarkic policy, electrochemical innovation, hydroelectric infrastructures, and the territorial organization of war.

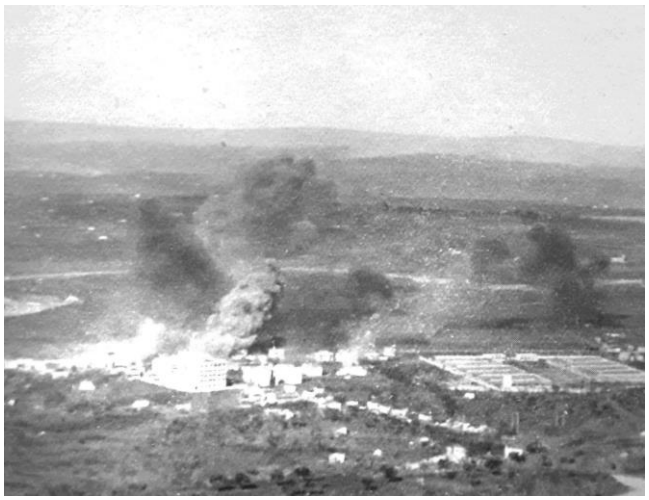

(Fig.5 Sabotage of the Celdit plant, 1943. Telephotograph by Avv. Sestini. Photograph published in A. Meloni, *Chieti città aperta. Relazione storica sulle vicende belliche del 1943-1944*, 2nd ed., Tip. Arte della Stampa, Pescara, 1966, p. 104.

Acknowledgements

Research described in the paper was supervised by Prof. PhDr. Marcela Efmertová, CSc, FEE CTU in Prague.

References

[1] R. Petri, Storia economica d'Italia: dalla Grande guerra al miracolo economico (1918-1963), il Mulino, Bologna 2002; V. Zamagni, Dalla periferia al centro: la seconda rinascita economica dell'Italia (1861-1990), il Mulino, Bologna 1993 (II ed.), pp. 349-376.

[2] L. D'Antone, L'architettura di Beneduce e Menichella, in Storia dell'Iri, vol. I, Dalle origini al dopoguerra (1933-1948), a cura di V. Castronovo, Laterza, Roma-Bari 2011, p. 235

[3] L. Scalpelli, Francesco Giordani (1896-1961), in I protagonisti dell'intervento pubblico in Italia, a cura di A. Mortara, Franco Angeli, Milano 1984, pp. 471-500.

[4] L. D'Antone, L'architettura di Beneduce e Menichella, in Storia dell'Iri, vol. I, Dalle origini al dopoguerra (1933-1948), a cura di V. Castronovo, Laterza, Roma-Bari 2011, p. 235

[5] La chimica e l'industria», 1, 1936, pp. 6-13. 56 Id., The Use of Electrolytic Chlorine for the Manufacture of Cellulose, in «Journal of the Electrochemical Society», 1, 1938, pp. 153-162.

[6] G. Galasso, Crisi e trasformazione dell'economia italiana, in Id. Storia dell'industria elettrica in Italia. 3. Espansione e oligopolio 1926-1945, Laterza, Roma-Bari, 1993, pp. 40-41.

[7] Fondo Società Meridionale di Elettricità (SME), Faldone "Pratiche Direzione Costruzioni Idrauliche – Centrale Triano Celdit", fasc. Telegramma dell'ing. Pomilio per impiantistica di collegamento elettrico tra Celdit e IV salto del Pescara, 5 agosto 1939, segnatura MO1A11S003001 / doc. n. 9377, Compartimento di Napoli.

[8] A. Meloni, Chieti città aperta. Relazione storica sulle vicende belliche del 1943-1944, 2ª ed.,
[1] Tip. Arte della Stampa, Pescara, 1966, pp. 104.

About Authors...

Jacopo BASSETTA, from Italy, he holds a degree in Philology, Linguistics, and Literary Traditions, with a thesis on the history of journalism and media from the G. d'Annunzio University of Chieti-Pescara (Italy). Currently, he is a PhD student in Digital Transition, Innovation, and Health Services at Leonardo da Vinci University (Italy) and a visiting doctoral student at the Department of Electrical Engineering, in the Historical Laboratory of Electrical Technology. His research focuses on the history of technology, particularly the history of artificial intelligence.

The Role of Licensed AVRM Aircraft Clock Production in the Development of Industrial Wristwatch Manufacturing in Czechoslovakia in the 1950s.

Mgr. David HAMR[1]

[1]Historical Laboratory of (Electro)Technology, K13116, FEE Czech Technical University, Technická 2, 166 27 Prague, Czech Republic

hamrdavi@fel.cvut.cz

Abstract. *This article examines the significance of the licensed introduction of Soviet AVRM aircraft clock production at the Chronotechna plant in Nové Město nad Metují in the early 1950s for the licensed production of MiG-15 aircraft in Czechoslovakia. The study argues that this step played an important role in the acquisition of technological capabilities necessary for the later industrial production of mechanical wristwatches. The AVRM clocks, manufactured in Czechoslovakia under the designation ALH, were technologically and structurally close to mechanical pocket watches, which from a manufacturing perspective represent an intermediate stage in the development toward mechanical wristwatch production. Through the transfer of complete technical documentation and the adoption of manufacturing procedures with Soviet assistance, Czechoslovak engineers and technicians gained valuable experience in industrial watchmaking production. The aim of this article is to describe the process of acquiring the production technology of this aircraft instrument and to evaluate its influence on the subsequent establishment of mechanical wristwatch manufacturing in Czechoslovakia, particularly the production of PRIM wristwatches in the late 1950s.*

Keywords

History of technology, history of fine mechanics, history of watch production, technology transfer; metal industry, electrical engineering and armament industry; know-how, history of innovations, centrally controlled economy, 1945-1960, Czechoslovakia

1. Introduction

In the summer of 1954, the national enterprise Chronotechna in Nové Město nad Metují completed the development of the prototype of the first Czechoslovak wristwatch, Spartak. Three years later, when serial production commenced at the Nové Město Chronotechna under the brand Prim, Czechoslovakia became the eighth country in the world capable of industrially producing mechanical wristwatches.[1] The first industrially manufactured Czechoslovak watch movement of a modern type, equipped with advanced and technically demanding components, most notably the so-called Swiss lever escapement, represented a major technological breakthrough in the domestic field of precision engineering and fine mechanics. The success of the serial production of wristwatches and their key component, the mechanical caliber 50, drew upon the country's rich industrial traditions; however, the influence of external factors was also significant. The design of the movement was based on the unauthorized replication of the French LIP R25-3 caliber[2], while the availability of a specialized machinery park preserved as a legacy of the fine mechanical wartime production of the Third Reich enabled the execution of highly demanding technological operations. Another critical factor was the indirect technological support provided by the Soviet Union through the introduction of licensed production of military aviation deck clocks AVRM/ALH, which supplied essential experience in large-scale manufacturing of precise timekeeping instruments. Particular attention will be paid to how specific aspects of the introduction of dashboard clock production contributed to the subsequent ramp-up of serial manufacturing of mechanical wristwatches. The analysis will focus primarily on the design similarities between dashboard clocks and mechanical wristwatches, as well as on manufacturing processes, assembly and maintenance procedures, and the

[1] HOVORKA, L. *Primky*. Brno: Host, 2018.

[2] This is reliably proven by archival documents deposited in the *Municipal State Archives in Hradec Králové*, and also indirectly by publications referring to the creation of the first Czechoslovak watches, especially Hovorka and Martínek.

materials and technologies employed. Organizational practices, technological discipline, and the prevailing production culture will also be examined as significant factors that facilitated the successful acquisition of industrial wristwatch manufacturing technology in Czechoslovakia.

2. The First Czechoslovak Wristwatches and the Role of Licensed Acquisition of Soviet Manufacturing Technology

In the early postwar years, Czechoslovakia faced a critical shortage of high-quality wristwatches due to the exhaustion of the consumer market after World War II.[3] Economic and strategic motivation to acquire advanced watchmaking technology was therefore high. Following the establishment of the Iron Curtain, aspirations to master sophisticated fine-mechanical technology also acquired a military dimension. The reputational and prestige aspects of this undertaking were significant, and the transition to a centrally planned economy added a propagandistic element. The adverse political and economic developments following the 1948 Communist coup accelerated the growth of the domestic watchmaking industry, fostering development that would have been unlikely under the normal market conditions of the First Republic.To this end, on 1 November 1949, a new production facility, Chronotechna 02, was established in Nové Město nad Metují specifically to initiate the production of wristwatches. Five years after the plant's founding, Nové Město Chronotechna produced the first prototypes equipped with caliber 50, marketed under the name Spartak. On 26 November 1954, these prototypes were approved for serial production by the Ministry's Commission. By early 1958, the national enterprise Klenoty proudly offered domestic wristwatches under the brand Prim to its first customers. Serial production of fine-mechanical timepieces was particularly challenging due to the miniature size of components, the stringent requirements for precision and cleanliness, and extremely low tolerances for error. It demanded a high proportion of manual labor and highly trained personnel. Early attempts to establish watchmaking at the Nové Město plant were accompanied by several setbacks. Initial efforts to recruit Swiss experts failed, as did attempts to secure technical support from East German watchmaking factories. Although the management of the enterprise lacked direct experience in mechanical wristwatch production, it was highly competent and well-versed in the principles of precision engineering. It was therefore correctly decided that the company would acquire production skills gradually. Similarly, the expansion of the production portfolio, logistics, technology, and organization was planned to proceed incrementally. Serial wristwatch production is an exceptionally specific and demanding discipline of precision engineering.

Accordingly, it was decided that preliminary tasks should first be completed—for example, the production of insert movements or cooperative manufacturing of time relays. The experimental production of pocket watches was also planned before progressing to the manufacture of high-quality Swiss-type wristwatches.It was wisely determined that the industrial production of fine-mechanical timepieces should be approached step by step. This strategy was reflected in a long-term plan for acquiring key technological competencies: first, the production of individual components, followed by pocket watches as a prelude to serial wristwatch production. Ultimately, it was also decided to adopt the design from the French LIP R25 movements from Besançon without authorization. The relatively robust construction of this modern caliber also offered a favorable prospect for technological mastery using the machinery available in Czechoslovakia, much of which remained as a legacy of Third Reich wartime fine-mechanical production.[4]The acquisition of wristwatch manufacturing technology was further "fortuitously" accelerated in the early 1950s by indirect Soviet involvement. In transferring licensed production of precise AVRM dashboard clocks for MiG-15 jet aircraft to the Nové Město Chronotechna, the Soviets provided invaluable know-how, technical documentation, and tooling sets. This enabled the Nové Město factory to gain crucial expertise in large-scale production of precision timekeeping instruments, significantly advancing its ability to achieve the ambitious goal. In fact, the gained competencies allowed the factory to bypass the initially planned experimental production of high-quality mechanical pocket watches and proceed directly to producing prototypes of the first Czechoslovak mechanical wristwatches, Spartak.[5]

2.1 AVRM / ALH Clocks – Their Licensed Production in Czechoslovakia

Aircraft clocks of the AVRM type represent a crucial chapter in the history of the Czechoslovak watchmaking industry. These clocks were produced by the company Chronotechna, later known as Elton, at its plant in Nové Město nad Metují between 1953 and 1990.[6] Production continued without interruption throughout this period, and approximately ninety thousand units were manufactured over these thirty-seven years. Such a long production cycle attests both to the reliability of the design and to the sustained demand for this type of aircraft clock. The AVRM clocks were a licensed product manufactured according to documentation originating from the Soviet Union. Although they were originally designed for the licensed production of

[3] MARTÍNEK, *Z. Dějiny československého hodinářského průmyslu I. a II.* Brno, Nové Město nad Metují, ELTON hodinářská, Technické muzeum, 2009

[4] It concerned the production of special timed igniters for anti-aircraft ammunition, commonly referred to as "flacks."

[5] Ibid.

[6] HOVORKA, L. *Primky*. Brno, Host, 2018.

MiG-15 jet aircraft, their use gradually expanded to other aircraft types manufactured in Czechoslovakia. Beyond aviation, AVRM clocks also found applications in ground-based military equipment. They were installed in combat vehicles, command vehicles, and communication vehicles used by the Czechoslovak and Polish armed forces.

The construction of the AVRM clock was highly robust and met the demanding requirements of aviation operation. The movement contained fourteen functional jewels, employed a Swiss lever escapement, and was equipped with a screw balance.[7] The gear train wheels were manufactured from brass, while the pallet fork and escapement wheel were gold-plated. The rate-regulating lever was heat-blued, and most other components were nickel-plated. This combination of materials ensured high durability, long service life, and stable operation even under demanding operating conditions.[8]

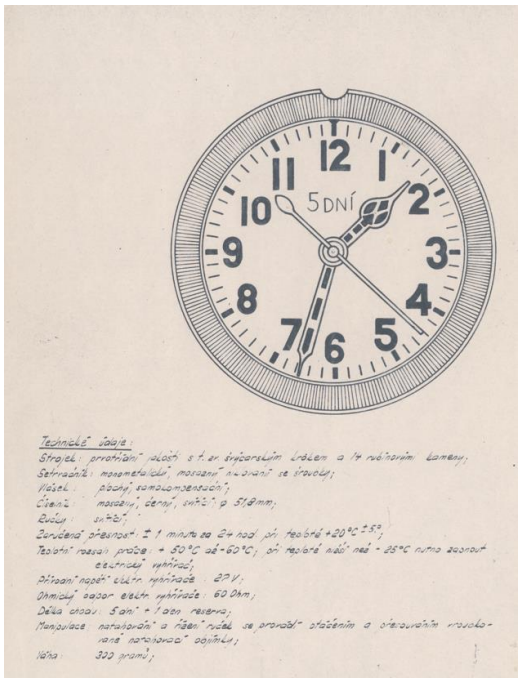

Fig 1. *Technical documentation of AVRM clock. Source: Municipal archive Hradec Kralove (Source:)*

Technically, the instrument was a precision aircraft clock with a movement diameter of sixty millimetres and a central seconds hand. It incorporated fourteen jewels, a monometallic screw balance, and a self-compensating hairspring. The accuracy of the clock was guaranteed within a range of ±1 minute per 24 hours at operating temperatures from −25 °C to +50 °C. For operation in low temperatures, the movement was equipped with an electric heating system.

To ensure good readability under low-light conditions, the hands, the triangular orientation mark on the bezel, the numerals, and the five-minute markers on the dial were coated with fluorescent pigments. The pigment most commonly used was Diu-Lux, produced in the German Democratic Republic. For a certain period, part of the production also employed radioactive luminous compounds. To allow easy identification of clocks containing radioactive pigments, the dial was marked with a yellow inscription “RA”.

2.1.1 The genesis of AVRM dashboard clock production in Czechoslovakia

At the end of 1951, the watchmaking enterprise in Nové Město nad Metují was entrusted with a classified military task: to establish the production of precision aircraft dashboard clocks based on Soviet documentation. Although the plant was not yet fully equipped and its technical facilities were still incomplete at the time, the management accepted the assignment. The documentation consisted of fourteen volumes containing design drawings, technological procedures, specifications for tools, fixtures and measuring instruments, as well as lists of state standards defining the required materials. For security reasons, the clocks were redesignated as ALH.

The manufacturing technology for the individual components was similar to that used in the production of pocket watches. The transfer of Soviet documentation proved extremely valuable, as it provided young designers, technologists and toolmakers with a unique practical education in precision mechanics. Preparation for production began immediately. The first step involved redrawing the documentation and translating it from Russian into Czech. A significant portion of the work fell to the tool shop, which had to produce a large number of complex stamping tools, cutting tools and measuring instruments. Consequently, the capacity of the tool shop was expanded, and its employees often had to work under extraordinary production regimes. By the end of 1952, most of the required tooling had been successfully manufactured. In the following year, trial production was initiated, and by mid-1953 serial production had begun. From 1954 onward, the clocks were produced at an approximate rate of two thousand units annually and supplied to the Czechoslovak armed forces. In response to military requirements, a variant intended for installation in tanks was also developed.

2.2 Contribution of the production of on-board clocks for the introduction of industrial watch manufacturing in Czechoslovakia

The mechanical calibre (movement), the functional heart of a wristwatch, represents an exceptionally precise and technologically complex product of precision engineering. Even in its simplest form it consists of dozens to hundreds of miniature components whose manufacture requires extremely high levels of accuracy and technological sophistication. Mechanical wristwatches therefore rank among the most demanding fine-mechanical devices

[7] From a constructional and structural perspective, these precise on-board clock mechanisms were practically identical to Swiss-type pocket or wristwatches.

[8] HOVORKA, L. *Primky*.. Brno, Host, 2018.

produced by conventional engineering methods. The need to compress such a complex timekeeping mechanism into a wearable size roughly comparable to that of a coin makes the mastery of industrial watch production a significant indicator of a country's technological and industrial maturity.Wristwatches, which became widely popular in civilian use after the First World War, evolved from pocket watches. From the late seventeenth to the mid-nineteenth century, pocket watches were primarily luxury objects and symbols of social status.[9] With industrialization, however, they gradually became more accessible and began to serve as practical instruments for organizing everyday life. By the late nineteenth century, industrial production—especially in Switzerland—had led to the spread of higher-quality watches equipped with the Swiss lever escapement.

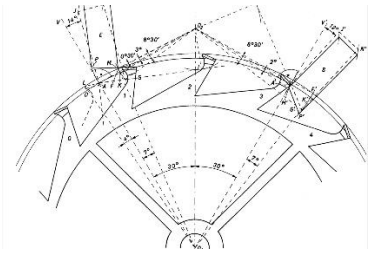

Fig.2 Scheme of swiss lever escapement. Source: Author

From a technical perspective, pocket watches were closely related to later wristwatches and also shared many characteristics with dashboard timekeeping instruments. Some of the earliest dashboard clocks were essentially modified pocket watches. In this context, the AVRM aircraft clock represents an important milestone in the history of Czechoslovak precision mechanics. Its production significantly strengthened the technological capabilities of the Chronotechna plant in Nové Město nad Metují and helped create the foundation for the later domestic production of wristwatches under the Prim brand.

2.2.1 Technical and Industrial Factors Through Which AVRM Clock Production Facilitated Technology Acquisition

The construction of the AVRM aircraft clock is in many respects similar to that of mechanical pocket watches. All moving components, particularly the gear train and escapement with balance, have parameters comparable to those found in high-quality pocket watches. Unlike typical wristwatch or pocket-watch movements, however, the gear train was not mounted between milled bridges but was instead precisely pressed into a milled base plate and spaced by distance pillars. This older construction method, historically used for example in marine chronometers, still required manufacturing procedures nearly identical to those used in Swiss-type pocket and wristwatches for the most sensitive components.

Dimensionally, the gear train corresponds to that of larger pocket watches. The wheel diameters and tooth modules are approximately twice those used in standard wristwatch calibres such as the French LIP R25, which served as the model for the first Czechoslovak wristwatches. From the perspective of precision machining and materials engineering, the manufacturing task remained similarly demanding, although the production of wristwatches becomes even more challenging due to their higher degree of miniaturization. The escapement itself—a classic Swiss lever escapement with ruby pallet stones, a polished steel escape wheel, and a balanced screw balance—required manufacturing precision comparable to that of high-quality wristwatch movements.

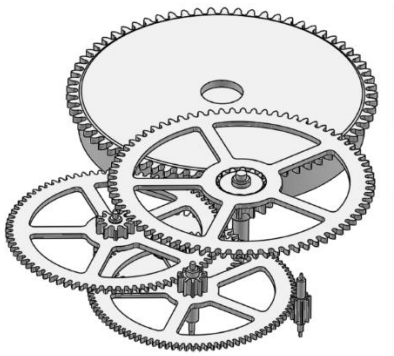

Fig. 3 Clasical scheme of watch gear train. Source: Author

Production also required the use of specialized hairsprings and jewel bearings for most moving parts, including the impulse jewel and balance staff cap stones. These demanding material requirements and the high degree of component similarity necessitated manufacturing techniques closely related to those used in wristwatch production, particularly in precision machining and surface finishing. Many components required galvanic treatment, polishing, and machining on specialized equipment.

The production of such miniature components relied heavily on sliding-head automatic lathes designed for parts with a high length-to-diameter ratio. These machines—often of Swiss manufacture—allowed precise and repeatable machining of long, slender shafts and other delicate components that would be difficult or impossible to produce using conventional lathes. In Czechoslovakia, a significant part of this specialized machinery originated from Swiss equipment preserved from wartime production of precision mechanisms such as fuzes and timing devices for aerial munitions.

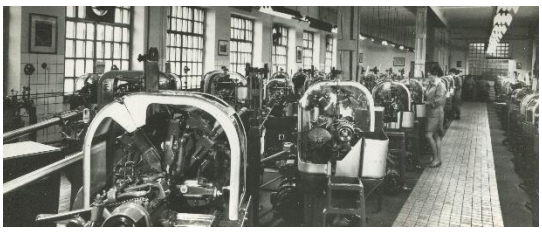

Fig 4. Sliding head lathes in Nove mesto plant. Source: State municipal Archive Hradec Kralove

[9] MICHAL, S. *Hodinářství a hodináři v českých zemích*. Praha, Libri, 2002.

Similar technologies were later used in wristwatch production. Gear cutting required specialized cycloidal cutters and dividing processes, followed by polishing, surface treatment, and heat processing to achieve the required mechanical properties and precision.

The implementation of the AVRM production line at Novoměstská Chronotechna represented a pivotal moment in the development of Czechoslovak precision manufacturing capabilities. Its primary significance lay not merely in the ability to replicate a licensed product, but in the systematic acquisition of a comprehensive production culture and specialized technical skills essential for high-precision horology. This encompassed the ability to interpret, generate, and apply complex technical documentation, including construction drawings, tooling designs, and manufacturing process specifications, which collectively established a standardized framework for the entire production cycle.

Personnel gained extensive hands-on experience with advanced machining techniques, forming, finishing, and surface treatments, as well as precise assembly, calibration, and testing of mechanical movements. Critical procedures, such as the installation and adjustment of jeweled bearings, fine regulation of the Swiss-style escapement, and quality control of highly miniaturized components, were rigorously practiced. As confirmed by members of the technical staff, these activities produced an "acceleration effect" in the process of technological acquisition, effectively bridging the gap between the production of larger, less intricate instruments like AVRM flight clocks and the highly miniaturized mechanisms required for mechanical wristwatches.

The AVRM project thus served as a foundational training ground, enabling the subsequent design, prototyping, and serial production of the PRIM mechanical wristwatches, and demonstrating the critical role of licensed military manufacturing as a conduit for broader technological and industrial advancement in postwar Czechoslovakia.

3. Conclusions

If one is to responsibly evaluate the role of the licensed acquisition of AVRM on-board watch production technology in the broader context of initiating Czechoslovak mechanical wristwatch production, it becomes clear that this episode must be considered alongside multiple contributing factors that positively influenced the ultimate goal of establishing domestic wristwatch manufacturing. Together with the heritage of advanced machine-cutting technologies and the successful reverse engineering of the French LIP R25 design, the licensing of the AVRM on-board watch was a decisive factor. It provided the Czechoslovak watch industry with critical technical knowledge for implementing specialized production processes, as well as the necessary skills for their execution. Moreover, it enabled testing and gradual mastery of production procedures according to established standards and, importantly, introduced a culture of high-precision, fine mechanical manufacturing into the domestic production environment.Within the context of the Czechoslovak watch industry—and particularly regarding its greatest achievement, the creation of the first domestic mechanical wristwatches under the PRIM brand—this technological and procedural transfer placed Czechoslovakia among the world's most technologically advanced nations in horology. By 1958, Czechoslovakia had become only the eighth country globally capable of industrially producing mechanical wristwatches. The licensed acquisition of AVRM production thus represents a pivotal chapter in the development of the country's fine mechanical manufacturing capabilities and the successful industrialization of wristwatch production.

Acknowledgements

Research described in the paper was supervised by Prof. PhDr. Marcela Efmertová, CSc. at the Historical Laboratory of (Electro)Technology, Faculty of Electrical Engineering, Czech Technical University in Prague (FEE CTU in Prague).

References

[1] HOVORKA, L. *Primky*. Brno, Host, 2018.

[2] KRÁLÍK, J. *Prima čas - Historie hodinek PRIM 1949-2019*. Praha, Grada, 2019.

[3] MARTÍNEK, Z. et all., *1949-1989, 40 let hodinářské výroby koncernového podniku Elton v Novém Městě nad Metují.* Nové Město nad Metují, Elton 1989.

[4] MARTÍNEK, Z. Časoměrná technika. In SMOLKA, I., FOLTA, J. (eds.). *Studie o technice v českých zemích 1918–1945*. Vol V., part 2., Praha, Národní technické muzeum v Praze, 1995, p. 637– 667.

[5] MARTÍNEK, Z. *Dějiny československého hodinářského průmyslu I. a II.* Brno, Nové Město nad Metují: ELTON hodinářská, Technické muzeum, 2009.

[6] MICHAL, S. *Hodinářství a hodináři v českých zemích*. Praha, Libri, 2002.

[7] VAJSAR, J. Technologie hodinkových ozubených kol. *Jemná mechanika a optika* 1962, vol 7, no 7, pp. 207 -212.

[8] ŽID, J. Náramkové hodinky Prim -významný úspěch čs. Strojírenství. Jemná mechanika a optika 1960, vol 5, no 3, pp. 77 – 85.

About Author

Mgr. David HAMR was born on May 18, 1979 in Liberec. He is employed as a curator of the watch collections of the National Technical Museum in Prague and is studying for a doctoral study program a History of Sciences and Technology at the *Historical Laboratory of (Electro)Technology*, K13116, Faculty of Electrical Engineering, Czech Technical University in Prague. His research interests are focused on the history of Czechoslovak mechanical wristwatches in the context of the broader topic of technology transfer in post-war Europe.

Building the Tunisian Educational System after Independence (1956-1965): the 1958 Reform and the Role of Mahmoud Messadi

MSc. Amani MANSOURI[1]

[1] Historical Laboratory of (Electro)Technology, Dept. of Economics, Management and Humanities, Czech Technical University in Prague, Technická 2, 166 27 Praguee, Czech Republic

mansoama@fel.cvut.cz

Abstract. *This article examines the formation of the Tunisian educational system during the first decade after independence, with particular attention to the school reform of 4 November 1958 and the role of Mahmoud Messadi in its implementation. It shows that this reform was part of a broader state-building project led by the regime of Habib Bourguiba, in which education was seen as a tool for social modernization, the training of national elites, and the strengthening of national identity. Starting from the institutional, linguistic, and social legacy of the French protectorate, the text highlights the will of the Tunisian authorities to unify, centralize, and nationalize education. It also shows that these changes cannot be understood in a simple linear way: the expansion of schooling and the gradual Tunisianization of educational staff were accompanied by long-lasting tensions, especially in the areas of bilingualism, regional inequalities, and social differences. The study therefore offers a historical and critical reading of educational reforms from 1956 to 1965, while placing Mahmoud Messadi's action within the broader institutional and political framework of postcolonial Tunisian state-building.*

Keywords. *History of technology, Tunisia, History of education, independence, 1958 reform, Mahmoud Messadi, Habib Bourguiba, bilingualism, state-building, postcolonialism.*

1. Introduction:

The development of the Tunisian educational system is a key element for understanding the building of the modern state after independence. Inheriting a school system deeply marked by the period of the French protectorate (1881–1956), independent Tunisia quickly began to transform its educational system in order to meet the administrative, political, and social needs of a state in formation.

The education law of 4 November 1958[1] was a founding moment in this process. It helped to shape a national, unified, and centralized educational system, aimed at expanding access to school, strengthening state control over education, and preparing new generations of administrative, technical, and intellectual elites. This reform was part of a broader political project led by President Habib Bourguiba[2], who saw education as a major tool for social modernization, the strengthening of national identity, and the legitimation of the new state.

The implementation of this reform was closely linked to the work of Mahmoud Messadi[3], an intellectual and Minister of National Education between 1958 and 1968. However, these changes cannot be understood only through the role of one individual actor. They must also be placed in the broader context of the choices made by the Tunisian government, administrative centralization, the Tunisianization of institutions, and tensions inherited from the colonial system, especially in linguistic, social, and regional terms.

This article analyzes the founding period from 1956 to 1965. It highlights the structural changes introduced by the 1958 law, the role played by Mahmoud Messadi in their implementation, and the tensions and limits that accompanied the building of the educational system of independent Tunisia.

[1] ANT, Series A – Republic of Tunisia, Law No. 58-118.

[2] Habib Bourguiba (1903–2000) was the father of Tunisian independence and the first president of Tunisia. He modernized the country, supported women's rights, and developed education. *(source: Encyclopædia Britannica, "Habib Bourguiba," Britannica Academic, updated February 16, 2024, accessed July 22, 2025).*

[3] A Tunisian writer, Arabic teacher, and leading intellectual, Mahmoud Messaadi was deeply influenced both by his education at Sadiki College and by French education. After independence, he became a central figure in Tunisian educational policy. As Minister of National Education from 1958 to 1968, he led the major school reform of 1958 and was one of its main initiators. See VERMEREN, Pierre, "L'appareil éducatif et les hommes (1956-1968)," in *La formation des élites marocaines et tunisiennes: des nationalistes aux islamistes, 1920-2000*, Tunis, Institut de Recherche sur le Maghreb Contemporain (IRMC), 2002, pp. 220–247.

2. Historical Context: Education at the Time of Independence

At the time of independence in 1956, Tunisia inherited an educational system deeply shaped by more than seventy years of French protectorate rule. This system was based on a hierarchical and socially selective organization, marked by the coexistence of several types of institutions. On the one hand, French schools, inspired by the educational model of the Third Republic and the reforms of Jules Ferry, provided secular, centralized education mainly in the French language. These schools were mainly intended for the children of European settlers, while access for Tunisians remained limited.

Fig. 1. Habib Bourguiba proclaimed the Republic of Tunisia[4]

On the other hand, traditional institutions of Islamic education, especially Zaitouna University[5], continued to play an important role in religious and legal training. Teaching there was in Arabic and focused mainly on religious sciences. Between these two poles, there were also Franco-Arab schools, which offered bilingual education combining some modern subjects in French with cultural and religious subjects in Arabic.

This organization created a strong educational duality. Mastery of French became a key factor for access to the administration and modern careers, while traditional education remained more closely linked to religious functions or less valued positions in the colonial order. On the eve of independence, most of the Tunisian population had very limited access to modern education, which resulted in a high rate of illiteracy and deep inequalities in the distribution of educational capital.

After independence, Tunisia faced several major challenges in the field of education. The system inherited from the protectorate seemed insufficient to meet the needs of a state under construction. One of the main problems was the very high level of illiteracy: at the beginning of the 1960s, nearly 85% of the adult population was illiterate, and this rate reached around 96% among women[6]. Most children, especially in rural regions, still had no access to school. Rapid population growth increased pressure on school infrastructure, while qualified teaching staff remained insufficient.

At the same time, the country lacked national elites able to ensure the functioning of administrative and economic institutions. A large part of the teachers and civil servants were still foreign cooperators, mainly French. Finally, the language question was a central issue: the strong presence of French in scientific and administrative education raised the question of the place of Arabic in the new national educational system.

In this context, Tunisian leaders saw education as a central element of the project to modernize the country. For Habib Bourguiba and the elites of the national movement, school had to contribute to the transformation of society, the strengthening of the state, and the training of new national elites. The government therefore invested in the building of schools, the training of teachers, and the creation of new school programs. The teaching of Arabic language, national history, and Tunisian culture became an important part of the new educational policies. The expansion of schooling also aimed to reduce some inequalities inherited from the colonial period, even if its effects remained uneven depending on regions, social backgrounds, and gender. In this context, the promotion of girls' education also became an important goal of the new government.

The adoption of the education law of 4 November 1958 was therefore part of an attempt to respond to these challenges through the creation of a unified national educational system, while combining goals that were sometimes contradictory: democratization of schooling, state-building, cultural affirmation, and adaptation to the country's administrative and economic constraints.

3. The 1958 Education Law: Foundation of the National Educational System

The adoption of the education law of 4 November 1958 was a decisive step in the building of the educational system of independent Tunisia. This text represented the first attempt to organize education within a national framework after the end of the French protectorate. Often described as a "school constitution," this law established the fundamental principles that would shape Tunisian education for several decades[7].

The reform took place in a political context marked by the will for modernization promoted by President Habib Bourguiba and the elites of the national movement. Education was then seen as a central tool for training the elites needed for the administration of the state, encouraging

[4] Source: https://gazetteducontinent.fr/histoire/le-25-juillet-1957-habib-bourguiba-proclamait-la-republique-de-la-tunisie. Accessed 10/12/2025.

[5] It is one of the oldest and most important Islamic universities and mosques in Tunisia. It is in the heart of the medina of Tunis and plays an essential role in Tunisian identity and religious education. It is often mentioned in history, Islamic culture, and relations with Europe.

[6] GESIS – Leibniz Institute for the Social Sciences. *Zugänge, Barrieren und Potentiale für die internationale Mobilität von Wissenschaftlerinnen. Länderbericht Tunesien*. 2020, p. 1 ; UNICEF. *The State of the World's Children 2007: Middle East and North Africa Edition – Women and Children: The Double Dividend of Gender Equality*. 2007.

[7] ANT, Série A – République Tunisienne, Loi n° 58-118.

economic development, and strengthening national identity. The 1958 law therefore aimed to reorganize an educational system inherited from the protectorate, which was marked by strong social, linguistic, and territorial inequalities[8].

The first goal of the reform was to create a unified national educational system. Under the protectorate, education was based on the coexistence of several separate institutions: French schools, Franco-Arab schools, and traditional institutions of religious education such as kuttabs, madrasas, and Zaitouna University. This fragmentation reflected a colonial logic of social and cultural separation. The 1958 reform tried to reduce this institutional plurality by establishing an educational system under the authority of the Tunisian state. This gradual integration made it possible to strengthen the coherence of the school system and ensure more direct public control over education.

The second goal concerned the expansion of schooling. The government believed that access to education had to be widened in order to fight illiteracy and support the development of the country. The 1958 law therefore introduced the principle of compulsory schooling for children aged six to twelve and affirmed free public education. This policy aimed to gradually include groups that had previously been largely excluded from the school system, especially in rural regions and inland areas. However, this expansion did not immediately remove the gaps between regions or the differences in access linked to social background.

The third goal was to prepare the administrative, technical, and intellectual staff needed for the functioning of the new state. After independence, Tunisia had to gradually replace foreign elites working in the administration, economy, and public institutions. School therefore became a strategic tool of Tunisianization. It had to train civil servants, teachers, technicians, doctors, and engineers who would take part in running the country. However, this goal did not automatically produce equal social mobility for all: the benefits of the reform often remained more accessible to groups that were already better placed in the social and linguistic space.

Finally, the educational reform sought to promote a new idea of the citizen. School had to train individuals able to take part in the social and political life of the country, while also developing critical thinking and openness to modern scientific knowledge. From this point of view, education appeared as a tool of social transformation, but also as a means of civic supervision in the service of a centralized state.

The 1958 law established a new organization of the Tunisian educational system based on a hierarchical and centralized structure. Primary education lasted six years and provided basic learning. Secondary education, which lasted seven years, ended with the baccalaureate, which gave access to higher education. Secondary education included several streams, literary, human sciences, scientific, and technical, intended to meet different educational and professional needs.

At the top of this structure was university education, which developed significantly after independence. The creation of the University of Tunis in 1960 was a major step in this process. For the first time, Tunisia had a national institution of higher education able to train its own elites and strengthen its academic sovereignty, even if higher education remained strongly dependent on human and intellectual resources inherited from the French model.

At the same time, the reform greatly strengthened the administrative centralization of the educational system. The Ministry of National Education played a central role in defining programs, organizing exams, and managing teaching staff. This centralization matched the government's wish to closely control the development of the school system and connect it to the political, economic, and social goals of the new state.

Fig. 2. University of Tunis El Manar[9]

The reform also introduced the gradual professionalization of the teaching profession. Teacher training became a national priority, and several specialized institutions were created to reduce dependence on foreign teachers and support the Tunisianization of educational staff.

However, one of the most characteristic features of the Tunisian educational system after independence was the adoption of a model of institutional bilingualism. Arabic was seen as a central element of national identity and Tunisian culture, while French kept an important place in scientific, technical, and administrative fields because of the legacy of the protectorate and the availability of teaching materials.

In the first years after independence, literary, historical, and cultural subjects were mainly taught in Arabic, while scientific and technical subjects often continued to be taught in French. This compromise responded to practical constraints, especially the lack of textbooks and teachers able to teach science in Arabic. It made it possible to maintain access to international scientific knowledge, but it also introduced an implicit hierarchy between languages: French remained associated with scientific knowledge and

[8] S. Bessis, *Histoire de la Tunisie: de Carthage à nos jours*. Paris, Tallandier, 2022, pp. 259–356.

[9] Source: https://utm.rnu.tn/utm/fr/ Accessed 4/2/2026.

the most valued sectors, while Arabic was more closely linked to cultural, historical, and identity-related subjects.

Thus, the 1958 law was indeed a major turning point in the history of Tunisian education, but its effects must be read in an ambivalent way: it opened access to school and strengthened state sovereignty, while also reproducing some inequalities inherited from the colonial period, especially through regional disparities and the linguistic hierarchy of knowledge.

4. Mahmoud Messadi and the Implementation of the Educational Reform

If the 1958 education law was the legal foundation of the new Tunisian educational system, its concrete implementation was closely linked to the action of Mahmoud Messadi. An intellectual, writer, and politician, he held an important place in the history of Tunisian education during the first years of independence. However, his role must be placed in a broader framework: that of the modernization policies of the Bourguiba regime, state centralization, and the institutional work carried out by the Ministry of National Education.

Messadi's action was part of a political and cultural project aimed at modernizing Tunisian society while preserving some basic references of its cultural identity. Through educational reform, he tried to connect several goals: training the qualified staff needed for the country's development, strengthening the place of Arabic culture in education, and maintaining openness to international scientific knowledge.

Born in 1911, Mahmoud Messadi received an education rooted in Arab culture and open to Western intellectual influences. After studies at the Sorbonne, he developed ideas about the relationship between tradition, freedom, and modernity. His literary and philosophical work shows a lasting interest in individual responsibility and in the place of human beings in society[10]. This intellectual path influenced his view of education, which he saw as a way to form individuals able to think independently and take part in national life.

After independence, as Minister of National Education, Messadi helped to strengthen the institutional foundations of the new educational system defined by the 1958 law. His action focused especially on the structuring of educational cycles, the development of teacher training, the organization of evaluation mechanisms, and the gradual Tunisianization of teaching and administrative staff. At the time of independence, many teachers were still foreign cooperators, mainly French. In this context, the creation of structures able to train a new generation of Tunisian teachers became a strategic priority.

The reform of school curricula was also part of this dynamic. The new content gave an important place to the teaching of Arabic language, national history, and Tunisian culture, while maintaining access to scientific and technical subjects. Messadi played an important role in giving intellectual direction here, but these choices must also be understood as responses to structural constraints: lack of qualified staff, the weight of the colonial legacy, the need to quickly train elites for the administration, and the search for a balance between national affirmation and international openness.

Messadi's thinking about education went beyond simple administrative reorganization. For him, school had to form not only educated students, but also citizens able to understand the world, use their judgment, and take part in the development of society. Education therefore appeared as a driving force of social modernization and as a means of transforming ways of thinking. In this view, school had to encourage both the spread of knowledge and the internalization of values such as responsibility, discipline, and civic commitment.

Messadi also gave great importance to the Arabic language, which he saw not only as a tool of communication, but also as a vehicle of thought and culture. The promotion of Arabic in education therefore appeared as a way to strengthen national cultural identity and revalue Arab intellectual heritage. However, his approach to the language question remained pragmatic. He recognized that French still had an important function in access to modern sciences, in higher education, and in international relations. Rather than breaking sharply with the linguistic heritage of the protectorate, he supported a balance between cultural affirmation and institutional efficiency.

This orientation resulted in the continuation of functional bilingualism in the Tunisian educational system, where Arabic and French occupied complementary but unequal positions. Arabic progressed in literary and cultural subjects, while French remained dominant in science and technology. This compromise allowed the system to function, but it also maintained a linguistic hierarchy that gave greater advantage to students from urban and French-speaking backgrounds.

The reforms implemented between the end of the 1950s and the mid-1960s produced important changes. School enrollment increased rapidly, new school infrastructure was built, and teacher training developed. These developments helped form new generations of Tunisian graduates who were called to occupy increasing positions in the administration, education, and some economic sectors. The creation of the University of Tunis in 1960 was part of this movement, offering a national space for higher education.

However, these changes also had limits. The rapid expansion of the school system sometimes led to overcrowded infrastructure, lack of teaching resources, and unequal quality of supervision. Regional and social inequalities continued to influence school paths, and the

[10] MESSADI, Mahmoud. *Nouvelle conception de l'enseignement en Tunisie : une récente réalisation du gouvernement Bourguiba, 1958–1959.* Tunis, Ministère de l'Éducation nationale, 1958.

linguistic compromise, while ensuring a certain institutional continuity, also helped maintain gaps between social groups. Thus, Messadi's role can be seen as essential in the implementation of the reform, but it was part of a broader process shaped by political, administrative, and social constraints that went beyond the action of one individual.

5. Conclusion

The period between 1956 and 1965 was a founding phase in the history of the Tunisian educational system. After independence, the Tunisian authorities began a deep transformation of the school system to meet the needs of the new state and support the modernization of the country. The 1958 education law was the central pillar of this reorganization. It established the foundations of a more unified national educational system, based on free education, the gradual expansion of schooling, and the administrative centralization of education under state authority.

The implementation of this reform was closely linked to the action of Mahmoud Messadi, but it must also be placed within the broader framework of the state-building policies of the Bourguiba regime, the administrative reorganization of the Ministry of Education, and the need to quickly train qualified staff. In this context, education became an essential tool of political legitimation, Tunisianization of institutions, and the production of new administrative and intellectual elites.

The reforms introduced during this period contributed to widening access to school, creating national training institutions, and strengthening an educational system placed at the center of the state project. However, these changes should not be understood in a simple linear or only positive way. They were also accompanied by long-lasting tensions. Educational bilingualism, adopted as a postcolonial compromise, made it possible to maintain access to international scientific knowledge, but it also reproduced a hierarchy between languages. In the same way, the expansion of schooling opened new possibilities for social mobility, without eliminating inequalities between regions, between urban and rural areas, or between social groups with different levels of linguistic and cultural capital.

The construction of the Tunisian educational system after 1956 was both modernizing and contradictory. It strengthened the state and expanded the school system, but it also reproduced some asymmetries inherited from the colonial period. The choices made during this period continue to shed light on several major debates in contemporary Tunisian history, especially questions of language policy, tensions between Arabization and the Francophone legacy, and structural inequalities in access to education and in the value given to school trajectories.

Acknowledgment

This paper was supervised by prof. PhDr. Marcela Efmertová, CSc. of Historical Laboratory of (Electro)Technology, Faculty of Electrical Engineering, Czech Technical University in Prague (FEE CTU in Prague), Technická 2, CZ-166 27 Prague. The author would like to thank her for this supervision.

References

[1] JAKUBOVÁ, I., RAIDA, Z. Exemplary Document for the paper in Radioengineering. *Radioengineering*, 2006, vol. 15, no. 1, p. 1 – 2.

[2] ANT, Série A – Construction de l'État.

[3] ANT, Série A – République Tunisienne, Loi n° 58-118.

[4] ANT, Série L – Évolution des écoles tunisiennes, in Documents diplomatiques français (1870–1969), Paris, 1956.

[5] ANT, Série L – Questions de la langue pour les écoles.

[6] ANT, Série L – Situation des enseignantes en 1958.

[7] ANT, Série L – Situation des enseignantes en Tunisie (années 1960).

[8] ANT, Série L – Mahmoud Messadi (bibliographie).

[9] Documents diplomatiques français (1870–1969), Paris, 1965.

[10] S. Bessis, *Histoire de la Tunisie: de Carthage à nos jours*. Paris, Tallandier, 2022, pp. 259–356.

[11] N. Sraieb, Le collège Sadiki de Tunis, 1875-1956 : enseignement et nationalisme. Paris, CNRS, 1995.

[12] N. Sraieb, "L'idéologie de l'école en Tunisie coloniale (1881-1945)," *Revue du monde musulman et de la Méditerranée*, no. 68–69, pp. 239–254, 1993.

[13] C. Bahbouh, *Tunisko*. Brandýs nad Labem, Dar Ibn Rushd, 2010, p. 46.

[14] L. Machuel, *L'enseignement public dans la régence de Tunis*. Paris, Imprimerie nationale, 1889, p. 69.

[15] H. Tullon, "Arabe et Français dans les systèmes éducatifs tunisien et marocain au tournant du XXIe siècle," *Synergies Tunisia*, no. 1, p. 41, 2009.

[16] [Encyclopædia Britannica, "Habib Bourguiba," *Britannica Academic*, updated Feb. 16, 2024, accessed Jul. 22, 2025.

[17] P. Vermeren, "L'appareil éducatif et les hommes (1956-1968)," in *La formation des élites marocaines et tunisiennes : des nationalistes aux islamistes, 1920-2000*. Tunis, Institut de Recherche sur le Maghreb Contemporain (IRMC), 2002, pp. 220–247.

[18] GESIS – Leibniz Institute for the Social Sciences, Zugänge, Barrieren und Potentiale für die internationale Mobilität von Wissenschaftlerinnen. Länderbericht Tunesien. 2020, p. 1.

[19] UNICEF, The State of the World's Children 2007: Middle East and North Africa Edition – Women and Children: The Double Dividend of Gender Equality. 2007.

About Authors

MSc. Amani MANSOURI is a PhD student in the History of Science and Technology at the Historical Laboratory of (Electro)Technology, Faculty of Electrical Engineering, Czech Technical University in Prague. Her research focuses on the history of education, particularly in technological disciplines in Tunisia and Europe.

The Walter Company, 1898–1935

Mgr. Daniel Kyselka

Historical Laboratory of (Electro)Technology, Dep. of Economics, Management and Humanities, Faculty of Electrical Engineering, Czech Technical University in Prague (FEE CTU in Prague), Technická 2, CZ-166 27 P

kyselda2@fel.cvut.cz

Abstract: *The text of the poster covers the history of The Walter Company. from 1908 to 1935. In 1908, engineer Josef Walter founded a bicycle repair shop in Prague's Smíchov district. The company subsequently began manufacturing bicycles as well. In 1910, the company also began producing motorized tricycles. During World War I, Walter a.s. manufactured artillery shells. After the war, Walter ramped up automobile production in full force. The Walter P1-P4 series of automobiles was particularly successful. In the first half of the 1920s, the Walter company began manufacturing aircraft engines. The burgeoning company was hit by the Great Depression, which broke out in 1929. This caused a decline in sales both domestically and abroad. The company suffered another blow with the occupation of the Czech lands by German troops on March 3, 1939. This led to the company falling behind the rest of the developed world in terms of technology. In 1945, the company was nationalized.*

Keywords: Josef Walter – bicycles – aviation industry - cars – aircraft engines - economic crisis.

1. Introduction

This poster focuses on Walter's factory from 1898 to 1935. The primary source of information for this text is archival material from the collection [1] Walter a.s., held at the State Regional Archive in Prague. In addition, professional literature and periodicals. The purpose of this poster is to trace the origins and development of the Walter factory between 1898 and 1935, covering both the period when the factory was managed by Josef Walter himself and the period when it was managed by the Kumpera family. I see the value of this text in that it can serve as a contribution to the history of engineering in Czechoslovakia, but also as an analysis of the company' s development within the Czechoslovak economy from 1898 to 1935. In other words, it describes the process by which a small and insignificant enterprise gradually transformed into a major company with extensive production capacity. Walter's factory was an example of the intellectual and technical work of the Czech nation. This nation, which found itself on the defensive within the Austro-Hungarian Empire, as it did not match the German nation in terms of either population or power. The Czech national movement therefore focused primarily on cultural and economic development. This stance was best illustrated by a quote from the prominent Czech politician František Ladislav Rieger [2] „ Our salvation lies in work and knowledge ‘‘ [3]. This is why the domestic industry experienced rapid growth between 1850 and 1900. The Czech engineering sector, in particular, saw significant development.The rise of domestic engineering and industry in general had a positive impact on the self-confidence of the Czech nation and also on its faith in technological progress. The strengthening of the domestic economy also had a positive impact on the development of the Czech national movement. This fact was positively noted by František Ladislav Rieger's son-in-law, Albín Bráf[4]. The success achieved by the domestic industry was also demonstrated by the fact that, like Paris and London, for example, the city of Prague was able to host a world's fair. This was the Prague Jubilee Exhibition in 1891 [5]. This development was accompanied by a successful technical education system, which consisted of secondary schools, secondary grammar schools, and technical universities. This educational structure also helped ensure that Czech industrial enterprises had access to skilled foremen, craftsmen, and engineers. A prime example of such an enterprise was Walter's factory. In the second half of the 19th century, significant domestic engineering companies were operating in the Czech lands.One example worth mentioning is ČKD [6] (Českomoravská-Kolben-Daněk), Škoda Works[7] or Ringhoffer Company[8]. In the 1890s, these companies dominated most of the engineering market in the Czech lands. It was difficult for other companies and entrepreneurs to compete with them. However, as a result of rapid scientific and technical progress at the turn of the century, even small

manufacturers were able to establish themselves in the domestic market. [9]

2. Walter's Factory, 1898–1918

The talented engineer Josef Walter also started out as a small-scale manufacturer. Walter was a gifted technician and also possessed an entrepreneurial spirit. In 1898, Josef Walter founded a repair shop in Prague's Smíchov district that specialized in repairing bicycles and commercial scales. [10] In 1902–1903, the Walter factory began manufacturing motorcycles. [11] In 1905, Josef Walter's business moved to 1120 Na Zatlance Street. [12] That same year, Walter began manufacturing motorcycles with up to five horsepower. Walter motorcycles were popular with customers for the technical precision with which they were built, as well as for their reliability. [13] A significant milestone came in 1910, when Walter's factory began manufacturing motorized tricycles - first for two people, and later for four. [14]

As mentioned above, it was characteristic of Czech engineering firms that, once they had established themselves in a given sector of the domestic market, they needed to expand their operations and increase production. This required financial resources, and so, at the turn of the century, major Czechoslovak companies began to transform into joint-stock companies. [15] In 1911, Walter's company was transformed into a joint-stock company. Notable shareholders included, for example, businessman Vítězslav Kumpera and builder Antonín Šimek. In 1911, Šimek also oversaw the construction of Walter's factory in Jinonice, Prague. Another turning point for the development of Walter's factory came in 1914, when the plant began manufacturing passenger cars. However, that same year also saw the outbreak of World War I. As a result, Walter's factory had to submit to the wartime needs of the Austro-Hungarian Empire, and thus artillery shells were manufactured at the Jinonice factory throughout the duration of the military conflict. After the end of World War I, the Walter company resumed its pre-war automobile production. [16] In 1919, the authorized capital of Walter a.s. was two million Czechoslovak crowns. Interested parties could purchase a share of the company for 200 crowns. It was precisely this share issuance that enabled the further development of Walter a.s. in the postwar period. [17]

3. The Walter Company, from 1918 to 1928

On October 28, 1918, an independent Czechoslovak state was established. This newly formed state lagged behind developed capitalist countries, both in automobile production and in the number of motorists. Another problem was the inadequately developed road infrastructure—specifically, the fact that there were few roads in the country suitable for automobile traffic. An obstacle to the development of the domestic automobile industry was the lower purchasing power of the Czechoslovak population compared to their counterparts in developed Western countries. [18] Another problem was the volume and efficiency of domestic production of road transport vehicles. In the 1910s and 1920s, Czechoslovak automobile and motorcycle manufacturers were not yet strong enough to meet the demand of the domestic market. For this reason, most of the cars and motorcycles sold in the Czech lands during this period were imported. This was also due to the fact that large foreign automakers like Ford had perfectly refined factory mass production. This was in contrast to Czech manufacturers, who produced cars and motorcycles in smaller batches. [19] This problem also affected the Walter company in the 1920s. Of course, Walter was not the only automobile manufacturer in Czechoslovakia. Other major automobile brands included Wikow, Laurin-Klement, Škoda, Praga, and Tatra. During the interwar period, Tatra, like Walter, focused on the production of luxury cars. [20] It should be noted here that the Czechoslovak government viewed car ownership as a sign of luxury. For this reason, car owners were required to pay a luxury tax. This, in turn, did not contribute to the development of motoring. [21]

In 1922, Josef Walter left the company. [22] Walter's departure was finalized at a meeting of the board of directors of Walter a.s., which took place on January 30, 1922. The meeting was chaired by Vítězslav Kumpera, chairman of the board of directors, and a decision was made regarding the financial settlement between Walter and its founder. Based on this decision, Josef Walter was paid a total of 140,000 Czechoslovak crowns during 1922. This amount consisted of his annual salary as director as well as his share of the company's profits. This settled Walter's financial obligations to its founder. [23] When he left, Josef Walter sold his stake in the

company. The Kumpera family thus gained control of the business. [24]

In 1922, the share capital of Walter Inc. more than doubled. It increased from 4,000,000 to 8,400,000 Czechoslovak crowns. [25] In 1924, Walter began manufacturing the Walter P. Over the next four years, a total of four versions of the Walter P were produced: the I, II, III, and IV. [26] The first model in the P series was the Walter P1. It was a car equipped with a four-cylinder engine producing 20 horsepower. The Walter P1 was equipped with a four-speed transmission and weighed 950 kg. The Walter P was available in various versions, either as a classic four-seater coupe or as a convertible. [27]

In addition to automobile manufacturing, Walter began producing aircraft engines in the first half of the 1920 s. Although, as already mentioned, Walter employed talented engineers and designers, the company began selling engines from foreign aircraft manufacturers under license in the first half of the 1920 s. These were primarily BMW engines. The first successful aircraft engine produced by Walter was the five-cylinder radial engine NZ60. This 60-horsepower engine sold well both in Czechoslovakia and abroad. [28] Thanks in part to the success of this engine, Walter introduced the Walter NZ 80 in 1926, which had an output of 80 horsepower. [29]

In 1926, a significant change occurred in the company's leadership, as Vítězslav Kumpera was not elected chairman of the Walter board of directors that year. This decision was made because a faction of the board led by builder Šimek feared a further increase in Vítězslav Kumpera's influence within the company. However, thanks to the support of his financially powerful business partners, Kumpera managed to take control of both the Walter company and the board of directors and oust his opponents from them. In 1927, both of Kumpera's sons, Antonín and Vítězslav, were elected to the company's board of directors. In the same year, Antonín Kumpera also became the company's chief executive officer. [30]

The Walter company achieved a significant success in 1928. That year, a commercial agreement was signed between the American company Spartan Industries and Walter Inc. Under this agreement, Spartan Industries purchased between 500 and 600 units of the Walter 120 engine from the Jinonice-based company each year. [31] In 1928, Walter a.s. also introduced a new line of cars to the Czechoslovak market. This was the B series, named after its chief designer, František Barvitius. The cars in this series were called the Walter 4B and Walter 6B. However, it was primarily the Walter 6B that achieved success. This car reflected Walter's ambition to break into the luxury car segment, which it successfully achieved. The Walter 6B was equipped with a 2.8-liter six-cylinder engine. The car weighed around 1.5 tons. In 1930, the car's name was changed from Walter 6B to Walter Standard. [32]

4. The Economic Crisis in Czechoslovakia. The Walter Company in the years 1929–1948.

The Great Depression, which began in 1929, marked a turning point for industrial enterprises not only in Czechoslovakia but around the world. While in the United States the negative consequences of the stock market crash began to manifest shortly after October 24, 1929, in Czechoslovakia the onset of the economic crisis was slower. In 1929, the Czechoslovak engineering and heavy industries were still showing growth. However, by 1930, production had already declined in these sectors as well. The main problem for large Czechoslovak companies was the collapse of sales and orders in the U.S. [33] The economic crisis hit the Czechoslovak automotive industry hard. In the early 1930 s, there were approximately 80 car manufacturers in Czechoslovakia. However, the vast majority of these manufacturers went out of business during the economic crisis. These were generally small businesses that produced custom vehicles according to specific customer requirements or manufactured cars in units or dozens of units. In contrast, automobile production survived in large Czechoslovak engineering companies. However, the price of a passenger car remained a problem. The average Czechoslovak car was twice as expensive as its American counterpart. Therefore, only members of the upper middle class and the upper echelons of society could afford a car. This was in contrast to the United States, for example, where broad segments of society could afford a car. [34] Just as with the Czechoslovak automotive industry, the economic crisis also had a negative impact on the aviation industry. As a result, state investment in aviation fell from 130,000,000 crowns in 1924 to 83,000,000 crowns six years later. This reduction primarily affected companies manufacturing aircraft or aviation components. Moreover, these firms also had

to cope with a decline in sales of their products abroad. Therefore, they had no choice but to expand their product range. [35] The aforementioned decline in government investment in the aviation industry did not only have a negative impact on the operations of aviation companies in Czechoslovakia. Czechoslovak aviation companies did not have sufficient financial resources to maintain strong research departments. The standard practice in the domestic aviation industry at the time was as follows: the Czechoslovak Ministry of National Defense would issue a contract, for example, for a new fighter aircraft. Subsequently, the aviation company that won the contract manufactured the aircraft and then billed the state for the costs associated with its research activities. However, as government contracts and investments declined rapidly, so too did the research activities of Czechoslovak aviation companies. [36] The technological lag of the domestic aviation industry was also evident in the fact that, in the 1930 s, Czechoslovak aviation companies primarily manufactured biplanes made of metal and wood, while countries with advanced aviation industries were producing all-metal monoplanes. Czechoslovakia was unable to catch up with the lag in its aviation industry even in the second half of the 1930 s. [37] Like other Czechoslovak companies, Walter a.s. struggled with the economic crisis. Although sales of the Walter Royal automobile began in 1931, the first half of the 1930s was otherwise a difficult period for Walter. Due to a decline in interest in the products of the Walter factory, both on the domestic and foreign markets, Walter was forced to switch to a more cost-effective mode of operation. As a result, investments were curtailed, both in technical equipment and in factory buildings. [38] One way Walter's factory responded to the economic crisis, which was still ongoing in 1932, was to expand its range of automobile models. More specifically, by introducing a new model into production. This was the Fiat 508 Balilla, which was manufactured under license under the name Walter Junior. This car was equipped with a four-cylinder engine producing 24 horsepower. [39] In the first half of the 1930 s, Walter's management had high hopes for its powerful new aircraft engines. These were the 120-horsepower Walter Jupiter and the 340-horsepower Walter Pollux. The Walter Jupiter, in particular, was a key export product for Walter a.s. [40] In 1934, the Walter Miron 4 engine also went on sale. [41] Smaller engines with lower power output also enjoyed success on the domestic market. One example was the Walter Mikron [42] aircraft engine. [43]

As the sense of threat from Germany grew in the second half of the 1930s, Czechoslovak military and political leaders began planning a potential relocation of Czechoslovak factories to Slovakia, where they would be out of reach of German bombers. This also applied to the Walter company, whose production facilities were to be moved to the Slovak part of the country. However, this relocation did not take place before the outbreak of the Munich Crisis. Nor was this plan implemented during the Second Republic. [44] The Munich Agreement was signed in September 1938, resulting in Czechoslovakia losing its border regions. Subsequently, on March 15, 1939, the German Wehrmacht occupied the remaining Czech territory. As a result, Walter a.s. was forced to manufacture aircraft engines and components for the German Air Force during World War II. The development of Walter's own engines was put on the back burner. [45] In May 1945, German forces were defeated in the Czech lands. Following the restoration of Czechoslovakia, sweeping changes were implemented in the national economy. As a result, the company Walter a. s. was nationalized in 1945. After nationalization, the company was renamed Let. On February 25, 1948, a coup d'état took place in Czechoslovakia, and the Communist Party of Czechoslovakia became the main holder of power in the state. [46] The state-owned company Motorlet was established in 1949. [47] Motorlet not only took over the buildings of the former Walter factory in Jinonice, Prague, but also continued to manufacture aircraft engines. These were the Mikron-III and Minor 6-III engines, which were intended primarily for export. In the first half of the 1950s, Motorlet began manufacturing Soviet jet engines under license. The same state-owned company also played a significant role in the development of the Czechoslovak M-701 jet engine. This engine powered the Czechoslovak L-29 Delfín jet aircraft. [48]

5. Conclusion

This poster explores the history of The Walter Company from 1898 to 1935. However, it also touches on the company's fate in later years. The example of Walter's company illustrates an interesting phenomenon: namely, that just as the Czech cultural national revival was driven primarily by the middle and upper-middle classes, so too was

the economic revival. This was in contrast, for example, to the Hungarian nation, which could rely on the assistance and material support of a patriotic nobility in developing its national economy and culture. In the Czech lands, however, the German-speaking nobility dominated. Therefore, the intellectual and material development of the nation was primarily ensured by the middle class. This fact, however, also presented an advantage. Czech society was moving toward a meritocracy, much like in the United States at the time. Another positive effect was the creation of a networked structure of the middle classes, particularly in Prague. The text mentions, for example, the builder Antonín Šimek, who not only sat on the board of directors of the Walter company but also built a new factory for it. These professional and cultural relationships facilitated the economic and spatial development of the city of Prague. It was precisely this middle class of entrepreneurs, doctors, lawyers, and the like that served as the foundation of Czech national society. And this was true not only in Prague but also in small towns.

Like many large companies in Czechoslovakia, Walter had a diverse production portfolio. As well as automobiles, the company began manufacturing aircraft engines in the 1920s. However, the Great Depression hit in 1929. This led to a slump and a decline across the entire Czechoslovak aviation and automotive industries. Walter's factory was hit hard by the crisis too, forcing it to cut back on investment in its own research and development. The signing of the Munich Agreement and the subsequent Nazi occupation posed further difficulties for the company. This meant that factory production was completely subordinated to the needs of the German Air Force. Moreover, the Second World War brought significant advances in aviation, such as the invention of the jet engine. These developments only served to confirm the obsolescence of the Walter company's products. The Walter company was nationalised in the same year that the war ended. At the same time, the company's original name ceased to exist. A clear successor to Walter during the communist era in Czechoslovakia was the state-owned enterprise Motorlet, which was also capable of manufacturing jet engines.

Acknowledgements

This paper was supervised by prof. PhDr. Marcela Efmertová, CSc. of Historical Laboratory of (Electro)Technology, Faculty of Electrical Engineering, Czech Technical University in Prague (FEE CTU in Prague), Technická 2, CZ-166 27 Prague. The author would like to thank her for this supervision.

References:

[1] SOA Praha, fond: J.Walter a. s 1902-1948 (1949)
[2] For more on František Rieger's position in Czech bourgeois society, see: ŠTAIF, Jiří, Palacký, Rieger, Bráf. Tři generace české národní elity mezi identitou a transnacionalitou, p. 41-61. In: PAVLÍČEK, Viktor (eds.) a VELEK, Luboš (eds.), Vůdce národa: František Ladislav Rieger a jeho místo v české politice, kultuře a vědě, Masarykův ústav a Archiv AV ČR, v. v. i. Praha 2021.
[3] It was a patriotic quote intended to motivate members of the Czech nation to work and pursue education. It was written by František Ladislav Rieger, who also included it on the title page of every volume of his encyclopedia.. See: RIEGER, František Ladislav Rieger , Slovník naučný, Part One , A-B, Kober & Markgraf, Praha 1860, p. [a].
[4] For more on Bráf's relationship with the Czech economy. See: DOLEŽALOVÁ, Antonie a kol., Učíme ekonomii, Wolters Kluwer ČR, Praha 2011, p. 126-129.; ŠTAIF, Jiří, Modernizace na pokračování: společnost v českých zemích (1770-1918), Argo, Praha 2020, p. 282, 304-305.
[5] For more information, see: HLAVAČKA, Milan, Jubilejní výstava 1891, TECHKOM, Praha 1991, 152 pp.
[6] For more information, see: STŘÍTESKÝ, Hynek, ed. Fenomén ČKD: příspěvek k dějinám pražského strojírenského koncernu Českomoravská-Kolben-Daněk, Mladá fronta, Praha, 2014, 326 pp.
[7] For more information, see: JÍŠA, Václav, Škodovy závody, 1859/1919, Práce, Praha 1964, 577 pp.
[8] For more information, see: HLAVAČKA, Milan a HOŘEJŠ, Miloš a kol., Fenomén Ringhoffer: rodina, podnikání, politika, Národní technické muzeum 2019, 570 pp.
[9] URBAN, Otto, Kapitalismus a česká společnost k otázkám formování české společnosti v 19. století, Svoboda,Praha1978, p. 96-97.
[10] Letectví + kosmonautika, Vol.47, No.25, MNO (Svazarm), Praha 1971, p. 987.
[11] MARČÍK, Libor, Naše motocykly, I.díl. Rakousko – Uhersko 1899-1918, Marčík, Jinočany 2001, p. 162.

[12] Letectví + kosmonautika, Vol.47, No.25, MNO (Svazarm), Praha 1971, p. 987.
[13] MARČÍK, Libor, Naše motocykly, I.díl. Rakousko – Uhersko 1899-1918, Marčík, Jinočany

2001, p. 163-164.
[14] Letectví + kosmonautika, Vol.47, No.25, MNO (Svazarm),Praha1971, p. 987.
[15] HORSKÁ, Pavla, Hlavní otázky vzniku a vývoje českého strojírenství do roku 1918, Nakladatelství Československé akademie věd, Praha, p. 173-175.
[16] Letectví + kosmonautika, Vol.47, No.25, MNO (Svazarm),Praha1971,p. 987.
[17] SOA Praha, f: J. Walter a. s 1902-1948 (1949), box. 1, inv.n. 9, Stanovy firmy ¨ Akciová společnost Walter, tov. na automobily a letecké motory“, 1931, p. 6,20.
[18] LACINA, Vlastislav, Zlatá léta československého hospodářství 1918-1929, Historický ústav AV ČR,Praha2000,p.195-196.
[19] Vynálezy a pokroky, Vol. 17, No. 1, Šolc a Šimáček,Praha1927-1928,p.13.
[20] VONDRÁČEK, Vladimír, Lékař vzpomíná (1920-1938), Avicenum, Praha 1977, p.270.
[21] KÁRNÍK, Zdeněk, České země v éře první republiky (1918-1938), díl třetí, O přežití a o život (1936-1938),Libri,Praha2003, p.191.
[22] Letectví + kosmonautika, Vol.47, No.25, MNO (Svazarm),Praha1971, p .987.
[23] SOA Praha, f: J. Walter a. s 1902-1948 (1949), box. 2, inv. n. 15, Doklady o opuštění J. Waltera místa ředitele a výstupu ze správní rady, 1922, p. 3-4.
[24] Letectví + kosmonautika, Vol.47, No.25, MNO (Svazarm),Praha1971,p.987.
[25] Čas, Vol. 32, No. 75, vydal Jan Herben, Praha 1922, p. 7.

[26] GOMOLA, Miroslav, Josef Walter a spol.- akciová továrna na automobily a letecké motory, AGM CZ,Brno2002,p.47
[27] KUBA, Adolf, Atlas našich automobilů 1914-1928,2.díl, Nakladatelství dopravy a spojů, Praha 1988,p.121-122.
[28] NĚMEČEK, Václav, Československá letadla (I.), 1918-1945, Naše vojsko, Praha 1983, p. 216-217.

[29] Letec: měsíčník věnovaný zpopularisování letectví, Vol. 3, No.1, Masarykova letecká liga, Praha 1927,p.44.
[30] SOA Praha, f: J.Walter a. s 1902-1948 (1949), volně vložená kniha, Kumperovic rodina. Kronika zámků Koloděje a rodiny Kumperů (kniha), 1937, p. 17.
[31] Letec: měsíčník věnovaný zpopularisování letectví, Vol. 4, No. 6, Masarykova letecká liga, Praha 1928,p.24.
[32] PROCHÁZKA, Hubert MARTOF, Jan, Automobily, Aero, Jawa, Walter,Wikow, ¨Z¨ : 1905--1946, Computer Press, Brno 2009, p. 80-81.
[33] LACINA, Vlastislav, Velká hospodářská krize v Československu 1929-1934, Academia, Praha 1984, p. 78-79.
[34] KÁRNÍK, Zdeněk, České země v éře první republiky (1918-1938), díl druhý, Československo a české země v krizi a ohrožení, (1930-1935), Libri, Praha,2002,p. 418-419.
[35] RAJLICH, Jiří a SEHNAL, Jiří, Vzduch je naše moře: Československé letectví 1918-1939, Naše vojsko,Praha2002,p. 81.
[36] NĚMEČEK, Václav, Československá letadla (I). 1918-1945, Naše vojsko, Praha 1983, p. 13-14.
[37] RAJLICH, Jiří a SEHNAL, Jiří, Vzduch je naše moře: Československé letectví 1918-1939, Naše vojsko,Praha2002,p. 82.
[38] GOMOLA, Miroslav, Josef Walter a spol.- akciová továrna na automobily a letecké motory, AGM CZ,Brno2002,p .67,69.
[39] KUBA, Adolf, Automobil v srdci Evropy, Nakladatelství dopravy a spojů, Praha 1986, p. 117.
[40] GOMOLA, Miroslav, Josef Walter a spol.- akciová továrna na automobily a letecké motory, AGM CZ,Brno2002,p. 69.
[41] The Walter Minor 4 was a four-stroke engine with an output of 85 horsepower. Like other Walter engines, this one was also air-cooled. If necessary, the aircraft propeller could be mounted directly onto the engine’s crankshaft. The crankshaft was manufactured at the Poldi Kladno plant from chromium-nickel steel. This material provided the shaft with both strength and durability. As mentioned above, the Walter Minor 4 had four cylinders. These cylinders were made of high-quality carbon steel, which provided them with the properties necessary for flight operations. These properties included considerable strength and resistance to damage. This contributed to the marketability of Walter a.s. aircraft engines. Source: Letadlový motor Walter Minor 4: popis a návod k obsluze a udržování, Akciová společnost Walter, Praha 1936, p. 9, 15-16.
[42] The Walter Mikron was a four-stroke engine with an output of 50 horsepower. The Walter Mikron had four cylinders. These were made of carbon steel, which gave them great strength. The engine was air-cooled, and an aircraft propeller could be attached to the engine’s crankshaft. The crankshaft was made of chromium-nickel steel, which gave it hardness and considerable resistance to damage. Source: Walter Mikron: popis a návod k obsluze a udržování, Akciová společnost Walter, Praha 1936, p. 9, 15-16.
[43] STREJČEK, Jaromír, Léta letání, NADAS, Praha1979,p. 46.
[44] KÁRNÍK, Zdeněk, České země v éře první republiky (1918-1938),díl třetí, O přežití a o život (1936-1938), Libri, Praha 2003, p. 475-476.
[45] Letectvo a PVOS: časopis letectva avojsk PVOS Československé lidové armády, Vol. 15, No.

10, Velitelství letectva a PVOS, Praha 1986, p. 41.
[46] Letectvo a PVOS: časopis letectva a vojsk PVOS Československé lidové armády, Vol. 17, No. 2, Velitelství letectva a PVOS, Praha 1978, p. 52.
[47] GOMOLA, Miroslav, Josef Walter a spol.- akciová továrna na automobily a letecké motory 1898-2003, AGM CZ, Brno 2002, p. 113.
[48] Letectví + kosmonautika, Vol. 14, No.3, MNO (Svazarm) 1978, p. 78.

About Author

Mgr. Daniel Kyselka is a graduate in Economic History at the Institute of Economic and Social History, Faculty of Arts, Charles University in Prague. He was also a student of the Master's degree programme History - General History at the Faculty of Arts of Charles University. He is currently a PhD student at the Historical Laboratory of Electrical Engineering at the Faculty of Electrical Engineering of the Czech Technical University.

Towards Reliable Programmer Attribution in Educational Source Code

Marek HORVÁTH[1]

[1]Department of Computers and Informatics, FEI TU of Košice, Slovak Republic

marek.horvath@tuke.sk

Abstract. *Programmer attribution aims to identify or verify the author of a software artifact based on measurable characteristics of individual coding style or development behavior. Unlike traditional authorship analysis in natural language, source code represents a structured and formally constrained medium, where stylistic signals emerge from lexical choices, syntactic constructions, structural design decisions, and development dynamics. This work focuses on programmer attribution in educational settings, where novice programmers produce heterogeneous solutions under shared assignment constraints. Such context introduces specific challenges related to limited experience, evolving style, and the presence of plagiarism or AI-assisted code. The proposed framework combines static stylometric features extracted from source code with behavioral signals derived from development activity logs. Feature extraction forms the core of the methodology and is followed by statistical analysis and supervised machine learning models for both attribution and anomaly detection. The objective is to evaluate whether integrating static and behavioral evidence improves robustness in real course environments and supports applications such as plagiarism investigation, identification of atypical submissions, personalized feedback, and educational analytics.*

Keywords

Authorship attribution, Code stylometry, Behavioral analysis, Educational data mining, Machine learning.

1. Introduction

Programmer attribution concerns the identification or verification of the author of a source code artifact based on measurable stylistic and structural characteristics. In contrast to natural language authorship analysis, source code represents a formally constrained medium in which individual differences are expressed through lexical choices, syntactic constructions, structural decomposition, and development behavior. In educational environments, this task acquires additional complexity: students solve identical assignments under shared constraints, exhibit evolving programming style, and differ substantially in experience.

Our research trajectory originated in large-scale analyses of student submissions focused on plagiarism detection. An experimental comparison of similarity-based tools on more than 1,000 student projects revealed both the strengths and the limitations of purely similarity-driven approaches [1]. Complementary work on binary decomposition and code clone analysis further demonstrated that structural transformations can obscure surface similarity while preserving deeper patterns [7]. These findings motivated a shift from pairwise similarity towards author-centered modelling.

Subsequent studies explored how machine learning models can capture programmer-specific patterns directly from source code features [4]. At the same time, experiments with GPT-generated variations of programming assignments showed that large language models can produce functionally correct solutions that attenuate or mask individual stylistic traits [2].

The availability of a large dataset collected through an automated assessment system for programming courses [3] enabled systematic feature extraction and longitudinal analysis. Beyond static stylometry, behavioral signals have been investigated in the context of personalized learning analytics [6], demonstrating that development dynamics can provide complementary information to static code structure. Further experimental work involving steganographic watermarks embedded in assignment templates examined whether deviations from expected fingerprints can reveal copying or AI-assisted code generation [5].

Building on this line of work, the present study formulates programmer attribution in educational source code as a unified modelling problem that integrates static stylometric features and behavioral development signals. The focus shifts from similarity detection to structured feature extraction and statistical modelling, aiming to evaluate attribution robustness and to support downstream tasks such as plagiarism investigation, anomaly detection, and educational analytics.

2. Ongoing Research Directions

The current stage of the project extends the attribution framework along several tightly connected methodological axes. A substantial part of the work concentrates on the construction of programmer-specific style profiles derived from structural properties of source code. This includes systematic extraction of stylometric attributes from abstract syntax trees, comparison of alternative code representations such as tokens, control-flow graphs and learned embeddings, and the design of vector-based representations suitable for downstream classification. The effect of different normalization strategies on attribution performance is evaluated in parallel, together with experiments analysing how the choice of programming language influences author identifiability.

In addition to representation-level questions, modelling and evaluation scenarios are being examined under controlled conditions. Reverse identification experiments are used to assess how attribution models behave when stylistic fingerprints are partially suppressed or transformed. A synthetic dataset generator is under development to simulate style-preserving and style-altering transformations, enabling controlled robustness testing beyond real course data.

Behavioral integration forms another active component of the framework. A sandboxed environment is being implemented to support secure collection of behavioral biometrics derived from development traces. These signals are incorporated into joint models that combine static and behavioral features, with the aim of detecting stylistic deviations and validating code integrity in suspicious submissions.

The framework is further connected to applied educational contexts. Automatic categorization of coding style, visualization of clustered solution patterns, and personalization of instruction based on combined static and behavioral indicators are explored as downstream applications of the attribution models.

3. Conclusion

The project is supported by a dedicated educational dataset comprising approximately 4,500 students, each contributing on average ten distinct programming assignments collected through an automated assessment system. From these submissions, structured static and behavioral attributes are systematically extracted and organized at the author level. The forthcoming phase focuses on statistical evaluation of feature stability and discriminative power, followed by controlled experiments with both classical machine learning models and deep learning architectures. The objective is to quantify attribution performance under realistic course conditions and to analyse robustness across assignments, temporal variation, and heterogeneous student populations.

Acknowledgements

This work was supported by project KEGA No. 061TUKE-4/2025 Building Bridges between University and High School ICT Education.

References

[1] HORVÁTH, M., PIETRIKOVÁ, E. An experimental comparison of three code similarity tools on over 1,000 student projects. In: *2024 IEEE 22nd World Symposium on Applied Machine Intelligence and Informatics (SAMI)*. IEEE, 2024, p. 423–428.

[2] HORVÁTH, M., BUBENKOVÁ, L., PIETRIKOVÁ, E. Exploring GPT-generated variations in C programming assignments. In: *2025 IEEE 23rd World Symposium on Applied Machine Intelligence and Informatics (SAMI)*. IEEE, 2025, p. 331–336.

[3] HORVÁTH, M., KORMANÍK, T., PORUBÄN, J. Adaptation of automated assessment system for large programming courses. In: *5th International Computer Programming Education Conference (ICPEC 2024)*. Schloss Dagstuhl–Leibniz-Zentrum für Informatik, 2024, p. 1–4.

[4] HORVÁTH, M., ČUPALKA, M., PIETRIKOVÁ, E. Detecting programmer identity from source code with machine learning methods. In: *2025 International Conference on Emerging eLearning Technologies and Applications (ICETA)*. IEEE, 2025, p. 236–241.

[5] HORVÁTH, M., BUBENKOVÁ, L., PIETRIKOVÁ, E., ČORBA, M. Detecting AI-generated source code in student assignments using steganographic watermarks. In: *2025 International Conference on Emerging eLearning Technologies and Applications (ICETA)*. IEEE, 2025, p. 229–235.

[6] HORVÁTH, M., PIETRIKOVÁ, E., GURBÁL', F. Personalized learning analytics through static code analysis in computer science education. *Acta Informatica Pragensia*, 2026, vol. 2026, no. 1, p. 54–71.

[7] HORVÁTH, M. Code clones: A novel approach to detecting plagiarism in binary decomposition of C programs. *Acta Electrotechnica et Informatica*, 2024, vol. 24, no. 2, p. 13–18.

About Authors...

Marek HORVÁTH Marek HORVÁTH was born in Slovakia. He is currently a PhD student in Informatics at the Faculty of Electrical Engineering and Informatics, Technical University of Košice. His research focuses on programmer identification based on source code stylometry and behavioral biometrics, with an emphasis on authorship attribution, plagiarism detection, and educational analytics. His work integrates static code analysis, feature engineering, and machine learning methods, supported by large-scale datasets collected from programming courses. He is also involved in teaching and supervising student projects in software engineering and programming-related subjects.

Gamified Cybersecurity Training Environments for Phishing Awareness and Secure Digital Practices

Lenka BUBEŇKOVÁ[1]

[1]Department of Computers and Informatics, Faculty of Electrical Engineering and Informatics, Technical University of Košice, Letná 9, 042 00 Košice, Slovak Republic

lenka.bubenkova@tuke.sk

Abstract. *Cybersecurity incidents continue to exploit human decision-making despite increasing awareness campaigns and regulatory pressure. This paper presents ongoing research focused on practical cybersecurity education through gamified and contextual training environments. The proposed approach combines several complementary training modalities, including phishing-detection exercises, scenario-based incident investigations, and contextual cybersecurity-risk simulations. The aim is to improve the practical understanding of cyber threats and to strengthen secure decision-making in everyday digital environments. The training activities emphasize realistic scenarios that reflect common attack vectors, including phishing, unsafe web browsing, credential misuse, and insecure network use. In addition, the research highlights the importance of integrating cybersecurity awareness with secure programming practices and defensive system design. The results suggest that contextual and interactive training environments can significantly support the development of practical cybersecurity competencies.*

Keywords

Cybersecurity education, gamification, phishing awareness, secure digital practices, cybersecurity training

1. Introduction

Cybersecurity has become a societal and organizational priority because many incidents still succeed due to human behavior rather than purely technical vulnerabilities. Phishing, social engineering, credential misuse, and poor response decisions remain among the most common causes of compromise [1]. This creates a well-recognized paradox: cybersecurity awareness programs and training initiatives are expanding across organizations, yet security incidents involving human interaction remain persistently high. According to the Verizon Data Breach Investigations Report, a significant proportion of security incidents still involve some form of human interaction or error [2]. A key limitation of traditional cybersecurity education is that it often focuses on knowledge transfer rather than on behavioral change. Users may understand security rules in theory, but real-world decisions are influenced by factors such as time pressure, trust, cognitive overload, and misleading contextual cues. For this reason, effective training should go beyond short quizzes and assess how people react in realistic situations. At the same time, cybersecurity education is becoming increasingly important in the context of regulatory frameworks such as NIS2, DORA, CRA, and the AI Act. These frameworks place stronger emphasis on organizational resilience and cybersecurity training, yet they provide limited guidance on how the effectiveness of such training should be evaluated. Existing research on gamified cybersecurity education highlights several recurring limitations [7, 8]. Many studies evaluate training interventions only immediately after the activity without examining whether the observed effects persist over time [6]. In addition, research samples are often small and homogeneous, frequently focusing on technically oriented students. Another limitation concerns the diversity of evaluation approaches. Some studies focus on motivation or engagement, while others measure knowledge acquisition or isolated behavioral indicators [3, 5, 4]. The lack of consistent evaluation methods makes it difficult to compare results across different studies and training environments. These limitations motivate the need for broader and more practical cybersecurity training experiments that integrate multiple gamified modalities and evaluate learning outcomes in realistic contexts [9]. The research presented in this paper addresses this need by exploring several complementary forms of cybersecurity training that target different aspects of cyber risk awareness and secure digital behavior.

2. Cybersecurity Training

The ongoing research investigates several complementary gamified cybersecurity training environments that simulate realistic cyber risk scenarios. The training activities are conducted through educational workshops and experimental learning sessions with participants from diverse technical and non-technical backgrounds.

- The first training modality is a rapid phishing-recognition game based on time-constrained classification tasks. Participants complete a pretest, an interactive game session, and a posttest. Initial observations suggest that this format strengthens reflexive recognition of visually explicit phishing cues, particularly in urgent or suspicious messages. However, more ambiguous scenarios remain challenging, indicating that rapid recognition training should be complemented with more analytical learning approaches.
- The second modality is a scenario-based collaborative investigation activity in which participants reconstruct a cyber incident timeline by analyzing and ordering events. This format helps participants understand that cyber incidents rarely occur as isolated events but rather develop through sequences of small security failures. The activity supports situational awareness and encourages participants to interpret cyber threats within a broader context.
- The third modality is a contextual cyber-risk investigation game that places participants in a narrative scenario involving everyday digital behavior. Instead of focusing solely on phishing messages, the game explores risks including unsafe web browsing, insecure Wi-Fi use, weak authentication practices, and inadequate incident response. This approach enables participants to better understand how individual decisions contribute to incident escalation.

The observations suggest that the applied training formats address different layers of cybersecurity awareness. Rapid-response phishing exercises strengthen recognition of common attack indicators, scenario-based investigations improve the understanding of incident development and attack progression, and contextual gameplay enables participants to relate everyday digital behavior to broader cybersecurity risk scenarios.

3. Conclusion

The presented work highlights the importance of practical and context-oriented cybersecurity education. While traditional awareness programs often focus on theoretical knowledge, real-world cybersecurity resilience requires users to understand threats within realistic operational contexts. Training formats such as phishing simulations, scenario-based incident investigations, and contextual cybersecurity games provide a more effective environment for developing practical security awareness. An important implication of this research is the connection between cybersecurity education and secure system development. Observing how users interpret risks, respond to suspicious situations, and interact with digital environments provides valuable insights for designing safer systems and improving secure coding practices. Security mechanisms should therefore not rely solely on user awareness, but should also incorporate protective design principles that reduce the likelihood of user error. Future research will focus on expanding cybersecurity training models that integrate awareness education, secure programming principles, and interactive learning environments. Such approaches can contribute to building stronger cybersecurity competencies across different user groups and educational contexts.

Acknowledgements

This work was supported by project KEGA 061TUKE-4/2025 “Building bridges between university and high school ICT education”.

References

[1] EUROPEAN UNION AGENCY FOR CYBERSECURITY. *ENISA Threat Landscape 2024*. 2024.

[2] VERIZON. *2025 Data Breach Investigations Report*. 2025.

[3] GALLO, A. Human factors in cybersecurity behavior and decision-making. *Journal of Cybersecurity Education*, 2024.

[4] BORITZ, J., et al. Factors affecting phishing susceptibility. *Computers & Security*, 2022.

[5] BEU, R., et al. Falling for phishing: cognitive and behavioral determinants. *Information Security Journal*, 2023.

[6] ARACHCHILAGE, N., LOVE, S. A game design framework for avoiding phishing attacks. *Computers in Human Behavior*, 2014.

[7] PUTZ, L., HOFBAUER, F., TREIBLMAIER, H. Can gamification help in security education? *Education and Information Technologies*, 2020.

[8] ZAINUDDIN, Z., CHU, S. K. W., SHUJAHAT, M., PERERA, C. The impact of gamification on learning and motivation. *Educational Research Review*, 2020.

[9] ROS, S., GONZALEZ, M., ROBLES, G., TOBARRA, L., CAMINERO, A., CANO, J. Gamified cybersecurity learning and perception. *IEEE Access*, 2023.

About Authors...

Lenka BUBEŇKOVÁ Lenka BUBEŇKOVÁ is a PhD student at the Department of Computers and Informatics, Faculty of Electrical Engineering and Informatics, Technical University of Košice. Her research focuses on cybersecurity education and the application of gamification and interactive learning environments in cybersecurity teaching. Her work explores practical approaches to improving cybersecurity competencies through realistic training scenarios, including phishing simulations, contextual cyber risk investigations, and collaborative incident analysis, and addresses the integration of security awareness with secure programming practices and software development education. She is particularly interested in how cybersecurity training can support the development of safer digital systems and more resilient user behavior in real-world environments.

Estimation of slip and slide effects in urban rail vehicles

Jiří Nábělek

Dept. of Control Engineering, Czech Technical University, Technická 2, 166 27 Praha, Czech Republic

jiri.nabelek@cvut.cz

Abstract.

Slip ratio estimation is a key topic in both the railway and automotive industries. When the applied torque exceeds the adhesion limit, the wheel can begin to slip, leading to slower vehicle acceleration. In such cases, the torque must be decreased to improve the efficiency of the energy used and to limit wear on the wheels and rails.

Estimation can be performed using the sensors with which modern rail vehicles are equipped. We have data available from GNSS, IMU and odometry sensors. In addition, for rail vehicles, we typically know a map of the track infrastructure. Based on this information, it is possible to estimate the actual acceleration of the vehicle with high accuracy using an iterated extended Kalman filter. In the event of wheel slip, we can observe that the acceleration calculated only from odometry develops faster than the estimated acceleration that combines information from all sensors. This work focuses on comparing these two estimates.

Keywords

Rail vehicles, Position estimation, Kalman filtering, Slip/slide effects

1. Introduction

Wheel slip ratio estimation in rail vehicles enables more efficient vehicle acceleration. Wheel slip is reflected in the odometry measurement output and is estimated by comparing the accelerations estimated from odometry with those from an iterative extended Kalman filter, which combines measurements from multiple sensors.

The aim of this work is to show that it is possible, based on data from the aforementioned sensors, to detect slip in real time and subsequently to develop a controller capable of regulating the acceleration at the adhesion limit.

2. Methodology

We present a method that compares longitudinal velocity estimates obtained from multi-sensor fusion with an estimate obtained only from odometry measurements. The goal is to evaluate the effect of wheel slip based on the estimated odometric velocity and acceleration.

2.1. Fused state estimation

The tram longitudinal motion was estimated using an iterated extended Kalman filter, combining measurements from the odometer, GPS, IMU, gyroscope, and map information. The filter was designed to estimate the position of the first bogie, the rotation of the first tram car, its longitudinal travel distance, speed, and acceleration.

The role of the filter is to compensate for inaccuracies in individual measurements and, above all, to compensate for wheel slip in the output estimate of velocity/acceleration. Let us denote the estimates of trams longitudinal motion as $\hat{s}(t)$, $\hat{v}(t)$, and $\hat{a}(t)$.

2.2. Wheel-based speed estimation

The odometer measures the cumulative pulses, whose frequency is proportional to the rotation speed of the motor $\omega_{\mathrm{motor}}(t)$. The measured pulses can be converted to longitudinal speed by dividing the rotation speed by the gearbox ratio n_{g} and multiplying by the wheel diameter r_{wheel} [1], which means

$$v_{\mathrm{odo}}(t) = r_{\mathrm{wheel}} \frac{\omega_{\mathrm{motor}}(t)}{n_{\mathrm{g}}}.$$

We will calculate the acceleration as the smooth, robust derivative of the velocity

$$a_{\mathrm{odo}}(t) = \frac{\mathrm{d}v_{\mathrm{odo}}(t)}{\mathrm{d}t}. \tag{1}$$

2.3. Slip-ratio

To express the speed discrepancy in a normalized form, let us define the slip ratio as

$$\kappa(t) = \frac{v_{\mathrm{odo}(t)} - \hat{v}(t)}{\max\left(|\hat{v}(t)|, v_{\min}\right)}, \tag{2}$$

where $v_{\min}$ is a small positive constant introduced to avoid numerical instability at low speeds [2].

3. Evalution

In this section, we summarize the results of the analysis based on data measured on the tram (model 52T ForCity Plus) when departing from the Chotkovy sady stop, which is slightly uphill and therefore a higher occurrence of wheel slip can be expected there. We focus on data measured in the winter months, when adhesion conditions are typically worse.

We can see a comparison of the acceleration calculated from odometry and from sensor fusion in Figure 1.

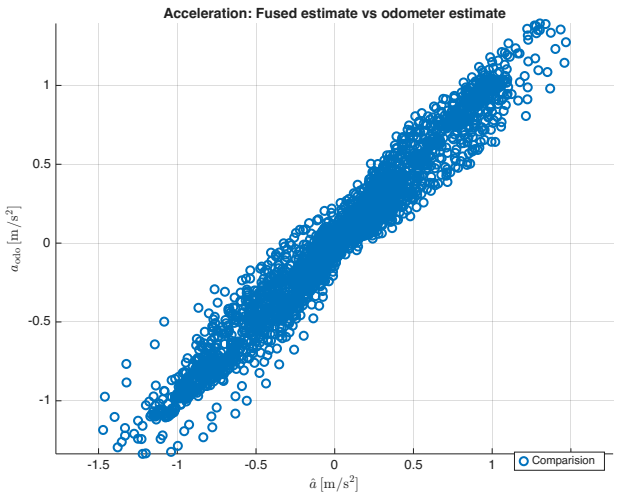

Fig. 1. Comparision of vehicle acceleration estimation from KF and from odometry only in winter mounths.

Similarly, the slip ratio calculated by (2) can be seen in Figure 2.

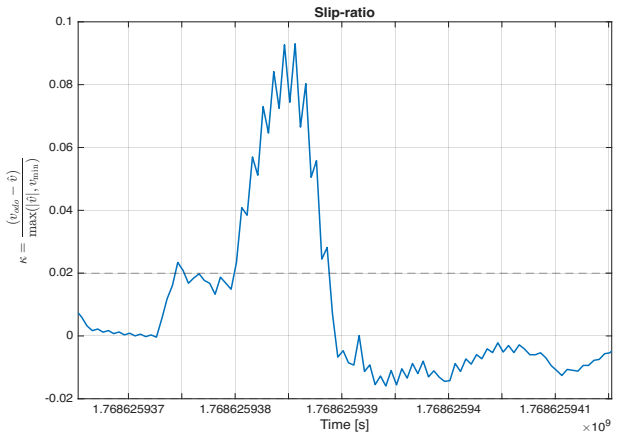

Fig. 2. Slip ration over time in winter mounths.

Finally, Table 1 summarizes the correlation between the velocity and acceleration calculated using the aforementioned methods in the winter and summer months.

	Speed		Acceleration	
	Pearson	Spearman	Pearson	Spearman
Summer	0.99999	0.99693	0.9626	0.92455
Winter	0.99998	0.99965	0.98267	0.96799

Tab. 1. Correlation

4. Conclusions and future work

A future extension of this work will be the ability to estimate the maximum possible acceleration and deceleration predictively over a longer time horizon. The predictive estimate of the maximum achievable acceleration provides key information for optimizing the energy consumption of rail vehicles. For the passage of a rail vehicle through an interstation section, a fixed time interval is typically specified, which must be met (within a certain tolerance).

The predictive estimate of the maximum achievable acceleration determines how quickly it is possible to accelerate to the optimal cruising speed. Without a predictive estimate, it is necessary to assume an acceleration that will be attainable even under poorer adhesion conditions, which forces a higher optimal cruising speed, because the time constraint must still be satisfied. The required kinetic energy to be generated (without accounting for losses) grows quadratically with speed, which, given the high mass of rail vehicles, creates a significant difference in the potential energy savings.

Acknowledgment

This research was supported by the Grant Agency of the Czech Technical University in Prague, grant No. SGS25/145/OHK3/3T/13 (1st author) and the Technology Agency of the Czech Republic (TACR) grant No. TN02000054 BOVENAC - *Božek Vehicle Engineering National Center of Competence* (thesis supervisor: prof. Ing. Vladimir Havlena, CSc.). The authors thank Skoda Digital company for providing the data used to evaluate the presented algorithms.

References

[1] Malvezzi, Monica Allotta, B. Rinchi, Mirko. (2011). Odometric estimation for automatic train protection and control systems. Vehicle System Dynamics. 49. 723-739. 10.1080/00423111003721291.

[2] Bernadin Namoano, Christos Emmanouilidis, Andrew Starr, Detecting wheel slip from railway operational data through a combined wavelet, long short-term memory and neural network classification method, Engineering Applications of Artificial Intelligence, Volume 137, Part B, 2024, 109173, ISSN 0952-1976.

Multi-Objective Model Selection Pipeline for Network Flow Classification

Jan SVOBODA[1]

[1]Dept. of Computer Science, FEE, Czech Technical University

svobo114@fel.cvut.cz

Abstract. *Training classifiers for network intrusion detection is hindered by two types of problems: data challenges (lack of labels, class imbalance, non-IID data, and concept drift) and engineering challenges (memory & compute efficiency, data ingestion, parallel training, and hyperparameter optimization). Existing ad-hoc scripts make it hard to reproduce results or compare models systematically across these conditions. An extendable machine learning pipeline is developed [1] to address both, targeting malicious network flow classifiers for the Stratosphere Linux IPS (Slips[2]). The output is a set of best-performing models at different FPR and F1 thresholds suitable for deployment in Slips.*

1. Introduction

Training deployable flow-based classifiers for intrusion detection is difficult because labeled data are limited/biased and experiments are hard to reproduce and compare across models and datasets. Moreover, selecting models with a single metric (e.g., best F1) can yield unacceptable false positive rates (FPR), especially under class imbalance and dataset shift.

Network flows are compact summaries (5-tuple + aggregated statistics such as bytes and packet counts). They enable fast training on tabular-like data, but discard packet-level detail. In typical IDS datasets, benign flows dominate and labels require manual pcap forensics; the Stratosphere datasets [3] are often malicious-heavy, which can amplify FPR.

The goal is to automate and standardize training and evaluation of flow-based malicious traffic classifiers for Slips, enabling reproducible and extensible experiments.

Contributions:

- A config-driven pipeline for flow parsing, Slips-aligned feature extraction, training, and evaluation of models, that is extendable to new libraries.
- Multi-objective Optuna tuning of flow classifiers for **F1** and **FPR**.
- Evaluation on captures of multiple malware families, producing deployable models for Slips.

Definitions. *Class imbalance* refers to the skew between benign and malicious flows in training data. *FPR* (false positive rate) is measured per flow. *Concept drift* refers to changes in traffic patterns over time, causing models to underperform in deployment [4].

2. Methodology

Pipeline procedure. Our methodology follows an end-to-end pipeline: ingest and preprocess flow records, compute features aligned with Slips, train candidate models, and evaluate them on a held-out test set while logging metrics and artifacts for reproducibility.

Data sampling. Models are trained on batched data, with sampling strategies selectable per experiment: sequential, random, label-balanced, or oversampling. The last two are designed to address the class imbalance present in our datasets.

Hyperparameter Optimization and evaluation The Optuna library [6] is used to tune hyperparameters. Each trial trains a model on the training split and is evaluated on the fixed test split, reporting per-flow **F1** (maximized) and **FPR** (minimized). Optimization is multi-objective, since single-metric tuning on F1 or accuracy is unreliable under class imbalance. Trials are run in parallel, with memory usage bounded.

The result is a **Pareto front** of non-dominated models; no model in the group is worse than another across both objectives. The final model is selected from this front by applying a FPR constraint: the model with the highest F1 among those meeting a maximum FPR threshold (0.05) is chosen. Dataset and split details are described in Section 3.

3. Data

Dataset Source. The datasets[3] vary in attack type, capture date, and network scenario, and are skewed toward malicious traffic. Observed attacks are various RATs (e.g. Dridex, Kovter, Trickbot).

Train/test split. The test set is fixed across all Optuna trials to ensure fair comparison between models. The split was manually designed by selecting datasets with varied relationships to each other: some test datasets separate from training data, some share the same attack type from a different capture, and some overlap directly with training data.

Data overlap. Under non-IID conditions, high performance on fully disjoint data does not imply good performance on overlapping data, and vice versa. By including test datasets at varying degrees of similarity to the training data, generalization across similarity regimes is assessed.

4. Results

Figure 1 plots FPR versus F1 for 710 Optuna trials; the most desirable models appear toward the lower-right region.

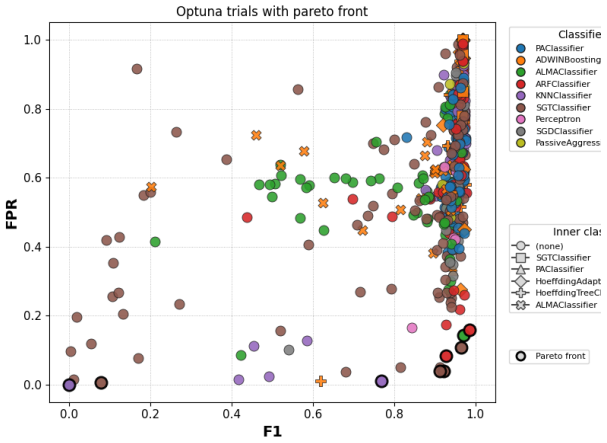

Fig. 1. F1–FPR trade-off across 710 Optuna trials; Pareto-optimal models are outlined.

Figure 2 highlights the Pareto front near the operating region used for selection, where lowering FPR trades off against F1. Two online models are selected for deployment (**SGT** and **ARF**); **SGT** is preferred due to its lower FPR. SGT is an online decision-tree model, and ARF [5] is an online random-forest ensemble.

	Test		Train	
Model	F1	FPR	F1	FPR
SGT	0.912	**0.041**	0.974	0.170
ARF	**0.927**	0.085	**0.996**	**0.076**

Tab. 1. F1 and FPR of two Pareto-optimal models. Train metrics reflect the optimizer's selected training subset.

5. Conclusion

This work delivers a modular pipeline for reproducible training and evaluation of malicious network flow detectors,

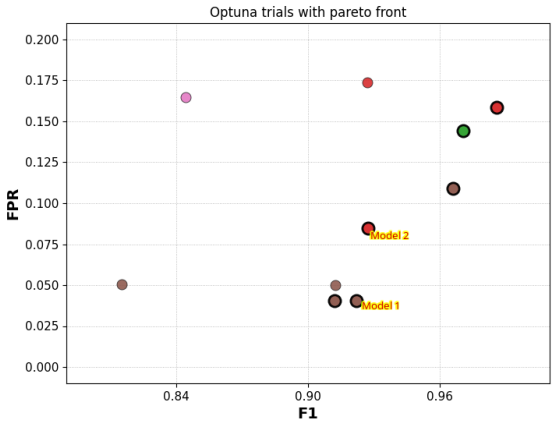

Fig. 2. Detail of the Pareto front near the operating region used for model selection.

producing models ready for the next Slips release. Online models are well-suited for deployment because they handle streaming data and drift without periodic retraining; SGT achieves FPR 0.041 at F1 0.912 and is recommended. A limitation is that concept-drift benchmarks and additional malware families were not explicitly evaluated.

Acknowledgements

I thank my supervisors, Sebastian García and Alya Gomaa of Stratosphere Laboratory, AIC, FEL ČVUT, for their guidance, and Sebastian García for his feedback on this submission.

References

[1] STRATOSPHERE LABORATORY, AIC FEL, CTU IN PRAGUE. *Slips-ML-Training-Pipeline: Machine-Learning Training and Evaluation Pipeline for Zeek Logs*. Code repository. https://github.com/stratosphereips/Slips-ML-Training-Pipeline (2026-03-22).

[2] STRATOSPHERE LABORATORY, AIC FEL, CTU IN PRAGUE. *Slips: Open-Source Behavioral Python IPS for Malicious Network Traffic Detection*. Code repository. https://github.com/stratosphereips/StratosphereLinuxIPS (2026-03-20).

[3] STRATOSPHERE LABORATORY, AIC FEL, CTU IN PRAGUE. *Stratosphere Laboratory Security Datasets for Testing*. Dataset repository. https://github.com/stratosphereips/security-datasets-for-testing (2026-03-20).

[4] GAMA, J., ŽLIOBAITÉ, I., BIFET, A., PECHENIZKIY, M., BOUCHACHIA, A. A survey on concept drift adaptation. *ACM Computing Surveys*, 2014, vol. 46, no. 4, article 44. DOI: 10.1145/2523813.

[5] GOMES, H. M., BIFET, A., READ, J., BARDDAL, J. P., ENEMBRECK, F., PFHARINGER, B., HOLMES, G., ABDESSALEM, T. Adaptive random forests for evolving data stream classification. *Machine Learning*, 2017, vol. 106, no. 9, pp. 1469–1495. DOI: 10.1007/s10994-017-5642-8.

[6] AKIBA, T., SANO, S., YANASE, T., OHTA, T., KOYAMA, M. Optuna: A next-generation hyperparameter optimization framework. *arXiv*, 2019. DOI: 10.48550/arXiv.1907.10902.

From Logic to Programming: A Computational Perspective on Transparent Intensional Logic

Samuel NOVOTNÝ

Dept. of Computers and Informatics, Technical University of Košice, Letná 9, 042 00 Košice, Slovak Republic

samuel.novotny@tuke.sk

Abstract. *Transparent Intensional Logic (TIL) has been traditionally viewed as a formal framework for the logical analysis of natural language. Despite the fact that its underlying formalism is grounded in a hyperintensional partial variant of typed λ-calculus equipped with procedural semantics, aspects related to its computational realization have remained largely unexplored.*

In this paper, we argue that TIL can be understood as a computationally realizable hyperintensional functional programming language, rather than merely a semantic framework. This claim is supported by two complementary developments: a refinement of the type system that resolves previously undetected type-theoretical incoherence, an embedding of TIL constructions into the Haskell programming language, and a shift towards an explicit evaluation perspective.

This reinterpretation clarifies the internal structure of TIL and opens new possibilities for its practical computational applications.

Keywords

constructions, functional programming, logic, Transparent Intensional Logic, type system.

1. Introduction

Transparent Intensional Logic (TIL) [2], introduced by Pavel Tichý [1], represents a formal framework for the logical analysis of natural language [4]. Its primary aim is to provide a mathematically precise model of Fregean senses of linguistic expressions in the form of abstract procedures, referred to as constructions [3]. Within this traditional setting, TIL has been primarily used as a tool for manual logical analysis of natural language expressions, typically performed by trained logicians.

Despite its formal proximity to typed λ-calculi, several aspects of TIL have not been developed with the level of rigor commonly associated with programming language theory. In particular, the formulation of its type-checking mechanism remains partially informal. This stems from the traditional methodological practice of TIL: given a meaningful linguistic expression, a corresponding construction is composed so as to capture its Fregean sense, and its type-theoretical coherence is subsequently verified. In this setting, type checking is typically carried out manually.

From the perspective of programming language theory, however, it is natural to consider the automation of this process. In particular, questions arise concerning the systematic type checking and type inference, as well as the ability of such procedures to detect type-theoretical errors.

This shift in perspective reveals limitations of the existing typing discipline. In particular, certain constructions corresponding to intuitively ill-formed or semantically nonsensical expressions may still be classified as well-typed. This observation motivates a more rigorous formulation of the type system together with explicit mechanisms for type checking and type inference.

At the same time, the procedural character of TIL constructions suggests that the system is naturally suited for computational realization. This observation further motivates a shift in perspective: instead of viewing TIL solely as a semantic framework, it becomes meaningful to investigate its properties from the viewpoint of programming language theory.

In this paper, we adopt such a perspective and argue that TIL can be understood as a computationally realizable hyperintensional functional programming language. This interpretation emerges from a combination of several developments: the refinement of the type system ensuring type-theoretical coherence [5], the embedding of TIL constructions into a strongly typed functional programming language [6], and the consideration of an explicit execution environment, namely, an extensional model of TIL [7].

2. Background

Transparent Intensional Logic is a hyperintensional variant of a typed λ-calculus with procedural semantics, in which expressions are associated with constructions—abstract procedures that produce objects of a given

type. These constructions form a stratified hierarchy governed by a ramified system of types, combining functional types with types of constructions.

Typing in TIL is traditionally expressed in two layers: one specifying membership of an object in a type, and another specifying the type of the object constructed by a constructional objects. While this distinction is sufficient for manual logical analysis, it lacks a fully explicit derivation-based formulation comparable to standard typing systems in programming language theory.

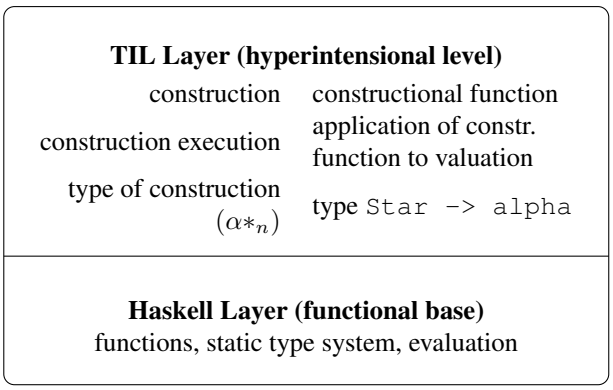

Fig. 1. Architecture of the TIL framework in Haskell as a two-layer system. The Haskell layer provides a functional base, while the TIL layer introduces a hyperintensional procedural level.

3. Type-theoretic issue and its resolution

A closer examination of the typing discipline of TIL reveals a structural issue arising from the interaction of rules governing constructions. In particular, certain rules propagate type information in a way that leads to a loss of information about the type of the constructed object, while others reintroduce such information without sufficient justification at the derivation level. As a consequence, the type-checking procedure may accept constructions that are internally type-theoretically incoherent.

To address this problem, we refine the notion of construction types. Instead of representing constructions solely by their order using types of the form $*_n$, we introduce types of the form $(\alpha*_n)$, which explicitly encode the type α of the constructed object.

This modification ensures that type information is preserved throughout the derivation process. As a result, type-theoretical incoherent constructions give rise to unsatisfiable constraint sets during type inference, and are therefore correctly rejected. The refined system thus establishes a derivation-based notion of typing consistent with principles of type safety known from programming language theory.

4. Computational realization

The refined typing discipline enables a computational interpretation of TIL constructions. In this setting, constructions can be viewed operationally as functions over a valuation, producing objects of a given type.

This interpretation is realized by embedding TIL into the Haskell programming language, where constructions are represented as higher-order functions called *constructional functions*, while the evaluation of constructions corresponds to application of such functions on specific valuation within the host language.

This relationship can be understood as a two-layer system (see Fig. 1). The underlying functional layer is provided by Haskell, which supplies a universe of non-procedural objects together with a statically typed evaluation mechanism. On top of this, TIL introduces a procedural layer, in which constructions represent hyperintensional entities operating over this base.

An important consequence of this embedding is that typing of TIL constructions is fully realized within the type system of Haskell. Consequently, correctness of typing is guaranteed by the underlying statically typed functional base.

Acknowledgements

Research described in the paper was supervised by Assoc. Prof. W. Steingartner, FEI TUKE and supported by the Cultural and Educational Grant Agency (KEGA) under project No. 052TUKE-4/2025, Modern Approaches in Educating IT Professionals in the Field of Type Theory and by KEGA project 028TUKE-4/2026 – Innovative approaches to teaching and researching formal methods in the context of modern software engineering, granted by the Cultural and Education Grant Agency of the Slovak Ministry of Education.

References

[1] TICHÝ, P. *The Foundations of Frege's Logic*. De Gruyter, 1988.

[2] DUŽÍ, M., JESPERSEN, B., MATERNA, P. *Procedural semantics for hyperintensional logic: Foundations and applications of transparent intensional logic*. Springer Science & Business Media, 2010.

[3] TICHÝ, P. Constructions. *Philosophy of Science*, vol. 53, no. 4, 1986, p. 514 – 534.

[4] DUŽÍ, M., MATERNA, P. Logical form. *Essays on the Foundations of Mathematics and Logic*, vol. 1, 2005, p. 115–153.

[5] NOVOTNÝ, S., DUŽÍ, M., STEINGARTNER, W., PERHÁČ, J. Towards resolving type incoherence in transparent intensional logic. In *Information Modelling and Knowledge Bases XXXVII*. Ostrava (Czech Republic), 2026, p. 335 – 348.

[6] NOVOTNÝ, S., DUŽÍ, M., STEINGARTNER, W. Implementation of transparent intensional logic framework in haskell. In *Information Modelling and Knowledge Bases XXXVII*. Ostrava (Czech Republic), 2026, p. 388 – 398.

[7] NOVOTNÝ, S., STEINGARTNER, W., NOVITZKÁ, V. On structure of Tichý-inspired logical spacetime. *Journal of Applied Mathematics and Computational Mechanics*, vol. 24, no. 4, 2025.

About Authors...

Samuel NOVOTNÝ was born in 1999 in Prešov, Slovakia. He received his Master's degree (Ing.) from the Department of Computers and Informatics at the Faculty of Electrical Engineering and Informatics, Technical University of Košice, in 2023. Currently he is a PhD student at the same department. His research focuses on non-classical logical systems in computer science and type theory.

Controlled Phase Transitions of a Water Droplets Observed using Advanced Environmental Scanning Electron Microscopy (A-ESEM)

Vojtěch Hlavička

Environmental electron microscopy, Institute of Scientific Instruments of the CAS, v. v. i., Královopolská 147, 612 00 Brno-Královo Pole, Czech Republic
The Faculty of Electrical Engineering and Communication, Brno University of Technology, Technická 3058/10, 616 00 Brno-Královo Pole, Czech Republic

vojtah@isibrno.cz

Abstract. *This work presents a study of controlled phase transitions of water droplets using advanced environmental scanning electron microscopy (A-ESEM). The aim of the study is to investigate condensation and freezing of water under precisely controlled pressure, temperature, and relative humidity inside the specimen chamber of an ESEM. Two experiments were conducted. In the first one, water was condensed inside a cavity fabricated in a silicon substrate placed on a cooled sample holder. The initial temperature was 1 °C, and the stage was subsequently cooled until freezing occurred. A-ESEM images of the condensed water droplet were acquired before and after freezing. In the second experiment, water vapor pressure was gradually increased around a Peltier cooling stage maintained at 0 °C until condensation of water droplets and subsequent freezing occurred, while continuously monitoring the environmental parameters. The experiments illustrate how A-ESEM enables in-situ observation, measurement, and control of phase transitions in small liquid volumes inside the specimen chamber.*

Keywords

Condensation, freezing, controlled thermodynamic conditions, advanced environmental scanning electron microscopy, in-situ observation.

1. Advanced Environmental Scanning Electron Microscopy (A-ESEM)

Scanning electron microscopy (SEM) enables high-resolution imaging and morphological characterization of solid samples. Conventional SEM typically operates under high-vacuum conditions, which limits the observation of wet, hydrated, non-conductive, or otherwise vacuum-sensitive specimens. Biological and other organic materials therefore often require dehydration and metal coating prior to imaging, which can alter their native structure [1,2].

Environmental scanning electron microscopy (ESEM) overcomes these limitations by allowing imaging in the presence of gas (< 2000 Pa) inside the specimen chamber. This enables both static and dynamic in-situ observation of specimens in their native state [3]. However, the imaging performance in ESEM is strongly influenced by thermodynamic parameters within the specimen chamber, such as pressure, temperature, and relative humidity. The presence of water vapor in the specimen chamber affects the scattering of the primary electron beam and limits the achievable resolution [4]. Variations in environmental conditions make the observation of wet samples complicated or even impossible. Precise knowledge and control of these parameters are therefore crucial for such experiments.

To overcome these limitations, ESEM was further improved, leading to the development of advanced environmental scanning electron microscopy (A-ESEM). Introduced in 2022 by Vilém Neděla's team at the Institute of Scientific Instruments of the Czech Academy of Sciences, A-ESEM enables precise control of chamber pressure, temperature, and humidity and has been applied in diverse research areas, including materials science, biology, and studies of hydrated or environmental samples [5].

2. Freezing of a Condensed Water Droplet under Controlled Conditions

In this experiment, water was condensed inside a cavity (500 µm in diameter and 50 µm deep) fabricated in a silicon substrate placed on a Peltier cooling stage inside the A-ESEM specimen chamber when the chamber pressure exceeded the saturation vapor pressure at 1 °C (≈657 Pa). An initial A-ESEM image of the liquid droplet was acquired.

The Peltier stage was then rapidly cooled to −10 °C (rate 44 °C/min). During cooling, the chamber pressure was maintained at approximately 50 Pa above the saturation vapor pressure to prevent evaporation. The cooling process continued until the droplet froze. Representative A-ESEM images before and after freezing are shown in Fig. 1.

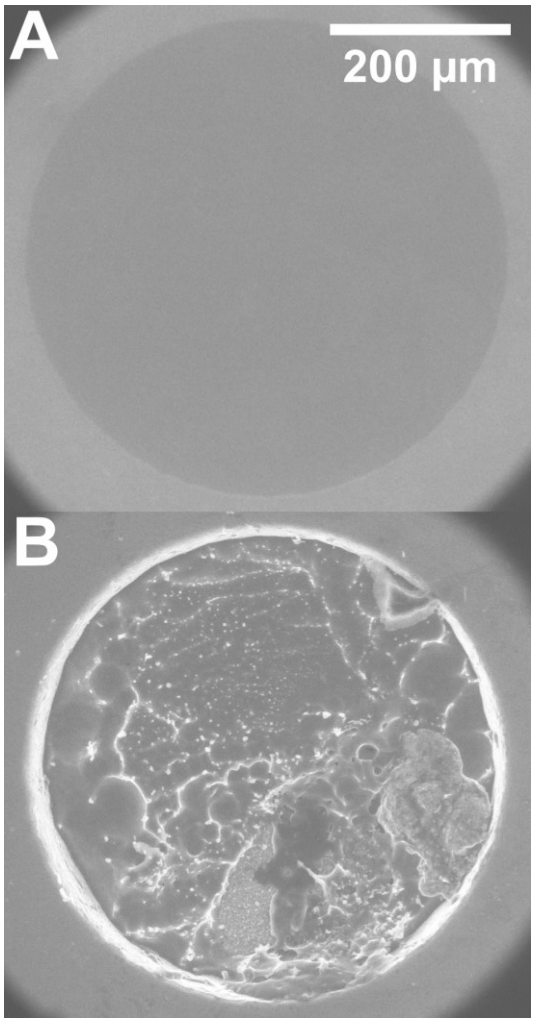

Fig. 1. A-ESEM images of a water droplet before (A) and after freezing (B).

3. Condensation and Freezing of Water Vapor at Increasing Pressure

In the second experiment, phase transitions were studied starting from a dry sample holder. The Peltier cooling stage was maintained at 0 °C, with water vapor as the imaging gas at an initial pressure of 50 Pa. The pressure was gradually increased in 50 Pa increments and fixed time intervals.

According to the phase diagram and the triple point of water, the state of the water (solid, liquid, or vapor) in the ESEM depends on both temperature and pressure. Condensation occurred on the cooled silicon sample plate, equipped with a temperature and relative humidity sensor, when the chamber pressure exceeded the saturation vapor pressure (≈613 Pa) and several water droplets were formed.

The latent heat released during the phase transition caused a temporary rise in the stage temperature. This led to an increase of Peltier stage cooling power, causing slight undercooling. The undercooling allowed the droplet to freeze, causing another cycle of temperature increase and undercooling, as shown in Fig. 2.

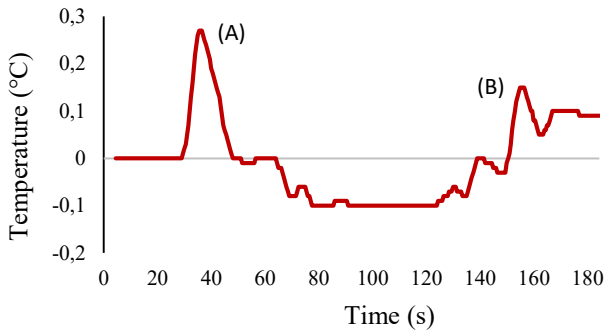

Fig. 2. Temperature changes during condensation (A) and freezing (B) of water vapor, showing latent heat release and subsequent freezing peak.

Acknowledgements

The research presented in this work was supervised by Assoc. Prof. Ing. et Ing. Vilém Neděla, Ph.D., DSc., Institute of Scientific Instruments of the CAS, Brno.

References

[1] ZHANG, Y., HUANG, T., JORGENS, D. M., NICKERSON, A., LIN, L.-J., PELZ, J., GRAY, J. W., LÓPEZ, C. S., NAN, X. Quantitating morphological changes in biological samples during scanning electron microscopy sample preparation with correlative super-resolution microscopy. *PLoS ONE*, 2017, vol. 12, e0176839. DOI: 10.1371/journal.pone.0176839.

[2] STOKES, D. J. Principles and practice of variable pressure/environmental scanning electron microscopy (VP-ESEM). *John Wiley & Sons*, Chichester, 2008. DOI: 10.1002/9780470758731.

[3] DANILATOS, G. D. Foundation of environmental scanning electron microscopy. In: *Advances in Electronics and Electron Physics*, vol. 71. Academic Press, 1988, p. 109–250. DOI: 10.1016/S0065-2539(08)60902-6.

[4] NEDĚLA, V., TIHLAŘÍKOVÁ, E., MAXA, J., IMRICHOVÁ, K., BUČKO, M., GEMEINER, P. Simulation-based optimisation of thermodynamic conditions in the ESEM for dynamical in-situ study of spherical polyelectrolyte complex particles in their native state. *Ultramicroscopy*, 2020, vol. 211, 112954. DOI: 10.1016/j.ultramic.2020.112954.

[5] NEDĚLA, V., TIHLAŘÍKOVÁ, E., CÁPAL, P., DOLEŽEL, J. Advanced environmental scanning electron microscopy reveals natural surface nano-morphology of condensed mitotic chromosomes in their native state. *Scientific Reports*, 2024, vol. 14, 63515. DOI: 10.1038/s41598-024-63515-9.

About Author

Vojtěch HLAVIČKA received the M.Sc. degree in Chemical and Process Engineering from the University of Pardubice, Czech Republic, in 2016. He is currently pursuing the Ph.D. degree in Microelectronics at the Brno University of Technology, Czech Republic. Since 2024, he has been a Researcher with the Institute of Scientific Instruments of the Czech Academy of Sciences, Brno. His research focuses on the integration of mass spectrometry with environmental scanning electron microscopy.

Fusion Proton Spectrometry in Z-pinch Plasma

Markéta Vlčková[1]

[1]Dept. of Physics, Faculty of Electrical Engineering, Czech Technical University, Technická 2, 166 27 Praha, Czech Republic

vlckoma7@fel.cvut.cz

Abstract. *This work presents measurements of energetic fusion protons generated in deuterium plasma produced by the PFZ-200 plasma focus device, operating at peak currents of up to* $270\,\mathrm{kA}$*, with an average current rise time of approximately* $1.8\,\mu\mathrm{s}$*. The device produced neutron yields on the order of* 10^7 *neutrons per discharge. Several diagnostic methods were used to characterise the discharge and the generated particles. Proton energies were determined using CR-39 nuclear track detectors in conjunction with aluminium filters of various thicknesses. Analysis of the etched tracks enabled identification of proton energies corresponding to D–D fusion reactions, with the detected energy spectrum extending up to approximately* $3\,\mathrm{MeV}$*. These results confirm the generation of fusion protons in Z-pinch plasmas and demonstrate the effectiveness of CR-39 diagnostics for measuring proton energies in plasma focus experiments.*

Keywords

Z-pinch, plasma focus, CR-39 detectors, proton spectrometry

1. Z-pinch

Magnetic pinch is a configuration of plasma confinement that originates from the interaction between an electric current and its magnetic field. For a Z-pinch to occur, high current values on the order of hundreds of kA are required. According to Ampère's law, an electric current flowing through plasma generates an azimuthal magnetic field.

$$\nabla \times \mathbf{B} = \mu_0 \mathbf{J}. \tag{1}$$

For a cylindrical current channel the azimuthal magnetic field can be expressed as

$$B_\theta = \frac{\mu_0 I}{2\pi r}. \tag{2}$$

Such an interaction between the current density and the magnetic field produces the Lorentz force, whose volume density is given by

$$\mathbf{f} = \mathbf{J} \times \mathbf{B}. \tag{3}$$

This force compresses the plasma column toward its axis. As a result, a hot and hight-density plasma is generated in which high-energy particles, including fusion protons and neutrons, can be produced [3].

1.1. D-D fusion reactions

In this work we aim to study proton production from D–D fusion reactions occurring in deuterium plasma. Through a beam–target mechanism, deuterons accelerated in the discharge collide with other deuterons in the plasma, enabling fusion reactions. During the D–D reaction two reaction channels occur with approximately equal probability [2]:

$$D + D \rightarrow T(1.01\,\mathrm{MeV}) + p(3.02\,\mathrm{MeV}) \tag{4}$$

$$D + D \rightarrow {}^3\mathrm{He}(0.82\,\mathrm{MeV}) + n(2.45\,\mathrm{MeV}) \tag{5}$$

This aspect is important for our experiment, because the number of detected neutrons allows us to estimate the discharge performance in terms of proton production. The emitted neutrons were therefore used as an indirect indicator of proton production. The experimental campaign was performed in deuterium gas at a pressure of $p = 360\,\mathrm{Pa}$.

2. PFZ-200

The plasma focus is a type of pulsed power Z-pinch device in which a plasma current sheath is accelerated along coaxial electrodes by electromagnetic forces. When the plasma current sheath reaches the top of the anode, an azimuthal magnetic field compresses the plasma toward the axis, forming a dense plasma focus. In this region the magnetic energy is rapidly converted into plasma heating and the production of energetic particles and x-ray radiation [1].

In our experiment the plasma focus PFZ-200 was used, which is a small compact pulsed power apparatus. It is a Mather-type plasma focus with a coaxial electrode system. The cylindrical anode is surrounded by 12 cathode rods made of stainless steel. The electrode system is placed in a vacuum chamber, which is kept under high vacuum

and during the discharge is filled with deuterium gas. The energy source is a capacitor battery with a capacitance of $16\,\mu\mathrm{F}$ connected to the electrode system by a air filled spark-gaps. During the experiment the charging voltage of the capacitor battery was set up to $20\,\mathrm{kV}$ and the maximum discharge current reached up to $270\,\mathrm{kA}$.

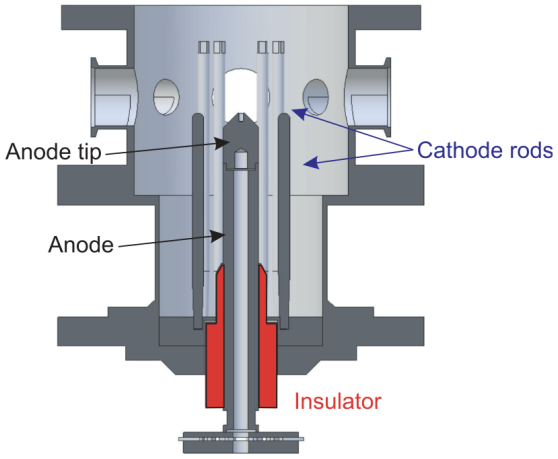

Fig. 1. PFZ-200 plasma focus cross-section [6].

2.1. Diagnostics

The experimental apparatus is equipped with several diagnostic systems. To measure the discharge current and its time derivative a Rogowski coil is used. The total neutron yield, which allows us to estimate the proton production during a single discharge, is measured by a silver activation counter (SAC) placed 40 cm from the anode axis. For additional neutron analysis two neutron Time-of-Flight (nToF) detectors were positioned at distances of 418 cm and 253 cm in the radial direction from the vacuum chamber . The nToF detectors operate on the principle of scintillation detectors and are sensitive to neutron and hard x-ray radiation. They allow us to estimate the neutron energy from their time of flight over a known distance. To visualize the discharge evolution, an x-ray pinhole camera equipped with a fast microchannel plate (MCP) was used. The MCP camera records four images that are time-shifted by 5 ns.

3. CR-39 Detectors

For proton detection, CR-39 nuclear track detectors were used. CR-39 belong to passive nuclear track detectors in which information about the detected particle energy is derived from the length of its stopping range and from the characteristics of the track formed in the detector material. Charged particles passing through the polymer CR-39 ($C_{12}H_{18}O_7$) create a region of damaged structure along their trajectory, known as a latent track. The amount of damage is related to the linear energy transfer (LET), defined as the

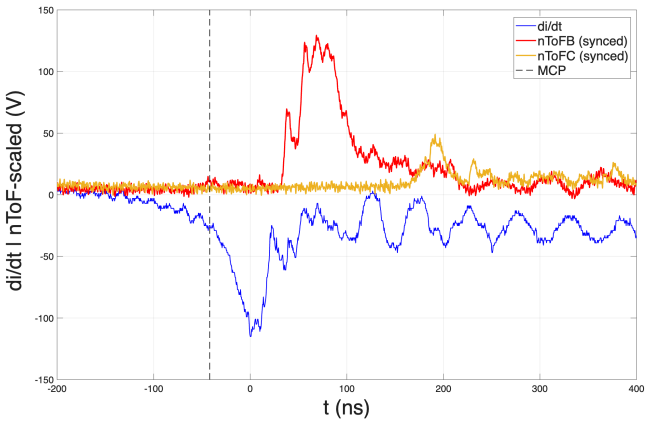

Fig. 2. Shot 25111403- nToF and current derivation signals with MCP mark.

energy loss per unit path length dE/dx. To visualize the latent tracks, the detector must be chemically etched, typically in a NaOH solution, where the damaged regions are etched faster than the undisturbed material and form characteristic conical pits. The diameter and shape of the tracks depend on the particle type, its energy, and the etching conditions [4]. CR-39 detectors are particularly suitable for fusion experiments due to their high detection efficiency for charged particles and their resistance to electromagnetic pulses and x-ray radiation. In the case of proton detection, the stopping range in CR-39 strongly depends on the proton energy as shown in fig. 3 [5].

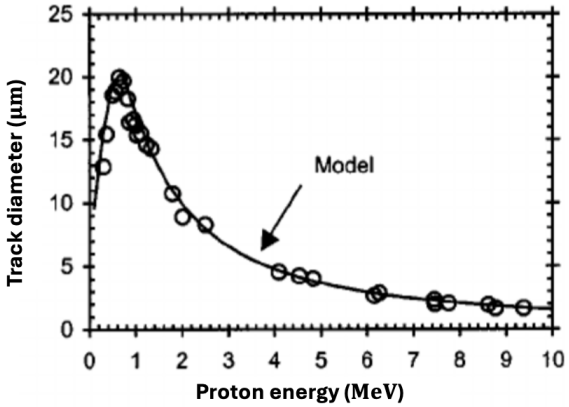

Fig. 3. Track diameter as a function of proton energy in etched CR-39 detectors [5].

To perform the spectral analysis, the detectors were placed behind a segmented mask covered by aluminium foils of different thicknesses. This masking system allows the estimation of proton energies based on their ability to penetrate materials of known thickness before reaching the detector surface.

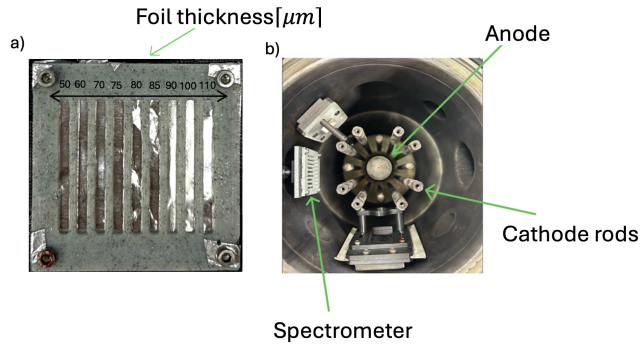

Fig. 4. a) Spectrometer mask with aluminium foil b) Detectors arrangement in the vacuum chamber

4. Experimental results

Several experimental series were performed using an aluminium absorber mask placed in front of the CR-39 detectors for spectral analysis. Before each shot the vacuum chamber was filled with fresh deuterium gas, while similar operating conditions were maintained to ensure reproducible fusion discharges. The tracks recorded in the CR-39 detectors were subsequently analyzed to estimate the energy distribution of the produced protons.

4.1. Plasma visualisation

To visualize the plasma implosion we used a fast x-ray pinhole camera equipped with a gated microchannel plate detector. In the figure 5 we present a representative example of the discharge captured at three different time points. Starting from t_0, the progressive narrowing of the plasma column can be observed until the moment of maximum compression, which occurs approximately 15 ns later. At this stage the Z-pinch effect takes place, shortly before the collapse of the plasma channel.

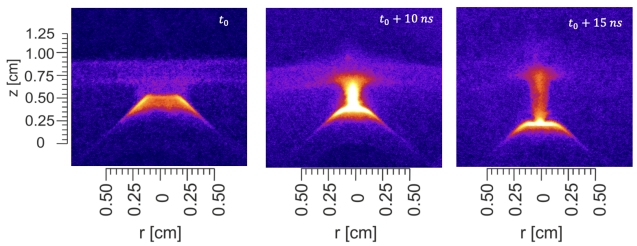

Fig. 5. Z-pinch discharge evolution captured by x-ray camera with MCP.

4.2. Proton energy spectra

The proton energy spectrum was estimated using CR-39 nuclear track detectors combined with aluminium foils of different thicknesses. Table 1 summarizes the nominal and measured thicknesses of the aluminium foils used in the segmented filter mask employed in our experiment, together with the corresponding proton energies required for their penetration.

Nom. foil thickness [μm]	Measured thickness [μm]	E_p [MeV]
50	51.3	2.28
60	61.0	2.53
70	70.6	2.77
75	75.1	2.88
80	80.2	3.00
85	84.7	3.09
90	89.8	3.21
100	102.7	3.48
110	112.3	3.67

Tab. 1. Aluminium foil thickness and corresponding proton energies.

Based on this calibration, the number and distribution of tracks recorded in the CR-39 detectors were analyzed for individual foil segments. By comparing the presence or absence of tracks behind specific aluminium layers, it is possible to estimate the energy range of the detected protons.

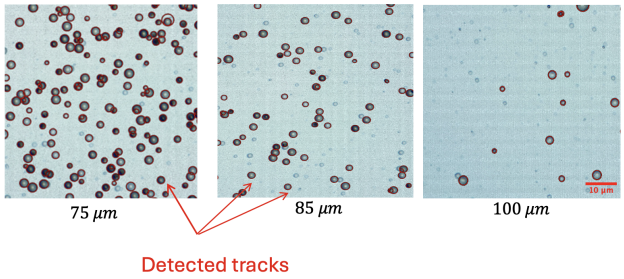

Fig. 6. Representative microscope images of etched CR-39 detectors for aluminium filters of 75, 85 and 100 μm. Red circles mark selected proton tracks.

In Fig. 6 three representative microscope images of etched CR-39 detectors are shown for aluminium filters with thicknesses of 75, 85 and 100 μm. The highest density of detected proton tracks is observed for the 75 μm filter. For the 85 μm foil a lower track density is visible, while for the 100 μm foil only a small number of tracks close to the background level remain. This behaviour reflects the energy filtering effect of the aluminium layers, since only protons with sufficiently high energies are able to penetrate thicker foils and reach the detector surface. In the case of the 75 μm filter the proton tracks also appear larger, which corresponds to the region near the Bragg peak, where the energy deposition of protons in the CR-39 detector reaches its maximum.

Table 2 summarizes the measured track density together with the corresponding average proton energies and the reconstructed differential spectrum dN/dE for individual aluminium filters. The differential quantity

dN/dE represents the number of detected protons per unit energy interval and forms the basis for the reconstruction of the proton energy spectrum shown in Fig. 7. The negative value in the first interval results from statistical fluctuations and from the numerical differentiation of discrete experimental data.

Al thickness $[\mu m]$	Avg. energy [MeV]	Track density $[\mathrm{cm}^{-2}]$	dN/dE $[\mathrm{MeV}^{-1}]$
60	2.66	1.70×10^5	-2.32×10^4
70	2.85	1.76×10^5	3.05×10^5
75	2.98	1.36×10^5	6.71×10^5
80	3.09	4.91×10^4	1.17×10^5
85	3.20	3.74×10^4	2.71×10^5
90	3.37	4.93×10^3	1.86×10^4
100	3.58	8.27×10^2	4.35×10^3

Tab. 2. Measured track density and reconstructed differential proton spectrum dN/dE for aluminium filters of different thicknesses.

To visualize the measured proton energies, a spectral diagram was constructed (Fig. 7). The reconstructed spectrum covers the proton energy range from about 2.6 to 3.6 MeV. A pronounced maximum is observed in the energy region between approximately 2.9 and 3.0 MeV, which corresponds well to the expected proton energy of 3.02 MeV produced in the D–D fusion reaction. Elevated proton counts are also observed in the neighbouring energy intervals around 2.8–2.9 MeV and near 3.2 MeV. The error bars represent the statistical uncertainty associated with the finite number of detected tracks in each energy interval. Overall, the distribution confirms that the majority of detected protons have energies close to the expected fusion proton energy, while only a smaller fraction of particles appears at different energies.

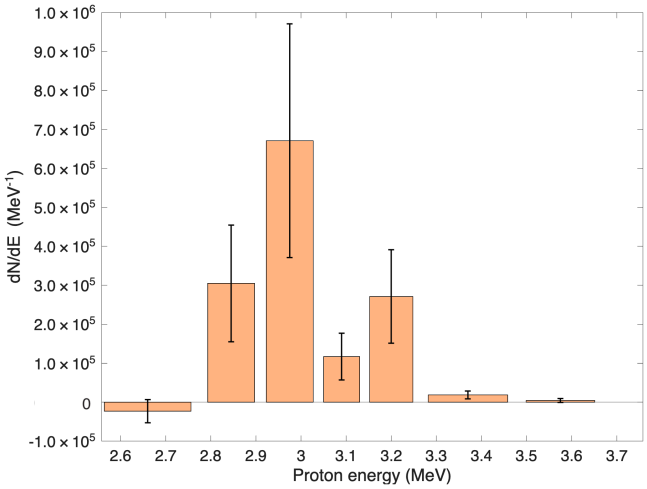

Fig. 7. Reconstructed proton energy spectrum obtained from CR-39 detector analysis.

5. Conclusion

During the experimental campaign conducted on the PFZ-200 plasma focus device, the generation of fusion protons and their energy spectra within the deuterium plasma were examined. Proton energies were determined using CR-39 nuclear track detectors in conjunction with aluminium filters of various thicknesses.

The measured proton energies were consistent with the expected values for D–D fusion reactions. Proton energies of up to approximately 3.6 MeV were observed, with most of the detected particles concentrated near 3 MeV. These results confirm the generation of fusion protons in Z-pinch plasma produced by the PFZ-200 device.

Acknowledgements

This research was supported by the Czech Technical University in Prague (Grant No. SGS25/138/OHK3/3T/13). The author would also like to thank Ing. Jan Novotny for supervising and to Dept. of Electrotechnology of FEE, CTU in Prague and Prof. Karel Dusek for providing access to the digital microscope.

References

[1] SCHOLZ, M. *Plasma-Focus and Controlled Nuclear Fusion*. Kraków: IFJ PAN, 2014.

[2] CHEN, F. F. *Úvod do fyziky plazmatu*. Praha: Academia, 1984.

[3] KLIR, D. et al. Production of energetic protons... *New J. Phys.*, 2020, vol. 22, no. 10, 103036.

[4] JEONG, T. W. et al. CR-39 track detector for multi-MeV ion spectroscopy. *Sci. Rep.*, 2017, vol. 7, 2152.

[5] FRENJE, J. A. et al. Spectrometry of charged particles... *Rev. Sci. Instrum.*, 2002, vol. 73, no. 7, p. 2597 - 2600.

[6] NOVOTNY, J. et al. Effect of anode shape on neutron and x-ray emission in dense plasma focus. *Phys. Plasmas*, 2023, vol. 30, no. 8, 082702.

About Authors...

Markéta Vlčková was born in 2003 in Ostrava. She is an undergraduate student of Electrical engineering, power engineering and Management of Faculty of Electrical engineering on the CTU in Prague since 2023. She actively participated in experimental campaigns performed on the plasma focus device PFZ-200.

Fusion Particle Source Characterization in Z-pinch Discharges

Veronika Matějková[1]

[1]Dept. of Physics, Faculty of Electrical Engineering, Czech Technical University in Prague, Technická 2, 166 27 Praha, Czech Republic

matejve4@fel.cvut.cz

Abstract.

This study presents an investigation into the production of fusion particles in z-pinch discharges, as observed in the PFZ-200 plasma focus device at the Faculty of Electrical Engineering at the Czech Technical University in Prague. The study focuses on deuterium–deuterium (DD) fusion reactions as a source of neutrons and charged particles. The main objective is to characterize proton emission and compare it with neutron production under identical experimental conditions. Protons are detected using CR-39 solid-state nuclear track detectors with aluminum absorbers, while neutrons are detected using activation counters and neutron time-of-flight measurements. Additional diagnostics, including a Rogowski coil and a fast microchannel plate (MCP) x-ray pinhole camera, are employed to monitor discharge dynamics and plasma behavior.

Keywords

PFZ-200, z-pinch, fusion reactions, neutrons, protons, plasma diagnostics, CR-39.

1. Introduction

Nuclear fusion is a process where light atomic nuclei combine to form a heavier nucleus, releasing a large amount of energy. It is the primary energy source of stars, and achieving controlled fusion on Earth could provide a future source of sustainable electrical energy. For this reason, the physics of fusion is researched using various experimental facilities, including tokamaks, laser-driven systems, and pulsed plasma devices. One such approach is the z-pinch, where a strong pulsed electric current generates a magnetic field that rapidly compresses plasma to high temperatures and densities, creating conditions suitable for fusion reactions. In this study, experiments are performed on PFZ-200, a pulsed power device designed to study plasma dynamics and the production of fusion particles during z-pinch discharges.

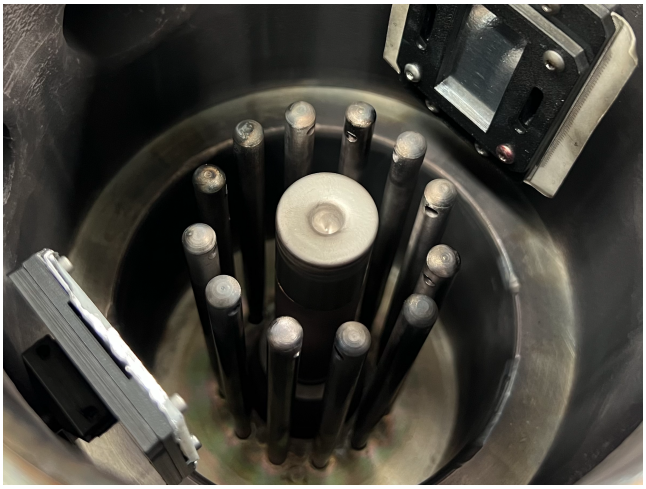

Fig. 1. The electrode system inside the vacuum chamber. On both sides CR-39 detectors are visible.

The plasma focus consists of a high-voltage capacitor bank and a coaxial electrode system. In the center, there is a cylindrical anode surrounded by twelve cathode rods. The electrode system is situated inside a vacuum chamber filled with deuterium at low pressure (in our experiments, 360 Pa). As high voltage is applied, the gas between the electrodes is ionized, and thus a plasma channel is formed. High electrical current (on PFZ-200, up to 250 kA) flows through this discharge and generates a strong magnetic field. This azimuthal field wraps around the plasma channel and creates the Lorentz force, which compresses the channel and causes the implosion. Assuming quasi-neutral plasma[1], the Lorentz force density is given by

$$\mathrm{f} = \mathbf{J} \times \mathbf{B}, \tag{1}$$

where $\mathbf{B}$ is the magnetic field and $\mathbf{J}$ is the current density.

The pressure compressing the plasma can also be interpreted in terms of the so called magnetic pressure p_m. As a counteraction to the magnetic pressure, the thermal motion of particles creates kinetic pressure p_k, which expands the plasma. When the gradients of these two forces become

[1]Quasi-neutrality of plasma means, that the positive and negative charge densities are approximately equal ($n_i \approx n_e$).

equal, we obtain the equilibrium magnetic pinch. In reality, due to inhomogeneities in the plasma, magnetohydrodynamic instabilities will develop, deforming the structure and eventually leading to its disrupture. [2, 3, 4]

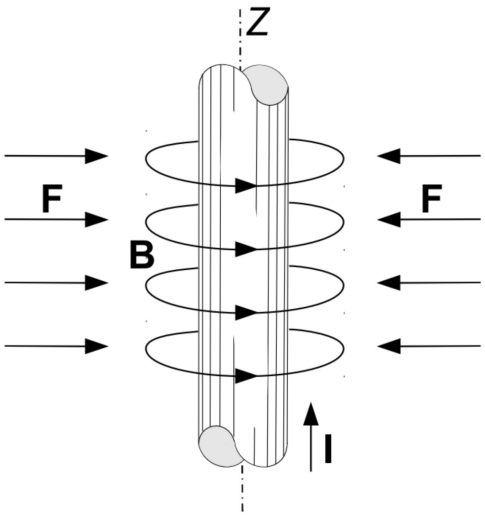

Fig. 2. The pinch effect. [1]

2. Fusion nuclear reactions

Fusion nuclear reactions occur when two light atomic nuclei collide and combine to form a heavier nucleus. During this process, a portion of the mass of the reacting particles is converted into energy. For a fusion reaction to occur, the initial energy of the reacting nuclei must be sufficiently high to overcome the Coulomb repulsion between them. For deuterons, this energy is typically on the order of hundreds of keV. [5]

The probability of a nuclear (fusion or fission) reaction occurring is typically expressed by its cross section. The total cross section can be expressed as

$$\sigma = \frac{R}{N \cdot \Gamma}, \tag{2}$$

where R is the reaction rate, N is the number of particles in the target plane, and Γ is the particle flux.

In our experiments, deuterons fuse – these reactions are called the DD reactions, and they can be described as follows

$$^{2}_{1}\mathrm{D} + ^{2}_{1}\mathrm{D} \longrightarrow ^{3}_{1}\mathrm{T} + ^{1}_{1}\mathrm{p}\ (3.02\ \mathrm{MeV}) \tag{3}$$

$$^{2}_{1}\mathrm{D} + ^{2}_{1}\mathrm{D} \longrightarrow ^{3}_{2}\mathrm{He} + ^{1}_{0}\mathrm{n}\ (2.45\ \mathrm{MeV}) \tag{4}$$

Both of these reactions have comparable cross sections and therefore approximately equal probabilities of occurring. This indicates that the total neutron and proton yield should be nearly equal. However, in experimental measurements the detected yields may differ due to the characteristics of the diagnostic methods. Neutron detectors, for instance, can register scattered neutrons, which may lead to an overestimation of the neutron yield.

3. Experiment

3.1. Proton detection

The CR-39 detector is commonly used for the detection of charged particles. It is a solid-state passive nuclear track detector made of a transparent polymer $(\mathrm{C_{12}H_{18}C_7})_n$ with high sensitivity. As charged particles pass through the detector material, the area surrounding their trajectory is ionized, and the chemical bonds are broken, damaging the structure. This process creates latent tracks, which are later enlarged and revealed by chemical etching. When etching the whole surface, the damaged regions are etched faster than the undamaged material, allowing the tracks to become detectable under a microscope.

During the experiments, aluminum absorbers were used with the CR-39 detectors, as only particles within a certain energy range can be measured. Approximately 70 μm of aluminum foil was used to filter the incoming particles so that only those with energies above 2.45 MeV could pass through. This energy threshold corresponds to protons produced in DD fusion reactions. Fig. 3 shows a CR-39 detector prepared for measurements and an image of an exposed and chemically etched detector. In the exposed detector image, brighter regions correspond to a higher track density and therefore indicate a stronger particle signal.

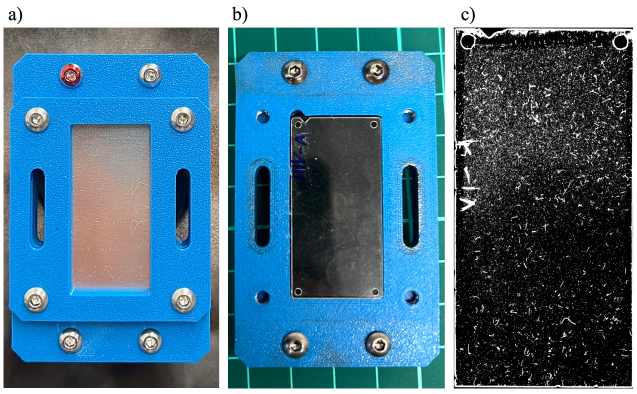

Fig. 3. CR-39 detectors used in the experiment. On the left (a), the detector is covered with a 70 μm aluminum absorber and prepared for measurements. The middle image (b) shows the detector uncovered. On the right (c), an image of the exposed and chemically etched detector is shown, where brighter regions correspond to a higher density of particle tracks. The length of the detector is 40 mm.

The signal intensity profile obtained from the exposed CR-39 detector is shown in Fig. 4. The horizontal axis represents the position along the detector surface, while the vertical axis corresponds to the normalized track density, which is proportional to the number of detected charged particles. During the experiment, the lower part of the detector was

partially covered by a shielding element. As a result, fewer particles were able to reach this region, leading to a significantly lower signal intensity compared to the upper part of the detector. The edge of the detector was completely covered, preventing particles from reaching this area; consequently, the measured signal drops to zero at this position.

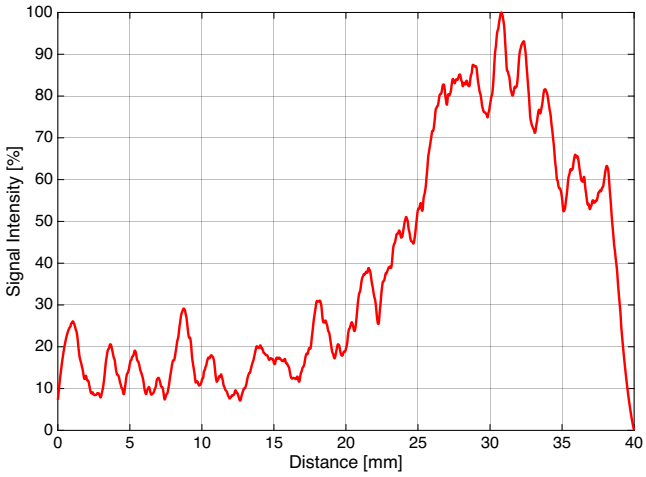

Fig. 4. Signal intensity profile on an exposed CR-39 detector. Distance 0 mm corresponds to the lower edge and 40 mm to the top edge of the detector, as shown in Fig. 3.

The exposed detectors are analysed using a microscope, where the number and size of tracks can be measured. Each circular track corresponds to the trajectory of a single charged particle that passed through the detector with the track size reflecting the particle energy loss. The density of these tracks is proportional to the fluence of protons incident on the detector and can therefore be used to estimate the proton yield. A microscope image of an exposed detector is shown in Fig. 5.

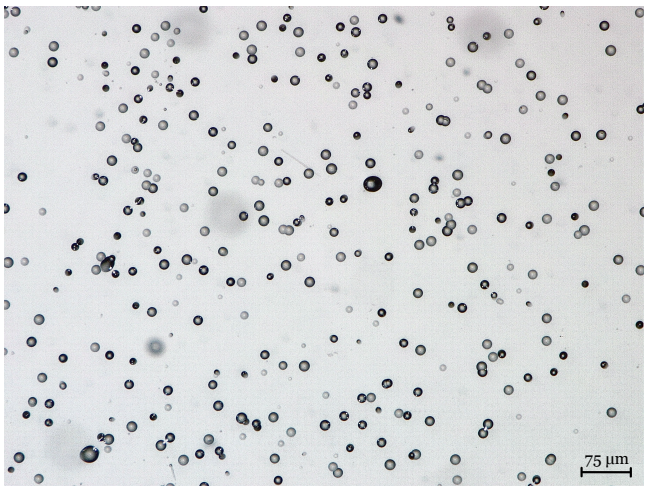

Fig. 5. Microscope image of an exposed CR-39 detector showing etched proton tracks. The density of circular pits corresponds to the number of detected charged particles.

3.2. Neutron detection

Neutrons are particles without an electric charge, therefore their detection is more complicated than the detection of protons or electrons, which ionize the surrounding environment and from which we can obtain an electrical signal. For this reason, neutrons must be detected indirectly.

One of the most commonly used detectors for neutron measurements is the silver activation counter. The neutrons from the discharge interact with stable isotopes of silver ^{107}Ag and ^{109}Ag, creating unstable isotopes ^{108}Ag and ^{110}Ag that undergo radioactive β^- decay. By measuring the radiation using Geiger-Müller tubes, we are able to calculate the approximate neutron yield using the formula below, [6]

$$Y_n = \Phi \cdot 4\pi r^2 = (C - C_B) \cdot 4.69 \cdot 4\pi r^2, \qquad (5)$$

where Y_n denotes the total neutron yield, Φ is the neutron fluence at the detector position, r is the distance between the neutron source and the detector, C represents the measured detector counts, C_B the background counts, and 4.69 is the detector calibration factor used to convert the net counts into neutron fluence.

Another way to measure neutrons is the neutron Time of Flight method, using a scintillation detector. When the particle enters the scintillator and interacts with the scintillator material, light pulses are generated. This light then continues into a photomultiplier, where it is converted into an electrical signal so that it is measurable by an oscilloscope. [1]

3.3. Rogowski coil

The current and its derivative are measured using a Rogowski coil, which is a sensor for measuring high-frequency currents. It is a toroidal coil placed around a conductor carrying the measured current. The current generates a magnetic field that links the coil winding, and according to Faraday's law of electromagnetic induction, induces a voltage in the coil. The induced voltage is proportional to the current derivative by the mutual inductance M between the coil and the conductor.

$$u_i(t) = -M \frac{\mathrm{d}i(t)}{\mathrm{d}t} \qquad (6)$$

The waveforms of the current and its derivative, measured by the Rogowski coil, together with the signal from a scintillation detector (nToF), are shown in Fig. 6. Time zero corresponds to the electrical breakdown on the insulator, when the discharge current begins to rise. The implosion of the plasma channel occurs approximately after 1.5 μs. Subsequently, magnetohydrodynamic instabilities develop and the current decreases rapidly, which is clearly visible as a dip in the current derivative. The green line represents the

signal from the scintillation detector. The first peak corresponds to the emission of hard X-ray radiation, while the second peak is associated with neutron emission. The radiation emission occurs approximately at the minimum of the current derivative.

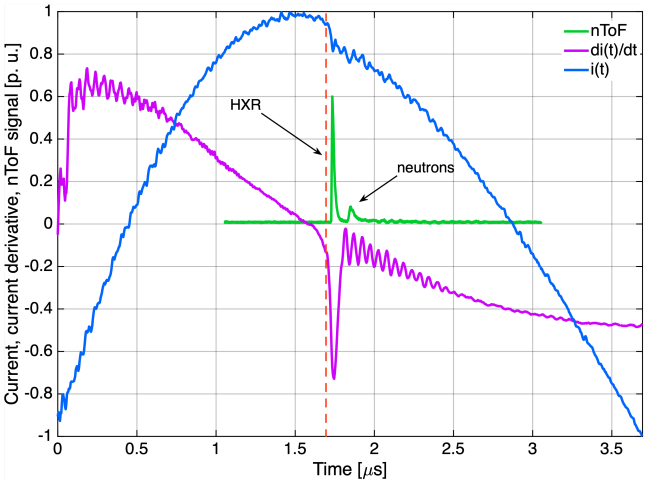

Fig. 6. Current (blue), current derivative (purple) and nToF signal (green) waveforms.

3.4. MCP fast x-ray camera

The implosion was observed using a fast x-ray pinhole camera equipped with a microchannel plate (MCP). The pinhole forms an image of the plasma without the use of lenses, which is suitable for x-ray diagnostics. The MCP operates as an ultrafast electronic gate, allowing the detector to be exposed only during a very short time window. This enables the imaging of extremely fast plasma dynamics. The images shown in Fig. 7 capture three consecutive stages of the implosion with a time delay of 10 and 15 ns. In Fig. 6, the red dashed line indicates the moment when the MCP images of the implosion were captured.

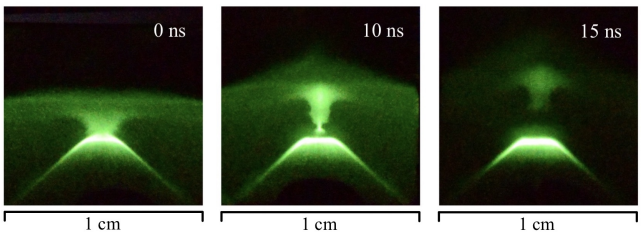

Fig. 7. Different stages of the discharge captured by a microchannel plate (MCP) x-ray pinhole camera. The green colour of the recorded images is caused by the phosphor screen used in the MCP detector – it does not correspond to the actual emission colour of the plasma.

4. Conclusion

Experiments performed on the PFZ-200 plasma focus device confirm that z-pinch discharges can produce measurable yields of fusion particles, including neutrons and protons. The combination of diagnostic techniques employed in this study was suitable for investigating both charged and neutral fusion products, as well as the temporal evolution of the discharge.

Although the cross sections of DD fusion reactions are comparable, experimental observations reveal a clear difference in the detected yields. The proton yield is approximately two to three times lower than the neutron yield. This discrepancy can likely be attributed, at least in part, to the neutron detection method. In particular, the silver activation counter may overestimate the neutron yield due to its sensitivity to scattered neutrons, which contribute to the measured signal. This effect highlights the importance of carefully interpreting neutron diagnostics and suggests the need to further refine measurement techniques.

Acknowledgements

This research was supported by the Czech Technical University in Prague (Grant No. SGS25/138/OHK3/3T/13). The author also would like to thank Ing. Jan Novotný for supervising and to Dept. of Electrotechnology of FEE, CTU in Prague and Prof. Karel Dušek for providing access to the digital microscope.

References

[1] CIKHARDT, J., *High Energy Density Plasma Diagnostics Using Neutron and Gamma Detectors. Ph. D. thesis.* Czech Technical University, 2017.

[2] KUBEŠ, P., *Impulse high-current discharges and their diagnostics.* Czech Technical University, 2004.

[3] KULHÁNEK, P., *Introduction to plasma theory.* AGA, 2017

[4] CHAN, F. F., *Introduction to Plasma Physics.* ACADEMIA, 1984

[5] KIKUCHI, M., LACKNER, K., TRAN, M. Q., *Fusion physics.* International Atomic Energy Agency, 2012

[6] NOVOTNÝ, J., *Optimizing of experimental load of PFZ-200 plasma focus.* FEE CTU, 2019

About Author…

Veronika MATĚJKOVÁ was born in 2004 in Prague, Czech Republic. She is currently an undergraduate student of Electrical Engineering, Power Engineering and Management at the Faculty of Electrical Engineering at the Czech Technical University in Prague.

PsyTools: An Open-Source Python Toolbox for Standardized Psychoacoustic Analysis

Eugen-Maximilian STANGL[1], Julia DONNERER[1]

[1]Institute of Fundamentals and Theory in Electrical Engineering (IGTE),
Graz University of Technology, Inffeldgasse 18/I, 8010 Graz, Austria

e.stangl@tugraz.at, julia.donnerer@tugraz.at

Abstract. *Psychoacoustic metrics provide insights into perceived sound quality beyond classical sound pressure level measurements. Implementations of standardized models such as ISO 532-1 (Zwicker loudness), DIN 45692 (sharpness), and ECMA-418 (tonality and the Sottek Hearing Model) are often proprietary or limited to MATLAB environments. This work presents PsyTools, an open-source Python toolbox for standardized psychoacoustic analysis implementing these established hearing models. The toolbox enables analysis of loudness, sharpness, fluctuation strength, roughness, tonality, annoyance, and classical noise metrics such as LAeq and LAmax. A simulated train pass-by example demonstrates the evaluation of noise mitigation effects. PsyTools facilitates reproducible psychoacoustic research and provides an accessible reference implementation for scientific and engineering applications.*

Keywords

Psychoacoustics, Sound Quality, Signal Processing

1. Introduction and Motivation

Psychoacoustic metrics complement objective measurements by incorporating aspects of human perception in the evaluation of sound quality, NVH engineering, and environmental noise [1]. While standards like ISO 532-1 [2] (Zwicker loudness), DIN 45692 [3] (sharpness), and ECMA-418 [4, 5] (tonality and the Sottek hearing model) exist, implementations are largely proprietary or MATLAB-based, which limits reproducibility. However, no fully validated open-source Python implementation covering these standards currently exists. Python is easy to read and use, works well with scientific libraries like NumPy and SciPy, and is widely used in both research and industry. PsyTools addresses this gap by providing an open-source Python toolbox implementing these standards with validated accuracy, making it suitable for scientific applications. Key features include time-dependent analysis of loudness, sharpness, fluctuation strength, roughness, tonality, and annoyance, as well as classical metrics such as LAeq and LAmax.

2. Methods and Implementation

PsyTools requires Python 3.8 or higher and implements standardized psychoacoustic models using NumPy and SciPy with optional MP3 decoding via Librosa. Table 1 shows the core modules. PsyTools accepts WAV and MP3 audio files and 1/3-octave band spectra (28 bands, 25 Hz–12.5 kHz, according to the ISO 532-1 Zwicker convention). Preliminary comparisons showed high numerical agreement between WAV and MP3 inputs for the tested signals; comprehensive validation across diverse signal types is ongoing. Outputs comprise structured CSV files, publication-ready PNG and PDF figures, and structured result dictionaries for further processing.

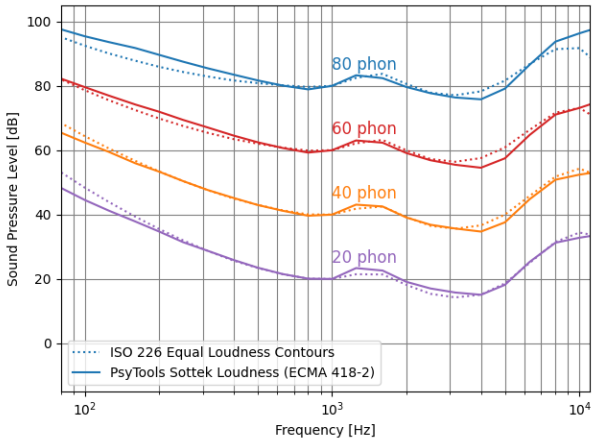

Fig. 1. Calculated equal-loudness-level curves (ISO 226:2023) demonstrating consistency of the Sottek hearing model.

3. Validation and Results

Zwicker loudness (ISO 532-1:2017) was validated against official reference test signals, achieving deviations below 5% and meeting standard accuracy requirements. Sharpness (DIN 45692) passed all normative Annex A test cases with deviations under 0.05 acum. Sottek hearing model metrics (ECMA-418-2) were verified using Appendix B reference signals, including time- and frequency-resolved

Module	Primary Output	Standards/Models
`loudness.py`	Specific/total loudness (sone)	ISO 532-1:2017 [2]
`sharpness.py`	Sharpness (acum)	Zwicker model, DIN 45692 [1, 3]
`fluctuation.py`	Fluctuation strength (vacil)	Zwicker model [1]
`roughness.py`	Roughness (asper)	Zwicker model [1]
`tonality.py`	Tonality (tu), TNR, PR	ECMA-418-1, Aures [4, 6, 7]
`sottek_hearing_model.py`	Loudness/tonality (sone_{SHM}, tu_{SHM})	ECMA-418-2 [5]
`annoyance.py`	Psychoacoustic annoyance	Zwicker, Di et al. [1, 8]
`classical_noise_metrics.py`	LAeq, LAmax, LAn, LAE	IEC 61672, ISO 1996 [9, 10]

Tab. 1. PsyTools core modules and implemented standards

specific tonality as well as equal-loudness-level contours. Calculated curves closely match the normative targets, confirming model accuracy, as shown in Figure 1. Remaining psychoacoustic parameters, for which no standardized validation exists, were cross-checked against synthetic stimuli and established implementations (MATLAB, SQAT [11]), showing high agreement.

Example evaluation A train pass-by was simulated using the SILVARSTAR simulation software [12]. The train speed was 150 km/h. Results were evaluated without and with a noise barrier. Figure 2 shows that the noise barrier reduces

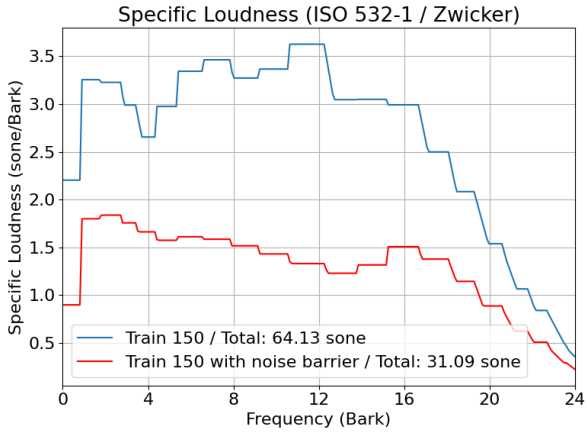

Fig. 2. Specific Zwicker loudness integrated over entire time.

the loudness across all frequencies by approximately half, demonstrating its effectiveness in reducing perceived loudness.

4. Conclusion

PsyTools makes standardized psychoacoustic analysis easy and accessible in Python. Psychoacoustic analysis methods allow more detailed conclusions to be drawn about sound quality and noise impact, as demonstrated by the SILVARSTAR train pass-by example (Fig. 2). The toolbox is suitable for environmental noise studies, NVH optimization, psychophysical hearing experiments, and other research on perceived sound quality. Its modular design allows easy extension for new models and applications and facilitates reproducible psychoacoustic research by providing an accessible reference implementation of standardized hearing models.

Availability `https://gitlab.tugraz.at/11F34386B3DC1474/psytools` [MIT license]

References

[1] Eberhard Zwicker and Hugo Fastl. *Psychoacoustics: Facts and Models*. Springer, Berlin, Heidelberg, 2 edition, 2007.

[2] International Organization for Standardization. Iso 532-1:2017 acoustics – methods for calculating loudness – part 1: Zwicker method. Technical report, International Organization for Standardization, Geneva, 2017.

[3] Deutsches Institut für Normung. Din 45692:2009 acoustics – measurement technique for the simulation of the auditory sensation of sharpness. Technical report, Deutsches Institut für Normung, Berlin, 2009.

[4] ECMA International. Ecma-418-1:2024 prominent discrete tones. Technical report, ECMA International, Geneva, 2024.

[5] ECMA International. Ecma-418-2:2025 methods for describing human perception based on the sottek hearing model. Technical report, ECMA International, Geneva, 2025.

[6] Wolfgang Aures. Berechnungsverfahren für den sensorischen wohlklang. *Acustica*, 59:130–141, 1985.

[7] Ernst Terhardt, Günter Stoll, and Manfred Seewann. Algorithm for extraction of pitch and pitch salience from complex tonal signals. *The Journal of the Acoustical Society of America*, 71(3):679–688, 1982.

[8] Guoqing Di, Xiaowei Chen, Kai Song, Bo Zhou, and Chengmin Pei. Improvement of zwicker's psychoacoustic annoyance model aiming at tonal noises. *Applied Acoustics*, 105:164–170, 2016.

[9] International Electrotechnical Commission. Iec 61672-1:2013 electroacoustics – sound level meters – part 1: Specifications. Technical report, International Electrotechnical Commission, Geneva, 2013.

[10] International Organization for Standardization. Iso 1996-1:2016 acoustics – description, measurement and assessment of environmental noise – part 1: Basic quantities and assessment procedures. Technical report, International Organization for Standardization, Geneva, 2016.

[11] Gil F. Greco, Roberto Merino-Martínez, and Alejandro Osses. Sqat: A matlab-based toolbox for quantitative sound quality analysis. *Applied Acoustics*, 210:109497, 2023.

[12] Empa. Silvarstar vr tools for simulation of train pass-bys. `https://www.empa.ch/web/silvarstar`, 2023. Accessed: 2026-02-26.

LTO Battery Storage Revival: BMS Design Correction and Long-term Validation of 0 V Discharge Resilience

Hanna Hoch[1,2,3]

[1] Chair for Electrochemical Energy Conversion and Storage Systems, Institute for Power Electronics and Electrical Drives (ISEA), RWTH Aachen University, Campus-Boulevard 89, 52074 Aachen, Germany
[2] Center for Ageing, Reliability and Lifetime Prediction of Electrochemical and Power Electronic Systems (CARL), RWTH Aachen University, Campus-Boulevard 89, 52074 Aachen, Germany
[3] Juelich Aachen Research Alliance, JARA-Energy, Germany

hanna.hoch@isea.rwth-aachen.de, batteries@isea.rwth-aachen.de

Abstract. *This paper presents a comprehensive failure analysis and successful recommissioning of a 193 kWh / 565 kW grid storage system utilizing 320 Ah Lithium-Titanate Oxide (LTO) cells. The system remained inactive and deeply discharged to 0 V for over one year. This study investigates the underlying communication architecture and identifies specific design flaws within the Battery Management System (BMS) that led to total system unavailability. Detailed repair procedures are documented, alongside a technical justification for the inherent tolerance of LTO chemistry to deep discharge cycles. This resilience is validated through longitudinal operating data collected over several years of subsequent service. By comparing nominal performance with post-revival data, this work demonstrates that extreme deep discharge does not necessarily compromise LTO cell longevity, providing critical insights for the maintenance and lifecycle management of high-power energy storage assets.*

Keywords

Lithium-Titanate ($Li_4Ti_5O_{12}$) (LTO), batteries, battery grid storage, battery storage system, deep discharge, Controller Area Network (CAN), Failure Analysis, Data Acquisition, Recommissioning.

1. Introduction

1.1. The M5BAT Modular Storage System

The Modular Multi-Megawatt Multi-Technology Medium Voltage - Battery Storage System (M5BAT) at RWTH Aachen University is a large-scale hybrid energy storage system with a power rating of $5.8\,\mathrm{MW}$ and a capacity of $5.6\,\mathrm{MWh}$. The facility was designed to evaluate the interaction, aging, and marketability of diverse battery chemistries within a single grid-connected asset [1]. The project's nomenclature, "M5BAT," reflects its core technical parameters: the five distinct initial battery technologies, its $5\,\mathrm{MW}$ power class, and its $5\,\mathrm{MWh}$ energy capacity.

The primary research objective is to analyze the reliability and lifecycle of varying storage technologies while optimizing auxiliary systems, including battery management system (BMS) architectures, thermal management, and safety protocols [1]. Originally, the system integrated five technologies: vented lead-acid (VLA), valve-regulated lead-acid (VRLA), lithium manganese oxide (LMO), lithium iron phosphate (LFP), and lithium titanate (LTO) [2].

In this hybrid configuration, the lithium-ion strings provide high-power, short-term frequency regulation, while the lead-acid units were historically utilized for medium-duration storage applications [1]. Reflecting the facility's modular and interchangeable design, the lead-acid strings were decommissioned in 2025 to facilitate the integration of next-generation storage technologies. This flexibility allows for the long-term comparative study of specific chemistries, such as the LTO system investigated in this work, under realistic grid-trading conditions.

1.2. Development and Procurement History

Fig. 1. Inside view of the LTO container

The LTO storage system is housed in a standard 20' High Cube container and serves as a core high-power component of the M5BAT facility. The procurement process began with a public tender on February 18, 2016, and the contract was awarded to Microvast in May of the same year [3]. Although physical delivery was completed by June 2017, the commissioning phase revealed significant technical discrepancies that prevented full integration into the M5BAT control architecture.

Documented shortcomings included critical failures in the communication interface with the central controller, thermal management malfunctions within the HVAC system, and a series of documented errors in the provided signal lists and operating parameters [3]. Despite multiple attempts at remediation, the manufacturer was unable to resolve these interoperability issues. Consequently, the procurement contract was legally rescinded; however, through a settlement agreement, the container remained at the RWTH Aachen site [3]. This left the system in a non-operational state, providing the unique opportunity for the independent reverse engineering and restoration efforts described in Section 2.

1.3. Deep Discharge and Cell Voltage Distribution

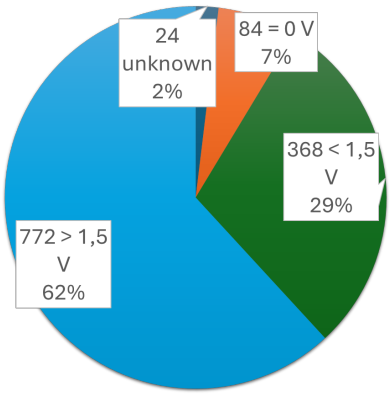

Fig. 2. distribution of cell voltages before manual recharge

Following the initial delivery in 2017 [3], the LTO system remained in a non-operational state for approximately three years pending legal and administrative clearance. Upon gaining access to the system in 2020, a comprehensive voltage survey revealed a significant degradation in the state of charge across the container. Out of 1,248 logical cell units, 476 were found in a severe undervoltage state, with a substantial portion of these measured at 0 V [4]. The distribution of these cell voltages is visualized in the pie chart in Fig. 2.

Several factors likely contributed to this extreme voltage excursion. Potential causes include unsuccessful remediation attempts by the manufacturer, software-level balancing errors, or accelerated self-discharge. A primary technical suspect is the quiescent current consumption of the LECU monitoring hardware. The integrated circuit utilized for cell supervision, the LTC6803, is powered directly from the battery cells rather than an external grid-isolated supply. This architecture allows the monitoring electronics to continuously drain the cells even during system standby, eventually depleting them till the critical 0 V threshold.

1.4. LTO Performance and Low-Voltage Characteristics

The use of $Li_4Ti_5O_{12}$ as an anode material provides several decisive advantages for grid-scale storage. As a "zero-strain" material, $Li_4Ti_5O_{12}$ undergoes negligible volumetric changes during lithiation and delithiation, ensuring high structural stability and an extended cycle life. Crucially, the high operating potential of $Li_4Ti_5O_{12}$ prevents the formation of lithium dendrites during charging, significantly mitigating the risk of separator penetration and subsequent internal short circuits [5]. While providing enhanced safety and thermal stability, $Li_4Ti_5O_{12}$ is also characterized by its non-toxic nature.

However, these benefits come at the cost of energy density. The theoretical specific capacity of $Li_4Ti_5O_{12}$ is typically cited as $175\,\mathrm{mAh/g}$, following the intercalation mechanism described in Eq. 1. This is considerably lower than the $372\,\mathrm{mAh/g}$ offered by conventional graphite anodes [5].

$$Li_4Ti_5O_{12} + 3e^- + 3Li^+ = Li_7Ti_5O_{12} \tag{1}$$

Alternative models suggest higher capacities are achievable at extreme discharge levels. Ge et al. [5] proposed that basing the number of mobile lithium ions on the titanium ion count yields a potential capacity of $293\,\mathrm{mAh/g}$ when operating between $0.01\,\mathrm{V}$ and $2.5\,\mathrm{V}$. While voltages below $1\,\mathrm{V}$ typically risk the decomposition of the electrolyte and the formation of a Solid Electrolyte Interface (SEI) layer, experimental data has shown that LTO can provide a significant capacity contribution near zero voltage with reversible characteristics exceeding the standard theoretical limit [5].

The specific cells investigated in this study are Microvast "LpTO" pouch cells, configured in 12S8P (twelve series, eight parallel) packs. These cells likely utilize a chemistry similar to those analyzed by Tong et al. [6], featuring a $Li_4Ti_5O_{12}$ surface enriched with an inert protective layer paired with a NiCoMnOx (NMC) cathode. The system operates at a nominal voltage of $2.3\,\mathrm{V}$, with standard charge and discharge cut-off limits set at $2.8\,\mathrm{V}$ and $1.5\,\mathrm{V}$, respectively.

2. System Analysis and Protocol Reverse Engineering

Due to the total failure of the proprietary communication interface with the external control center, a comprehensive analysis of the internal container network was required. This involved the reverse engineering of internal communication protocols to decode the status and control signals of the LTO storage system.

Based on these findings, a custom signal converter was developed and implemented. This gateway facilitated the seamless integration of the battery storage system into our local control center, enabling real-time monitoring and active power management of the previously inaccessible hardware.

2.1. System Architecture and Control Hierarchy

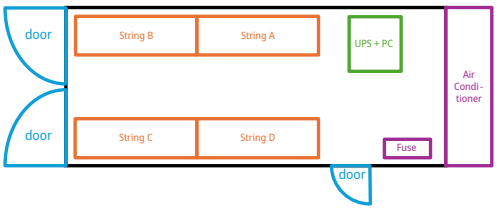

Fig. 3. Container Layout

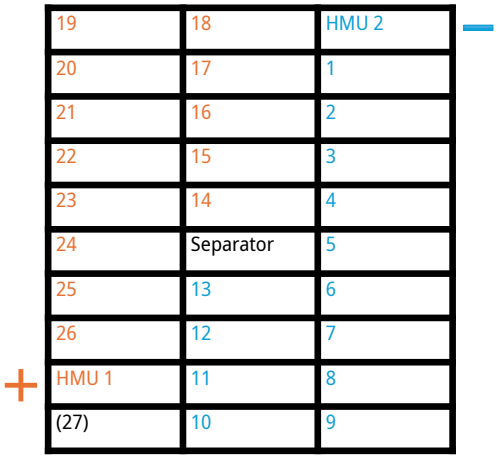

Fig. 4. String Layout

The LTO storage system is based on a hierarchical configuration of 312 series-connected units (312S). Each unit consists of four parallel-connected strings (4P), where each string element is itself a battery pack composed of eight individual pouch cells in a permanent parallel arrangement. Consequently, while the system physically contains 9,984 individual cells, the LECU monitors each 8-cell parallel group as a single logical entity. This hard-parallel configuration ensures voltage equalization across the eight cells, though it precludes the detection of internal resistance deviations or degradation within individual cells of the group.

The physical layout within the container is organized into four distinct strings, labeled A through D (see Fig. 3). Each string is further subdivided into 26 battery packs (see Fig. 4), each equipped with a dedicated Local Electrical Control Unit (LECU) for individual cell voltage monitoring.

Data aggregation follows a hierarchical topology: groups of 13 LECU modules (comprising half a string) are managed by a single High voltage Management control Unit (HMU), which monitors the segment's current. At the string level, a Battery Management Unit (BMU) evaluates local data and transmits only the extrema (minimum and maximum values) to the centralized Battery Control and Monitoring Unit (BCMU). While this hierarchical approach reduces bus traffic, it inherently limits the granularity of remote diagnostics, as individual cell performance data is inaccessible once condensed at the BMU level. This BCMU serves as the primary controller for the entire container, processing these aggregated data streams to manage system-wide operations.

Final data telemetry is transmitted to the external control center via a CAN-to-Modbus gateway. Internal communication across all hierarchy levels is facilitated by several independent Controller Area Network (CAN) buses. The primary control cabinet houses the BCMU, a Uninterruptible Power Supply (UPS) for backup power, and a Panel PC for local HMI visualization. The complete control and communication topology is illustrated in Fig. 5.

2.2. Data Acquisition and Interface Implementation

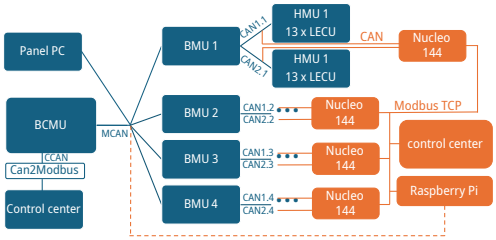

Fig. 5. Communication Structure (blue) with Implemented Additions (orange)

To overcome the diagnostic limitations of the original hierarchy, the internal CAN protocols were reverse-engineered to gain direct access to individual cell-level telemetry. To achieve this, STM32 Nucleo-144 development boards were integrated into the system architecture as high-performance CAN-to-Modbus TCP gateways.

By interfacing directly with the lower-level CAN buses, these converters bypass the superior BMU and BCMU layers, which previously filtered the data. This modification ensures full transparency, allowing the retrieval of all individ-

ual cell voltages rather than just string extrema. The Nucleo-144 boards facilitate a direct communication link with the control center via Modbus TCP, providing a high-granularity data stream for real-time monitoring and historical logging. This parallel monitoring topology, highlighted in orange in Fig. 5, allows for precise cell-balancing analysis and early detection of degradation without interfering with the original safety-critical control loops.

3. Results and Operational Validation

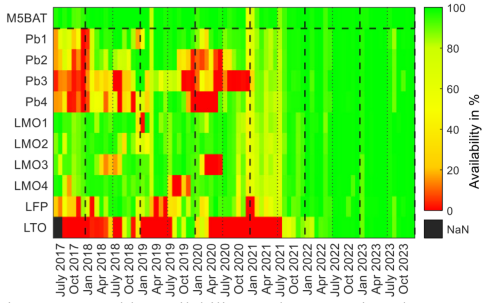

Fig. 6. Monthly operational availability of the M5BAT facility and its individual battery strings. The end of 2021 increase in availability marks the successful restoration of the LTO unit following the resolution of communication and deep-discharge issues. Reproduced from [7].

Following the manual recharge of the deeply discharged LTO modules, the LECU network resumed data transmission, facilitating a detailed post-mortem analysis. The investigation revealed a critical systemic failure loop: the LECU monitoring chips—which require a minimum operating voltage of $10\,\mathrm{V}$—are powered directly by the battery cells they oversee.

When the system initially reached a low-voltage state, the monitoring hardware lost power and ceased communication. Consequently, the high-level safety systems, detecting a loss of telemetry, entered a permanent lockout state that prevented any charging of the battery string. This created a failure loop where the battery could not be recharged, yet the LECU hardware continued to act as a parasitic load. Over a period of one year, this continuous draw provided ample time for the monitoring electronics to exhaust the remaining energy, eventually driving the cells to a deep discharge state of close to $0\,\mathrm{V}$.

To prevent a recurrence, new software-defined discharge limits were implemented at the control center level. Furthermore, the system's reliability was improved by simplifying the communication hierarchy; reducing the number of protocol conversion layers significantly decreased the probability of communication timeouts and bus collisions. Following these interventions, the LTO container was successfully commissioned into full operation in Spring 2022 (see Fig. 6).

Since its restoration, the system has been actively participating in electricity grid trading, with its high-resolution data contributing to an extensive body of research [8, 9, 10, 11, 12, 13, 14, 7, 15]. By April 2023, the system had completed over 85 equivalent full cycles (EFC) [16].

Current operational challenges focus on inter-pack balancing. While the LECU modules can balance individual cells within a pack, the lack of an automated global balancing strategy across the 26 packs leads to significant voltage divergence. These imbalances prematurely trigger system cut-offs and reduce usable capacity. As demonstrated in [14], the usable capacity had diminished to $62.4\,\%$ by September 2023, but was subsequently restored to $90.7\,\%$ through manual string balancing. This high state-of-health (SoH) after eighteen months of high-power operation—preceded by a year-long deep discharge—underscores the exceptional durability and $0\,\mathrm{V}$ resilience of LTO chemistry.

4. Future Work

To maintain high system capacity without manual intervention, an automated inter-pack balancing strategy must be developed. Future research will focus on two potential implementation pathways. First, a comprehensive protocol analysis will be conducted to identify any undocumented CAN commands that may allow for the remote triggering of LECU balancing routines via the supervisory controller.

If such functionality is non-existent within the proprietary protocol, a more radical approach involving the firmware restructuring of all 104 LECU modules may be required. Successfully automating this process is critical for maximizing the long-term energy density and operational availability of the LTO grid storage system.

Acknowledgements

Research described in the paper was supervised by Alexander Blömeke and Lucas Koltermann under Prof. Dr. rer. nat. Dirk Uwe Sauer.

References

[1] MEYER, D.F., Modularer Batterie speicher liefert Regelenergie Technik und Geschäftsmodelle großer Batteriespeicher für das Stromnetz im Feldtest, *BINE Informationsdienst*, 2017, vol. Projektinfo 12/2017, no. Energieforschung konkret.

[2] KOLTERMANN, L., 5 MW multi-technology battery storage systems for grid services, 2020.

[3] MÜNDERLEIN, J., MERTEN, M., STOREK, T., STEIN, D., Vorhabenbezeichnung: Modularer multi-Megawatt multi-Technologie Mittelspannungsbatteriespeicher (M5BAT) : Abschlussbericht : Berichtszeitraum: 01.07.2013-31.12.2018, Tech. Rep., Rheinisch-Westfälische Technische Hochschule Aachen, 2019, artwork Size: 1 Online-Ressource (106 Seiten, 7,37 MB) Medium:

application/pdf Version Number: 1.0.

[4] HOCH, H., *Battery Management System for Data Logging of a High-Power Home Storage*, Master's thesis, RWTH Aachen University, Aachen, 2021.

[5] ZHAO, B., RAN, R., LIU, M., SHAO, Z., A comprehensive review of Li4Ti5O12-based electrodes for lithium-ion batteries: The latest advancements and future perspectives, *Materials Science and Engineering: R: Reports*, 2015, vol. 98, pp. 1–71.

[6] TONG, T., GROESBECK, C., 10 Minute Lto Ultrafast Charge Public Transit Ev Bus Fleet Operational Data - Analysis of 240,000 km, 6 Bus Fleet Shows Viable Solution, *World Electric Vehicle Journal*, 2012, vol. 5, no. 1, pp. 261–268.

[7] KOLTERMANN, L., CELI CORTÉS, M., VAN OUWERKERK, J., SAUER, D.U., Lessons learned from operating a large-scale battery storage system – challenges and improvements, *IET Conference Proceedings*, 2025, vol. 2024, no. 16, pp. 16–24.

[8] THIEN, T., AXELSEN, H., MERTEN, M., SAUER, D.U., Energy management of stationary hybrid battery energy storage systems using the example of a real-world 5 MW hybrid battery storage project in Germany, *Journal of Energy Storage*, 2022, vol. 51, p. 104257.

[9] KOLTERMANN, L., CELI CORTÉS, M., FIGGENER, J., ZURMÜHLEN, S., SAUER, D.U., Power curves of megawatt-scale battery storage technologies for frequency regulation and energy trading, *Applied Energy*, 2023, vol. 347, p. 121428.

[10] MA, Z., JIA, M., KOLTERMANN, L., BLÖMEKE, A., DE DONCKER, R.W., LI, W., SAUER, D.U., Review on grid-tied modular battery energy storage systems: Configuration classifications, control advances, and performance evaluations, *Journal of Energy Storage*, 2023, vol. 74, p. 109272.

[11] KOLTERMANN, L., CELI CORTÉS, M., FIGGENER, J., ZURMÜHLEN, S., SAUER, D.U., Improved rule-based power distribution algorithm for hybrid battery storage systems and real-world validation, *Journal of Energy Storage*, 2024, vol. 86, p. 111360.

[12] CORTÉS, M.C., NSIR, N., KOLTERMANN, L., ZURMÜHLEN, S., VAN OUWERKERK, J., UWE SAUER, D., M5Use: An Optimization Framework for the Multi-Use Operation Scheduling of Large-Scale Battery Storage Systems, *2024 IEEE PES Innovative Smart Grid Technologies Europe (ISGT EUROPE)*, IEEE, Dubrovnik, Croatia, 2024 pp. 1–5.

[13] KOLTERMANN, L., CORTÉS, M.C., ZURMÜHLEN, S., SAUER, D.U., Energy Management of Large-Scale Battery Storage Systems: Field Evaluation of Battery Aging and System Efficiency, *2024 IEEE PES Innovative Smart Grid Technologies Europe (ISGT EUROPE)*, IEEE, Dubrovnik, Croatia, 2024 pp. 1–5.

[14] KOLTERMANN, L., CORTÉS, M.C., ZURMÜHLEN, S., JUNKER, M., SAUER, D.U., Limitations of cell imbalances on the operation of a large-scale battery storage system: example LTO batteries, *IET Conference Proceedings*, 2025, vol. 2024, no. 16, pp. 815–820.

[15] CORTÉS, M.C., DANIEL DANG, T., SCHWARZ, P., KOLTERMANN, L., SAUER, D.U., Simulative Analysis of the Operation of Large-Scale Battery Storage Systems in the Frequency Containment Reserve Market, *2025 IEEE PES Innovative Smart Grid Technologies Conference Europe (ISGT Europe)*, IEEE, Valletta, Malta, 2025 pp. 1–5.

[16] KOLTERMANN, L., CELI CORTÉS, M.E., ZURMÜHLEN, S., VAN OUWERKERK, J., SAUER, D.U., M5BAT Large-Scale Battery Storage System Dataset: Evaluation Operation Report 04/2023; V1, 2024.

About Authors...

Hanna HOCH was born in Dortmund. After her Abitur in the area of Münster she studied electrical engineering in Aachen. She finished her Master thesis at the ISEA RWTH Aachen about the presented topic in April 2021 and continued working there as a research associate and doctoral student. Her research focuses mainly on test automation and battery characterization.

Deciphering Relaxation Time Distributions in Prussian Blue-based Sodium-Ion Batteries

Roman MOROZOV[1,2], Tom PÖHLMANN[1,2]

[1]Junior Professorship for Artificial Intelligence and Digitalization for Batteries, Institute for Power Electronics and Electrical Drives (ISEA), RWTH Aachen University, Campus-Boulevard 89, 52074 Aachen, Germany
[2]Center for Ageing, Reliability and Lifetime Prediction of Electrochemical and Power Electronics Systems (CARL), RWTH Aachen University, Campus-Boulevard 89, 52074 Aachen, Germany

roman.morozov@isea.rwth-aachen.de, tom.poehlmann@rwth-aachen.de, batteries@isea.rwth-aachen.de

Abstract. *Sodium-ion (Na-ion) batteries utilizing Prussian Blue Analogue (PBA) electrodes present a sustainable, high-longevity alternative to lithium-ion (Li-ion) systems. For applications precise electrical performance modeling is required. While Electrochemical Impedance Spectroscopy (EIS) is essential for capturing dynamic cell behavior, it traditionally suffers from poor interpretability due to overlapping electrochemical processes. This study applies the Distribution of Relaxation Times (DRT) method with robust Generalized Cross-Validation (rGCV) to a PBA-based cell to deconvolute the charge-transfer kinetics. Results demonstrate that charge transfer resistance is the primary performance bottleneck when the battery is fully charged or discharged and during sub-zero temperatures. Conversely, under moderate operational conditions, charge transfer kinetics become facile, and performance is governed by SEI and mass-transport resistances. These decoupled phenomenological insights provide a critical foundation for advanced BMS modeling, state estimation, and aging diagnostics.*

Keywords

Sodium-ion battery, prussian blue, electrochemical impedance spectroscopy, distribution of relaxation times, charge-transfer kinetics.

1. Introduction

Sodium-ion (Na-ion) batteries are emerging as a promising alternative to lithium-ion (Li-ion) systems. By relying on abundant raw materials, they bypass the supply chain and ecological issues of lithium while offering higher power densities. [1]

The electrochemical performance of Na-ion batteries is fundamentally dictated by their electrode chemistry. These materials are generally grouped into three established categories: layered oxides, Prussian Blue Analogues (PBAs), and polyanionic compounds. While layered oxides frequently rely on critical elements like nickel, and polyanionic frameworks often incorporate problematic transition metals such as vanadium, PBAs are synthesized from abundant, non-critical materials. Although this favorable ecological and economic footprint comes at the expense of comparatively lower energy density, PBA electrodes exhibit an exceptionally high cyclic lifetime, making them highly attractive for longevity-focused energy storage applications. [1]

To effectively deploy these battery cells in practical applications, a fully functional Battery Management System (BMS) is essential. The foundation of such a system relies heavily on accurate electrical performance modeling [2]. To capture the dynamic performance and resistive behavior necessary for this modeling, Electrochemical Impedance Spectroscopy (EIS) serves as an indispensable, non-invasive characterization technique [3].

However, traditional EIS analysis often suffers from limited interpretability, as overlapping electrochemical processes obscure the distinct impedance responses, making it difficult to extract phenomenological insights [4]. To overcome this limitation, the Distribution of Relaxation Times (DRT) method is employed to deconvolute the impedance spectrum. Consequently, this work aims to investigate the presented PBA-based Na-ion cell through comprehensive EIS and subsequent DRT analysis. By elucidating the electrochemical processes, this study lays the essential groundwork for future electrical performance modeling, which will ultimately inform robust state estimation and aging diagnostics.

2. Fundamentals

2.1. Electrical Impedance Spectroscopy (EIS)

EIS operates by applying a small-amplitude alternating current (AC) perturbation to the battery cell and measuring the corresponding voltage response across a spectrum of frequencies, states of charge (SOC) and ambient temperatures (see Fig. 1). While this galvanostatic approach (current

perturbation) is standard, the inverse potentiostatic method (voltage perturbation with current measurement) is equally viable. [4]

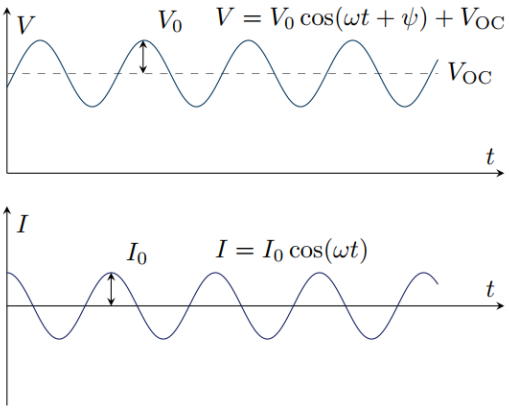

Fig. 1. The working principle of the EIS [4].

Superimposed on the open-circuit voltage V_{OC}, the impedance $Z(j\omega)$ represents the system's resistance to the AC, defined by the ratio of the voltage response's amplitude and phase shift ψ to the excitation current:

$$Z(j\omega) = \frac{V_0 cos(\omega t + \psi) + V_{OC}}{I_0 cos(\omega t)} \quad (1)$$

The resulting frequency-domain data is classically visualized using a Nyquist plot (see Fig. 2). The real part of the impedance is plotted on the x-axis, and the negative imaginary part is plotted on the y-axis. Notably, the frequency sweeps inversely across the plot, increasing from right to left. [4]

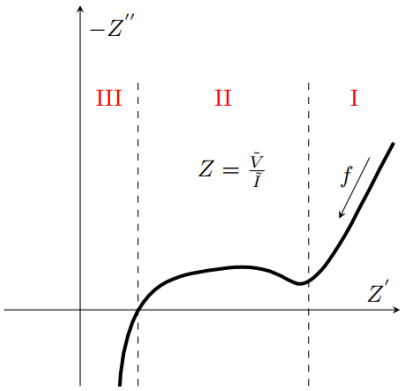

Fig. 2. A typical Nyquist plot, inherited from EIS of a Li-ion battery [4].

Phenomenologically, the Nyquist spectrum of a typical battery cell can be segmented into three distinct frequency regions:

I. **Low-Frequency**: Dominated by solid-state diffusion within the active materials, this region appears as a sloped line, often referred to as the Warburg diffusion tail.

II. **Middle-Frequency**: Manifesting as one or more depressed semicircles, this region captures the electrochemical kinetics, including charge transfer processes and SEI properties.

III. **High-Frequency**: Appearing as an inductive tail below the real axis, this region primarily reflects the stray inductance of the cell geometry and measurement equipment.

The local minimum that bridges the middle and low-frequency regions serves as a critical transition point, delineating the shift from kinetic-dominated processes to mass transport phenomena. [4]

2.2. Distribution of Relaxation Times (DRT)

While the Nyquist plot provides a macroscopic view of the cell's impedance, distinguishing overlapping electrochemical processes, particularly the kinetic and interfacial phenomena located in region II, requires translating the frequency-domain data into the time-constant domain. This transformation is achieved through the DRT method [5].

The DRT approach classically models the polarization behavior of the battery as an infinite series configuration of infinitesimal, parallel Resistor-Capacitor (RC) elements:

$$Z(j\omega) = j\omega L_0 + R_{Ohm} + \int_0^{\inf} \frac{G(\tau)}{1 + j\omega\tau} dln\tau \quad (2)$$

Here, L_0 represents the stray inductance, R_{Ohm} denotes the pure ohmic resistance, and $G(\tau)$ represents the relaxation time distribution function. To solve this continuous integral numerically, the equation must be discretized [4]. By substituting the continuous relaxation constant with a logarithmic distribution function $P(t)$, where $t = \log_{10}(\tau)$, the integral is transformed into a discrete summation:

$$Z(j\omega) \approx j\omega L_0 + R_{Ohm} + \sum_{j=1}^{N_t} \frac{P(t_j)\Delta t}{1 + j\omega 10^{t_j}} \quad (3)$$

Determining the distribution P_{opt} from the experimental impedance data ($\mathbf{Z}_{\text{exp}}$) requires a numerical inversion. However, this deconvolution is a fundamentally ill-posed mathematical problem; minor experimental noise in the EIS measurement can trigger massive, non-physical oscillations in the calculated distribution.To stabilize the solution, the inversion is framed as a penalized linear least-squares optimization problem based on Tikhonov regularization [6]:

$$P_{opt} = \underset{x \geqslant 0}{\operatorname{argmin}} \left(\|\mathbf{A}x - \mathbf{Z}_{\exp}\|^2 + \lambda \|\mathbf{K}x\|^2 \right) \tag{4}$$

In this equation, $\mathbf{A}$ is the design matrix representing the RC model elements, x is the distribution vector to be solved (constrained to non-negative values, $x \geqslant 0$, as negative resistances lack physical meaning here), and λ is the regularization parameter governing the trade-off between data fidelity and solution smoothness.Because neighboring time constants in physical electrochemical systems exhibit strong correlation, the regularizing Tikhonov matrix $\mathbf{K}$ is typically defined as a discrete second-order derivative operator:

$$\mathbf{K} = \begin{bmatrix} 1 & -2 & 1 & 0 & \dots \\ 0 & 1 & -2 & 1 & \dots \\ \vdots & \vdots & \vdots & \vdots & \ddots \end{bmatrix} \tag{5}$$

This matrix structure penalizes strong curvature in the solution vector. By suppressing erratic oscillations, it forces the algorithm to return a smooth, physically plausible distribution. Once computed, each individual peak in the DRT corresponds to a distinct electrochemical relaxation process (e.g., solid-state diffusion, solid-electrolyte interphase (SEI) and cathode-electrolyte interphase (CEI) formation) [5]. The peak's position on the logarithmic timescale (x-axis) identifies the characteristic time constant of the underlying physical mechanism, while the integrated area under the peak is directly proportional to its associated polarization resistance contribution.

3. Material and Methodology

3.1. Investigated Cell

The cell under investigation was extracted from the module BlueTray™ 4000, made by U.S.-based Natron Energy. Before the measurements, it was exposed to one year of calendrical ageing at room temperature due to shipping and storing in-between.

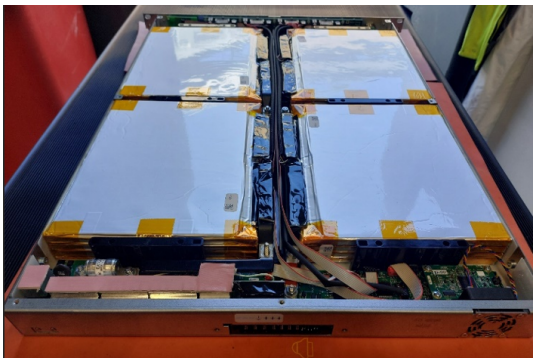

Fig. 3. Disassembly of the BlueTray™ 4000 module.

In contrast to currently commercially available PBA-based batteries, where the negative electrode is typically made from hard or soft carbon, both electrodes are based on similar PBAs, which differ in the transition metal that forms the second active redox centre. The positive electrode material is based on sodium manganese hexacyanoferrate, also called prussian white, and the anode on sodium manganese hexacyanomanganate. [7]

Parameter	Value
Nominal capacity	4.6 Ah
Nominal voltage	1.56 V
Voltage range	1.05–1.85 V
Positive electrode material	$Na_xMn_y[Fe(CN_6)])$
Negative electrode material	$Na_xMn_y[Mn(CN_6)])$

Tab. 1. Natron Energy V6.1 cell parameters [7].

3.2. EIS Analysis

Building upon the fundamental principles of EIS, the investigated cells were stimulated using a quasi-galvanostatic approach. In this configuration, the amplitude of the alternating excitation current is dynamically adjusted by the system to ensure a constant, specified voltage deflection of 10 mV. The complete measurement settings are summarized in table 2.

Parameter	Value
Measurement device	Safion Inspectrum EISmeter
EIS method	quasi-galvanostatic
Voltage amplitude	10 mV
Frequency range	0.01 Hz–10 kHz
Frequencies per decade	48
Periodes per frequency	4

Tab. 2. EIS measurement settings.

Evaluating the temperature dependence, a clear trend emerges: as the ambient temperature decreases, the half-arcs located in the middle-frequency range shift significantly upwards and to the right. This shift is accompanied by a marked increase in the purely ohmic resistance, R_{Ohm}, visible as the high-frequency intercept shifting along the real axis. At higher temperatures, the accelerated electrochemical kinetics cause the distinct processes to merge, resulting in a single dominant semicircle.

The SOC dependence further influences the impedance signature. In the middle SOC ranges, the overall impedance is strongly compressed. However, at the SOC boundary regions (near fully charged or fully discharged states) and particularly at low temperatures, the middle-frequency region elongates to reveal two distinct, superimposed semicircles. This structural grouping indicates that the discrete time constants of the underlying electrochemical processes only sep-

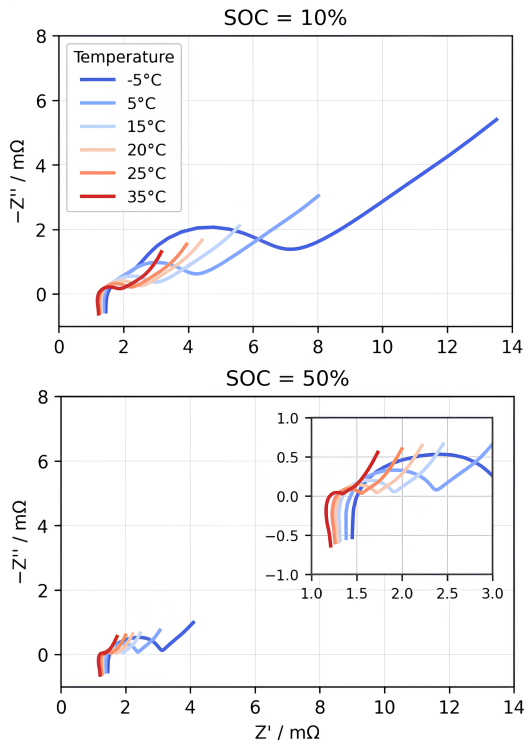

Fig. 4. Nyquist plots at fixed SOCs.

arate enough to become visually distinguishable under specific operational extremes.

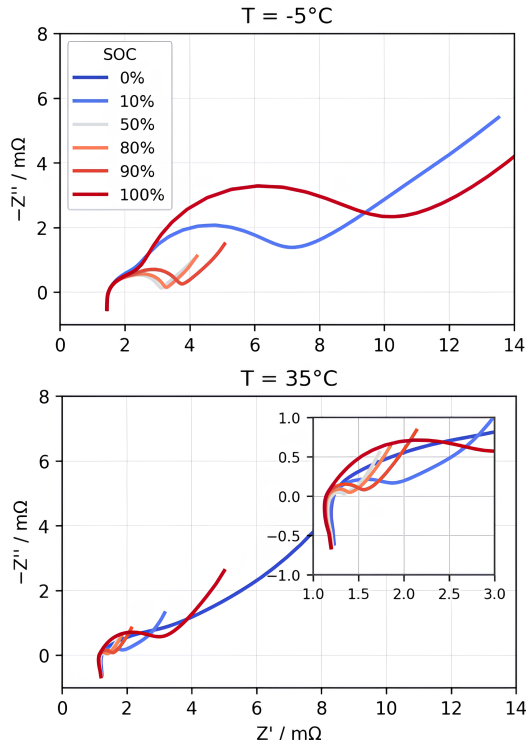

Fig. 5. Nyquist plots at fixed ambient temperatures.

3.3. Regularisation DRT Transformation

To avoid subjective bias from manual tuning, this work employs an automated selection process for λ based on robust Generalized Cross-Validation (rGCV), aligning with current literature recommendations [6]. The foundation of this automated selection is the standard Generalized Cross-Validation (GCV) function, which minimizes the predictive mean squared error. It is defined mathematically as:

$$GCV(\lambda) = \frac{\left(\frac{rss(\lambda)}{m}\right)}{\left(1 - \frac{df(\lambda)}{m}\right)^2} \quad \text{with} \quad df(\lambda) = \text{trace}(H_\lambda) \tag{6}$$

In this formulation, $rss(\lambda)$ represents the residual sum of squares (the residual error between the modeled and experimental impedance), m denotes the total number of experimental data points, and $df(\lambda)$ signifies the effective degrees of freedom, which is calculated from the trace of the influence matrix H_λ.

$$rGCV(\lambda) = (\xi + (1 - \xi)\mu_2(\lambda))GCV(\lambda) \tag{7}$$

The rGCV method modifies the standard equation by introducing an additional robustness parameter $\mu_2(\lambda)$. This extended formulation specifically reduces the strong algorithmic punishment that standard GCV naturally applies to highly smooth solutions. By intentionally shifting the penalty to favor stronger smoothing, the rGCV method prevents overfitting to experimental measurement noise, ultimately guaranteeing a significantly more robust, stable, and physically reliable DRT spectrum. [6]

4. Results and Discussion

Applying the DRT method to the given EIS data yields additional insights, though the separation of the two electrodes is not entirely straightforward. Because both they share a similar PBA-based chemical composition, the assignment of specific peaks to either the anode or the cathode remains subject to a degree of reservation.

The stability and resolution of the DRT deconvolution are strongly tied to the evaluated parameter set. The algorithm provides easily interpretable solutions at low temperatures and extreme SOCs (e.g., 5% and 100% SOC). Under these conditions, the EIS data exhibit pronounced capacitive semicircles, and the underlying relaxation processes are distinctly distributed across the high, medium, and low-frequency ranges.

Conversely, in the medium SOC range, the overall impedance is significantly reduced and compressed. Although the sampling step size during the EIS measurement

is extraordinarly fine, the spectral information within these mid-range frequencies is highly condensed. Consequently, superimposed relaxations with low amplitudes become extremely difficult to separate.

The peaks emerging in the high-frequency region primarily reflect the migration of sodium ions through the SEI and CEI, alongside the contact resistance between the active materials and the current collectors. A defining characteristic of this region is its independence from the SOC; the high-frequency peaks exhibit remarkably similar profiles at both 5% and 40% SOC. However, as a physical barrier, this resistance is heavily dependent on temperature. As the cell warms up, these peaks visibly shift to the right (towards higher frequencies), reflecting the thermally activated nature of the ion migration.

The mid-frequency region captures the most dynamic and critical processes: the charge transfer kinetics and double-layer capacitance. This represents the actual electrochemical process: the desolvation of the sodium ion from the liquid electrolyte and its subsequent insertion into the solid electrode lattice. Because charge transfer is fundamentally a chemical reaction, it is governed by Arrhenius behavior. At cold temperatures (e.g., -5 °C), the reaction is highly sluggish, resulting in massive resistance peaks. As the temperature increases to 35 °C, the reaction kinetics accelerate drastically, causing the peaks to shrink in amplitude and shift toward higher frequencies. Furthermore, this region is highly charge-dependent: At 5% SOC, the battery is effectively "starving"; the scarcity of available sodium ions and vacant lattice sites at the reacting interface creates a highly resistive charge transfer process. In contrast, at 40% SOC, the electrodes possess a well-balanced availability of sodium and vacant sites, allowing the interfacial reaction to proceed smoothly with minimal resistance.

The sweeping tails observed at the far-left, low-frequency end of the DRT spectra represent solid-state diffusion (often modeled macroscopically as Warburg impedance). This corresponds to the slow, continuous mass-transport journey of sodium ions diffusing deep into, or out of, the bulk of the solid active material particles. Because diffusion is not a rapid surface reaction but a sustained transport mechanism, it dominates the lowest frequencies. Consequently, within the DRT framework, this process rarely resolves into a neatly closed peak; instead, it manifests as a sharply rising tail as the frequency approaches zero.

In summary, a hierarchy of performance bottlenecks can be established for the investigated cell: the primary limiting factor is the charge transfer resistance, but this bottleneck is conditionally isolated to states of full charge or discharge combined with cold ambient temperatures. Under moderate operational conditions (e.g., 40% SOC and room temperature), the charge transfer kinetics are facile and the SEI/CEI migration and solid-state diffusion resistances become the dominant limiting factors for the cell's dynamic performance.

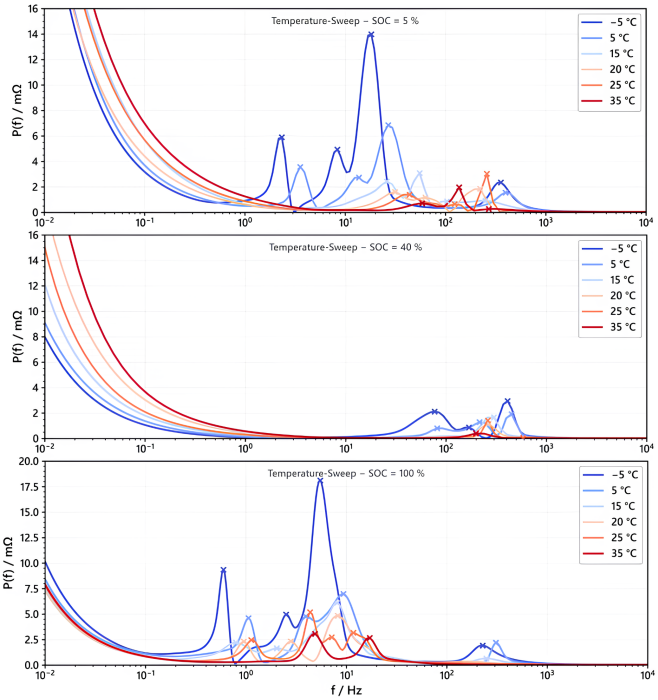

Fig. 6. Relaxation time distribution for the Natron Energy V6.1 cell.

5. Conclusion and Future Work

This study characterized the dynamic electrochemical performance of PBA-based Na-ion cells. By applying a rGCV regularized DRT method to quasi-galvanostatic EIS data, we deconvoluted superimposed relaxation processes. The analysis revealed that charge transfer resistance acts as the primary bottleneck only under severe conditions (e.g., low SOC, sub-zero temperatures). Under moderate conditions, this kinetic limitation vanishes, and overall cell impedance is governed predominantly by solid-state diffusion and interfacial (SEI/CEI) resistances.

Future work will utilize these insights to parameterize Equivalent Circuit Models (ECMs) and Physicochemical Models (PCMs). Translating these physical mechanisms into robust models will directly enable precise state estimation and advanced aging diagnostics, ultimately driving the development of highly predictive and adaptive BMS architectures for Na-ion systems.

Acknowledgements

The author would like to thank Prof. Dr.-Ing. Weihan Li for his supervision of this research. This work was funded by the Federal Ministry for Economic Affairs and Climate Action of Germany through the project EchNaTon (grant number 03EI4075C).

References

[1] XIE, M., WU, F., HUANG, Y., PUBLISHING HOUSE OF ELECTRONICS INDUSTRY, P. H. O. E. *Sodium-Ion Batteries: Advanced Technology and Applications*. De Gruyter STEM. Berlin Boston: De Gruyter, 2022. ISBN 978-3-11-074903-8 978-3-11-074906-9. doi: 10.1515/9783110749069.

[2] PLETT, G. L. *Battery Management Systems: Volume 1: Battery Modeling*. Artech House Power Engineering and Power Electronics. Boston London: Artech House, 2015. ISBN 978-1-63081-023-8 978-1-63081-024-5.

[3] BAKENHASTER, S. T., DEWALD, H. D. Electrochemical Impedance Spectroscopy and Battery Systems: Past Work, Current Research, and Future Opportunities. *Journal of Applied Electrochemistry*, 2025, vol. 55, no. 7, p. 1657–1681.

[4] ZHAO, Y. Parameter Estimation of Lithium-ion Batteries Using Distribution of Relaxation Times.

[5] WANG, Z., WANG, Y., PY, B., MARADESA, A., LIU, J., WAN, T. H., SACCOCCIO, M., CIUCCI, F. DRTtools: Freely Accessible Distribution of Relaxation Times Analysis for Electrochemical Impedance Spectroscopy. *ACS Electrochemistry*, 2025, vol. 1, no. 12, p. 2680–2689.

[6] MARADESA, A., PY, B., WAN, T. H., EFFAT, M. B., CIUCCI, F. Selecting the Regularization Parameter in the Distribution of Relaxation Times. *Journal of The Electrochemical Society*, 2023, vol. 170, no. 3, p. 030502.

[7] HE, M., DAVIS, R., CHARTOUNI, D., JOHNSON, M., ABPLANALP, M., TROENDLE, P., SUETTERLIN, R.-P. Assessment of the First Commercial Prussian Blue Based Sodium-Ion Battery. *Journal of Power Sources*, 2022, vol. 548, p. 232036.

About Authors...

Roman MOROZOV was born in Sankt-Petersburg, Russia. He studied Mechanical Engineering at Technical University Darmstadt, Germany. Currently, he is PhD candidate at the Chair for Electrochemical Energy Conversion and Storage Systems, RWTH Aachen University. His research mainly focuses on modelling the ageing behaviour of sodium-ion battery cells.

Tom PÖHLMANN was born in Kempen, Germany. He is studying Business Administration and Mechanical Engineering at RWTH Aachen University. Currently, he is working as a Student Research Assistant at the Institute for Power Electronics and Electrical Drives, supporting the investigations on sodium-ion battery cell behavior.

Evaluation of Heat Transfer and Mechanical Trade-offs in SLA-Printed Boron Nitride (BN) Composites

Adriana Nováková[1], Ondřej Pražák[1], Jaroslav Pazourek[1]

[1]Dept. of Electrotechnology, Czech Technical University, Technická 2, 166 27 Praha, Czech Republic

novakadr@fel.cvut.cz, prazaon2@fel.cvut.cz, pazoujar@fel.cvut.cz

Abstract. *This study investigates the development and characterization of a thermally conductive composite material designed for stereolithography (SLA) 3D printing. A commercial SLA resin was reinforced with 25 wt% of hexagonal boron nitride (h-BN) micro-particles, homogenized via ultrasonic dispersion to ensure uniform filler distribution. Mechanical testing revealed a performance trade-off in which tensile and flexural strength decreased significantly (by 45% and 9%, respectively), while compressive properties remained largely unaffected, with the compressive modulus showing a marginal increase of 1%. Thermal analysis via infrared thermography demonstrated that the h-BN composite exhibits a significantly accelerated thermal response. Active cooling tests further confirmed the practical benefit of the composite, achieving a 27.4% increase in cooling efficiency compared to the pure resin.*

Keywords

Stereolithography, 3D printing, Boron Nitride, Polymer composites, Thermal conductivity, Cooling, Mechanical properties

1. Introduction

Due to the current trend of electronic miniaturization, thermal management has become an increasingly critical aspect of the manufacturing process. This necessitates the integration of materials with high thermal conductivity, as inadequate heat dissipation can lead to significant component damage or system failure [1].

In this context, the use of plastics produced through 3D printing is becoming increasingly popular in industrial manufacturing. However, a major challenge arises from the fact that the thermal conductivity of most polymers ranges only between 0.1 and 0.5 $\mathrm{W\,m^{-1}\,K^{-1}}$ [2]. Specifically, for the epoxy-based photopolymer resins utilized in Stereolithography, thermal conductivity is typically limited to a narrow range between $0.17\,\mathrm{W\,m^{-1}\,K^{-1}}$ to $0.21\,\mathrm{W\,m^{-1}\,K^{-1}}$ [3].

Thermally conductive polymer composites produced by additive manufacturing are of particular interest for compact electronic systems, including integrated heat sinks, battery housings for small satellites, and structural components requiring simultaneous heat dissipation and electrical insulation [1]. Among the available additive manufacturing techniques, SLA offers key advantages over fused filament fabrication (FFF), as its liquid photopolymer input greatly simplifies the incorporation of ceramic fillers through direct mixing, without the need for filament extrusion [4]. Furthermore, SLA produces parts with high dimensional accuracy and superior surface quality, enabling the fabrication of complex geometries for applications in biomedicine, aerospace and prototyping [5, 6].

Several ceramic fillers have been explored in polymer composites to enhance thermal conductivity, including alumina, silica, and carbon-based materials [1]. Among these, hexagonal boron nitride (h-BN) is an exemplary candidate, offering exceptional in-plane thermal conductivity of up to $420\,\mathrm{W\,m^{-1}\,K^{-1}}$ [7] while remaining electrically insulating — unlike metallic fillers, h-BN prevents electrical short circuits, making it ideal for heat sinks and battery housings in aerospace systems [8].

Beyond thermal management, SLA-printed ceramic-polymer composites have also been investigated for other functional applications, such as piezoelectric sensors and actuators, further demonstrating the versatility of this fabrication approach [9].

While previous studies focused on filler concentrations up to $12.5\,\mathrm{wt\,\%}$ [4], this research pushes the boundary to a $25\,\mathrm{wt\,\%}$ loading. The goal is to maximize the formation of a percolating thermal network within the SLA resin to significantly increase cooling efficiency.

2. Materials and Methods

2.1. Input materials and preparation

The polymer matrix used in this study was a commercial photopolymer resin, specifically Prusament Resin Model Transparent Clear, produced by Prusa Polymers (Czech Republic). The thermal conductive reinforcement consisted of pure hexagonal boron nitride (h-BN) ceramic powders, procured from ZYP Coatings Inc [10].

The composite was prepared using a systematic multi-step process. Homogenization was achieved using an ultrasonic bath for 30 minutes at an elevated temperature of 50°C. This step was essential to ensure uniform dispersion of the ceramic microparticles in the resin.

Additive manufacturing was performed on a Prusa SL1S desktop 3D printer, utilizing Masked Stereolithography (MSLA) technology. Given that the h-BN microparticles interfere with UV light transmission through scat-

tering and absorption, a modified exposure strategy was implemented to ensure complete photo-polymerization.

The layer height was set to $50\,\mu\mathrm{m}$ and the exposure time for the initial layers was increased to 120 s to ensure reliable adhesion to the build platform. This adjustment was necessary because the prepared composite is significantly more viscous than standard resins. Due to this high viscosity, it was also necessary to implement a very slow movement of the build platform.

After printing, samples were washed in IPA, air-dried, and UV-cured for 10 minutes to ensure maximum cross-linking density at the h-BN/polymer interface. The complete workflow, from material preparation to final UV post-curing, is illustrated in Figure1.

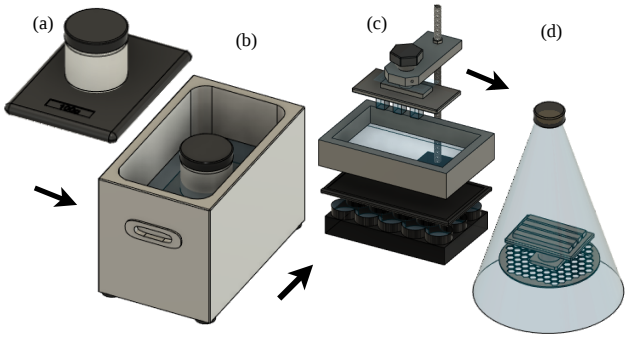

Fig. 1. Schematic of the composite preparation workflow: a) material weighing,b) ultrasonic bath homogenization, c)SLA printing, d)UV post-curing.

2.2. Mechanical testing

Mechanical properties were evaluated using a universal testing machine Testometric X250-3. Tensile testing was performed according to ASTM D638 on dog-bone specimens scaled to 75% of the standard Type IV geometry, with a gauge length of $24.75\,\mathrm{mm}$ and a crosshead speed of $10\,\mathrm{mm\,min^{-1}}$. (Figure 2, 3). Compressive testing was conducted on cylindrical specimens under axial loading. Flexural properties were determined via three-point bending (Figure 4).

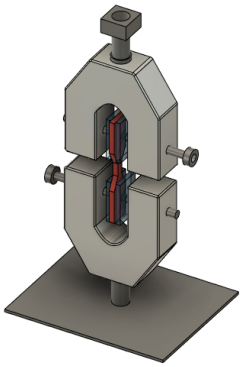

Fig. 2. Universal testing machine configured for tensile testing (clamping detail).

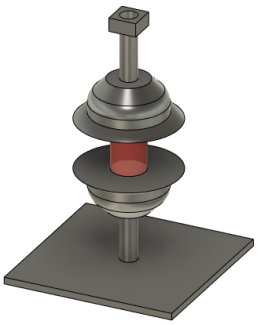

Fig. 3. Axial view of the tensile test setup and load cell interface.

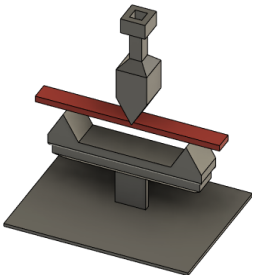

Fig. 4. Three-point bending setup for evaluating flexural strength.

2.3. Analyses of composite structure

Scanning electron microscopy (SEM) was used to evaluate the internal morphology and distribution of ceramic particles in the photopolymer matrix. The analysis was performed using a Phenom ProX instrument (Thermo Fisher Scientific, USA). The investigation focused on the side view of the printed samples. This cross-sectional perspective allowed for detailed observation of the dispersion of h-BN microparticles and their integration into the polymer layers. Such analysis is essential for understanding how the filler distribution correlates with the observed mechanical properties and the formation of thermally conductive pathways.

2.4. Infrared thermography

Since no professional measuring equipment was available to determine absolute thermal diffusivity, a comparative method of transient thermography was developed to evaluate the relative thermal performance of the samples. This approach focused on observing real-time heat propagation from a heat source through the thickness of the samples using a FLIR i7 infrared camera (FLIR Systems, USA).

The samples were prepared as disks with a radius of 20 mm and a thickness of 3 mm. To ensure high data fidelity and eliminate errors resulting from material reflectivity, all samples were treated with a thin, uniform coat of matte black paint. The experiment was conducted by simultaneously placing the samples onto a heating surface preheated at a temperature of 60 °C with a total heating power of 80 W. To minimize interphase thermal resistance (contact resistance) between the heat source and the samples, a thermally conductive paste was applied to the contact surfaces. The top surfaces of the samples (not in direct contact with the heat source) were monitored for a duration of one

minute. This allowed for observation of heat propagation through the thickness of the material and provided a clear comparison of the thermal response between the neat resin and the composite.

2.5. Cooling tests

To verify the practical cooling effectiveness of the composite materials a custom-built experimental apparatus was developed, as illustrated in Fig. 5. The setup consists of two metal parts: a lower heating unit and an upper cooling unit. The heating block integrates two heating elements with a combined power of 80 W (2 x 40 W) and a DS18B20 digital temperature sensor. An identical sensor is installed within the upper cooling block to monitor the heat sink temperature.

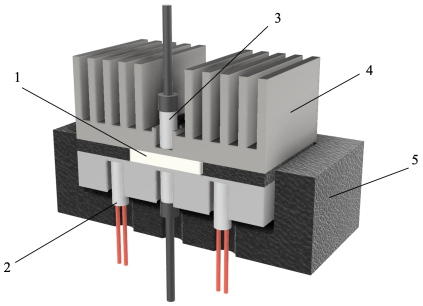

Fig. 5. Schematic cross-section of a device for verifying cooling efficiency in practice - 1) sample 2) heating element 3) temperature sensor 4) heat sink 5) insulation

The test sample was a disc with a diameter of 20 mm and a thickness of 3 mm. To ensure minimal thermal contact resistance and consistent heat transfer, a thermal paste was applied to both surfaces of the sample before it was integrated as a thermal bridge between the units. To minimize parasitic heat loss to the environment, both the heating block and the sample were encased in thermal insulation. The system was maintained at a constant target temperature of 60°C for a duration of 60 minutes. Temperature regulation was managed by an MCU-controlled relay employing a fine hysteresis logic and a fast response to ensure stability. The total energy consumption of the system, was quantified based on the cumulative duty cycle of the relay and the known power rating of the heating elements. This setup allowed for a comparative analysis of the material's ability to function as a thermal bridge over an extended period.

3. Result and Discussion

3.1. Mechanical Properties

The addition of 25 wt% h-BN resulted in significant deterioration of tensile properties. The ultimate tensile strength declined by 45.0% (from 35.94 MPa to 19.75 MPa) and Young's modulus decreased by 23.6% (from 0.267 GPa to 0.204 GPa), as summarised in Table 1.

These reductions are attributed to the poor interfacial adhesion between the chemically inert h-BN platelets and the epoxy-based photopolymer matrix. Without coupling agents, the platelet surfaces act as stress concentrators, promoting crack initiation under tensile loading. At 25 wt% loading, the high filler content also reduces the effective crosslinking density of the cured polymer network [4].

Property	0 wt%	25 wt%	Δ
Max. Force F_{max} [N]	482.98	391.02	-19.0%
Tensile Strength σ_{UTS} [MPa]	35.94	19.75	-45.0%
Elongation ε [%]	17.90	15.40	-14.0%
Young's Modulus E [GPa]	0.267	0.204	-23.6%

Tab. 1. Mechanical properties of neat resin and 25 wt% BN composite.

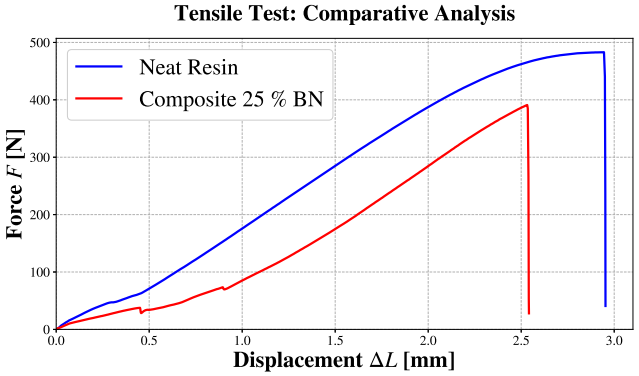

Fig. 6. Force-displacement curves for 0 wt% and 25 wt% h-BN samples.

Compressive properties were largely unaffected, with peak force remaining virtually identical (-0.1%) and compressive modulus showing a marginal increase of $+1.3\%$ (Table 2). Compressive strength declined by 17.9%, which is nonetheless considerably less than the tensile strength reduction. Under compressive loading, the rigid h-BN platelets redistribute the applied stress laterally, acting as a mechanical scaffold within the polymer matrix.

Property	0 wt%	25 wt%	Δ
Max. Force F_{max} [N]	2903.52	2900.46	-0.1%
Comp. Strength σ_c [MPa]	79.95	65.65	-17.9%
Young's Modulus E_c [GPa]	0.238	0.241	+1.3%

Tab. 2. Mechanical properties under compression for neat resin and 25 wt% BN composite.

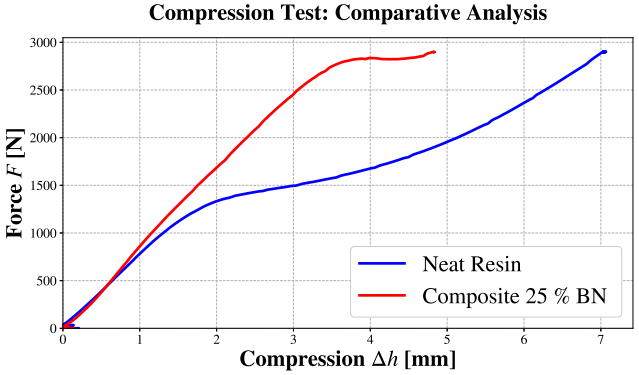

Fig. 7. Compression test results: force-displacement curves for neat resin and 25 wt% BN composite.

Flexural strength and modulus declined moderately by 9.2% and 19.5% respectively (Table 3). The smaller magnitude of these decreases compared to the tensile case reflects the mixed stress state in bending, where the compressive zone partially benefits from the platelet reinforcement described above.

Property	0 wt%	25 wt%	Δ
Max. Force F_{max} [N]	66.12	60.10	-9.1%
Flexural Strength σ_f [MPa]	49.63	45.07	-9.2%
Flexural Modulus E_f [GPa]	2.122	1.708	-19.5%

Tab. 3. Flexural properties of neat resin and 25 wt% BN composite.

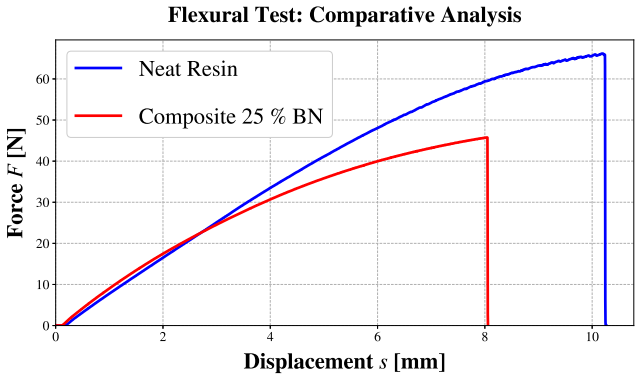

Fig. 8. Flexural test results: force-displacement curves for neat resin and 25 wt% BN composite with zero-point correction.

3.2. Material structure

The images captured using a scanning electron microscope (SEM) in Figure 9 reveal, when viewed from the side, a marked contrast in the morphology of the layered structure between the two groups of samples.

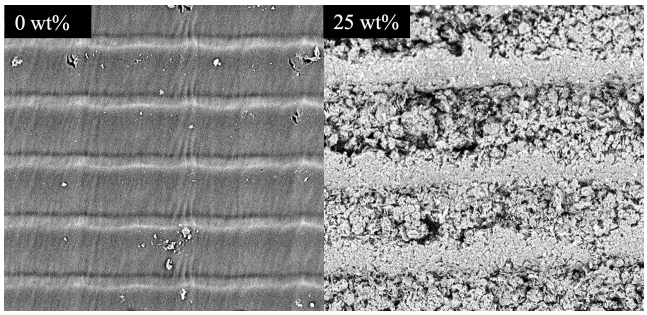

Fig. 9. SEM micrographs (1000x) of lateral surfaces: neat resin (left) and 25 wt% h-BN composite (right)

As expected, the neat resin sample (0 wt%) exhibits a relatively smooth and homogeneous surface. A characteristic layered structure is clearly discernible, where fine horizontal stripes correspond directly to the nominal layer height of 50 µm set during MSLA production. The interfaces between these polymerized layers appear continuous and tight.

In contrast, the addition of 25 wt% h-BN dramatically alters the microstructural picture. While the layered structure remains clearly discernible as distinct stripes, these stripes are heavily populated and densely filled with filler microparticles. The particle density indicates the successful integration of a large volume of ceramic reinforcing material, which supports the permeable heat pathways necessary for the accelerated heat transfer.

A crucial morphological observation, highlighted through comparison at identical magnification (1000×), concerns the resulting layer dimensions. Despite the same 50 µm nominal setting, the layers in the 25 wt% composite are visibly and distinctly thicker than those in the neat resin. This significant increase in layer height is a direct consequence of the markedly elevated viscosity of the BN-loaded photopolymer slurry. During the printing process, when the build platform is pressed down toward the FEP film at the bottom of the tank to form a new layer, this highly viscous composite material cannot flow sufficiently, which ultimately results in a wider layer dimension after UV curing.

3.3. Thermal Imaging and Heat Transfer

The surface temperature evolution was captured using a FLIR infrared thermography system. Upon activation of the heat source, the 25 wt% BN composite exhibited a significantly accelerated thermal response compared to the neat resin control group. Within the first 60 seconds of heating, a temperature gradient began to stabilize, revealing a surface temperature difference of approximately 6 °C in favor of the BN-reinforced sample. This rapid increase in surface temperature indicates that the h-BN micro-particles successfully established a percolating thermal network, effectively reducing the material's internal thermal resistance.

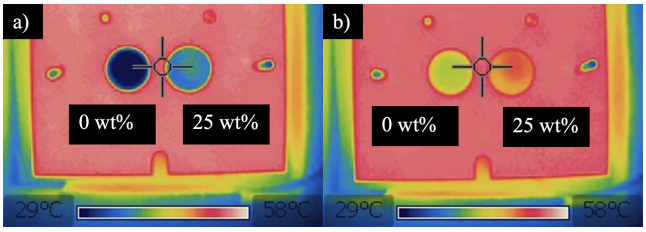

Fig. 10. IR thermograms of neat resin (0 wt%) and 25 wt% h-BN composite (a) at heating onset and (b) after 60 s.

Sample:	0 wt%	25 wt%
t (s)	ϑ (°C)	ϑ (°C)
5	29.3	30.2
30	35.8	38.9
60	40.2	46.2

Tab. 4. Comparison of surface temperature (ϑ) for neat resin (0%) and 25 wt% BN composite.

3.4. Cooling test

The thermal performance analysis revealed a substantial enhancement in heat dissipation for the 25% BN-loaded composite. Real-time monitoring (Fig.11) showed that the composite exhibits a more rapid increase in power consumption over time compared to the neat resin, indicating a faster thermal response and superior heat-bridging capabilities. Furthermore, despite identical cooling conditions, the composite reached a higher steady-state temperature on the heatsink interface (T = 28.4 °C) than the pure resin (T = 26.3 °C). This higher temperature at the cooling interface is a direct physical proof that the BN particles successfully facilitate a higher heat flux from the source to the cooler.

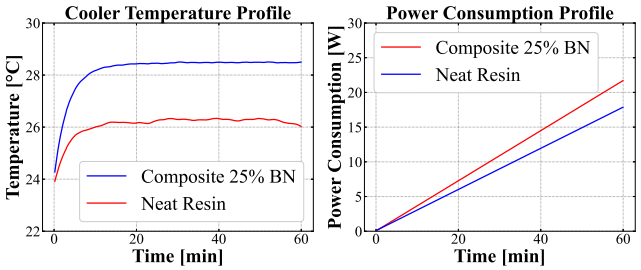

Fig. 11. Cooler temperature (left) and power consumption (right) profiles for neat resin and composite

The recorded 27.4% increase in total system energy consumption is inherently limited by the design and parasitic losses of the experimental setup; however, the experiment serves as a compelling demonstration of the material's practical efficiency. It can be assumed that upon the removal of parasitic phenomena inherent to the measuring apparatus, the difference between the samples would be even more pronounced, further highlighting the composite's potential for thermal management applications.

4. Conclusion

This study successfully demonstrated the fabrication and characterization of a thermally conductive stereolithography (SLA) composite using a commercial resin reinforced with 25 wt% hexagonal boron nitride (h-BN) microparticles. The integration of this high filler volume established a percolating thermal network, which significantly accelerated the material's thermal response. Infrared thermography revealed a surface temperature difference of approximately 6 °C compared to the neat resin after 60 seconds of heating. Furthermore, active cooling tests confirmed a 27.4% increase in total system energy consumption, validating the composite's superior heat-bridging capabilities.

However, the microstructural analysis highlighted that the high viscosity of the composite slurry led to an increased layer thickness despite the 50 µm nominal setting. Mechanically, the composite exhibited a performance trade-off, primarily due to poor interfacial adhesion between the chemically inert h-BN platelets and the photopolymer matrix. While compressive properties remained highly stable, showing a marginal 1% increase in compressive modulus , the tensile and flexural strengths decreased by 45% and 9%, respectively.

Overall, the findings indicate that with further development, the 25 wt% h-BN SLA composite holds significant promise for the future additive manufacturing of compact electronic systems. While its immediate applicability is currently limited by the observed mechanical trade-offs and processing challenges , future advancements such as the introduction of coupling agents to improve interfacial adhesion could eventually make it a highly viable material. Once optimized, it will offer a valuable solution for applications such as integrated heat sinks or battery housings, where rapid heat dissipation and electrical insulation are paramount.

Acknowledgements

Research described in the paper was supervised by Ing. Petr Veselý, Ph.D., FEE CTU in Prague and supported by the Czech Grant Agency of Czech Technical University in Prague, grant no. SGS24/137/OHK3/3T/13.

References

[1] ZHA, J.-W., WANG, F., WAN, B. Polymer composites with high thermal conductivity: theory, simulation, structure and interfacial regulation. *Progress in Materials Science*, 2025, vol. 148, p. 101362.

[2] HUANG, C., QIAN, X., YANG, R. Thermal conductivity of polymers and polymer nanocomposites. *Materials Science and Engineering: R: Reports*, 2018, vol. 132, pp. 1–22.

[3] TSEKMES, I. A., KOCHETOV, R., MORSHUIS, P. H. F., SMIT, J. J. Thermal conductivity of polymeric composites: a review. In *2013 IEEE International Conference on Solid Dielectrics (ICSD)*. IEEE, 2013, pp. 678–681.

[4] VESELÝ, P., NOVÁKOVÁ, A., LANG, V., DUŠEK, K. Novel ceramic-polymer composite for stereolithography with enhanced thermal conductivity. In *2025 International Spring Seminar on Electronics Technology (ISSE)*. IEEE, 2025, pp. 1–6.

[5] ALSHIHABI, M., KAYACAN, M. Y. Effect of nanosized carbon nanotubes, titanium nitride and cubic boron nitride powders on mechanical and thermal properties of SLA 3D printed resin composites. *Polymer Composites*, 2024, vol. 45, no. 17, pp. 15561–15573.

[6] NGO, T. D., KASHANI, A., IMBALZANO, G., NGUYEN, K. T. Q., HUI, D. Additive manufacturing (3D printing): a review of materials, methods, applications and challenges. *Composites Part B: Engineering*, 2018, vol. 143, pp. 172–196.

[7] YUAN, C., LI, J., LINDSAY, L., CHERNS, D., POMEROY, J. W., LIU, S., EDGAR, J. H., KUBALL, M. Modulating the thermal conductivity in hexagonal boron nitride via controlled boron isotope concentration. *Communications Physics*, 2019, vol. 2, no. 1, p. 43.

[8] YAO, C., LEAHU, G., HOLICKY, M., LIU, S., FENECH-SALERNO, B., LAI, M. C., LARCIPRETE, M. C., DUCATI, C., DIVITINI, G., VOTI, R. L. et al. Thermally conductive hexagonal boron nitride/polymer composites for efficient heat transport. *Advanced Functional Materials*, 2024, vol. 34, no. 46, p. 2405235.

[9] PAZOUREK, J., PRAŽÁK, O., PROCHAZKA, R., STRAKA, L., VESELÝ, P. Development of piezoelectric polymer composites for stereolithography. *IEEE Transactions on Components, Packaging and Manufacturing Technology*, 2025, vol. PP, pp. 1–1.

[10] ZYP COATINGS, INC. BN Powder ZG [Online]. Available: `https://www.zypcoatings.com/product/bn-powder-zg/`. Accessed: 12-Mar-2026.

About Authors. . .

The authors are Master's students at the Faculty of Electrical Engineering (FEL), Czech Technical University in Prague, and belong to the 3DP Lab Research Group at the Department of Electrotechnology. Their research centers on the development of innovative materials for FFF and SLA 3D printing, with a specific focus on high-performance applications within the electronics and power engineering industries.